Detector Performance and Upgrades of the Pierre Auger Observatory

Dissertation

zur Erlangung des akademischen Grades eines

Doktors der Naturwissenschaften (Dr. rer. nat.)

der Fakultät Mathematik und Naturwissenschaften
Fachgruppe Physik
der Bergischen Universität Wuppertal

vorgelegt von

Sven Querchfeld

Juni 2023

1. Gutachter:
Prof. Dr. Karl-Heinz Kampert
Bergische Universität Wuppertal

2. Gutachter
Prof. Daniele Martello
Università del Salento

Abstract

Open questions in cosmic ray physics persist regarding the unknown composition and acceleration mechanisms at the highest energies. The Pierre Auger Observatory, measuring cosmic rays via extensive air showers developing in the Earth's atmosphere, has already provided evidence suggesting a heavier composition at these highest energies and aims to definitively determine the particle types by upgrading its detectors.

Equipping the Fluorescence Telescopes, which observe the air shower development in the atmosphere from the side via fluorescence light, with more efficient photosensors enhances their field of view and thus the exposure. Since the more efficient sensors do only come with round faceplates, a new light guide is introduced to cover the dead space between the pixels of the nearly hexagonal grid on a spherical surface. Based on the Winston cone design, a concentrator was developed to fit into the existing camera optics. A prototype with 48 pixels was installed to test the new system consisting of a more efficient photomultiplier (PMT) plus modified Winston cone and a performance analysis using various calibration methods is done.

As an essential part of the AugerPrime upgrade, the Surface Detector will be equipped with an additional scintillation detector on top of the Water-Cherenkov stations. Being more sensitive to the electromagnetic component of the air shower in comparison to the water volume below, it will enhance the discrimination ability to determine the mass of the primary cosmic ray. In this work, the selection of an appropriate PMT to read out the scintillator is presented. A suitable sensor is found in a selection process based on characteristics measured in the laboratory. The integration of the selected PMT into the detector is achieved by introducing a voltage divider with the emphasis on low power consumption while still keeping the high linearity over a wide dynamic range. Their usage in the first prototype stations is presented and a first analysis of the raw data shown.

Kurzfassung

Offene Fragen in der Physik der kosmischen Strahlung bleiben mit der unbekannten Zusammensetzung der Primärteilchen sowie den Beschleunigungsmechanismen zum Erreichen der höchsten Energien. Das Pierre-Auger-Observatorium, welches die kosmische Strahlung über ausgedehnte Luftschauer vermisst, die sich in der Erdatmosphäre entwickeln, hat hierfür bereits erste Hinweise zu einer schwereren Zusammensetzung bei den höchsten Energien geliefert und will durch die Aufrüstung seiner Detektoren die Komposition endgültig klären.

Die Ausstattung der Fluoreszenz-Teleskope, welche die Luftschauerentwicklung in der Atmosphere von der Seite mittels Fluoreszenzlicht beobachten, mit leistungsfähigeren Photosensoren vergrößert deren Sichtfeld und erhöht damit die Anzahl der beobachtbaren Luftschauer. Da die leistungsfähigeren Sensoren jedoch nur mit runden Photokathodenflächen erhältlich sind, wird ein neuer Reflektor vorgestellt, um den toten Raum zwischen den einzelnen Pixeln des nahezu sechseckigen Gitters auf einer kugelförmigen Oberfläche abzudecken. Auf der Grundlage des Winston Cone Designs wurde ein Reflektor entwickelt, der in die bestehende Kameraoptik passt. Ein Prototyp mit 48 Sensoren wurde installiert, um das neue System zu testen, das aus einem effizienteren Photomultiplier (PMT) und einem modifizierten Winston Cone besteht, und es wurde eine Leistungsanalyse mit verschiedenen Kalibrierungsmethoden durchgeführt.

Als Hauptteil des AugerPrime-Upgrades werden die Oberflächendetektoren mit einem zusätzlichen Szintillationsdetektor oberhalb der Wasser-Cherenkov-Stationen ausgestattet. Da er empfindlicher auf die elektromagnetische Komponente des Luftschauers im Vergleich zum darunter liegenden Wasservolumen reagiert, wird er die Unterscheidungsfähigkeit zur Bestimmung der Masse der primären kosmischen Strahlung verbessern. In dieser Arbeit wird die Auswahl eines geeigneten PMTs zum Auslesen des Szintillators vorgestellt. Ein geeigneter Sensor wird in einem Auswahlverfahren auf der Grundlage von im Labor gemessenen Eigenschaften gefunden. Die Integration des ausgewählten PMT in den Detektor wird durch die Einführung eines Spannungsteilers erreicht, wobei der Schwerpunkt auf einem geringen Stromverbrauch liegt, während die hohe Linearität über einen großen dynamischen Bereich erhalten bleibt. Ihre Verwendung in den ersten Prototyp-Stationen wird vorgestellt und eine erste Analyse der Rohdaten gezeigt.

Contents

Chapter 1

Introduction

The Earth is constantly hit by particles from space. Their first detection dates back more than 100 years ago, when the origin of radiation present at the Earth's surface was found to be extraterrestrial [1, 2]. This opened up the field of astroparticle physics, which led to many great discoveries (e.g. using cloud chambers). Many questions have been answered since then, and the spectrum of cosmic rays is one of the best measured quantities, spanning a range of 11 orders of magnitude in energy and 32 orders in flux. The low energy part is well known, but there are still fundamental aspects to be discovered for the highest energies. Most prominent questions include how particles can be accelerated to these extreme energies, exceeding the LHC, the world's highest-energy particle collider, by seven orders of magnitude. As the flux of cosmic rays at the highest energies above 10^{18} eV is steeply falling, space or airborne experiments are not able to detect these extreme events with accurate statistics. In order to detect enough events in a reasonable amount of time, it is necessary to utilise the detection of secondary particles, products of a primary cosmic ray interaction with the Earth's atmosphere that creates an extensive air shower.

The largest detector to measure cosmic rays at the highest energies is the Pierre Auger Observatory located in the Argentinian Pampas. It combines independent detection mechanisms to measure the cascade of secondary particles. The Surface Detector (SD), a ground array of detector stations, is covering an area of about $3000\,\mathrm{km}^2$ and the Fluorescence Detector (FD) is measuring the particle shower development during dark nights. Since the start of the construction of the observatory in 2000, newer hardware components have become available and could increase the overall performance of the detectors. This thesis is focused on upgrades of the two main detector parts of the Pierre Auger Observatory, the fluorescence telescopes and the surface detector stations.

With the FD's taking data since 2004, the sensitivity of the optical sensors used in the telescopes could be enhanced. A possible upgrade of these sensors is discussed, including the modifications needed to implement the currently available options into the existing hardware frame. This includes changes in the optical system to efficiently concentrate light to the sensitive area of the sensors.

In order to tackle the question of mass composition of cosmic rays at the highest energies, the 'AugerPrime' upgrade will introduce new detectors to increase the discrimination power of primary particles interacting with the Earth's atmosphere. One new part will be an additional scintillation detector on top of each SD station. This thesis concentrates on the optical sensor to read-out the scintillator, covering the sensor selection, development of prototype stations, and the first analysis of raw data from the operation in the field in Argentina.

Thesis Outline

Chapter 2 will give a brief overview on cosmic ray physics and their detection, focusing on the highest energies. The Pierre Auger Observatory will be introduced in Chapter 3. Both major detector systems, which are topic to an upgrade in this thesis, namely the Fluorescence Detector and the Surface Detector, are described.

Chapter 4 will discuss a possible upgrade of the FD telescopes by using newer optical sensors. This requires changes to the optical system, in particular the light collectors which need to be adapted to the new sensors. Therefore the development of a Winston cone and the installation of a prototype in one telescope will be presented.

In the course of the AugerPrime upgrade the existing detector stations will be equipped with an additional scintillation detector on top. The selection and installation of an appropriate photomultiplier used to read out the detector are presented in Chapter 5. Measurements of the optical properties of the sensors were performed to ensure the sensors are satisfying the comprehensive demands to the optical detector. Finally the first SD stations were equipped with prototypes of these detectors and a first analysis of the raw data will be presented.

Chapter 6 gives a summary and future prospects of the performed upgrades.

Chapter 2

Cosmic Rays

This chapter gives a short introduction and brief overview of the current status in cosmic ray physics.

High energetic particles travelling through space are called cosmic rays. Primary cosmic rays consist mainly of protons (about 90%), 9% alpha particles, and the rest being heavier nuclei, with the composition varying over the energy range [3]. At energies $E \lesssim 10^{16}\,\mathrm{eV}$ they originate from astrophysical sources like the Sun or supernova remnants, and come from inside or outside our galaxy. The origin at the highest energies ($E \gtrsim 10^{18}\,\mathrm{eV}$) remains still unknown, with possible candidate sources being starburst galaxies, active galactic nuclei, radio galaxies or quasars [4].

Started already over 100 years ago, there are still questions to be answered regarding the composition and origin at the highest energies.

2.1 Energy Spectrum

The energy spectrum of cosmic rays is one of the widest measured quantities, ranging several orders of magnitude in energy and flux. It describes the number of incoming cosmic rays with respect to their energy. Over a wide energy range, the spectrum follows a power law. The differential flux (J) is given by

$$J(E) = \frac{dN}{dE} \propto E^{-\gamma} \tag{2.1}$$

with the spectral index γ which for most part is equal to 2.7. Figure 2.1 shows the all-particle cosmic ray spectrum ranging over several orders of magnitude measured by various experiments. The spectrum is scaled by a factor of $E^{2.6}$ to make prominent features more visible.

A change of the spectral index at an energy of about $5 \times 10^{15}\,\mathrm{eV}$ from 2.7 to 3.1 is called the *knee*. First reported in [6], the steepened spectrum is thought to originate in galactic sources reaching their maximum energy to accelerate protons. This maximum energy is reached gradually for nuclei with higher charges. A further steepening occurring at about $10^{16.9}\,\mathrm{eV}$ is referred to as *second knee* or *heavy knee*. This suggests that the theoretical maximum energy for iron from galactic sources is reached.

At an energy of $\sim 5 \times 10^{18}\,\mathrm{eV}$, the spectrum hardens again. The index changes to about 2.5 (see Fig. 2.2), creating a kink in the spectrum, referred to as *ankle*. With the galactic sources believed to have reached their maximum acceleration, this suggests a transition to sources with extragalactic origin.

The data implies a softening at $1.4 \times 10^{18}\,\mathrm{eV}$ to $\gamma = 3.08$ and at an energy of about $5 \times 10^{19}\,\mathrm{eV}$ a strong cutoff with a spectral index of about 5.2 is found [7]. As the sources and the composition at the highest energies are unknown, the reason for the cutoff is under debate. A possible scenario was proposed already in 1966 by Greisen [8] and independently by Zatsepin and Kuzmin [9], known as the GZK cutoff. Here the assumed all-proton UHECRs interact with the cosmic microwave background (CMB) photons creating a Δ resonance, and producing pions via:

$$p + \gamma_{\mathrm{CMB}} \rightarrow \Delta^{+} \rightarrow n + \pi^{+} \tag{2.2}$$

$$p + \gamma_{\mathrm{CMB}} \rightarrow \Delta^{+} \rightarrow p + \pi^{0}. \tag{2.3}$$

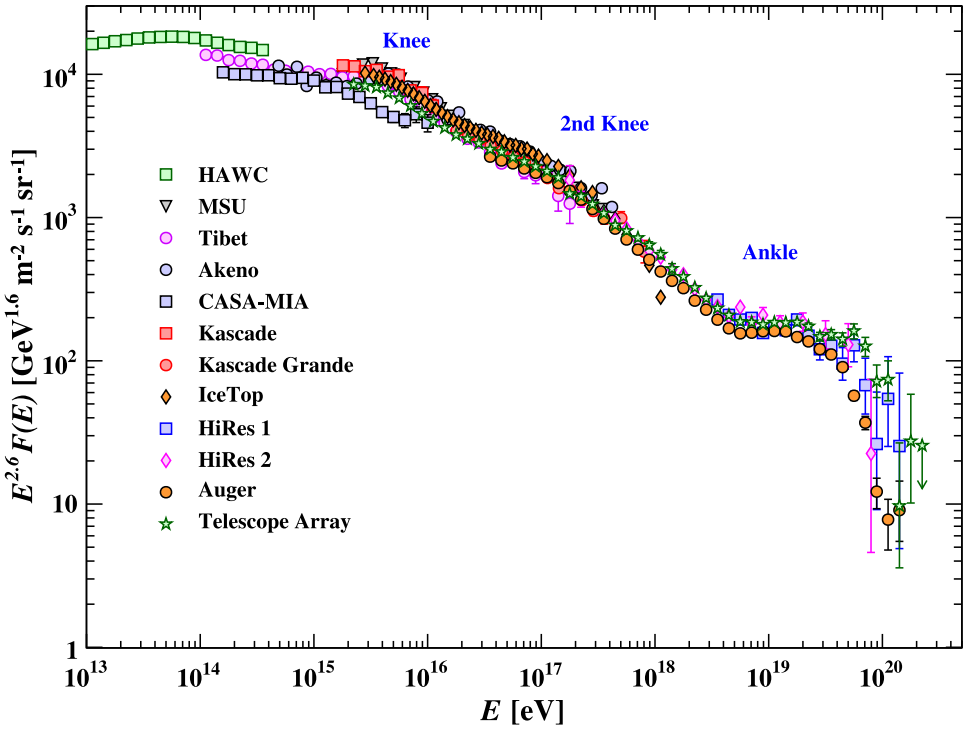

Figure 2.1: Energy spectrum of cosmic rays measured by various experiments. The spectrum is scaled by a factor of $E^{2.6}$ to highlight prominent features [5].

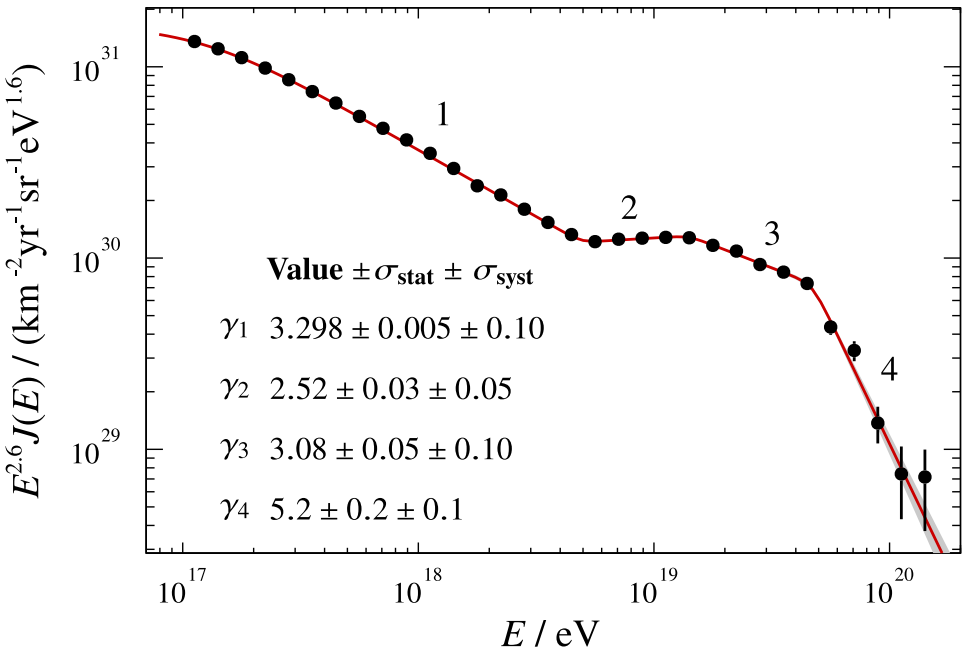

Figure 2.2: Cosmic ray energy spectrum at the highest energies measured by the Pierre Auger Observatory. Modified from [7].

The cross section for this reaction has a threshold for proton energies at $\sim 5 \times 10^{19}$ eV, limiting the distance to observe higher energies to less than 100 Mpc.

Somewhat similar to the GZK cutoff is the situation for nuclei with an $A > 1$. Also reacting with the CMB or the infrared background, nuclei undergo the process of photodisintegration [8, 9], where up to several nucleons can be ejected from the nucleus. This process gradually reduces the range of heavier CRs, limiting the range of e.g. a 2×10^{20} eV iron nucleus to less than 10 Mpc [10, 11].

Another explanation is the acceleration limit of extragalactic sources. Similar to the limit at the *knee* for the galactic sources, extragalactic sources could reach their maximum achievable acceleration energy. This again is proportional to the charge of the nucleus, which would imply the composition at the highest energies is iron dominated.

Thus, measuring the composition and origin of CRs at the highest energies would help to answer these unresolved questions.

2.2 Detection

The cosmic ray spectrum spans one of the widest ranges of energy and flux in science, respectively. To cover these extreme ranges with various experiments, different approaches need to be used. With the flux being quite high at low energies, direct detection can be done with satellite experiments, such as the AMS-02 detector at the ISS [12]. As the flux decreases with increasing particle energy, the detectors aperture need to get bigger in order to measure ultra high energy particles with sufficient statistics in a reasonable amount of time. With space and airborne experiments reaching a feasible limit at an energy of a few TeV, detectors with a suitable size will need to be earthbound. As primary particles hit the Earth, they interact with the Earth's atmosphere, generating extensive air showers.

2.2.1 Extensive Air Showers

As the flux of cosmic rays decreases to less than one particle per km^2 and century, the direct detection of UHECRs is no longer feasible. To build detectors with a reasonable size, it is necessary to rely on ground based experiments. Reaching Earth, primary cosmic ray particles interact with the Earth's atmosphere, creating secondary particles. These cascade into further reactions, generating many new particles travelling down to the ground, and are called extensive air showers (EAS).

The development of such an EAS can be categorised into three different types of interactions. At the first interaction of the incoming primary with a nucleus of e.g. an N_2 molecule, the production of charged and neutral kaons and pions along with spallation products occurs. These particles interacting further are called the hadronic component of an extensive air shower. If these secondary kaons and charged pions decay before further interacting, they produce muons and neutrinos. With a long mean lifetime of 2.197×10^{-6} s [5] most muons reach the ground without interacting any further in the atmosphere and are referred to as the muonic component. If a muon does decay or gamma rays from the neutral pion decay perform pair production, electrons and positrons are produced. If energetic enough, these will produce more gammas via bremsstrahlung, which can perform pair production again. Thus, it develops a cascade of $e^{\pm}$ and γ. This is the electromagnetic component of the particle shower and can be modelled by the Heitler model [13].

2.2.2 Measurement Techniques

Through the measurement of these secondary particles, properties of the primary particle can be deduced. Ranging from the recording of the shower development in the atmosphere to measuring the 'footprint' of particles reaching the ground, a variety of different detection techniques have

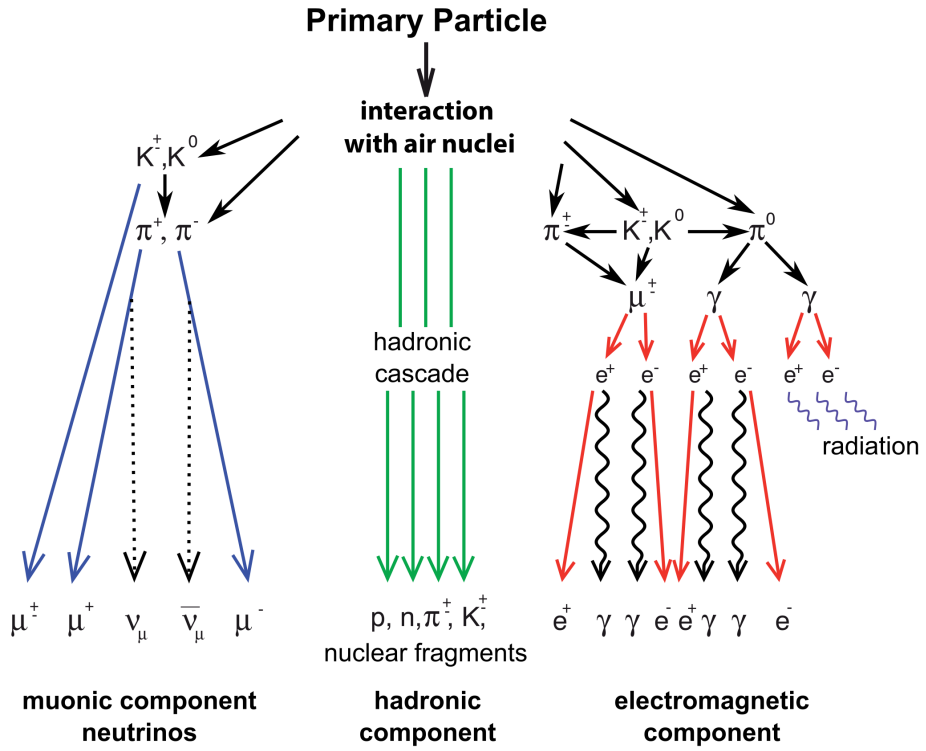

Figure 2.3: Schematic of cosmic ray interactions in the atmosphere. The air shower development can be divided into three different parts, the electromagnetic component, the hadronic component, and the muonic component including neutrinos. Taken from [14].

been developed. Figure 2.4 depicts a sketch of various detection methods used by leading experiments in UHECR cosmic ray physics, observing different parts of the shower. Directed searches, such as Cherenkov telescopes, are looking for point sources at the sky, utilising Cherenkov light emission of charged particles travelling trough the atmosphere. Similarly, radio antennas detect the EM component in the megahertz range. When detecting particles at ground level, different enclosed detector types come into play. Calorimeters or tracking detectors can measure the particles at ground level, while buried detectors are designed to measure only the highly penetrable muonic component.

In this thesis the focus is on the measurement of fluorescence light, tracking the longitudinal development of the EAS, and on water-Cherenkov detector stations and scintillator detectors. For high energetic cosmic rays ($E \gtrsim 10^{17}\,\mathrm{eV}$) fluorescence telescopes can measure the particle shower development from the side view. For particles interacting with the atmosphere, N_2 molecules can be excited and upon de-excitation release photons in the UV spectrum. The release is isotropic and the measurable signal quite faint, limiting observations to dark moonless nights. The measurement is almost calorimetric. The shower development is described by the number of particles, N, for the traversed atmospheric depth, X, given in $\mathrm{g/cm^2}$. The longitudinal shower profile can be described by the Gaisser-Hillas function [15],

$$N(X) = N_{\max} \left(\frac{X - X_0}{X_{\max} - X_0} \right)^{\frac{X_{\max} - X_0}{\lambda}} \exp\left(\frac{X_{\max} - X}{\lambda} \right), \tag{2.4}$$

where $N_{\max}$ is the maximum number of particles at the shower depth $X_{\max}$. X_0 and λ are fit parameters related to the primary particles energy and mass. Showers are typically observed in a distance between 5 to 35 km, depending on the energy and shower geometry, but due to measurements done in moonless nights, the duty cycle is only about $10 - 15\%$ [3].

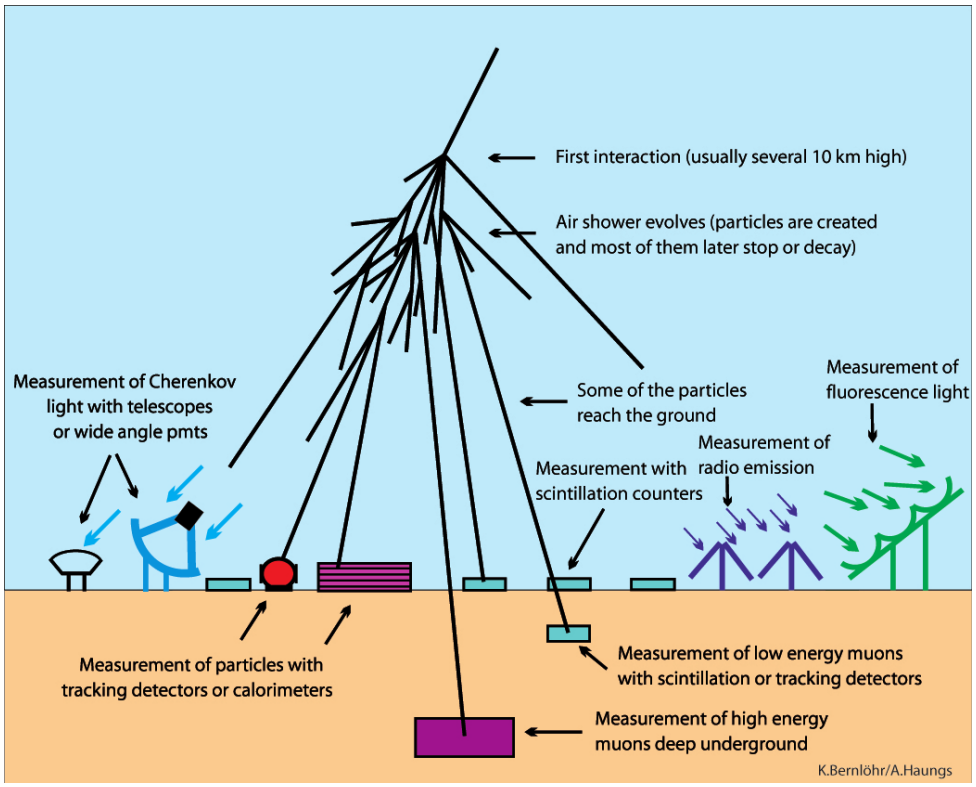

Figure 2.4: Illustration of the various detection techniques to measure extensive air showers. Adopted from [19].

While the fluorescence telescopes record the shower development in the atmosphere, water-Cherenkov detectors and scintillator detectors on the other hand detect only a small time fraction of the EAS. Usually placed in a regular grid on the ground, these surface detectors measure EAS by looking for time coincidences of signal in neighbouring stations. WCDs detect particles moving faster than the speed of light in the respective medium. Scintillators emit a small flash of light when struck by a traversing particle or radiation, due to excitation of atoms and molecules. Coupled to a light detector, e.g. a photomultiplier, the measured signal can be converted to a number of particles. With the timing information of each detector, the arrival direction can be reconstructed. Due to the measurement at discrete spots on the ground, the core position can be found by fitting a lateral distribution function (LDF) to the signal response of the detectors. From this the energy of the primary particle can be derived (see Section 3.1.3). The energy range of the detector is depending on the spacing of the stations as well as the atmospheric height. Advantages of surface detectors are a duty cycle of almost 100%. But with detecting just a fraction of the particle shower, the energy reconstruction depends on the modelling of the shower development.

With the different detection systems being sensitive to different properties of the primary particle, a combination enables an accurate reconstruction. A hybrid concept using at least two independent types of measurement at the highest energies has been pioneered by the Pierre Auger Observatory [16] and is now utilised also by experiments such as e.g. the Telescope Array [17], and the Large High Altitude Air Shower Observatory [18].

2.3 Mass Composition

The composition of cosmic rays varies depending on their energy. The low energy spectrum is dominated by light particles emerging from the Sun. These can be measured directly with

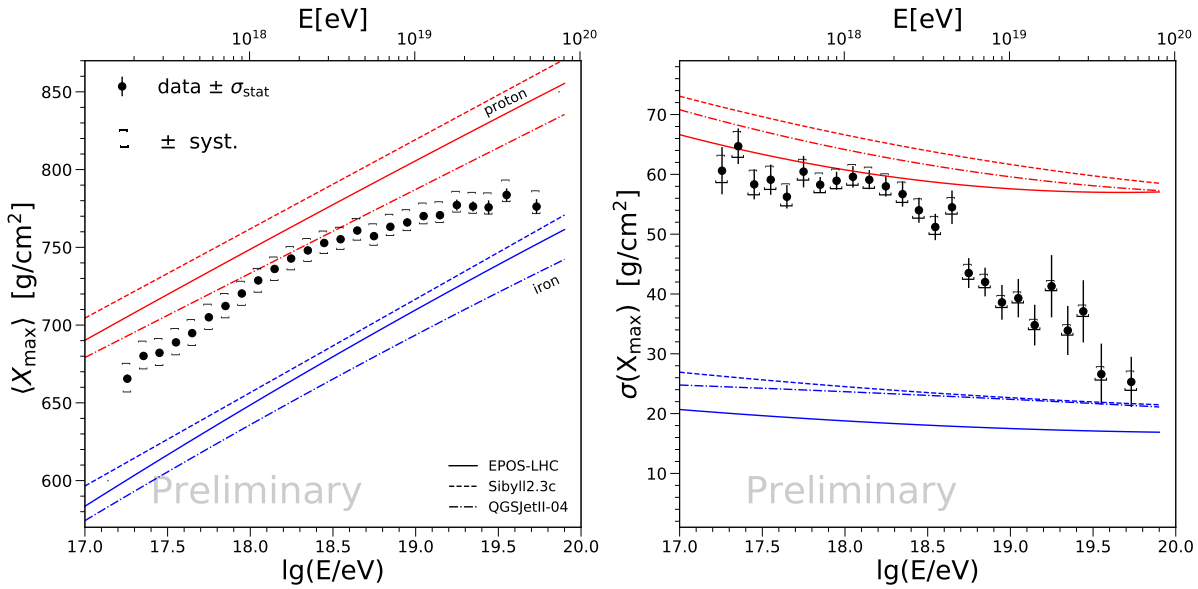

Figure 2.5: $\langle X_{\max} \rangle$ and $\sigma(X_{\max})$ measurements of the Pierre Auger Observatory in comparison to recent model predictions for pure proton and iron nuclei composition. From [23].

spaceborne detectors, such as the AMS.

As UHECRs are measured via secondary particles, the determination of the primary particle depends on models describing the air shower development within the atmosphere. To derive the primary type of an EAS, the atmospheric depth of the shower maximum is a good measure. Heavier primaries do not penetrate as deep into the atmosphere and develop their shower maximum ($X_{\max}$) at higher altitude compared to lighter primaries. The shower development is measured in terms of atmospheric depth, given in $\mathrm{g/cm^2}$. Latest measurements of the maximum shower depth of the Pierre Auger Observatory are shown in Fig. 2.5. For comparison, purely proton or iron based predictions of recent hadronic interaction models, such as EPOS-LHC [20], Sibyll2.3c [21], and QGSJetII-04 [22], are also shown. These energies cannot be reached with current experiments, e.g. at the LHC. Thus, the models, based on collider data with relevant statistics, are extrapolated to the highest energies. The composition at the energy of the ankle appears to be proton dominated. Here, the Auger measurement is in agreement with the Telescope Array measurement. For the highest energies though, the trend tends towards a heavier composition in the Auger measurements.

Due to the different multiplicity of protons and heavier ions, air showers initiated by lighter primaries have a more pronounced electromagnetic component, while those from heavier primaries produce a larger number of muons. Therefore, the shower development can give a hint on the primary as well. Measuring the ratio of electromagnetic and muonic component can offer insights into the origin of the primary particle. Combining e.g. scintillators with water-Cherenkov detectors (as will be done in the Auger Prime Upgrade, see Chapter 5), will increase the detectors discrimination powers and allow a more precise determination of the primary mass.

Chapter 3

The Pierre Auger Observatory

The largest detector to measure cosmic rays at the highest energies is currently the Pierre Auger Observatory. It is located in the Pampa Amarilla, near the city of Malargüe in the Province of Mendoza, western Argentina. Constructed on a high plain at an altitude of about 1400 m, the detectors span over an area of about 3000 km^2 [16]. The observatory uses a hybrid concept, with a Surface Detector (SD) array to measure the footprint of an extensive particle shower on the ground, and a Fluorescence Detector (FD) on the sides, observing the shower development in the atmosphere. While the SD array has a duty cycle of nearly 100% above a primary particle energy of $10^{18.5}$ eV, the fluorescence telescopes only record particle showers in clear moonless nights, with an observation time of about 13% [24]. With the possibility of cross-calibration between the two independent detector systems, using hybrid events (seen in both detector systems simultaneously), the shower energy measurement of the FD can be used to perform an absolute calibration of the SD signal. The construction of the observatory was finished in 2008 and was already taking data since 2004 with the first few hundred stations starting to operate. Besides the two baseline detectors, several extensions have already been tested with the most prominent addition, a radio antenna array, being included into the official detection mechanism.

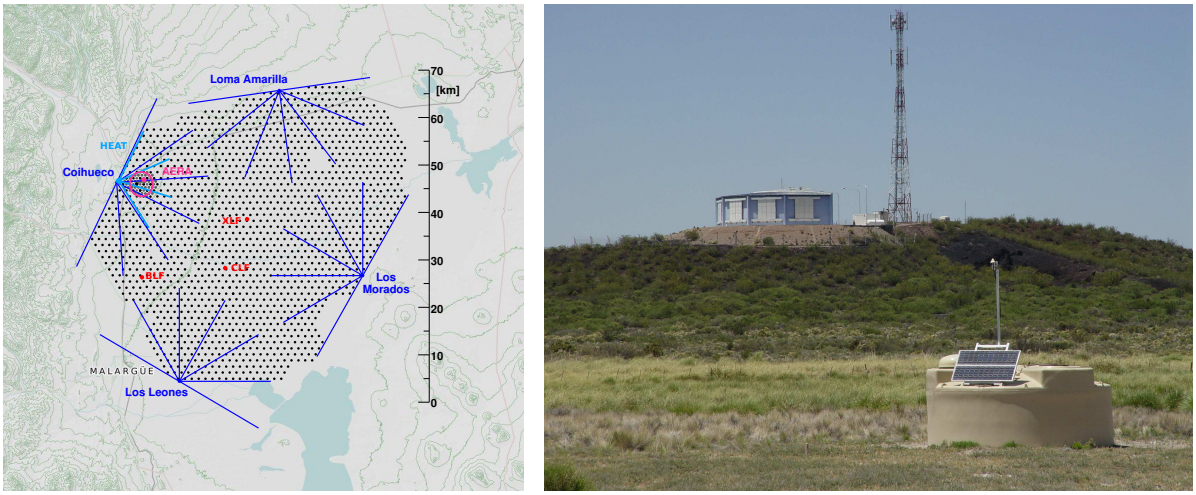

Figure 3.1: Map of the Pierre Auger Observatory (left), with each dot representing one of the 1660 surface detector stations. The field of view of the 24 surrounding fluorescence telescopes is indicated in blue, and three additional telescopes with a higher elevation angle at the Coihueco site (light blue). The AERA radio array (magenta) is shown next to the denser *infill*-array. The two laser facilities, CLF and XLF, are placed in the middle of the array. An SD station in the Pampas with an FD building next to a communication tower in the background (right).

3.1 Surface Detector

The surface detector array of the Pierre Auger Observatory consists of about 1660 water-Cherenkov detectors (WCD), which are arranged in a triangular grid with a spacing of 1.5 km, covering an area of about 3000 km^2 (see Fig. 3.1). At an energy threshold of 3×10^{18} eV its duty cycle is nearly 100% for zenith angles smaller than 60°. As an extension to the regular array, a small area is equipped with additional stations. Placed at a denser spacing of 750 m, the *infill*-array reduces the energy threshold down to 3×10^{17} eV [25].

A single SD station consists of a polyethylene water tank with a diameter of 3.6 m and a height of 1.2 m. Inside, a highly reflective liner contains 12.000 ℓ of ultra-pure water. On top, three 9 inch photomultiplier tubes (PMTs) look downwards into the liner volume through clear polyethylene windows, recording the Cherenkov light produced by particles passing through or stopping inside the water volume. The read-out electronics is combined with the communications and power control on the Unified Board (UB). The PMT signals are digitised by 10-bit analogue-to-digital converters (ADC) at a rate of 40 MHz [16]. To increase the dynamic range of the signal read-out, which is limited by the ADC, each PMT signal is split into two channels. While one channel takes the signal from the PMT's anode, a second channel is connected to the last dynode (inverted and amplified by a factor of 32) [26]. Combined, the two channels cover a signal range resulting in a total dynamic range of 15 bits for one PMT.

Each station works autonomously, with power being provided by two solar panels combined with two 12 V, 105 Ah, low-maintenance batteries. The communication is done via radio [27] to the central data acquisition system (CDAS), while timing and positioning is done by a GPS module.

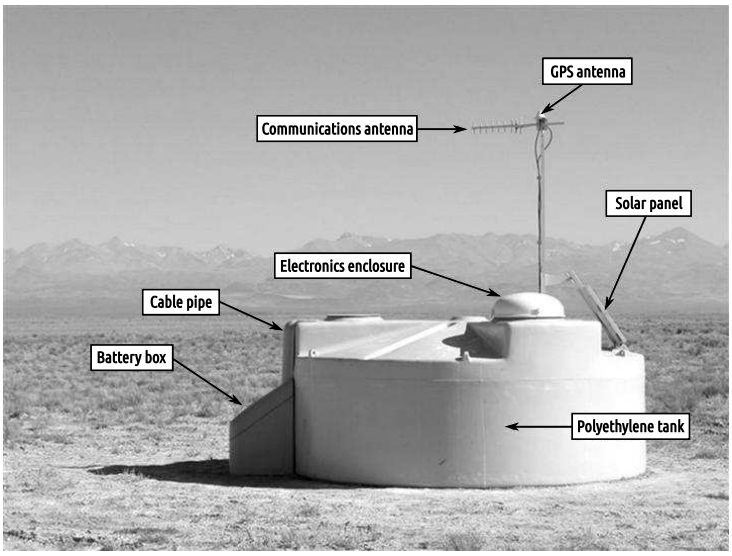

Figure 3.2: A surface detector station with labelled components [16].

3.1.1 Calibration

Due to the large amount of detectors and the remoteness of the stations, the calibration of an SD station is automated. To level the signal of the different stations, the signal of atmospheric muons is used to perform a calibration. With a rate of approximately 2500 Hz, single muons hit the detector [28]. For the three large PMTs, the peak and charge of small signals is measured every minute. Stored in a separate memory from the event files, a histogram is obtained, giving a mean ADC value for the single muon charge (Fig. 3.3, right). Since the atmospheric muons arrive not only vertically but from different angles, and thus impact the mean signal due to different trajectories inside the water volume, this needs to be corrected for. In a reference measurement

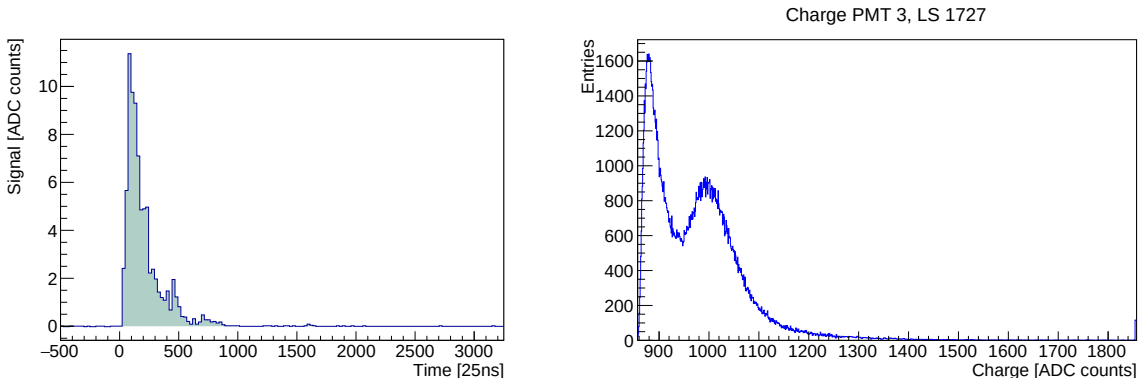

Figure 3.3: Sample trace and charge histogram for a single SD station (St. 1727, Event 45012136). The charge distribution gives the conversion from ADC channels to VEM units.

for a single station, additional scintillation counters were used as muon telescopes to verify the trajectory of the muons [29]. The extracted charge is used to determine the conversion to the energy deposition of a vertical and central through-going muon. The introduced unit is a vertical equivalent muon (VEM) and converts the measured mean charge of the calibration histogram to approximately 1.09 VEM for the sum of the three PMTs.

3.1.2 Trigger

Due to the large amount of stations and limited bandwidth for communication, different levels of trigger are introduced to allow a preselection and on-site discrimination. At station level the signal needs to pass a threshold of 3.2 VEM for a simple threshold trigger (T2) or 0.2 VEM for 13 time bins for a time-over-threshold (ToT) trigger. The data is only recorded when at least three clustered stations fulfil these requirements (T3) [30]. The data is sent to the central data acquisition system (CDAS). More advanced triggers based on the geometry of triggered stations is performed offline.

3.1.3 Reconstruction

For an SD-only reconstruction the events are reconstructed by analysing the footprint on the ground. From the sent T3 triggers, the size and start times of the signals are inspected and quality cuts, such as minimum number of stations etc., applied to identify candidate shower events. With the exact positioning from the GPS modules of the stations, main particle shower properties, such as the direction of the shower axis and the shower core position on the ground, are calculated from the timing information of the stations for these events, assuming a spherical shower front travelling with the speed of light [31].

The shower size is estimated using the lateral distribution of the signal perpendicular to the shower axis, which is described by a modified Nishimura-Kamata-Greisen function [32, 33],

$$S(r) = S(r_{\text{opt}}) \left(\frac{r}{r_{\text{opt}}}\right)^{\beta} \left(\frac{r + r_1}{r_{\text{opt}} + r_1}\right)^{\beta+\gamma} \tag{3.1}$$

with a fixed $r_1 = 700\,\text{m}$. The optimal value for the distance r_{opt}, so that the estimator $S(r_{\text{opt}})$ is minimised, is dependent on the structure and spacing of the detector array. For the isometric triangular SD array with a spacing of 1500 m, the optimal distance, r_{opt}, is about 1000 m. To account for increased slant depth for inclined showers, the $S(1000)$ is converted to the median zenith angle, 38°, of all showers using the constant intensity cut (CIC), via $S_{38} = S(1000)/f_{\text{CIC}}(\theta)$ [15]. This corrects for a smaller observed shower size for more inclined

showers, which have a more attenuated electromagnetic cascade. The shower size estimator $S(1000)$ can be used to derive the energy of the air shower. With an additional correction for atmospheric and geomagnetic effects, S_{38} can be used as zenith independent energy estimator. Utilising the almost-calorimetric energy measurement from the FD (see Section 3.2), using hybrid events with independently measured FD and SD energy estimate, one can set the energy scale and parametrise it using a power law with the fitting parameters A and B [34]:

$$E_{\mathrm{FD}} = A\,(S_{38}/\,\mathrm{VEM})^{B}. \tag{3.2}$$

This results in an SD energy of

$$E_{\mathrm{SD}} = A\,(S(1000)/f_{\mathrm{CIC}}(\theta)/\,\mathrm{VEM})^{B}, \tag{3.3}$$

with a resolution of about $\sigma_{E_{\mathrm{SD}}}/E_{\mathrm{SD}} \simeq 20\%$ at an energy of $2 \times 10^{18}\,\mathrm{eV}$ and tending smoothly down to $\simeq 7\%$ at the highest energies above $2 \times 10^{19}\,\mathrm{eV}$ [34].

3.2 Fluorescence Telescope

As a complementary detection technique, fluorescence telescopes are placed around the SD array, observing the sky during clear moonless nights. On four sites, Coihueco in the northwest, Los Leones in the southwest, Los Morados in the southeast and Loma Amarilla in the north, the telescopes oversee the WCD array (see Fig. 3.1). A building at each site is hosting six telescopes (bays), covering a field of view of $30° \times 30°$ each. In addition to these 'standard' telescopes, three additional telescopes are placed at the Coihueco site, which can be elevated by 30°. This HEAT extension (High Elevation Angle Telescopes) looks higher into the atmosphere and can see the shower stage at an earlier age, which lowers the energy threshold down to $10^{17}\,\mathrm{eV}$ [35].

The telescopes operate only on dark moonless nights to detect the de-excitation of nitrogen molecules. The wavelength of the emitted light is in the near UV-range, between $300 - 430\,\mathrm{nm}$. The design of the detector is based on a Schmidt telescope, such as the previous fluorescence telescopes at the Fly's Eye or HiRes experiments [36, 37]. The light enters the telescope building through an entrance window, made of Schott MUG-6 glass [38], to filter stray light with wavelengths higher than 410 nm. The total aperture has a diameter of 2.2 m, with an opening of 1.7 m and a corrector ring covering the outer rim of the entrance window (see Fig. 3.5). This enlarges the aperture by almost a factor of 2, while keeping the angular spread of the light spot within 0.5°. The incoming light is collected by a $12\,\mathrm{m}^2$ segmented spherical mirror and directed to a camera.

Figure 3.4: Building of the fluorescence telescopes at Los Leones (left) and the three high elevation telescopes (HEAT) at the Coihueco site (right).

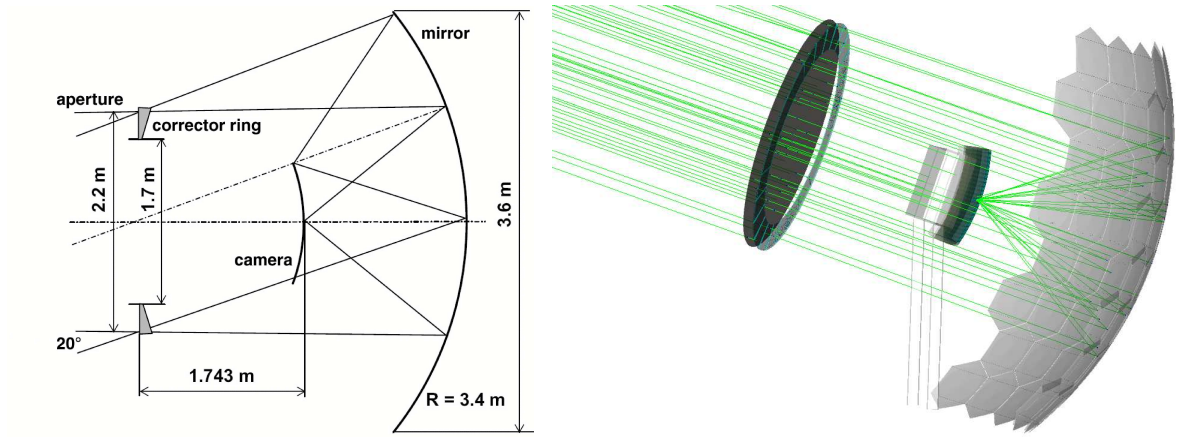

Figure 3.5: Schematic layout of the optical FD telescope system (left). Geant 4 ray tracing simulation illustrating the working principle of the telescope (right) [24].

The camera is placed at the focal plane of the mirror and has a spherical shape as well. It consists of 440 PMTs arranged in a 22×20 hexagonal grid. The FOV of a single pixel is 1.5°. The PMTs also feature a hexagonal photocathode. To minimise dead space between the pixel of the camera, light guides made of reflective foil cover the gaps between the sensors.

The PMT is the 1.5 inch XP3062 by Photonis [39]. It has a hexagonal bialkali photocathode with a quantum efficiency (probability of an incoming photon to produce an electron via the photoeffect) of about 27%. The DAQ electronics for the 440 pixel camera are split into 20 analogue boards (ABs) hosting one column of 22 PMTs each. These front-end boards handle the triggering and data read-out, adapted for the high dynamic range of the expected signals. The signal is digitised with a rate of 10 MHz and has a dynamic range of 15 bit. To reduce costs of power supplies, two ABs with 44 PMTs share a single high voltage channel (one supply per AB for the HEAT telescopes). For this reason, the PMTs were tested extensively prior to installation and classified into groups of similar gain to keep their response homogeneous. The PMTs are operated with positive supply voltage, keeping the photocathode and the camera front at ground level to avoid dust deposition due to electrostatics [40].

3.2.1 Calibration

In order to get an accurate energy determination with the FDs, a proper calibration is needed. To get the conversion factor between light entering the telescope and the measured signal at the PMT, all components need to be considered in a calibration. For the conversion factor, a full absolute calibration is performed. In addition, relative calibrations are done to monitor changes in response from sensitive detector components.

3.2.1.1 Absolute Calibration

The absolute calibration of the telescope has been called 'Drum Calibration'. An absolute calibrated light source was placed outside of the telescope in front of the diaphragm. In order to get a uniformly distributed illumination, the drum, a cylinder coated with Tyvek[1], was placed onto the telescopes entrance window, covering the whole aperture [42, 43]. With the known light flux, the PMT signals, measured in ADC counts, could be converted to the amount of incoming photons. Since this calibration is quite time consuming, it cannot be performed on a daily basis. The drum calibration is now being replaced by an XY-scanner calibration, with a steerable calibrated light source in front of the telescope aperture [44].

[1] A synthetic material made from high-density polyethylene fibres, diffusely reflective in the UV range [41].

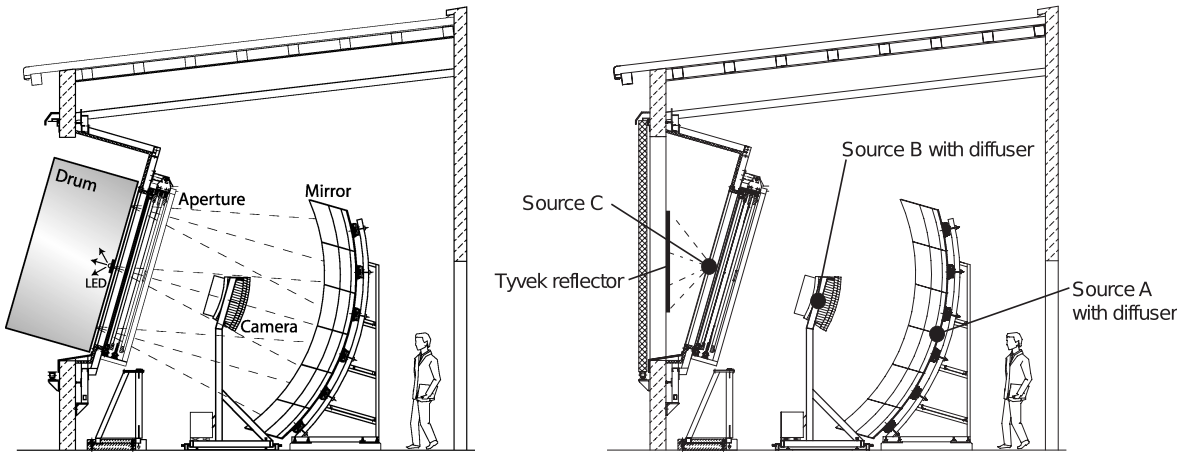

Figure 3.6: Schematics of the different calibration systems [24]. Drum system for absolute calibration (right) and different spots for relative telescope calibrations (left).

For cross-checks, the signal response from a roving laser is measured as well [45]. Here, a nitrogen laser with a wavelength of 337 nm is driven to a distance of about 4 km to the telescope and fired vertically, 'simulating' an air shower event. With the known Rayleigh scattering cross section, the photon flux can be predicted and correlated with the measured PMT signal. Since only a small number of pixels are triggered by the corresponding light track of the roving laser, this procedure is not suitable to calibrate a whole camera.

3.2.1.2 Relative Calibration

In addition to the absolute calibration, three relative calibrations are performed on a more frequent basis, to identify changes in the response of different detector parts [46]. The different types can be seen in Fig. 3.6, right. The light source for calibration A is placed in the middle of the segmented mirror. It is a 375 nm LED with an attached diffusor, illuminating the camera directly to spot differences in the PMTs response. Calibration B is placed on the side of the aluminium frame of the camera and directed to the telescope mirror to identify possible changes in the mirrors reflectivity. Calibration C is placed outside of the aperture pointing outwards. A Tyvek sheet at the inner part of the shutter doors reflects the light, measuring the response of the complete telescope system and thus capable of detecting changes due to the filter glass or the corrector ring. Calibration B and C use a xenon flash lamp with additional wavelength filters for a multi-wavelength calibration [47]. All calibrations were performed every night until 2018. Since then, only calibration A is used twice per measurement night to spot a possible drift in the cameras response.

3.2.1.3 Atmospheric Monitoring & Laser Facilities

Besides the exact calibration of the hardware components, the atmospheric conditions need to be monitored for a precise calorimetric measurement of air showers with the FD telescopes. At the four FD sites, lidar systems are installed to measure the atmospheric scattering and cloud coverage during data taking every hour [48]. In addition, a scan is performed within $2-4$ minutes to the recording of a high energy 'hybrid' event to have a more precise modelling of the atmosphere. While the lidar system is placed outside the FOV of each FD telescope, two systems are designed to provide 'test beams' for calibration purposes. The central laser facility (CLF) [49] and the extreme laser facility (XLF) are placed in the middle of the SD array (see Fig. 3.1, left). The lasers are steerable, making it possible not only to shoot vertically but to 'simulate' a more horizontal shower, appearing in multiple telescopes at the same site.

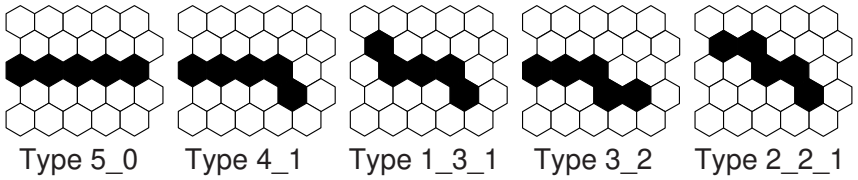

Figure 3.7: Trigger pattern for the FD second level trigger, including rotational or mirrored transformations.

3.2.2 Trigger

The sensitive camera can detect very faint light in a large distance from the telescope. Thus, several trigger levels are implemented to identify air showers from background light. As a first trigger level, a threshold trigger per front-end board (22 PMTs) is required. To compensate for changing background light, the threshold is adjusted by keeping a trigger rate of 100 Hz. In a second stage, track identification is applied by a pattern search for at least 4 out of 5 conjunctive pixels to fire (see Fig. 3.7). A third trigger level is implemented for background rejection, caused by lightning or muons interacting with the camera directly.

Afterwards, events will be sent to the EyePC, where events in adjacent telescopes are merged and a T3 trigger is sent to CDAS. This will trigger the SD readout at the stations around the FD building (about one-quarter of the array), since the array is not fully efficient for energies below 3×10^{18} eV. Data from both detectors is merged offline for a subsequent hybrid analysis.

3.2.3 Reconstruction

The first step in the reconstruction of an FD event is to establish the shower geometry. This is done by determining the shower detector plane (SDP), which is defined as the plane containing the shower axis and the observing telescope (see Fig. 3.8, left). The SDP is given by fitting the pointing directions of the pixels, weighted by their signal. To determine the shower axis within the SDP, the timing information of the participating pixels is fitted. While FD mono reconstruction, with only one telescope observing the shower, is possible, the fit is improved considerably by an additional signal in the SD stations, so called hybrid events, pinning the shower axis on the ground. Even better reconstruction is achieved with two FD sites observing the same particle shower simultaneously, in a stereo reconstruction.

From the shower profile the light at the aperture as a function of time is converted into energy deposition as function of slant depth (see Fig. 3.9, left). For the energy determination, a disentanglement of the light contributions from fluorescence light and direct and scattered Cherenkov light is performed. The energy of the shower is derived by fitting a Gaisser-Hillas function to the shower profile (Fig. 3.9, right). The energy is calculated by integrating the profile and corrected for 'invisible energy', carried by neutrinos and high energy muons. After quality cuts, the energy resolution is $< 10\%$ and almost energy independent.

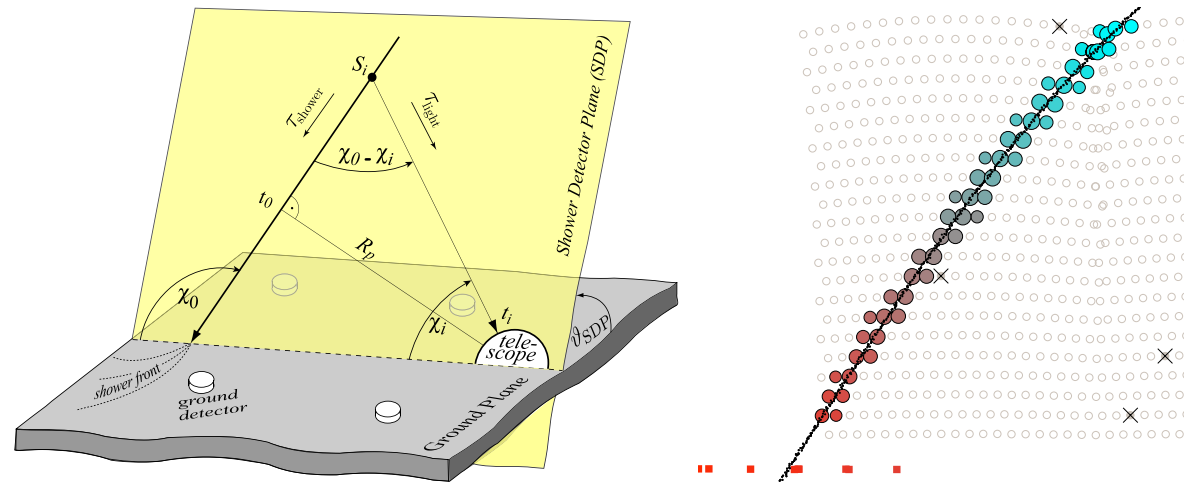

Figure 3.8: Sketch of the shower geometry reconstruction and derived observables [50] (left). Light track of an event recorded with the FD telescopes [24] (right). Colour-coded is the timing sequence of the triggered pixels and the fitted line indicates the SDP. Red squares on the bottom represent the triggered SD stations of this event.

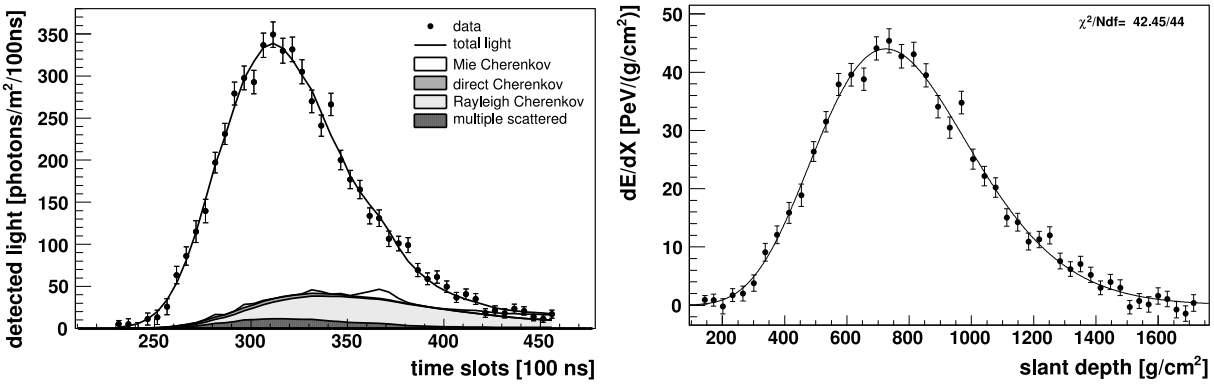

Figure 3.9: Example of a measured FD profile. The left plot shows the light at telescope aperture and different light contributions. It is converted to energy deposit versus slant depth and a Gaisser-Hillas fit is applied, as shown on the right [16].

3.3 Further Enhancements

Besides the two baseline detector systems, SD and FD, different techniques to measure extensive air showers are tested at the observatory. The most prominent extension is an array of radio antennas [51] close to the Coihueco site, partly in overlap with the Infill array, measuring the electromagnetic component of the particle shower in the MHz regime. Providing a calorimetric energy measurement with an uptime of almost 100% [52, 53], the radio detection is a promising addition to the FD telescopes and the 20 km^2 array will be extended as part of the observatory upgrade. Other detectors types include buried scintillation detectors, the *Auger Muon and Infilled Ground Array* (AMIGA) to measure the muonic part of an air shower.

3.4 Upgrade

To investigate the unresolved question of the composition at the highest energies, the current detector setup will be upgraded, i.e. to improve the discrimination between the electromagnetic and muonic component of an air shower on an event-by-event basis. The upgrade, called Auger-

Prime, consists of the installation of additional scintillators on top of the current WCD (see Chapter 5). In addition, the radio antenna array will be enlarged to the SD array and the uptime of the FD telescopes will be increased by running at a lower gain when more moonlight is present.

3.5 Offline Framework

With a large and complex detector system such as the Pierre Auger Observatory, the analysis is quite complex. For simulation and reconstruction of the detector data, the internal Offline framework [54] was developed. Implemented in C++, the framework provides access to detector information, event data, and administers the different analyses.

The read-only detector description is given in XML files, and time dependent information, such as calibrations etc., is taken from MySQL databases. Simulation and data reconstruction algorithms are organised in different self-contained modules. With the generalised event data structure, different modules can be combined into a module sequence, to perform a complete analysis.

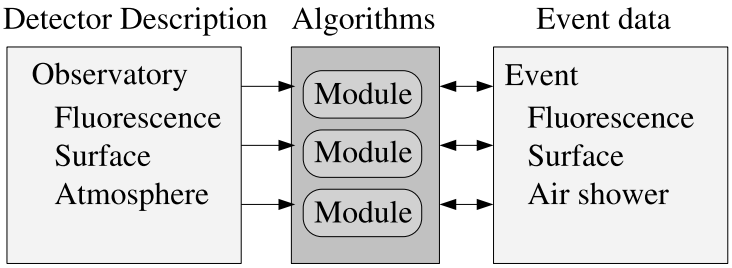

Figure 3.10: Basic structure of the Offline framework. Reconstruction and simulation modules can access the event data and the read-only detector description with a generalised event output format [54].

Chapter 4

Fluorescence Detector Upgrade

Parts of this chapter have been published in:

S. Querchfeld, K.-H. Kampert, and J. Rautenberg,
"Development of a highly efficient PMT Winston-cone system for fluorescence measurement of extensive air showers", PoS(ICRC2015)677 Proceeding of 34th ICRC, 2015

The Pierre Auger fluorescence telescopes measure the faint light signal of extensive air showers in the UV range. The light is cumulated by a spherical mirror and detected by a camera consisting of photomultiplier tubes (PMTs). In combination with the Surface Detector, this hybrid detector system is observing the same particle shower with two independent measurements, with the FD giving a more accurate energy determination of the primary particle. The Fluorescence Detector was constructed starting in 2002 and measures air showers in dark moonless nights. With PMT developments ongoing, recent models have shown an increase in detection efficiency. These more efficient devices could enhance the detection capabilities of the FD. In addition, the original PMT model is no longer available and a potential upcoming new Auger site in the north would need to switch to a modern model if the same FD telescope design is used. In this chapter, the possible upgrade of the FD camera and the modifications needed for implementation are discussed.

4.1 Motivation

In the current setup, the fluorescence telescopes are placed on the side of the observatory, with their field of view covering the large area instrumented with surface detectors. Observing the air shower from different sites in stereo mode, the distances between the FD buildings can be up to 60 km[1]. With the prospect of building an even larger counterpart observatory in the northern hemisphere to increase the exposure at the highest energies, the telescopes effective area needs to be increased to cover even large distances[2].

Relying on conventional photomultiplier tubes as pixel sensors in the FD camera, improving the effective area would need the PMTs to be more sensitive. Photomultiplier development has led to an increase in their efficiency in recent years. Especially focusing on the quantum efficiency (QE), the probability of an incoming photon to create an electron at the photocathode via the photoelectric effect has been increased, which enhances the overall performance. While the PMTs, available for building the FD cameras with about 12.000 units in 2002, had a QE of about $26 - 28\%$, refined materials and manufacturing processes have led to an increase in this value up to 43% QE in peak. How this translates to an increased field of view is shown in the next paragraph.

[1] Depending on the energy.
[2] If the telescope design stays the same.

Following [55], the signal of an air shower observed by an ideal FD telescope depends on the shower size and the distance to the telescope, R. At a given stage of the shower development, the number of emitted fluorescence photons is given by $N_\lambda^{shower}(h) = E_{dep}^{shower}(h)\, Y(\lambda, p, T)$, where $E_{dep}^{shower}(h)$ is the energy deposited by the charged particles in the air volume, air pressure p, temperature T at the altitude h and the fluorescence yield in air Y (with $Y_{337} = 5.61 \pm 0.21_{syst}$ photons per MeV deposited energy [56])[57]. With the fluorescence light being emitted isotropically, the light observed by a telescope with aperture A is the fraction of $\frac{A}{4\pi R^2}$. Losses due to Rayleigh and Mie scattering are accounted for by a combined attenuation length ξ. With the PMT's quantum efficiency QE and gain G, the measured signal, S, in number of electrons is:

$$S = E_{dep}^{shower}\, Y \cdot \frac{A}{4\pi R^2} \cdot e^{\frac{-R}{\xi}} \cdot QE \cdot G. \tag{4.1}$$

An improved QE would not only result in higher signals, but also make the system more sensitive to the night sky background. The background light observed by a pixel with solid angle Ω due to the night sky photon flux ϕ_{BG} (about 40 photons per μs per m^2 per deg^2 passing a UV filter) in a time interval t is given by $\phi_{\mathrm{BG}}\, t\, \Omega\, A$. This results in a PMT signal spread of

$$N = \sqrt{\phi_{\mathrm{BG}}\, t\, \Omega\, A \cdot QE \cdot G}, \tag{4.2}$$

and a signal-to-noise ratio of

$$S/N = \frac{E_{dep}^{shower}\, Y}{4\pi R^2} \sqrt{\frac{A \cdot QE \cdot G}{t\, \phi_{\mathrm{BG}} \cdot \Omega}} \cdot e^{\frac{-R}{\xi}} \propto \sqrt{\frac{A \cdot QE \cdot G}{t\, \Omega}}. \tag{4.3}$$

Thus, the signal-to-noise ratio for an ideal fluorescence telescope can be increased by either enlarging the aperture (here the mirror size) or changing the PMT properties. While a change in aperture of the current setup is not feasible, tweaking the PMT properties is possible. The currently used PMTs have a QE of about 28%. Manufacturers have been able to increase the QE, e.g., by adjusting the photocathode thickness. Hamamatsu introduced two new categories: super-bialkali photocathodes with a QE of 35% (SBA) and ultra-bialkali cathodes with a QE of 43% (UBA). The influence on the detection capabilities was investigated in dedicated detector simulations using the Offline framework [58]. The detector performance was evaluated for CORSIKA [59] showers with an energy between $10^{17.5}$ eV and 10^{20} eV and mixed composition. Reconstructions considering the increase in quantum efficiency of the FD camera show an increased trigger efficiency for particle showers further away (Fig. 4.1, left). While the relative gain in detection efficiency of already bright high energy showers is only moderate, the main improvement is seen for low energy events. Figure 4.1 (right) shows the effective area compared to the current standard, which increases more than 25% for SBA photocathodes at the lowest energy bin. Although the increase is reduced to less than 10% for both enhancements at the highest energies. With more showers being detected and the improved S/N ratio, the resolution for quantities derived by the Gaisser-Hillas fit to the shower profile increases as well. Figure 4.2 shows the energy (left) and X_{max} resolution (right) for different QE settings. Again, the biggest impact is seen for the low energy particles.

Ultra-bialkali PMTs with the highest QE are only available as metal packaged PMTs. With dimensions and read-out pinning different than the head-on glass bulb PMTs, modifications to enable implementation into the current FD system are not feasible. A super-bialkali PMT to replace the existing XP3062 1.5 inch PMT was found instead. Keeping impact on the running system low, in a first step[3] only one FD telescope would be equipped with the new detectors. To determine where the impact would be the highest, simulations considering different stages

[3] after a prototype test

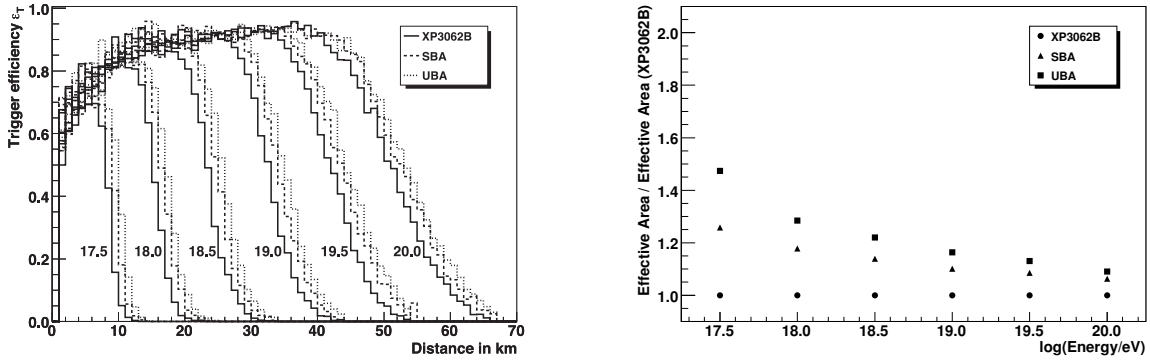

Figure 4.1: Trigger efficiency dependence on the distance to the telescope for different energies (left). Considered are different quantum efficiencies of 28% (XP3062), 35% (SBA), and 43% (UBA). Change in effective area versus energy (right). Figures taken from [58].

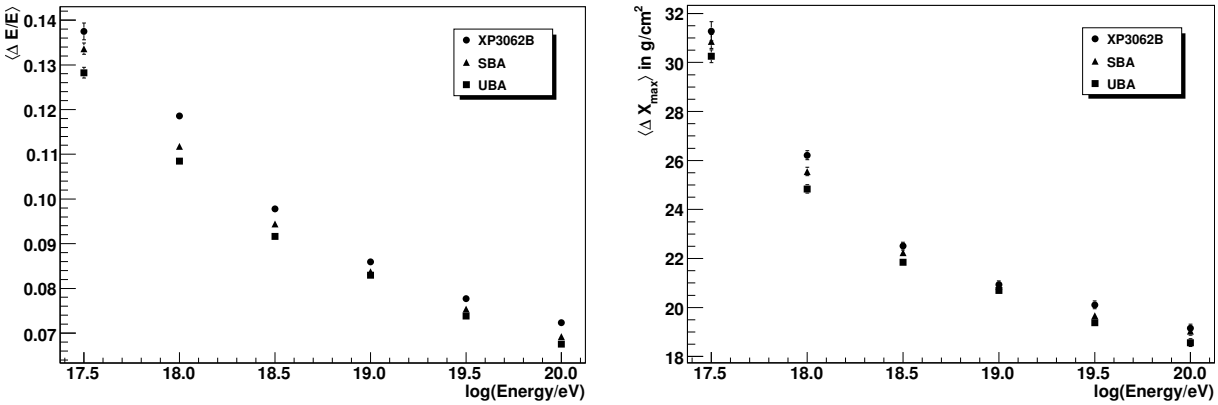

Figure 4.2: Energy resolution (left) and $X_{\max}$ resolution (right) for different quantum efficiencies. From [58].

of interchanging PMTs were performed [60]. As reconstructions of low energy shower profit the most, FD telescopes close to the low energy SD extensions (Infill and AERALet), namely Coihueco and HEAT, seem most promising. Different setups were investigated, with changing PMTs only in one HEAT telescope compared to changing all three cameras in HEAT or all six cameras in the Coihueco telescopes. In Fig. 4.3 (left), the effective area for the three setups using SBA PMTs is shown for proton and iron showers with energies between $10^{16.5}$ eV and $10^{19.5}$ eV. The standard telescopes in Coihueco are only fully efficient above $10^{17.5}$ eV, with low energy showers not reaching as deep into the atmosphere. On the other hand, the HEAT telescopes benefit at these energy ranges, with a single telescope already gaining significantly towards the AERALet energy range. For showers resampled according to the Auger spectrum, the increase in reconstructable showers versus the shower core distance to the telescope is shown in Fig. 4.3 (right). Due to the steep spectrum, the gain for the new PMTs in Coihueco is quite steady for distances above 10 km. HEAT profits from the upgrade for distances up to 15 km, with the SD low energy extensions being at around $5 - 10$ km distance from the building.

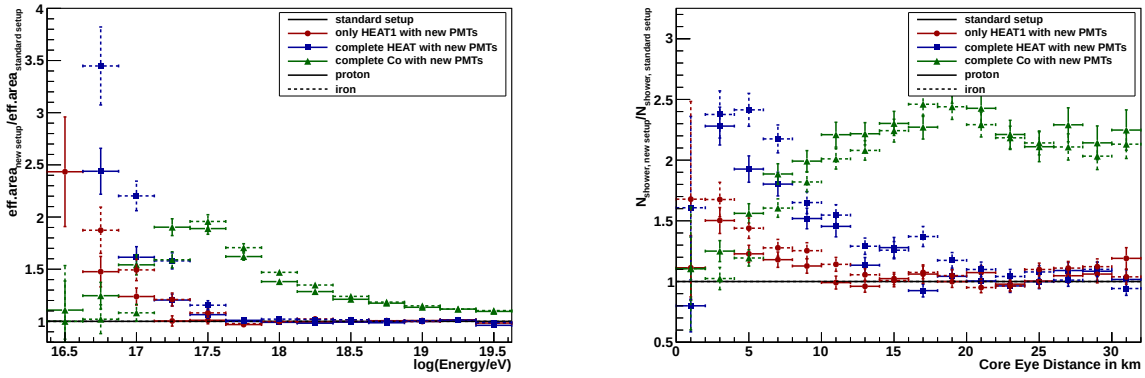

Figure 4.3: Increase in effective area for different camera setups in Coihueco and HEAT by energy (left). Relative increase of reconstructable showers for core-telescope distances (right). From [60].

4.2 PMT Candidates

To test more efficient PMTs in one of the FD cameras, several candidate PMTs were evaluated for their usability in the Auger framework. The main requirement for the new devices is a matching response to the light of the fluorescence spectrum of air. In Fig. 4.4, the fluorescence emission from dry air, measured by the AIRFLY collaboration, is depicted. Ranging from about 290 nm to 430 nm, the most prominent emission lines are at 337.1 nm and 357.7 nm [57]. Matching this spectrum and protecting the FD building from unwanted background light as well as dust, a MUG-6 filter glass [38] covers the aperture. It reduces the spectrum to about 300 nm to 400 nm, while becoming translucent again for wavelengths higher than 700 nm (see Fig. 4.5). Besides the higher efficiency, a form factor and operational conditions, like supply voltage and gain, that are similar to the existing PMTs would ease the integration into the read-out electronics. As mentioned in Section 4.1, UBA PMTs were only available as metal-packaged PMTs, with their form factor not fitting to the existing camera body. Thus, the selected candidate PMTs are head-on glass tubes with SBA photocathodes.

In order to verify the higher QE and to test other properties of the PMTs, extensive test were performed on two new candidate PMTs, matching the stated requirements.

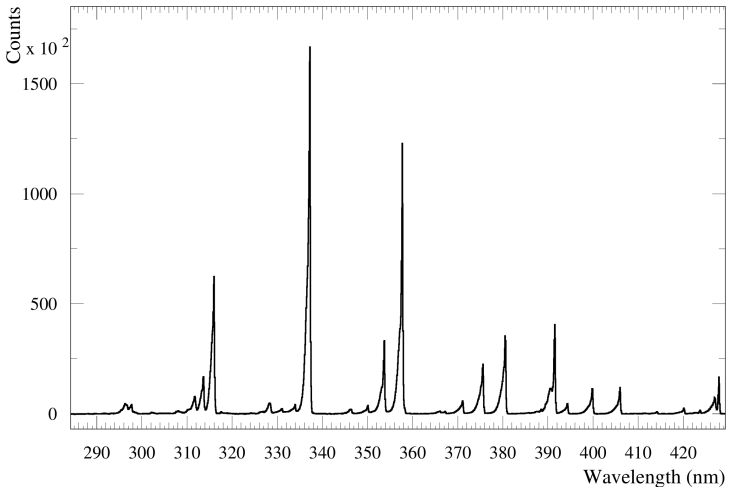

Figure 4.4: Fluorescence spectrum of dry air at 800 hPa and 293 K measured by AIRFLY [57].

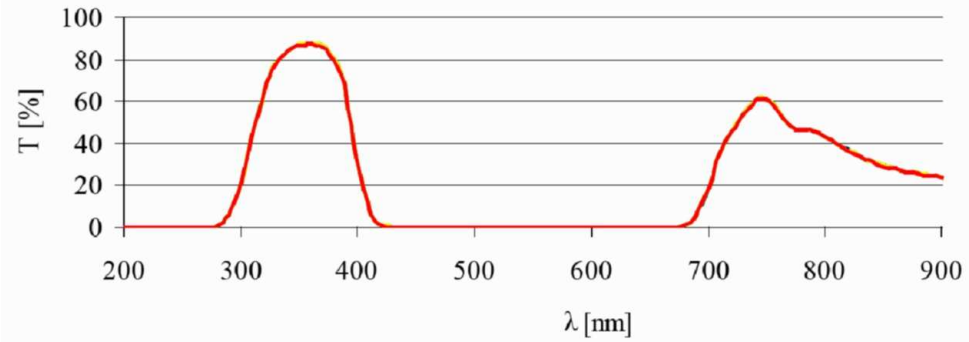

Figure 4.5: Filter transmission of the M-UG6 glass covering the FD entrance window [61].

Hamamatsu R9420-100

As a replacement for the Photonis XP3062 PMT in the standard telescopes, the Hamamatsu R9420-100 was chosen [62]. It is a 1.5 inch tube PMT with 8 dynode stages and similar specifications like the Photonis PMT (see Table 4.1). The key factor is the benefit of the higher quantum efficiency, which is 35% at peak wavelength. A drawback is the slightly higher dark current, which might effect the ageing of the PMT. Instead of the hexagonal head of the XP3062, the Hamamatsu PMT has a circular sensitive area. To verify the usability of this new PMT, extensive tests were performed, considering the higher QE and problems like afterpulse and dark current [62]. For implementation into the existing FD camera, only the voltage divider PCB needed adjustment to offer high linearity. Since the operating supply voltage is similar, the hybrid board of the head electronics could be attached to the active voltage divider and connected to the DAQ.

Hamamatsu R11920-100

PMTs are used in a variety of experiments, with the standard version being an evacuated glass bulb with a photosensitive area at the head. They provide a cost-efficient way to equip a large photosensitive area. Since ultra-bialkali photocathodes are not available for these glass tubes, presumably due to the manufacturing process and the way of applying the photocathode into the glass tube, research is going on as how to increase the efficiency even more. In a joint collaboration between the Cherenkov Telescope Array [64] and manufacturers Hamamatsu and Electron Tubes, a novel super-bialkali PMT with improved properties was developed, the R11920-100 [65]. Here, a 1.5 inch R9420-100 PMT with super-bialkali photocathode was combined with the electron multiplier system of a 1 inch R8619, to increase the collection efficiency. The glass bulb of the R9420-100, which already featured a spherical photocathode on the inside, was modified and matches the cathode shape on the outer part as well (see Fig. 4.7). In addition, a frosted layer was added to the PMT glass. The idea is, to increase the net QE by introducing a scattering layer (see Fig. 4.6). While the rough surface will enhance the reflectivity of the PMT's front, and therefore a loss of QE, it also enables photons to be trapped between the coating and the photocathode as well as backscatter-

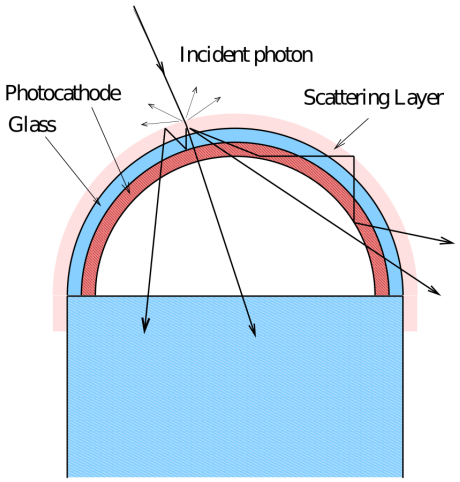

Figure 4.6: Working principle of a frosted layer applied to a PMT surface, taken from [63].

Figure 4.7: The Hamamatsu R11920-100 PMT (bottom, left) is an upgrade from the R9420-100 PMT (top, left) with a frosted, spherical entrance window and an optimised dynode system. It is available with (black cover, left side) and without (right side) a μ-metal sheathing for magnetic field shielding.

		Phot. XP3062	Ham. R9420	Ham. R11920-100
Tube size		1.5 inch		
Photocathode		bialkali	super-bialkali	
Shape		hexagonal	round	
Peak wavelength [nm]		420	420	400
Radiant sensitivity [mA/W]		90	110	110
Dynode stages		8/linear focussing		
Gain		1×10^5	5×10^5	4×10^4
Supply voltage [V]	typ.	1000	1300	1000
	max.	1300	1500	1500
Dark current [nA]	typ.	1	10	5
	max.	20	100	20

Table 4.1: Datasheet comparison of the currently used Photonis XP3062 [39], the Hamamatsu R9420-100 [66], and the R11920-100 [67].

ing of photons reflected by the cathode. In combination with the hemispherical shape, it is also possible for scattered photons to hit the cathode twice, increasing the conversion probability and resulting in a net plus in QE. As this PMT was still under development, individual devices were tested for their compatibility with the FD.

4.2.1 Quantum Efficiency Measurement

The QE was measured in a dedicated test setup [62, 68]. Here, a set of deuterium and tungsten lamps are combined to provide a spectrum ranging from 200 nm up to more than 800 nm. Connected to a monochromator and a filter wheel, the PMT's response to different wavelengths was scanned. To get the efficiency of the PMT's photocathode, the dynodes are short-circuited together with the anode. The PMTs response is measured in reference to a calibrated photodiode, taking into account the respective dark currents.

Figure 4.8 shows a QE measurement of a Hamamatsu R9420-100 and R11920-100 in comparison to the current Photonis XP3062. The super-bialkali photocathode of the R9420-100 already shows a large improvement versus the standard PMT. Between $300 - 400$ nm, the region

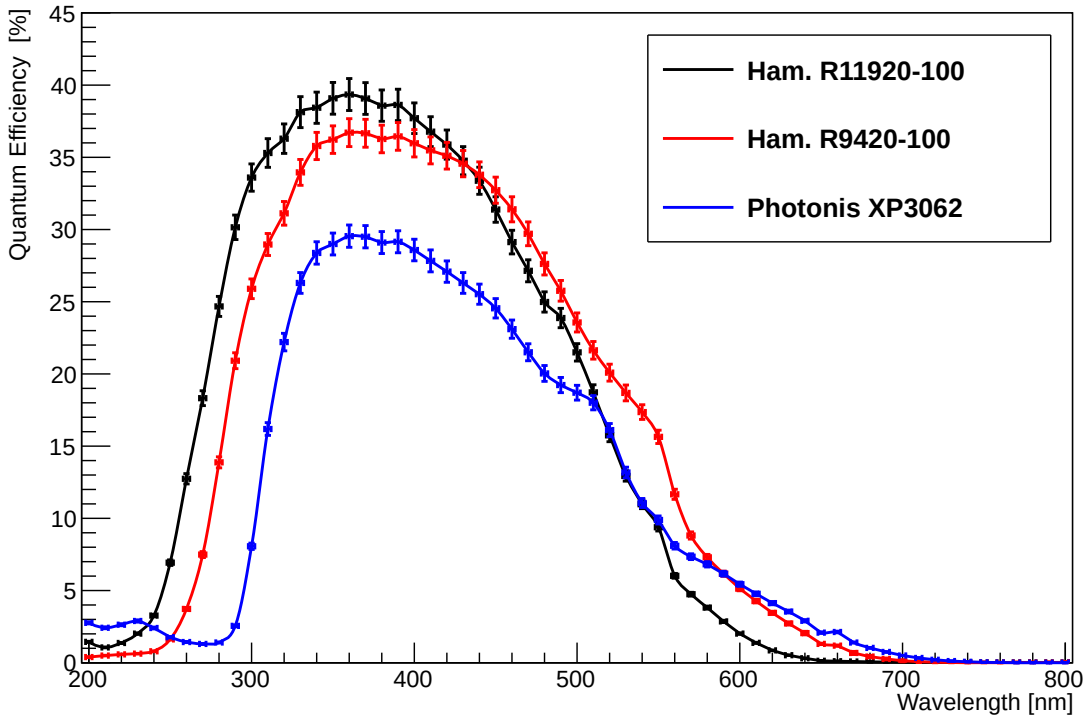

Figure 4.8: Measured quantum efficiency of the currently used FD PMT Photonis XP3062 (blue) and the two candidate PMTs R9420-100 (red) and R11920-100 (black) by Hamamatsu.

of interest for fluorescence light detection, it gains up to 24% in detection efficiency versus the XP3062 (36% QE versus 29% QE at peak wavelength of about 360 nm).

The R11920-100 PMT with its frosted entrance window gains additional $\sim$ 3% in absolute terms at the peak wavelength. The overall response is shifted about 20 nm towards lower wavelength, improving the overlap of high QE region with the fluorescence spectrum of dry air. The efficiency of both new PMTs drops towards higher wavelengths, reaching a similar level as the XP3062 just above 600 nm. With the filter glass becoming translucent just before 700 nm (see Fig. 4.5), there is no additional noise from longer wavelengths to be expected for the more efficient PMTs in comparison to the XP3062.

4.2.2 Uniformity Measurement

While the QE measurement gives the mean QE of the whole illuminated photocathode, local hot spots or deficits in sensitivity can appear due to a limited collection efficiency of the specific dynode construction or the manufacturing process of applying the photocathode material inside the glass tube. To measure how uniform the PMT's photocathode response is, the surface was scanned with a small light spot. A 405 nm laser diode was attached to a fibre with a collimator, reducing the light spot size to about 1 mm in diameter. The collimator was attached to a XY-scanner, moving perpendicular to the PMT's axis, scanning the photosensitive area.

Figure 4.9 shows the uniformity scans of the currently used XP3062 and the R9420-100. Normalised to the centre of the PMT, the scans show structural features, caused by the collection efficiency of the first dynode or the focusing grid of the XP3062 respectively. With the photosensitive area being smaller than the glass tube, there is still some efficiency outside of the photocathode. On the outer rim of the PMT, there is even an increase in efficiency due to a lens effect of the glass body with its plane outer and spherical inner surface. In the full camera this effect will be suppressed by the light guides covering this area. In comparison, the scan of

the R11920-100 in Fig. 4.10 shows a more homogeneous output. Featuring a dip in the centre due to the higher reflectivity of the milky surface and the asymmetrical response due to the collection is less prominent. The hemispherical outer window and the taped glass body outside of the photocathode results in a sharper cutoff at the edge.

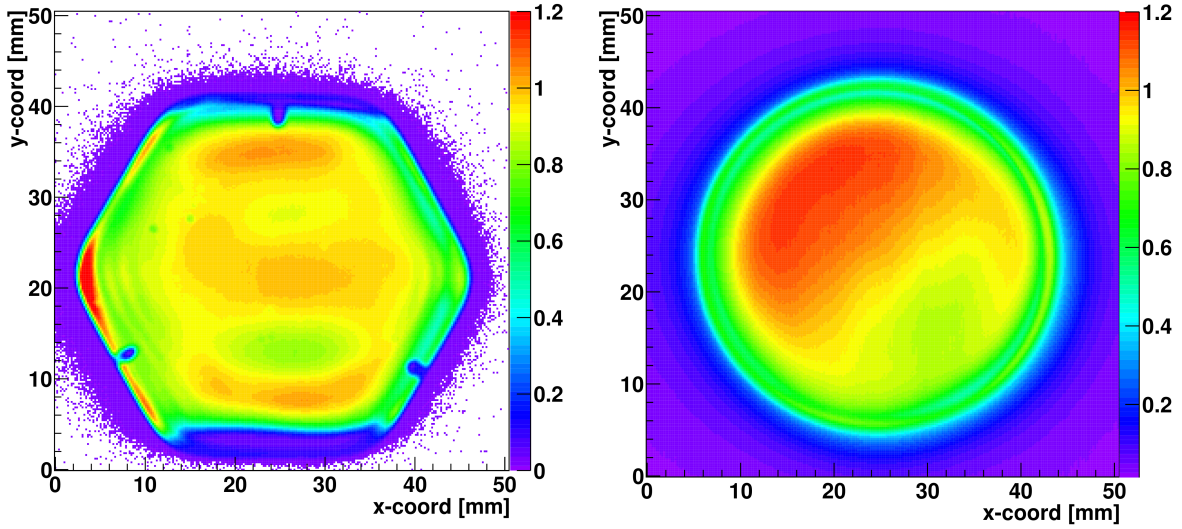

Figure 4.9: Space-resolved QE measurement of the Photonis XP3062 (left) and the Hamamatsu R9420-100 (right) [62], normalised to the PMT's centre. XY-scan performed at 405 nm with a fibre spot size of about 1 mm.

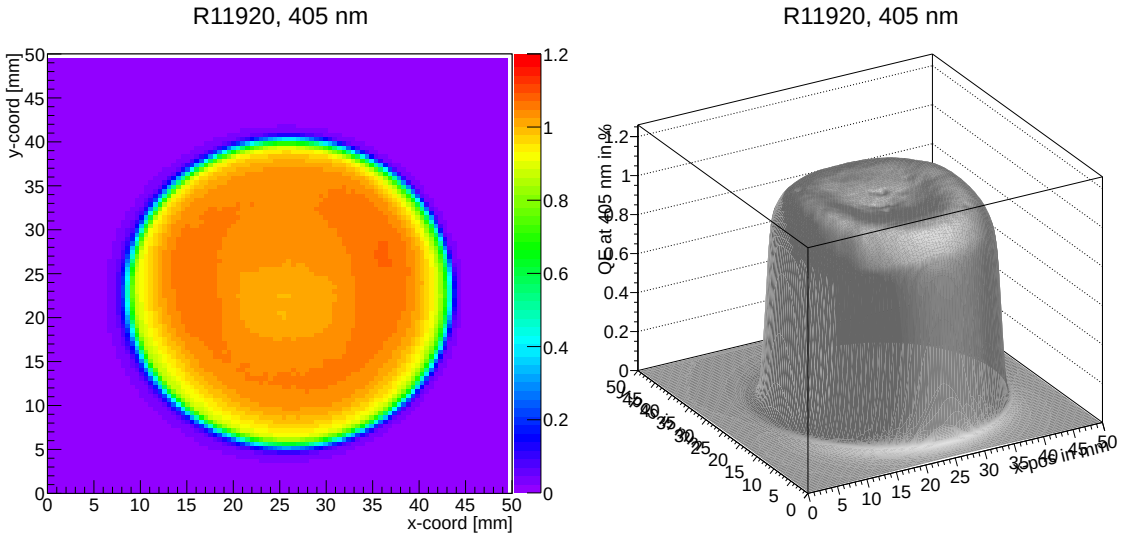

Figure 4.10: Space-resolved QE measurement of the Hamamatsu R11920-100, normalised to the PMT's centre. XY-scan performed at 405 nm with a fibre spot size of about 1 mm.

4.2.3 Linearity

While the fluorescence light of air showers far from the telescope is quite faint, the light for more energetic particles and showers closer to the telescope can be bright. Thus, the sensors need to cover a high dynamic range to measure the variety of showers. To determine the capability of the new PMTs to measure several orders of magnitude difference in signal heights, the setup

from the mass production test of the FD camera was used [69]. Here, a set of calibrated neutral density filters is used to attenuate the light of a blue LED (470 nm). The mean charge of 1000 pulses of 1 μs width is measured. A linear fit is applied and a deviation for large signals would indicate an insufficient linear response. The neutral density filters used have a transmission of 30%, 10% and 1% and are combined to cover a range of three orders of magnitude, matching the dynamic range of the 12 bit FADC used in the read-out electronics. Figure 4.11 shows the linearity measurement of the XP3062 (left) and the R9420-100 (right). The upper plots show the measured charge versus the light transmission and a power law fit ($< Q >= p_0 \cdot T^{p_1}$) is applied, to check whether p_1 is consistent with unity. The lower plots show the relative deviation from the expected linear behaviour[4]. As for both PMTs the voltage divider was optimised for a high linear output (for the Hamamatsu R9420-100 see [62]), the new Hamamatsu PMT shows the same response as the Photonis PMT. Being capable of measuring at least three orders of magnitude in signal difference.

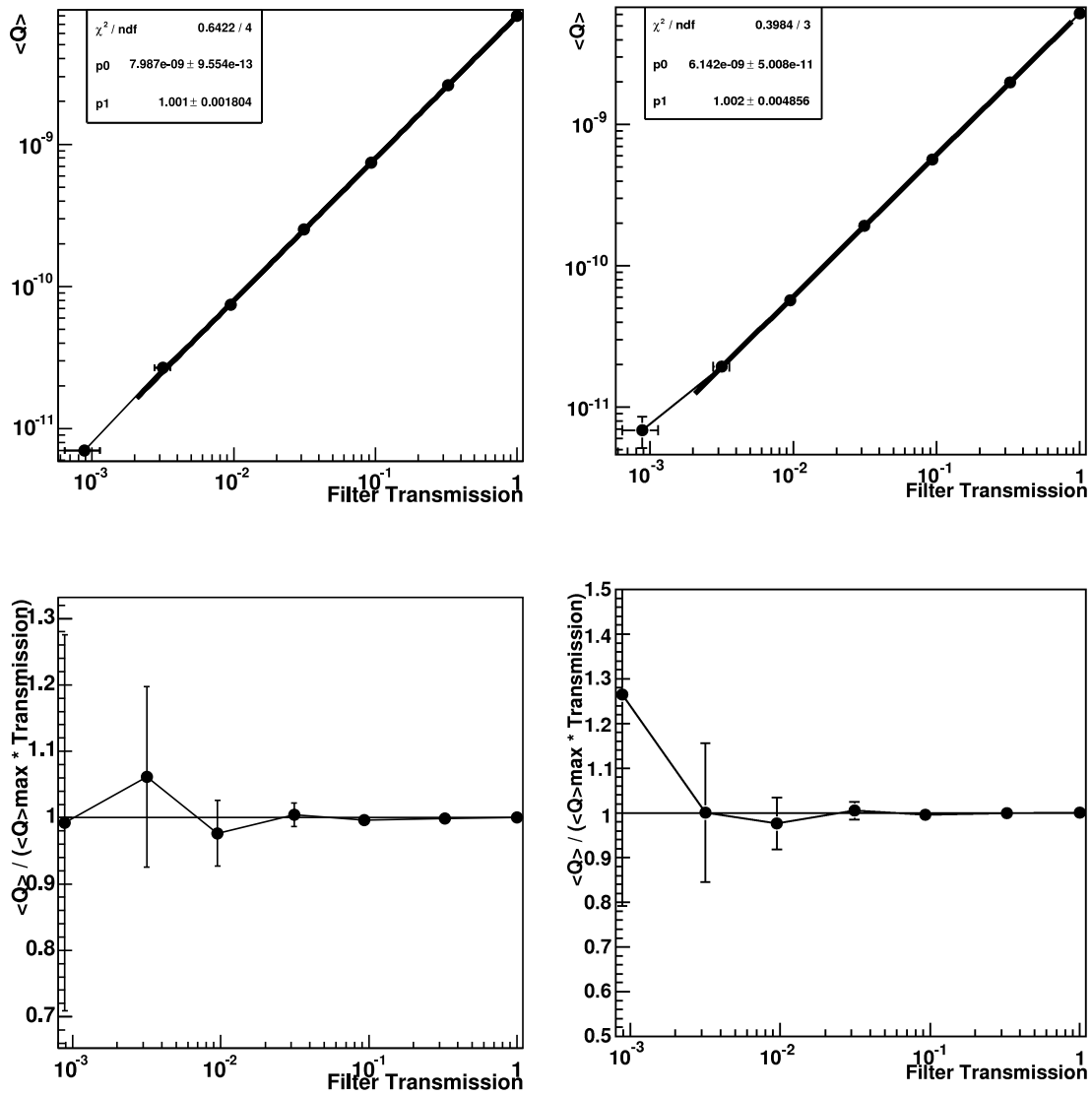

Figure 4.11: Linearity measurement of the Photonis XP3062 (left, from [70]) and the Hamamatsu R9420-100 (right). Upper plots show measured charge versus the light transmission and an applied power law fit. Lower plot shows the relative deviation from the expected signal.

[4]Normalised to the measured charge at 30% transmission.

The measurement was done for the R11920-100 as well. In Fig. 4.12 two measurements of the same R11920-100 PMT are shown. On the left side the linearity measurement is shown using the voltage divider for standard operation recommended by Hamamatsu. A clear drop in measured versus expected charge can be seen for high light intensity. The plot on the right side shows the voltage divider ratio optimised for high linearity output, keeping the deviation at the percentage level.

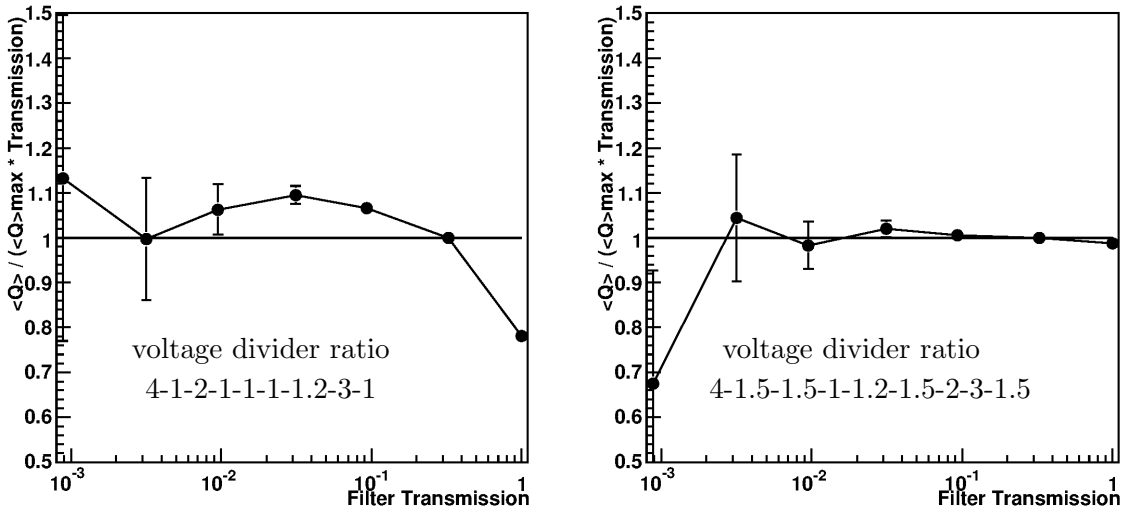

Figure 4.12: Linearity measurement of the R11920-100 for two different voltage dividers. Left side shows the standard voltage divider recommended by Hamamatsu and right side shows the linearity optimised divider ratio.

4.2.4 Afterpulsing

A drawback of using PMTs is the appearance of afterpulses. These are pulses arriving later than the initial pulse. The main cause of these kind of pulses, especially in PMTs with a glass tube, are residual gases in the vacuum tube. Hit by an accelerated electron, the gas atom is ionised and accelerated towards the photocathode. Here it can release electrons, thus inducing a late pulse, arriving up to several microseconds after the initial pulse[5]. Afterpulsing was investigated during the mass production testing. While the XP3062 had a afterpulsing ratio of $0.5-4\%$ of the initial pulse [70], the ratio was considerably higher for the R9420-100, with almost up to 5.5% for typical test pulses of 1 μs length [62]. For the R11920-100 besides the enhanced QE, improvements have also been made in the afterpulse behaviour. In Fig. 4.13 an afterpulse comparison between the Hamamatsu R9420-100 and the R11920-100 can be seen. It shows the PMT response to a LED pulse with a width of 100 ns, averaged over 1000 individual pulses. The disappearance of the signal after the initial LED pulse can be seen for the R11920-100 (black). This was achieved by usage of the smaller dynode structure of the R8619 and a stronger evacuation during the manufacturing process, leaving less residual gasses inside the glass tube.

Not important for the usage in a fluorescence telescope, but rather for the fast timing signals in imaging Cherenkov telescopes, is the possibility of dynode glow. Here, electrons accelerated in the dynode system can produce light while hitting the next focusing dynode. These photons can emerge from the dynode structure with the speed of light, hit the photosensitive cathode, and start a new cascade resulting in an afterpulse very close to the initial signal. Analogue to [65, 71], this was investigated for the R9420-100. A DSLR camera with long exposure was used, looking at the side of a R9420-100 in operation at a supply voltage of 1500 V. As the right

[5]Depending on the mass of the atom and the voltage difference between the dynode and cathode.

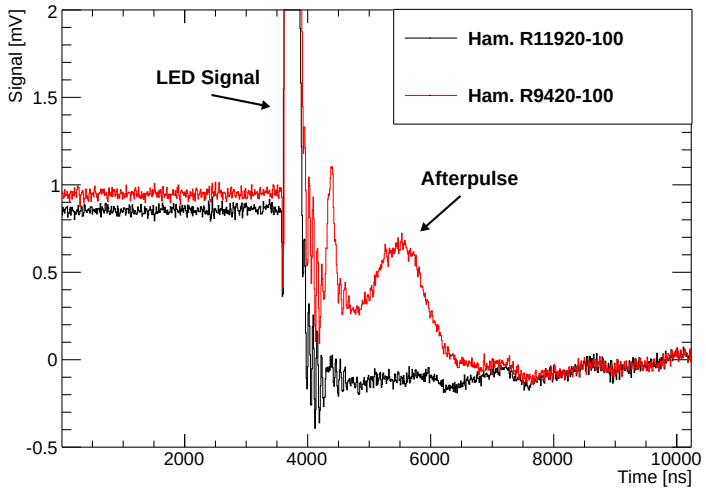

Figure 4.13: Afterpulse comparison of the Hamamatsu R9420-100 (red) and the newer R11920-100 (black). Shown is the average recorded PMT signal of 1000 LED pulses with a width of 100 ns.

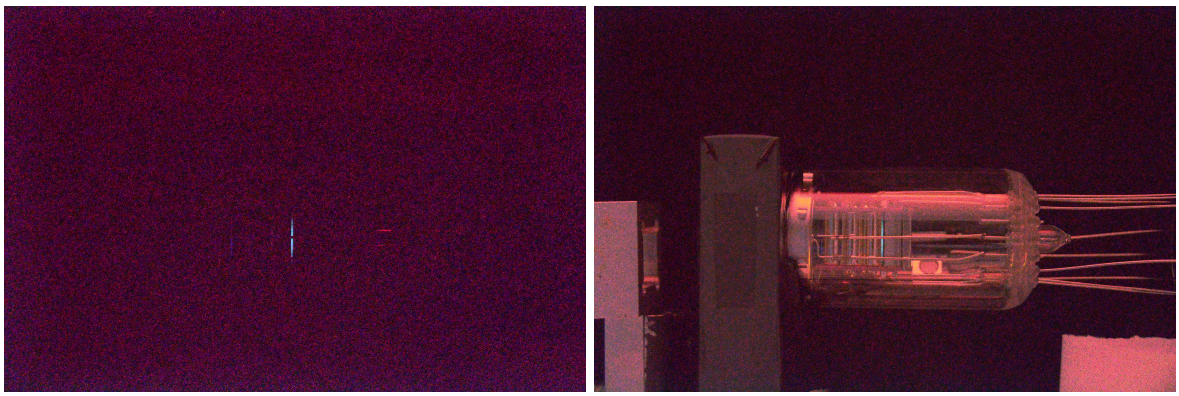

Figure 4.14: Luminous afterpulses of a R9420-100 PMT. The left side shows the glowing dynodes (dim blue line) of a PMT in operation observed from the side. The right image shows a superposition of the left image with a picture of the test setup, locating the glow to the last dynode stage.

picture in Fig. 4.14 shows, a dim line of blue light was recorded, emerging from the side of the PMT. Superimposing the image with the test setup, the origin of this light can be located to the last dynode stages. The timing of these kind of afterpulses is determined by the electron transit time of the PMT. For the R9420-100, the typical electron transit time is given with 17 ns and a transit time spread (FWHM) of 0.55 ns (see Section A.1.2) for the standard voltage divider. For the voltage divider optimised for high linearity, this time might differ slightly but will be in the same order[6]. Thus, it will be indistinguishable from the signal, digitised by the 10 MHz FADC. As will be seen in Section 4.3, in contrast to the currently used Photonis PMT, the new PMTs will sink into the aluminium camera body. This shields each PMT from its surrounding neighbours, preventing cross-talk by glowing dynodes. In addition, the R11920-100 can be purchased with a Mu-metal shielding to reduce the effect of external magnetic fields and further covering the glass tube of the PMT to prevent cross-talk.

[6] As for the XP3062 the signal transit time for the standard divider is given with 30 ns and for the linearity optimised divider with 31 ns, see Section A.1.1.

4.2.5 Modifications for FD Implementation

Implementing the new sensors into the existing FD setup requires only small modifications. Due to the same tube size, the new PMTs fit into the existing aluminium frame of the camera body. HV supply and signal read-out is provided through the head electronics [24, 40]. It consists of three PCBs, with one hosting the voltage divider. For the new PMTs, the voltage divider ratio was ascertained to provide high linearity (see Section 4.2.3) and a new voltage divider PCB produced. The adjusted head electronics can be seen in Fig. 4.7, attached to the R9420-100. Using the gain-vs-HV measurement of the FD calibration test bench [69], the new PMTs were classified into different gain classes. PMTs with similar gain are operated at the same HV supply to keep the camera response uniform. The main difference in using the new PMTs is the shape of the sensitive area. With the round faceplate of the new PMTs instead of the hexagonal shape of the XP3062, the dead space between each sensor is increased and a new type of light guide needs to be used.

4.3 Winston Cone

The higher quantum efficiency would enlarge the field of view of the fluorescence telescopes. But with the changed (and smaller) face plate of the new PMTs, the package density of the circular PMTs compared to the hexagonal ones decreases. To close the gaps between the single pixels, light guides are used to reflect the light onto the photosensitive area. The current setup with the hexagonal PMTs uses simple prism-shaped reflectors to cover the gaps between the PMTs (due to its shape they are called 'Mercedes stars', see Fig. 4.15). They are coated with Mylar foil, reflecting the light onto the photocathode.

The positioning of the pixels centres is illustrated in Fig. 4.16 (left, middle). Starting with a regular hexagon in the centre of the camera with a side length $a = 26.35\,\mathrm{mm}$ and an area of about $1804\,\mathrm{mm}^2$. The pixels centres are placed with a side to side angle of $\Delta\vartheta = 1.5°$ which corresponds to 45.6 mm at the focal distance of 1743 mm [72]. The upper and lower rows are displaced by $\Delta\varphi = 1.3°$ and $\Delta\vartheta/2$. In total the 440 pixels are arranged in a 20×22 matrix with a coverage of 30° in azimuth and 28.6° in elevation. Towards the outer edge of the pixel grid, the hexagons become increasingly irregular. The smallest side length is 25.45 mm and the area of about $1693\,\mathrm{mm}^2$. However, the segmentation of the Mercedes stars construct offers a certain flexibility in the hexagons sizing. With the right fit for the smallest hexagon, protruding Mylar foil at the stars edges covers the gap of almost 1 mm. The placement of the Mercedes' vertices with respect to the pixels centre is obtained by moving in steps of $\Delta\vartheta/2$ and $\Delta\varphi/3$ (Fig. 4.16, right).

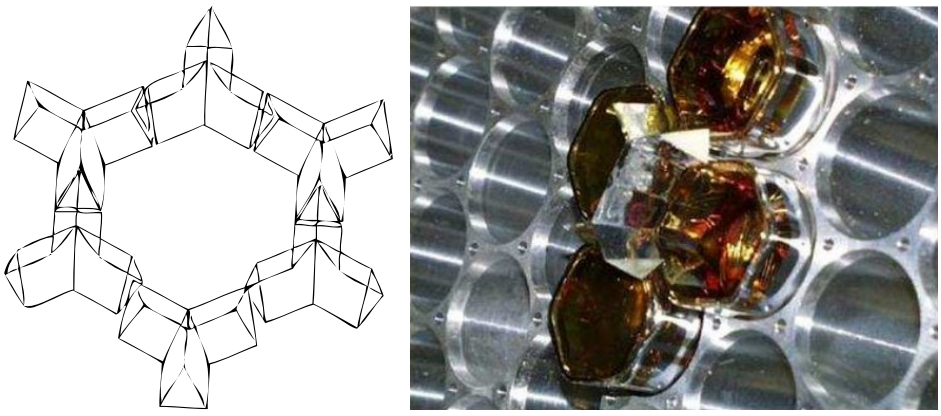

Figure 4.15: Schematics of six individual light guides covering one pixel of the current FD telescope (left) and photo of a single 'Mercedes star' installed (right) [24].

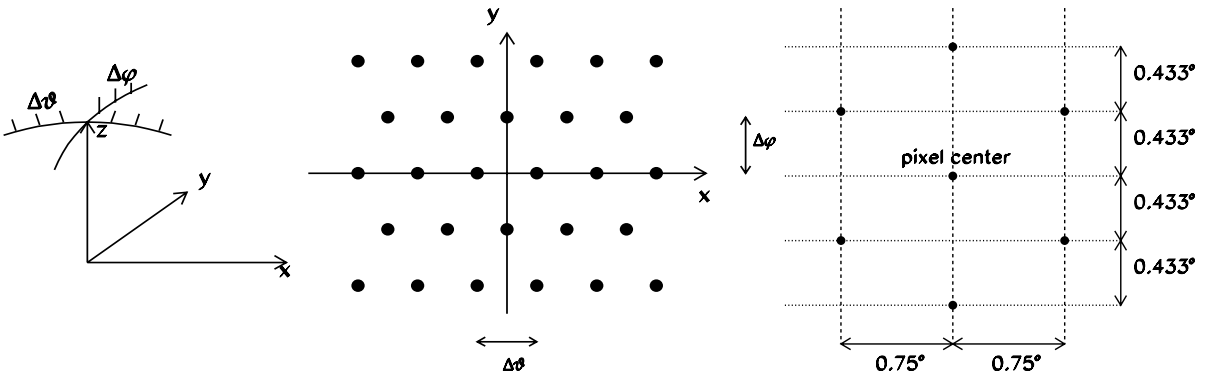

Figure 4.16: Positioning of the pixel centres on the spherical focal surface with $\Delta\vartheta = 1.5°$ and $\Delta\varphi = 0.866°$ (left, middle). Vertex positioning of the Mercedes stars surrounding a pixel centre (right).

This structure is not ideal for the circular shaped PMTs, as the current Mercedes stars would still leave blind spots in the camera surface and an enlarged version would cover some of the PMT's sensitive area, unnecessarily reducing the actual pixel size. To adapt to the new circular shape of the photocathode, a new light guide needs to be introduced. The shape facing the mirror side is still hexagonal to ensure a high package density, but the new light guide must provide a transition between the hexagonal entrance aperture and a round exit aperture. While one could consider a simple cone with a straight slant, Winston cones might be a more efficient solution. The design and production of a Winston cone will be discussed in this section.

4.3.1 Design

Starting in the mid-1960s, the field of non-imaging optics became more prominent, with application in solar energy collectors to increase their efficiency. The main goal is to maximise the concentration of incoming light to a smaller output area. The concentration ratio C is defined as

$$C = A/A', \tag{4.4}$$

where A is the entrance aperture and A' the exit aperture. The theoretical maximum concentration ratio for 3D axisymmetric concentrators with incoming rays to a maximum angle up to θ_i in a medium having a refractive index of unity is

$$C_{\max} = 1/\sin^2(\theta_i), \tag{4.5}$$

with rays exiting from A' in angles up to $\pi/2$ [73]. Despite ideal assumptions of perfect reflective materials etc., there is no cylindrical symmetric 3D concentrator achieving the ideal concentration ratio. Coming close to the ideal concentrator in terms of efficiency is the compound parabolic concentrator (CPC). It was first described by Baranov [74] and for application in Cherenkov counters in combination with a PMT by Hinterberger/Winston [75]. In this design, the edge ray principle is applied to the cone, which has all rays from the maximum accepted incident angle, $\theta_{\max}$, forming a sharp image on the outer rim of the exit aperture with the radius a' (see Fig. 4.17). The focal length of the parabola is given by

$$f = a'(1 - \sin(\theta_{\max})). \tag{4.6}$$

This gives a total length of the concentrator of

$$L = a'(1 + \sin(\theta_{\max}))\cos(\theta_{\max})/\sin^2(\theta_{\max}) \tag{4.7}$$

and an entry aperture radius with

$$a = a'/\sin(\theta_{\max}). \tag{4.8}$$

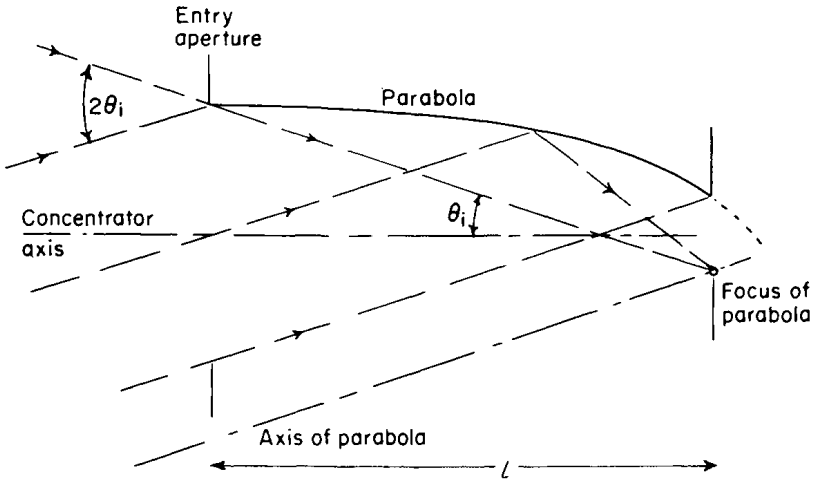

Figure 4.17: Construction principle of the Winston cone via the edge ray principle [76].

By rotating the parabola around the concentrator axis (see Fig. 4.18), the CPC (often called Winston cone) can be described in polar coordinates by

$$r = \frac{2a'(1+\sin(\theta_{\max}))\sin(\phi-\theta_{\max})}{1-\cos(\phi)} - a', \qquad z = \frac{2a'(1+\sin(\theta_{\max}))\cos(\phi-\theta_{\max})}{1-\cos(\phi)}. \tag{4.9}$$

Thus, the design is determined by only fixing two of the four parameters, length, radius of exit and entrance aperture, and maximum acceptance angle.

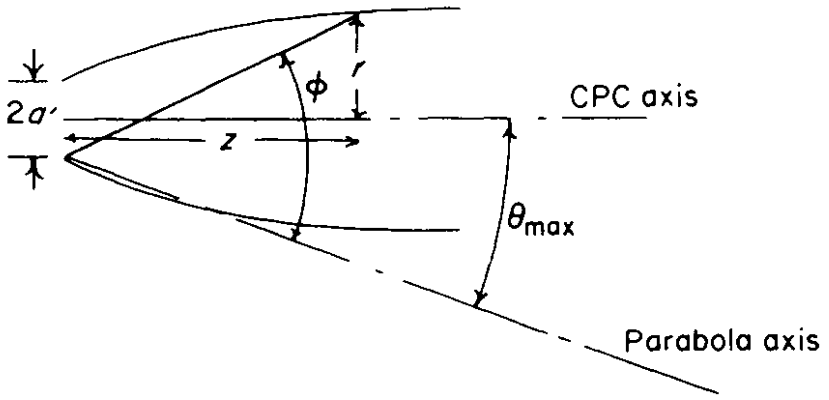

Figure 4.18: Coordinate system and design properties of the Winston cone [76].

The advantage of a Winston cone compared to a straight cone is illustrated in Fig. 4.19. The transmission curves for the straight cone show the losses in efficiency especially for the larger incident angles and its total transmission is in the order of 80%, whereas the Winston cone for the same $\theta_{\max}$ is at about 97% [76]. Also rays with larger incident angles are suppressed more efficiently.

For the usage in the fluorescence telescopes the dimensions of the Winston cone are given by the active area of the new PMT (radius of 17 mm) and the area per pixel at the focusing area. Here, the outer radius of the hexagonal space on the side of the camera is taken with a radius of 25.6 mm. These two parameters fix the Winston cone design with a length of 48 mm. Since by design the Winston cone is rejecting incoming light with an angle larger than $\theta_{\max}$. The maximum acceptance angle for this design is 41.6°. This fits well to the telescope design with its maximum occurring angle of 40° for pixels on the outer rim of the camera (see Fig. 3.5).

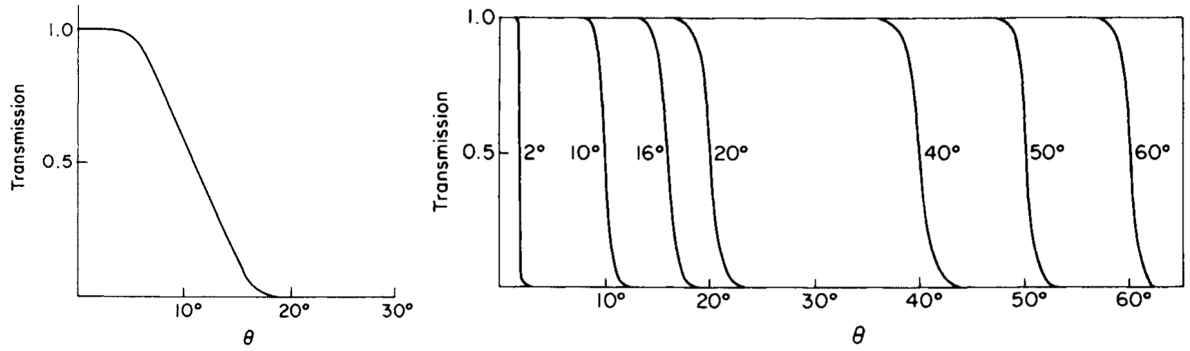

Figure 4.19: Transmission angle curves for a straight cone with $\theta_{\max} = 10°$ (left) and Winston cones for multiple $\theta_{\max}$ (right) [76].

4.3.2 Simulations

The CPC seems to be an efficient choice to enlarge a single PMTs aperture. But the ideal CPC features the same circular entrance and exit-aperture geometry. To maintain the dense packing of the FD camera and keep dead space between the pixels to a minimum, a hexagonal structure at the entrance aperture of the cone is required. While maximising the use of the PMTs circular sensitive area, a transition between these two geometries is needed. There is no obvious solution for an ideal Winston cone with a transition between different types of aperture. Therefore, ray tracing simulations were done to investigate the influence on the performance for different designs.

To study the concentration efficiency of different light cones, simulations were performed using the ROBAST library[7] [77]. ROBAST, the ROOT-based simulator for ray tracing, is written in C++ and uses the geometry library of the ROOT framework [78]. It was developed to perform optical simulations for the Cherenkov Telescope Array (CTA) [64], especially to simulate hexagonal light concentrators, and to offer an open-source solution for ray tracing in the cosmic ray community.

For the simulations, a single cone was modelled and scanned with one ray per $100\,\mu\text{m}^2$ for incident angles up to 60°. A sample distribution of the rays at the exit aperture is displayed in Fig. 4.20. The collection efficiency is calculated as ratio of number of rays passing through the entrance and exit aperture.

The Winston cone form as a tilted parabola has the edges of its entrance aperture in parallel to the cones orientation. This leads to a conflict when arranging the concentrators side by side on a spherical plane as done in the FD telescopes. Thus, a conical inclined cut, as indicated in Fig. 4.23, is used. Figure 4.21 shows the influence of this cut on the collection efficiency for a simulated Winston cone with a reflectivity of 85%. The overall collection efficiency decreases linearly by about 5% in absolute terms per degree of inclination for the cut for the incident angles of interest. In addition the effect of suppressing higher unwanted incident angles is softened.

In addition to the design, the reflectivity of the concentrator material also has an influence on the cone's efficiency. In Fig. 4.22, the collection efficiency of a simulated Winston cone with an inclined cut of 0.75° is shown with its reflectivity being reduced from 100% to 80% in steps of 5%. This effects the overall efficiency, reducing the number of incoming photons up to the maximum acceptance angle. For higher incident angles the efficiency converges for the different reflectivities, with the rejection power of the cone being mainly originating from the cones design.

With the given PMT parameters, the given geometry by fitting into the existing camera optics, and the manufacturer's constrains, there is not much room for flexibility on the cone's design. In order to retain the circular Winston cone shape as much as possible, a composite of a circular Winston cone and a tilted hexagonal cone is used for the final design (see Fig. 4.23).

[7]This study used version 1.5.0 beta.

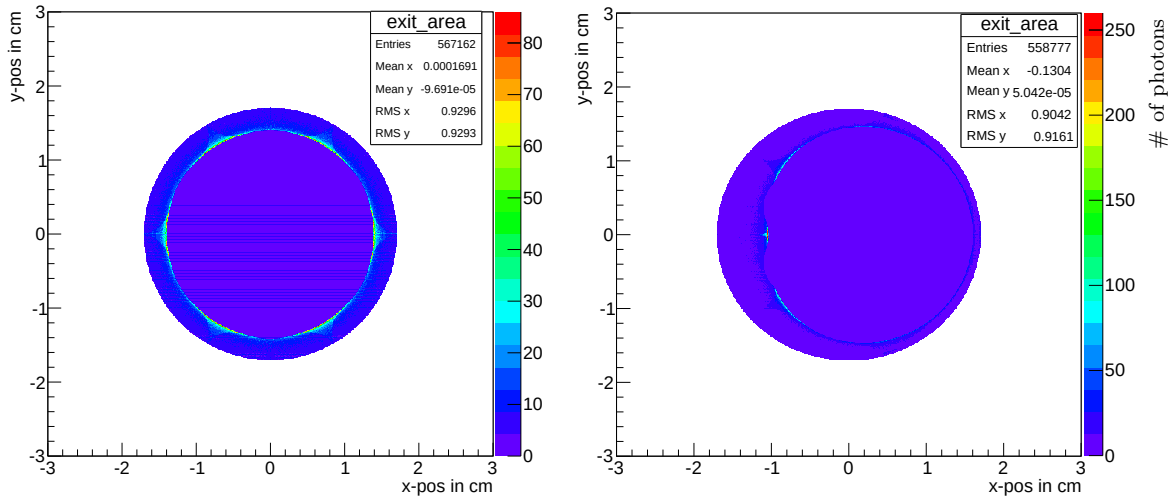

Figure 4.20: Photon distribution of a hexagonal Winston cone at the detector plane for an incident angle of 0° (left) and 10° from the left (right).

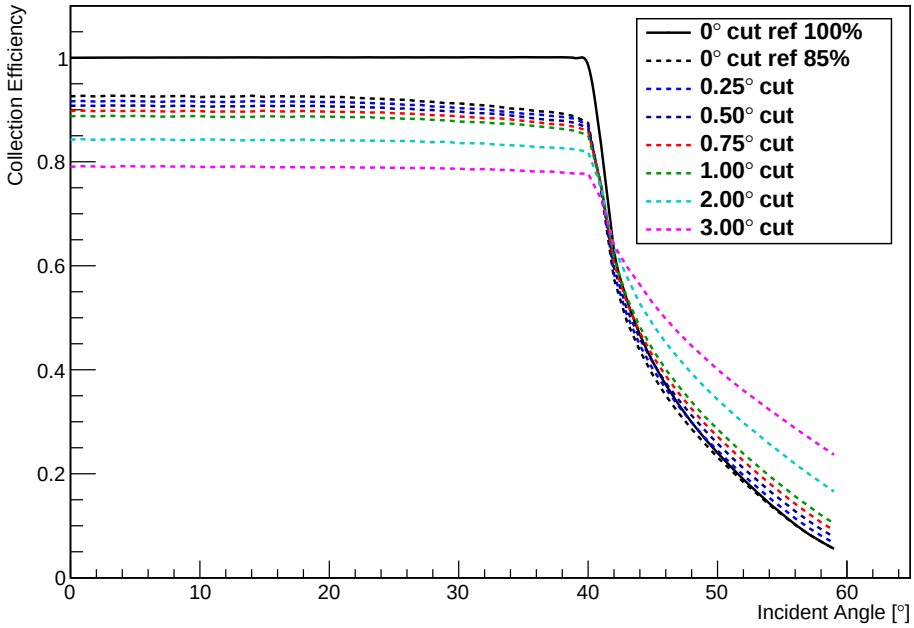

Figure 4.21: Collection efficiency versus incident angle for simulated Winston cones with a reduced material reflectivity of 85% and different inclined cuts into the Winston cone shape.

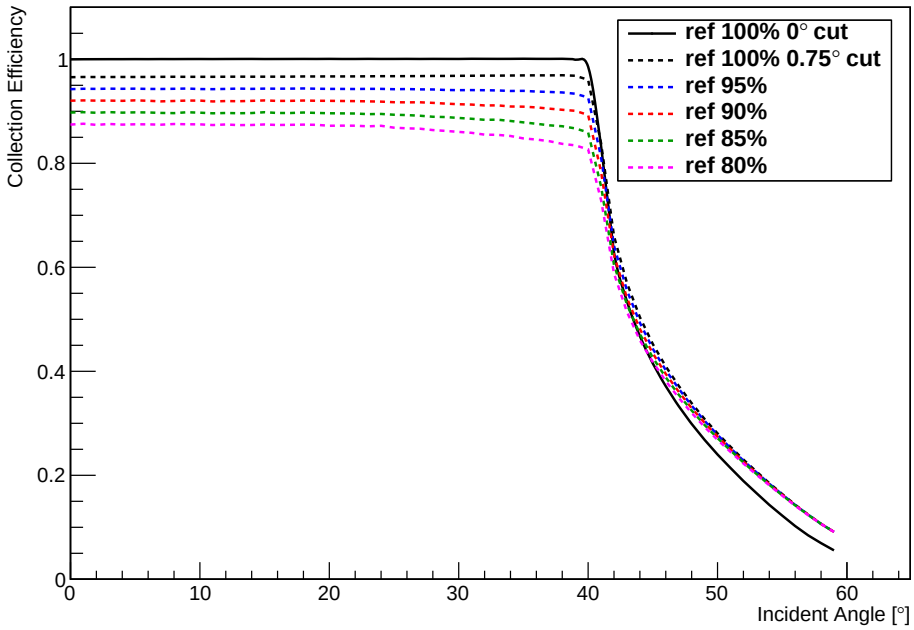

Figure 4.22: Collection efficiency versus incident angle for simulated Winston cones with an inclined cut of 0.75° and different reflectivities.

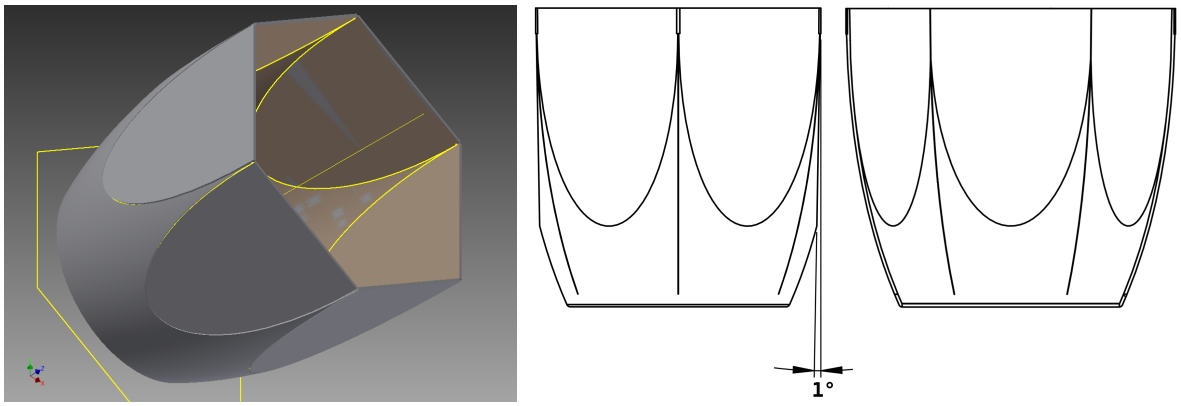

Figure 4.23: Schematics and CAD design of the Winston cone. For a densely packed pixel arrangement, a hexagonal structure is cut into the ideal Winston cone shape. To account for the spherical mounting frame, the cut has an inclination of 1°.

4.3.3 Manufacturing

As shown in the simulations, the reflectivity of the cone material directly influences the overall performance of the concentrator and also that a highly reflective material for the fluorescence light is needed. A suitable material was found in the anodised aluminium 4300UP by Alanod [79]. It has a high reflectivity in the UV range and can be machined to the Winston cone shape. A measurement of the specular reflection with a commercially available spectrometer (CM-2500 by Konica Minolta [80]) can be seen in Fig. 4.24. Within the measurement range of the spectrometer from 360 nm to 740 nm the reflectivity is as high as 90% with an average value of about 85%. The measurement is in agreement with the manufacturer's specifications. The reflectivity towards deeper UV wavelengths stays at slightly above 90%, as the mean reflectivity between 280 nm and 380 nm is given with 90%, and drops again for the UV-C range [81].

The final cones were produced by Alux Luxar [82] in Langenfeld, Germany. The form was cut via laser from a sheet of 4300UP with a thickness of 0.5 mm and the lower part moulded

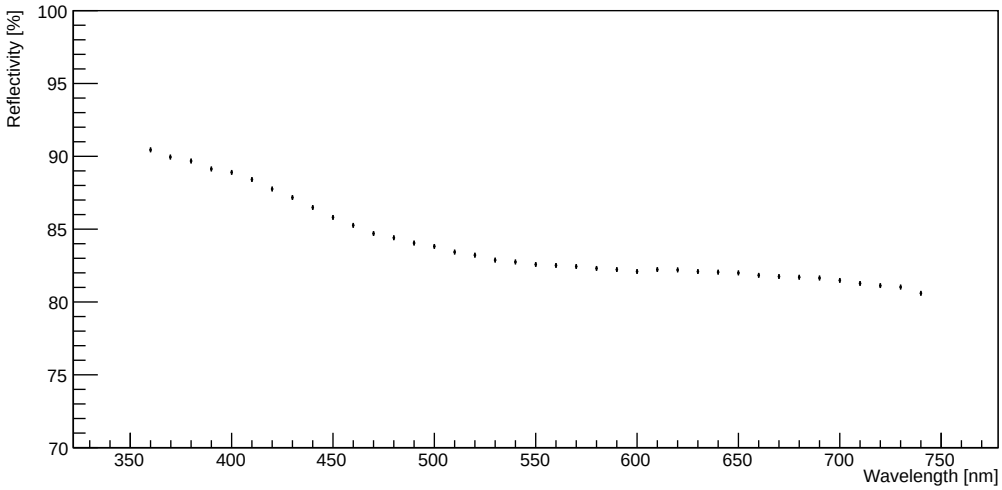

Figure 4.24: Reflectivity measurement of the anodised aluminium 4300UP [79] with the spectrometer CM-2500 by Konica Minolta [80] for the spectrometer range of 360 nm – 740 nm.

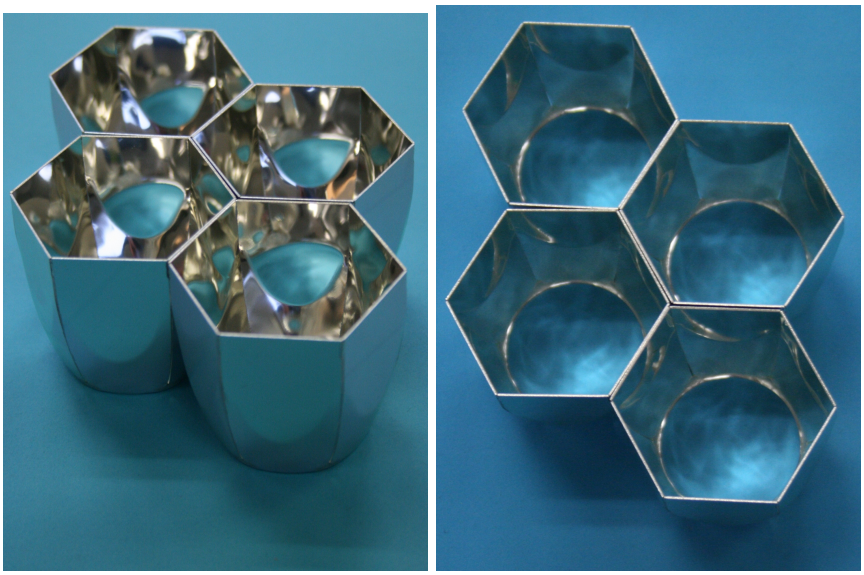

Figure 4.25: Fabricated Winston cones.

to the Winston cone shape. The upper part was bent to the hexagonal shape accordingly and welded at the top. A slope of 1° was implemented to account for the spherical arrangement. Figure 4.25 displays a set of finalised Winston cones. They are supplied with a protective film on the mirror surface to prevent dust from accumulating on the surface during further installation or shipment.

4.3.4 Efficiency Measurements

As an estimate of how well the Winston cones perform with an actual PMT, a uniformity scan was performed. Using the same setup from Section 4.2.2, with a coarser step size of 1 mm, the PMT's response to a 405 nm laser LED was measured. With a point spread of about 1 mm, the active area of the R9420-100 is scanned at the same distance to the light source without and with an attached Winston cone. The results are depicted in Fig. 4.26. By a simple comparison

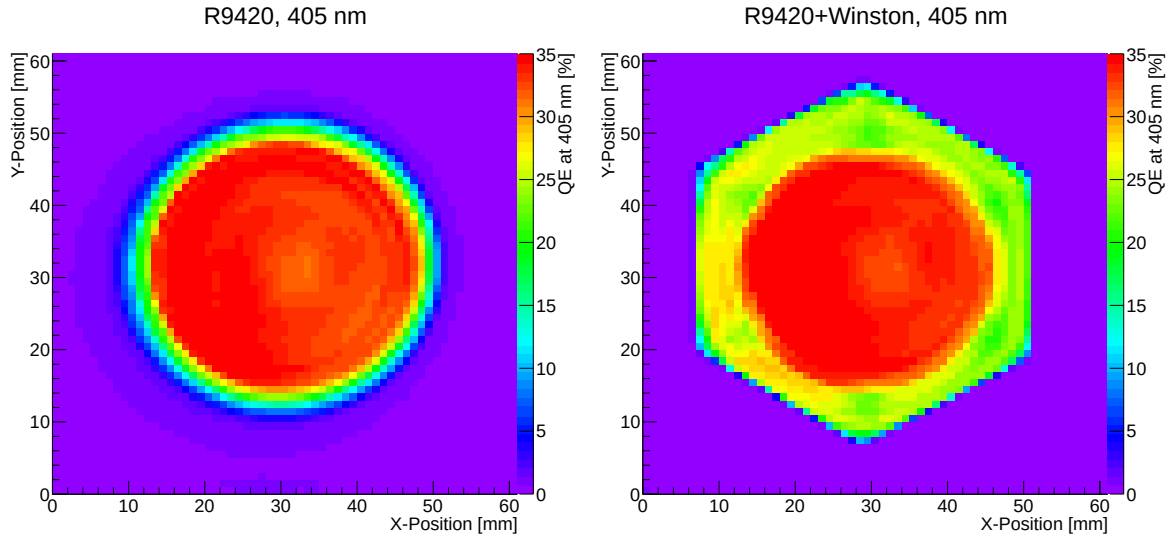

Figure 4.26: Uniformity scan of a R9420-100 PMT without (left) and with (right) an attached Winston cone.

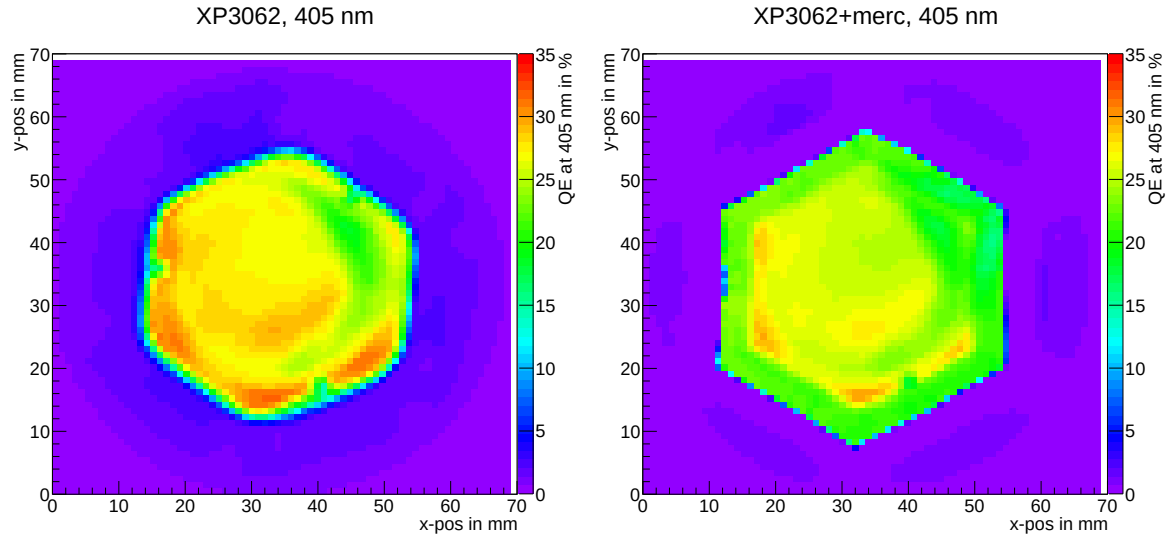

Figure 4.27: Uniformity scan of a XP3062 PMT without (left) and with (right) attached Mercedes stars.

of summing up the efficiencies above a threshold of 10%, the effective area with the Winston cone is enlarged by more than 30%. In addition, by design, the steep entrance aperture results in a sharp cut of detection efficiency at the border of the cone.

The same measurement was done for a XP3062, and attaching a Mercedes star setup. The QE scans are shown in Fig. 4.27. The increase in effective area (again for QE $> 10\%$) is about 19%, in total covering the same area as the Winston cone.

A comparison of the uniformity measurements is done in Fig. 4.28, showing all entries with a QE $\geqq 10\%$ from Figs. 4.26 and 4.27. With their respective light guide installed, both setups cover the same area and with a mean QE of $29.4\% \pm 0.14$ of the Winston cone compared to the $23.6\% \pm 0.08$ of the Mercedes stars, the efficiency ratio is 1.245 ± 0.11. This reflects nearly the QE ratio of the PMTs from the QE measurement of the photocathode in Section 4.2.1 (about 1.23 ± 0.06 at 410 nm). Given the smaller size of the R9420-100's photocathode, the combination with the Winston cone compensates the loss in effective area.

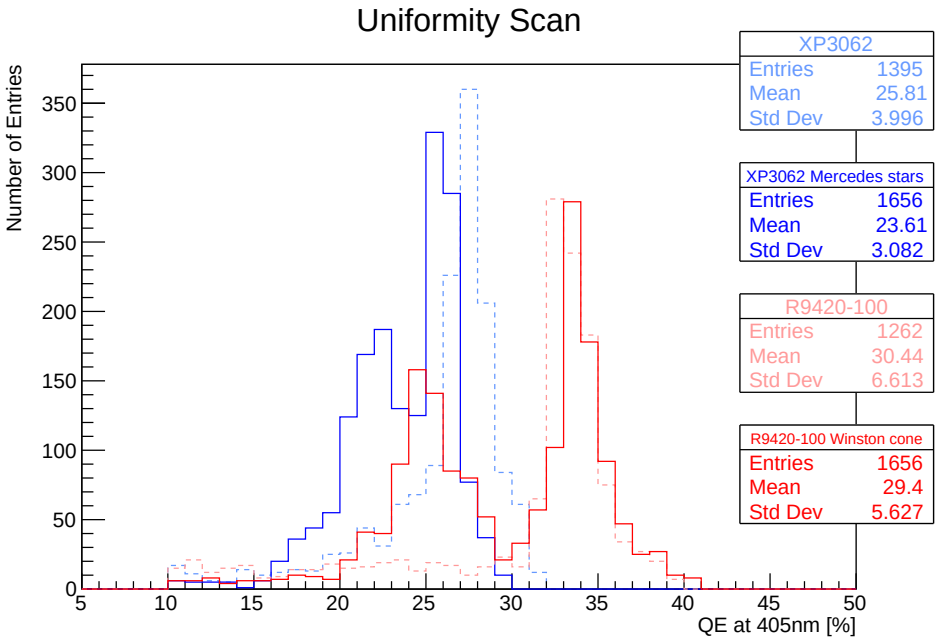

Figure 4.28: Comparison of the uniformity scans of the XP3062 and R9420-100 without and with attached light collectors for QE values $\geqq 10\%$.

In order to try to measure the angular response of the Winston cone in the laboratory, uniformity scans were done for different incident angles. The setup was turned from frontal 0° up to 40° to the right side in steps of 10° in one symmetry axis. The results are shown in Fig. 4.29. As can be seen in the simulations, the highest efficiency is still achieved by hitting the photocathode directly, which moves out of focus as the part of the Winston cone hit first increases with incident angle. The lower right graph shows the integrated QE per incident angle, α, divided by the reference QE measurement at 0° and corrected for the reduced surface area with $1/\cos^2\alpha$. Although it was difficult to maintain the correct distance and the point spread of the scanning light spot inducing high uncertainties which are not considered here the measurement shows a qualitatively well working Winston cone with up to 84% efficiency for an incident angle of 30° followed by a drop towards higher angles.

In a first test, the R11920-100 was measured with an attached Winston cone. Figure 4.30 shows a fine scan of the PMTs response to the 405 nm LED. The weakest points in terms of reflectivity are the corners of the cone, as the welding spots reduce the surface's specular reflection. Due to its curved face plate, the PMT reaches a few millimetres into the cone's volume. Thus, rays with a large exit angle would hit the photocathode at a shallower angle, increasing the detection probability. Although, this will reduce the rejection power of incoming rays with an angle larger than the maximum acceptance angle of the Winston cone.

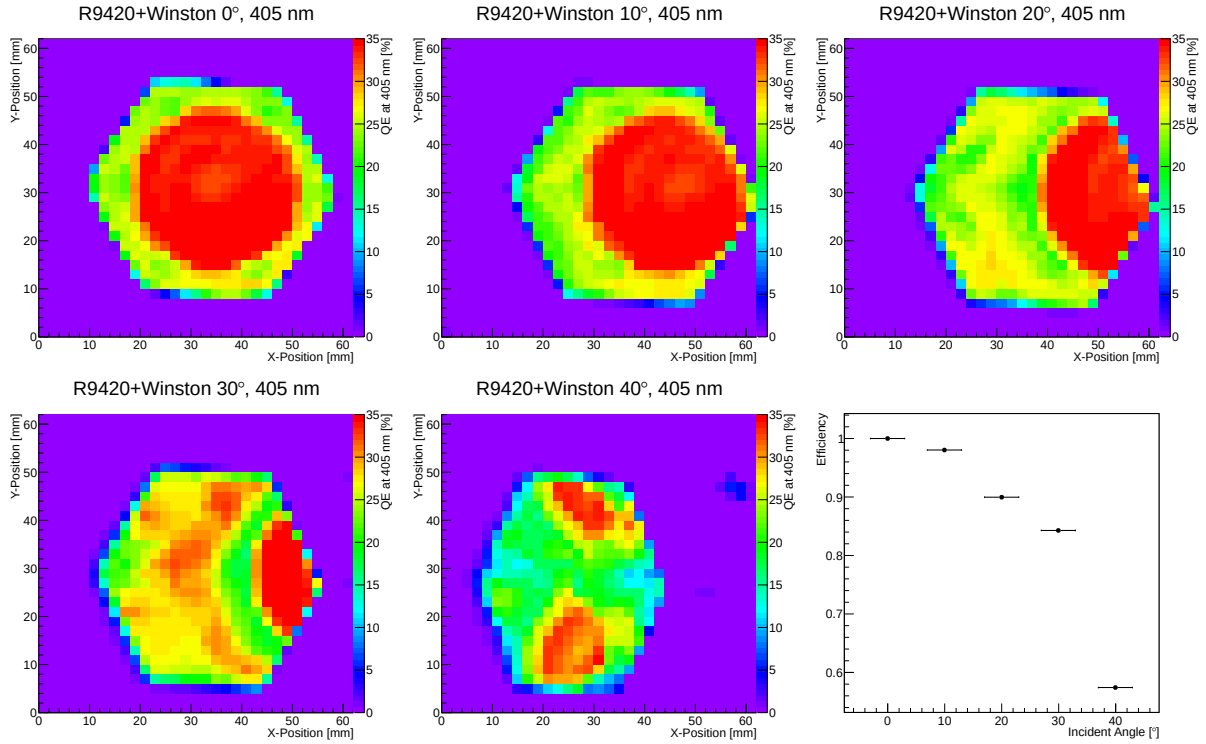

Figure 4.29: Measured angular response of R9420-100 with Winston cone at 405 nm. The step size of the scan was 2 mm. The relative efficiency to 0° response shown in the bottom right [83].

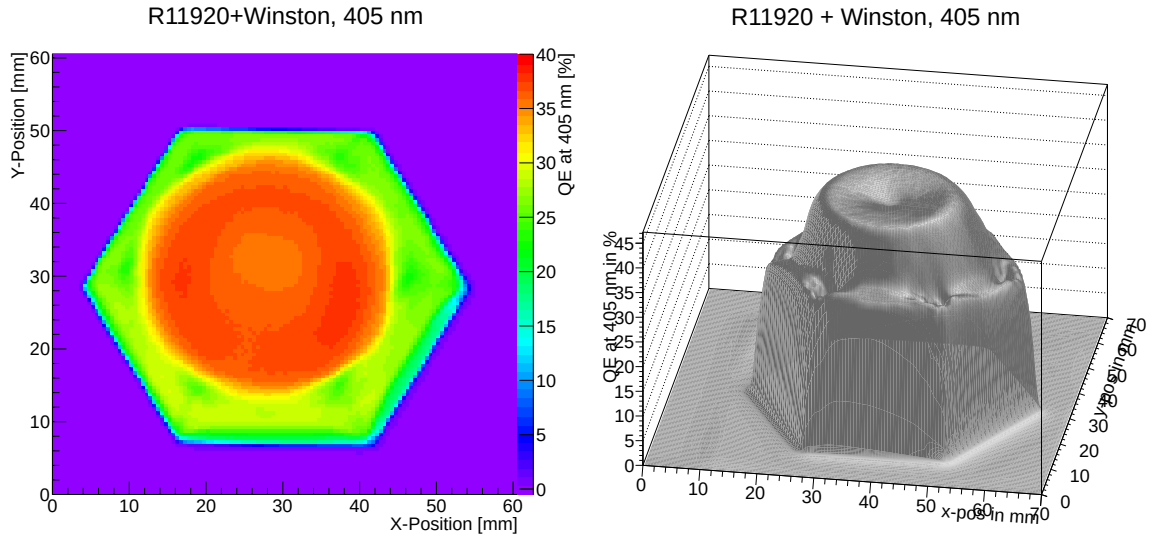

Figure 4.30: Uniformity scan of a R11920-100 PMT with an attached Winston cone.

4.4 Telescope Performance

To test the performance of the new setup of PMTs and Winston cones in the fluorescence detector, a small fraction of the camera from a telescope at the Los Leones (LL) site was equipped with new PMTs. As can be seen in Fig. 3.1, the FOV of both outermost bays in LL is not in overlap with the SD array. For this reason, the PMTs of these parts of the cameras were used to equip the later built three HEAT cameras, which offered the opportunity to test a subset of the new PMTs plus Winston cones in these empty slots of LL bay 6.

4.4.1 Prototype Installation

After a suitable PMT with a higher efficiency for the FD telescopes was found, a first set of 22 R9420-100 PMTs was installed in March 2012 to test the integration and performance of the sensors. As described in Section 4.2, the new PMTs have a similar size and fit into the existing aluminium frame of the camera. However, with a manufacturing error of ± 1 mm for the slightly larger new PMTs (tube diameter of $38\,\text{mm} \pm 1\,\text{mm}$ versus max.37.3 mm for the Photonis PMT) the foam rubber keeping the PMTs in place were replaced by thinner ones (see black stripes in the cavities at the right side of Fig. 4.31).

In a first test to check the compatibility of the new sensors with the read-out chain, a simple version of a light collecting cone bent from highly reflective aluminium was used. The cones were glued to an aluminium ring, which fits into the camera body punch hole (see Fig. 4.31, left). Five PMTs were equipped with these kind of cones. The PMTs were installed in conjunction to the installed XP3062s. While one of the new PMTs was installed with a 'Mercedes star' type reflector, the rest of the PMTs next to the former installation is covered half by these type of reflectors.

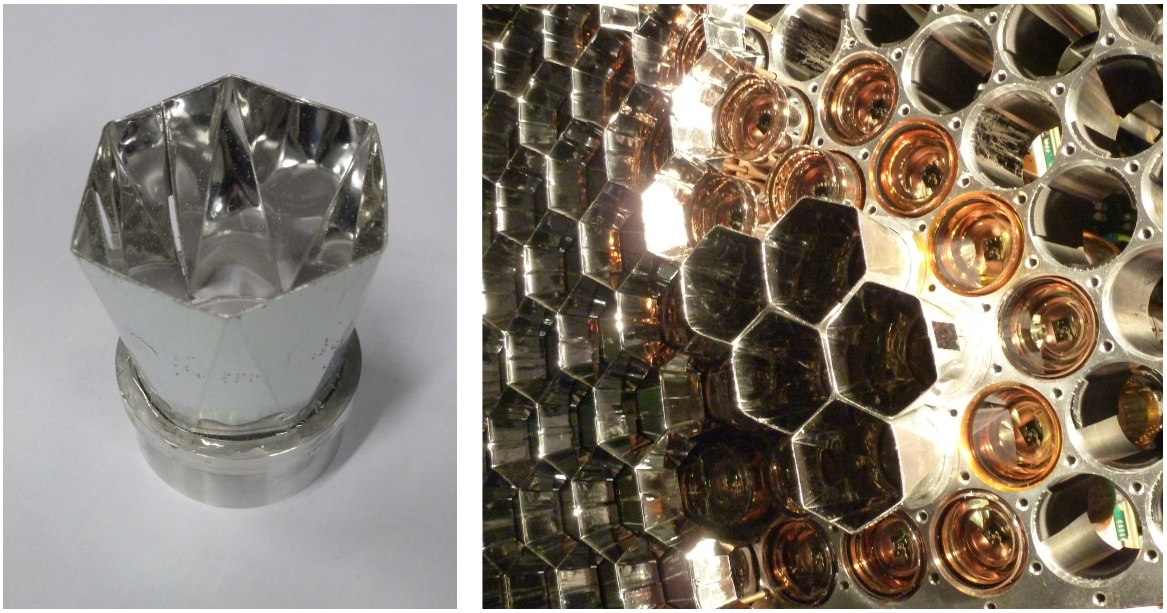

Figure 4.31: Left: Simple cone made from UV-reflective aluminium. Right: A set of five cones was installed in Los Leones bay 6 in 2012.

With the development of a new light cone for the R9420-100, an additional part of the camera in bay 6 was equipped with a new set of PMTs in December 2014. The prototype to test the new system consists of 48 PMTs with attached Winston cones. Due to the limited space between the cones, the mounting pins of the Mercedes stars could not be used to fix a single cone. Thus, a second plate similar to the camera body was produced, holding the 48 cones all at

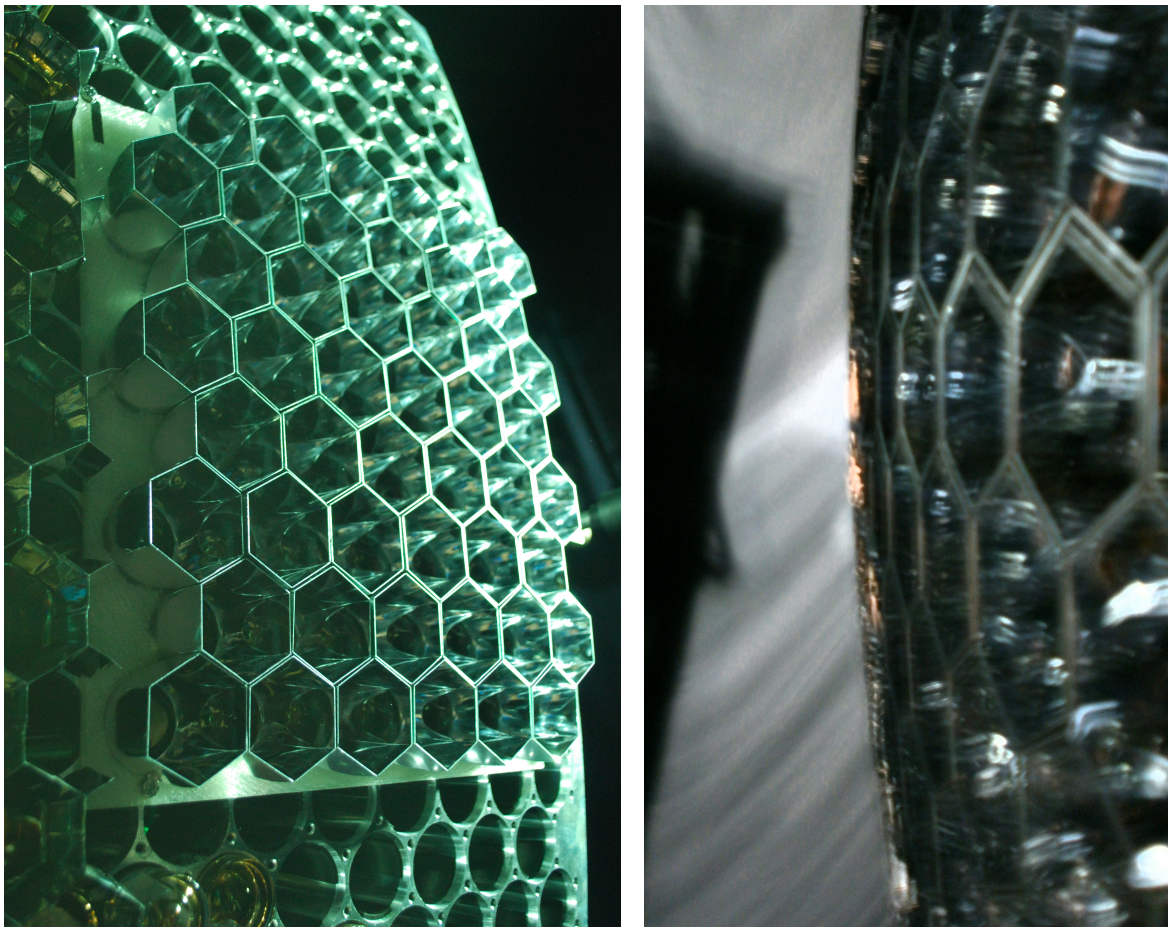

Figure 4.32: Prototype of 48 Winston cones on a mounting plate (left) in Los Leones, bay 6 [83], ending at the same focal plane as the Mercedes stars (right).

once. The plate was designed with the dimensions of 294.4 mm × 314.1 mm, a thickness of 5 mm, and a curvature matching the outer radius of the spherical aluminium frame. The position of the Winston cones is cut into the plate to fix their orientation. The plate was produced using a 3D-printer with PLA material and the cones were glued to the plate with a two component epoxy glue. Figure 4.32 shows the plate with Winston cones, which was fixed to the camera body with screws on the outer edges.

As mentioned in the beginning of Section 4.3, the hexagons on the camera surface are not perfectly regular. Due to the design and production of the Winston cones, their size is not as flexible as for the Mercedes stars. Thus, the system is shifted from maximum coverage to an evenly distributed field of view for each pixel. The total loss in active area of the detector plane is about 3%.

Since the whole camera of 440 PMTs is operated with only ten HV power supplies, 44 PMTs are set on the same HV. Thus, the PMTs had to be classified prior to their use in the telescope to group PMTs with similar gain characteristics and ensuring a homogeneous response. This has been done for the Photonis XP3062 PMTs in laboratory tests [69, 70, 84] and was repeated for the R9420-100 as well. About 500 PMTs were measured in reference to four standard PMTs of the setup [62] and new gain classes were defined accordingly to fit 22 PMTs each (see Appendix A.3). The new 48 PMT arrangement is covered by four different HV supplies. The HV was set to 811 V, 816 V, 821 V, and 827 V (gain classes P,Q,R,S), to match the gain of 5×10^4 of the preexisting camera.

4.4.2 Calibration Tests

As a first test on the performance of the new light guides in combination with the more efficient PMTs, the FD standard calibration measurements were used to compare the update to the existing setup. As described in Section 3.2.1.2, the relative calibrations A, B, and C were performed on a regular basis and provide different incident angles onto the camera surface. In addition, the free-running signal of the night sky background and a pixel scanner measurement were analysed.

4.4.2.1 Calibration A

To minimise the influence of other optical parts of the FD telescope, calibration A (CalA) was analysed. Here, a 365 nm LED[8] in combination with a diffusor is placed at the distance of the mirror, directly illuminating the camera. The charge of the 57 μs square-wave pulses with a rate of 1/3 Hz is measured by a FADC [85]. In Fig. 4.33, a single pulse trace of the CalA is shown in the event display, with the isolated 'isle' of new PMTs on the left side of the camera. The mean charge $< Q^{\mathrm{CalA}} >_{j,k}$ of PMT j for the k^{th} CalA measurement of 50 pulses is determined.

$$< Q^{\mathrm{CalA}} >_{j,k} = \sum_{i=1}^{N_{\mathrm{LED}}=50} Q^{\mathrm{CalA}}_{i,j,k} / N_{\mathrm{LED}}, \tag{4.10}$$

where $Q^{\mathrm{CalA}}_{i,j,k}$ is the sum of FADC counts in 100 ns time bins subtracted by the signals pedestal.

Since the light sources of CalA are not calibrated, the measurement is not an absolute but only a relative measurement. The reference is a CalA measurement which is done within one hour after an absolute calibration. This allows a time dependent analysis of the PMTs signal. The relative calibration constant is defined by

$$C^{\mathrm{rel}}_{j,k} = \frac{< Q^{\mathrm{CalA}} >_{j,k}}{< Q^{\mathrm{CalA}} >^{\mathrm{ref}}_{j}}. \tag{4.11}$$

CalA is performed twice during a FD measurement night, once after a warm-up time with HV set for the camera at the start of the night as well as at the end before shutting down the power supply.

With the reference CalA measurement and the absolute calibration correction C^{abs}_{j} obtained from the drum calibration, the nightly absolute calibration constant for pixel j and the k^{th} measurement is

$$C^{\mathrm{abs}^*}_{j,k} = \frac{C^{\mathrm{abs}}_{j}}{C^{\mathrm{rel}}_{j,k}} = \frac{< Q^{\mathrm{CalA}} >^{\mathrm{ref}}_{j}}{< Q^{\mathrm{CalA}} >_{j,k}} \cdot C^{\mathrm{abs}}_{j}. \tag{4.12}$$

These constants are stored in the monitoring files for the FD telescopes and used in the Offline analyses.

Figure 4.34 (left) shows one of the first CalA responses with the installed Winston cones. In order to compare the different sensors, subgroups are introduced in Fig. 4.34 (right). While the 'XP3062' group contains all XP3062 Photonis PMTs of LL bay 6, the 'reference set' corresponds only to a subset of 48 XP3062 PMTs with their positions mirroring the positions of the Winston cones with regard to the camera symmetry. Thus, only four different gain groups[9] each are taken into account and the sensors have the same elevation with a similar sky coverage[10], which allows a direct comparison to the 'Winston cones'. Denoted as 'simple cones', this subgroup

[8] In use since Nov. 2011 to better reflect the actual fluorescence spectrum of nitrogen. Prior a 470 nm LED was used.

[9] With their separate HV supply.

[10] Not important for the calibrations with closed shutters, though.

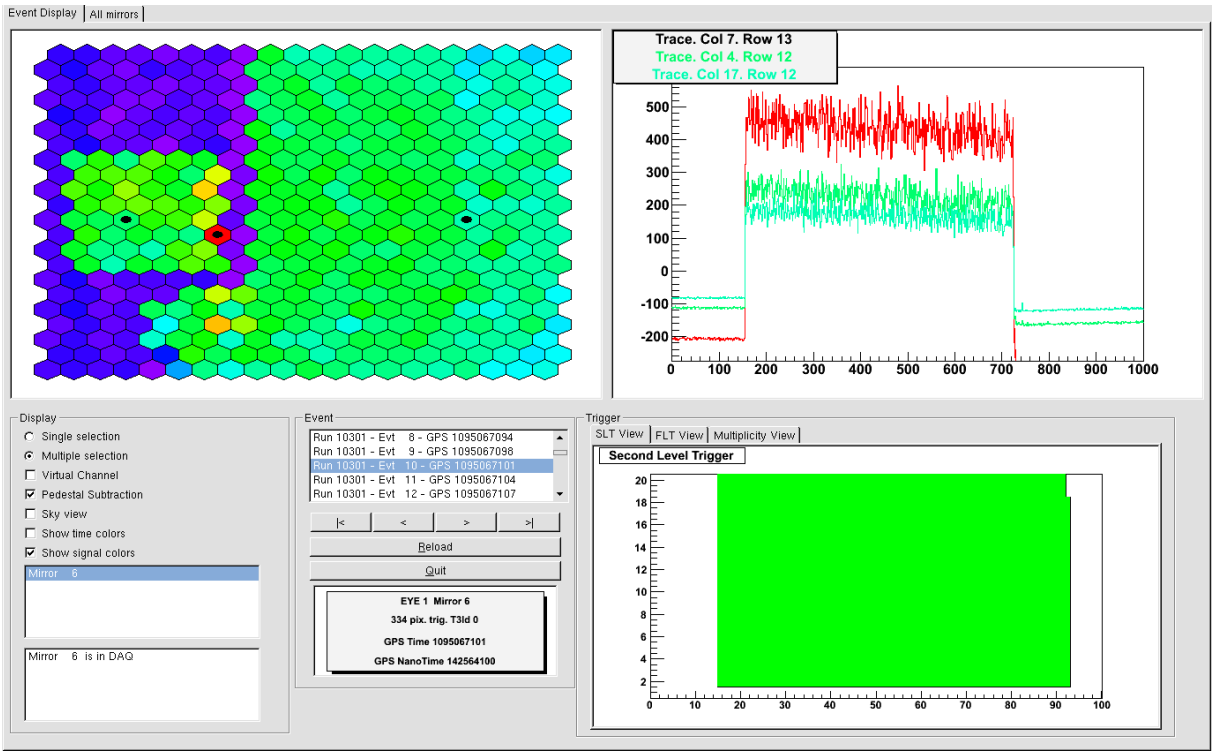

Figure 4.33: Event display showing the response to a single calibration A LED pulse of bay 6 in Los Leones. 48 new PMTs are at the left side (camera view) and running at the same gain as the other PMTs.

includes all R9420-100 PMTs which were installed in 2012. Looking at the single measurement from 14.01.2015 the Winston cone subgroup has about 22% higher signal with a mean CalA response of 1.91 ± 0.02 while the 48 PMTs of the reference set have a mean CalA of 1.57 ± 0.02 (given errors are just statistical errors). Again, this fits to the expected increase due to the higher quantum efficiency and reflects the measurement from Section 4.3.4.

The sensors are running in parallel to the regular FD measurements since without any failure or incidence. After a settling-in phase and looking at the sensors' response after some time of operation, the comparison of the daily mean CalA response of both subgroups for a full year from mid 2018 to mid 2019 is presented in Fig. 4.35 (left) and the daily ratio (right). The mean signal increase after a settlement phase for continuous operation is still at 19%, with the mean CalA response of the R9420-100 at 1.91 and the XP3062's at 1.60. The two sensors have nearly the same spread for the full year, which means the effect of seasonal modulation is the same for both.

Systematic uncertainties are e.g. due to the use of different gain classes and the PMTs' individual gain within these classes. The spread within a gain class for the XP3062 is estimated to be 5% [70]. For the Hamamatsu PMTs this spread is even smaller [62], as the classification was strictly aligned with the new PMTs and the HV values are even closer together (details see Appendix A.3). Since the camera is illuminated directly, there is no additional optics involved to contribute to an inhomogeneous response despite the light source orientation itself. To correct for a bias in the light source orientation, the Winston cone PMTs are compared to the Photonis PMTs at the same position. There was no absolute calibration of the Los Leones' bay 6 telescope since the change of PMTs, thus the comparison to the previously installed Photonis PMTs at the same position from 2009 can only be done via the reference group. To take time evolution of the CalA into account (which is the original idea of CalA), the reference group was compared to the Photonis PMTs at the Winston cone position for the last year with PMTs present. The correction factor obtained for the old CalA measurement is 0.94 (further details

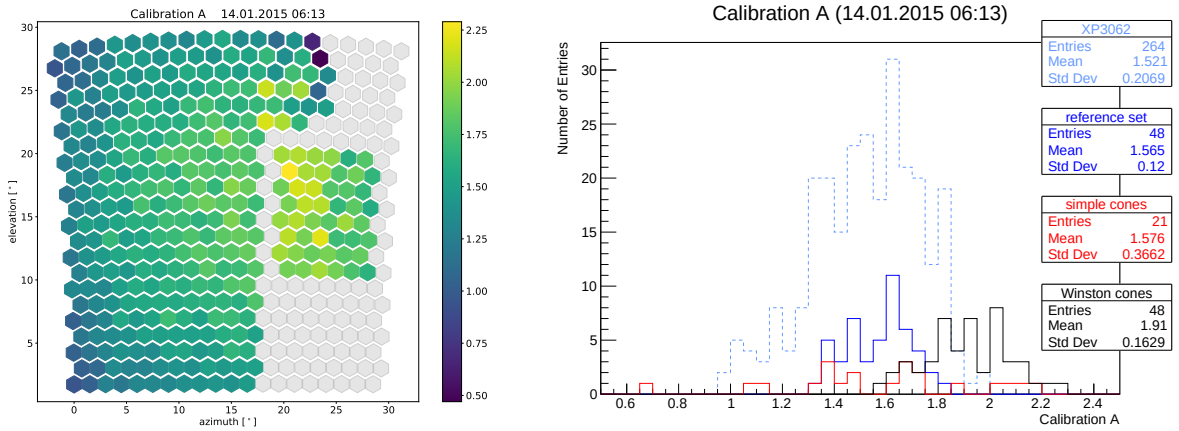

Figure 4.34: Calibration A from 14.01.2015 at 06:13. Left side shows the camera response in sky view of Los Leones bay 6 with the new PMTs installed in the right half. Response of different subgroups on the right, with the new PMTs plus Winston cones in black and a reference subgroup of the XP3062 in solid blue.

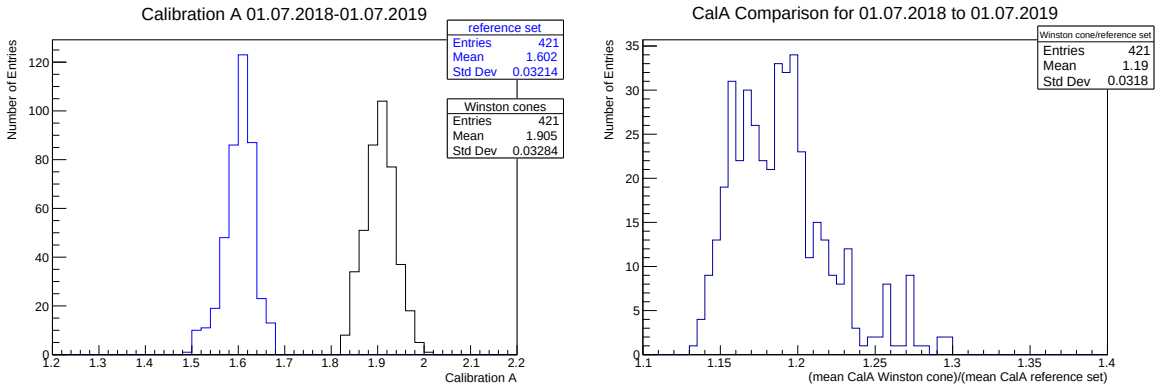

Figure 4.35: Mean calibration A comparison of the new Winston cone PMTs and the reference group (left) and the ratio of the CalA response of the Winston cones/reference group (right) for a year starting from 01.07.2018.

in Appendix A.4). This would reduce the improvement to about 12% for the calibration A. But it should be noted, that the CalA light source was changed in 2011, which might have affected its orientation. On the other hand it is reminded that the area of the Winston cones is slightly smaller than that of the Mercedes stars. With a fixed hexagon size equal for each pixel, the particular 48 cones cover an area which is in total about 3% smaller. Since CalA is illuminating the whole camera, this reduces the measured signal for the new PMTs. However, the light track of a measured particle shower is smaller than the pixel size, and therefore this effect will be not as prominent in the observation.

In addition, the noise level of the CalA is stored as well. Again, Fig. 4.36 shows the single measurement from 14.01.2015. The difference between both PMTs is basically at the level of signal increase with about 21% higher noise for the R9420-100. After a period of constant operation, comparing the noise for a full year, the noise settles to a value of 3.06 ± 0.01 (see Fig. 4.37). For the 48 Photonis PMTs the mean noise is at 2.94 ± 0.01 and the increase of the new system shrinks to about 5%.

Calibration B & C were only performed up until 2018, with details found in Appendix A.5. The new PMTs showed no differences in terms of linearity or spectral response compared to the XP3062. A more accurate comparison can be achieved by a new absolute calibration.

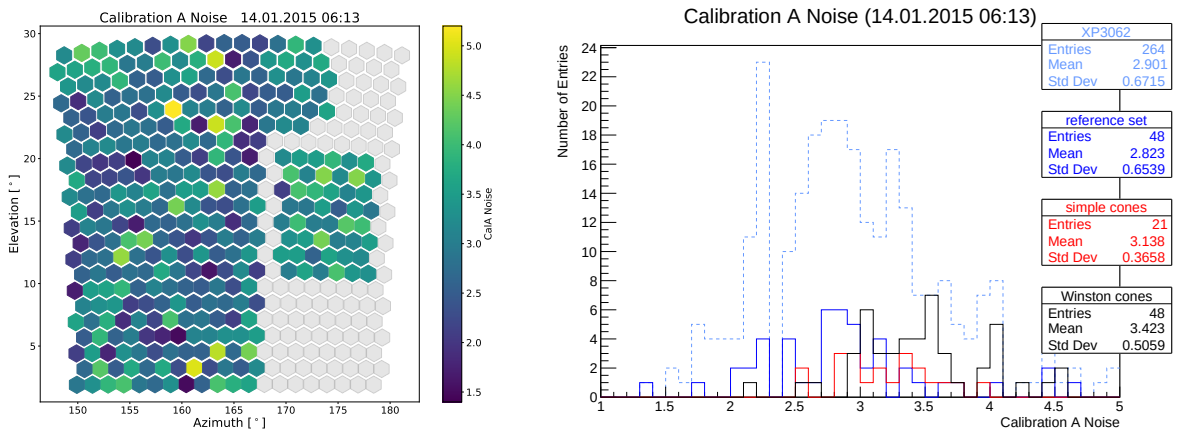

Figure 4.36: Noise level of calibration A from 14.01.2015 at 06:13. Left side shows the camera response in sky view of Los Leones bay 6 with the new PMTs installed in the right half. Response of different subgroups on the right, with the new PMTs plus Winston cones in black and a reference subgroup of the XP3062 in solid blue.

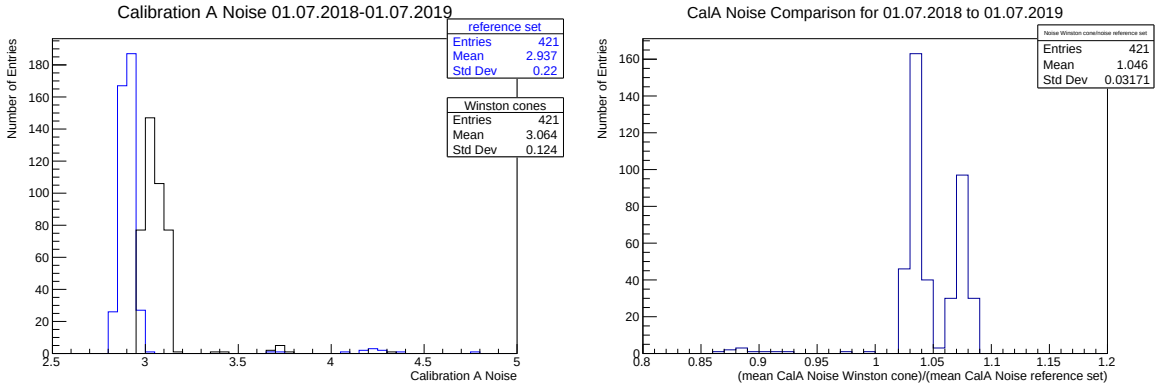

Figure 4.37: Mean calibration A noise comparison of the new Winston cone PMTs and the reference group (left) and the ratio of the CalA noise of the Winston cones/reference group (right) for a year starting from 01.07.2018.

4.4.2.2 Night Sky Background

During observation runs, the FD camera is constantly exposed to the night sky background light which is not blocked by the filter glass. Due to the AC coupling of the PMT signals to the analogue read-out electronics, the shifting DC component of an increased light level can not be observed directly. However, originating mostly from airglow and zodiacal light [86], there is a random nature to the arrival of incoming background photons. With these photons obeying Poisson statistics, the variance is proportional to the mean signal. For calculating the mean and variance of the signal, a hardware integrated algorithm takes a sample size of $(2^{16} - 1)$ for each channel. With the integration time per sample of 100 ns, a total time of 6.5 ms per pixel is analysed, with an accuracy of 0.5% [87]. To limit the disruption of the actual measurement, the night sky background (NSB) is measured every 30 s during normal operation. A sample measurement of the NSB at a random time in the night is shown in Fig. 4.38 with the same subgroups from Section 4.4.2.1, comparing the Winston cone group with a subgroup of old PMTs. The NSB variance of the new PMTs is at 32.38 ± 0.37 ADC counts^2 and for the reference set is at 21.85 ± 0.30 ADC counts^2. However, individual measurements are very sensitive to the numerous light sources passing over the night sky.

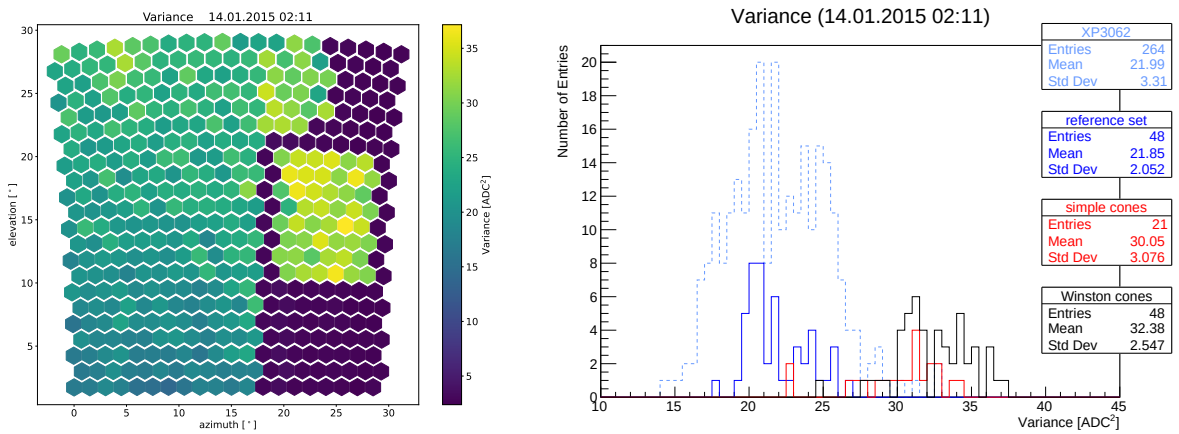

Figure 4.38: Night sky background measurement of the 14.01.2015 at 02:11. Camera response in sky view on the left side and different subgroups on the right side.

The measured variance is a combination of the NSB and the noise variance combining the electronic noise and the PMT noise,

$$[\sigma^2_{\mathrm{ADC}}]^{\mathrm{total}} = [\sigma^2_{\mathrm{ADC}}]^{\mathrm{NSB}} + [\sigma^2_{\mathrm{ADC}}]^{\mathrm{noise}}. \tag{4.13}$$

Since the NSB measurement is started during the calibration procedure before and after each measurement night, the variance is also recorded with closed shutters[11]. Analogue to [88], the variance of these periods is considered to contain only the noise contributions and is subtracted to retain the corresponding NSB. In Fig. 4.39 the NSB measurement from mid 2018 to mid 2019 is displayed. The noise level for the new set with 3.49 ± 0.005 ADC counts^2 is about 6% larger compared to the reference group with 3.28 ± 0.005 ADC counts^2, and fits well to the noise measurement of the previous section. With the considered noise, the increased NSB signal for the new PMTs is at $17.57\% \pm 0.002$. While both set cover the same elevation, the orientation of the new PMTs is more directed towards the city of Malargüe (see map in Fig. 3.1). However, not directly oriented at the city and at an elevation coverage from about 12° to 21°, an additional constant contribution to the measured NSB is expected to be rather small but might be of interest for more in-depth studies.

4.4.2.3 Pixel-by-Pixel Calibration

To identify miscabling of single pixels in the FD telescopes, the so called 'Pixel-by-Pixel' calibration was introduced in 2010 [89]. While the standard calibration procedures (A, B, C) illuminate the entire camera, here the light of an UV-light LED with a wavelength of 375 nm and a pulse duration of 20 μs is collimated to a single spot smaller than the camera pixel size. Via two steerable mirrors the light spot can be navigated across the camera and scan the entire PMT matrix. The system is attached to the camera frame and two arms holding the scanner in front of the centre of the spherical segmented mirror, close to the light source of CalA. With the fixed position of the scanner of about 1.6 m in front of the curved camera surface, the light spot size and incident angle are not uniform across the camera. Even though no miscabling was found after installing the prototype of the Winston cones, one can also use these measurements to identify how well the new cones cover the dead space between the PMTs. In Fig. 4.40 a scan of the 48 new PMTs is shown for the prototype without (left) and with (right) attached Winston cones. The focal plane is changed for the installed light guides, and thus some of the PMTs

[11] Identified by a higher repetition rate of 5 s instead of the 30 s.

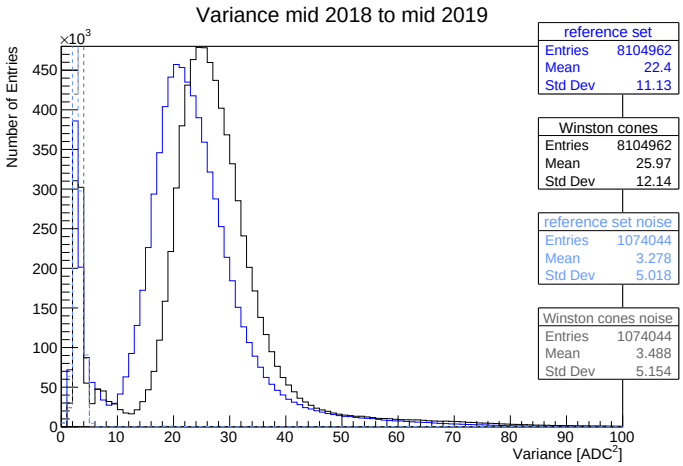

Figure 4.39: Night sky background measurement for the Winston cone and reference group from mid 2018 to mid 2019. In dashed lines the measurement with closed shutters is shown.

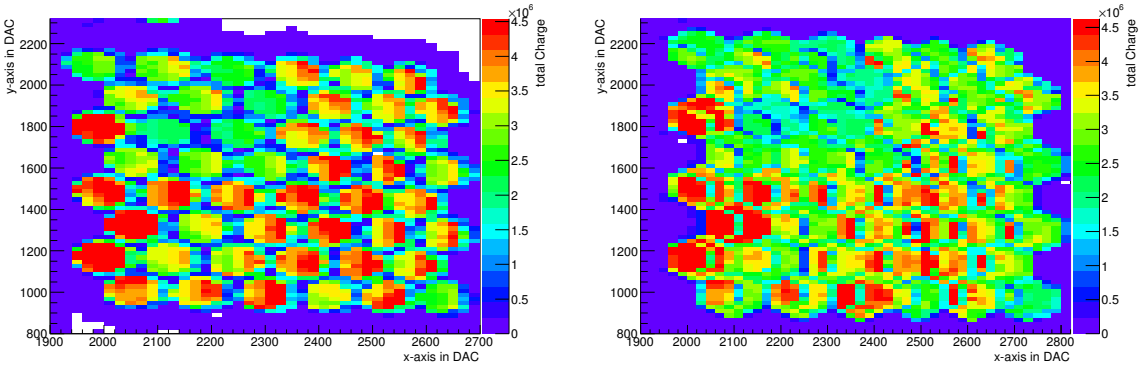

Figure 4.40: Pixel scan of the new PMTs without (left) and with (right) installed Winston cones.

sensitive area is shadowed by a cone, causing less high charge measurements. However, the gaps between the single pixels vanish almost completely and the response is more uniform.

A fine scan of a single pixel was performed. With an even finer resolution and step size compared to the laboratory measurement in Section 4.3.4, more detailed structures of the reflectivity can be seen. In Fig. 4.41 the scan of a R9420-100 with attached Winston cone at column 6 row 12 is shown. The pixel centre corresponds to an incident angle of almost 13°. Here, the measured charge on the Winston cone decreases by less than 25% compared to the direct light onto the PMT, whereas the charge for the Mercedes stars decreases by 1/3 [89]. However, with its narrow incident angle, this measurement does not reflect the optics of the telescope well. This measurement also illustrates the problem caused by the plane glass front with a curved photocathode. The light can emerge at the edge of the PMT where the photocathode bends away from the glass front. This is especially crucial for the Winston cone, where the focus for the largest acceptance angles is on the outer rim of the exit aperture. The total efficiency is still better with the Winston cone and the new PMTs compared to the XP3062 and the Mercedes stars, despite its smaller effective area. The R11920-100 with its curved photocathode would even benefit from the large angles. Reaching about a centimetre into the cone, the photons could hit the cathode a second time, if not converted or scattered in the first place.

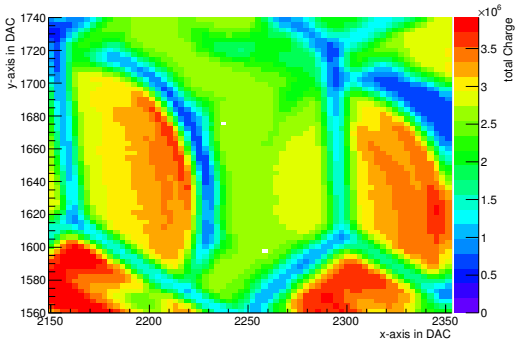

Figure 4.41: Fine pixel scan of a new R9420-100 PMT with Winston cone at column 6 row 12 in Los Leones bay 6.

4.4.3 Long-term Performance

The system of 48 new PMTs plus Winston cones was installed in 2015. Running continuously since, the PMTs were used along the normal detector operation. With no major incident or failure happening, the long-term performance can be derived from the frequently executed calibrations and the measurement of the night sky background. Calibrations are executed regularly before and after each measuring night.

The daily mean CalA responses of the PMTs with Winston cones and the reference set are shown in the top of Figs. 4.42 and 4.43 from 2015 to the end of 2022. In order to look for a trend in the long term behaviour of the CalA data, a time series analysis was done using the Seasonal Trend decomposition using Loess (STL) procedure [90]. With a period of 365 days, the decomposition into a trend, a seasonal, and a residual part is shown. In both cases the fluctuations are around $\pm 5\%$, with the seasonal contribution accounting for about half of the effect and the residuals. From the fit, there is no obvious connection between the two trends, but also no hint of permanent performance loss over time.

In contrast to the calibrations, the night sky background is measured during data taking. Since the schedule for FD measurements is based on the lunar cycle, the contribution of moonlight may vary. Thus, a second seasonal component is introduced and the time series analysis is extended using the Multiple-Seasonal Trend decomposition using Loess (MSTL) procedure [91] with a period of 29 days for the lunar cycle and 365 days for a year. Figures 4.44 and 4.45 show the recorded background light data for the Winston cones and the reference group. The daily mean value is calculated for each subgroup, with no extra cut on outliers, e.g. bright stars crossing the field of view. While the fluctuations for the NSB are quite large, the resulting fits show very similar patterns for both seasonal components. Also the trend is align for the two subgroups, demonstrating that the surplus in efficiency for the new sensors did not decrease over the last eight years of operation.

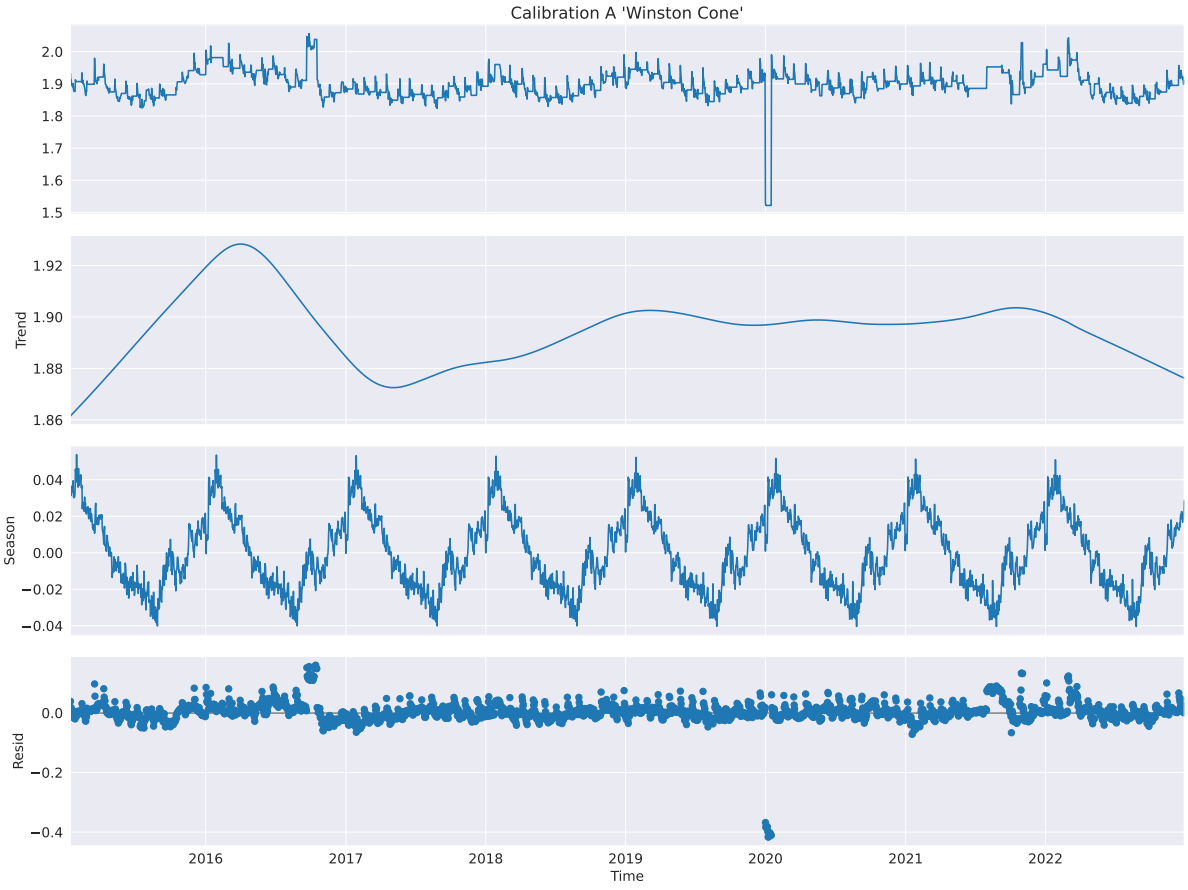

Figure 4.42: Long term evolution of the CalA constant averaged for the 48 new PMTs with attached Winston cones in Los Leones bay 6. Decomposition to trend, seasonal and residual components are shown below.

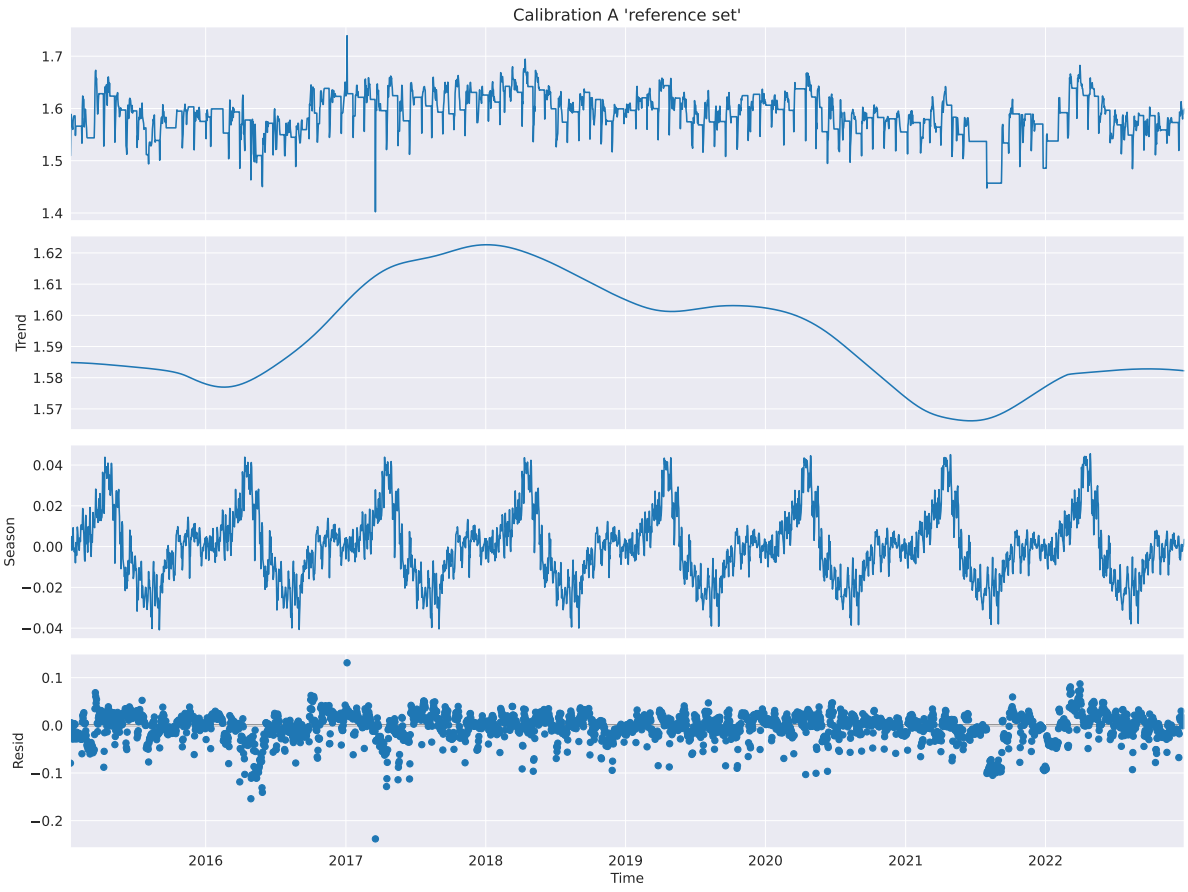

Figure 4.43: Long term evolution of the CalA constant averaged for the 48 XP3062 PMTs of the reference group in Los Leones bay 6. Decomposition to trend, seasonal and residual components are shown below.

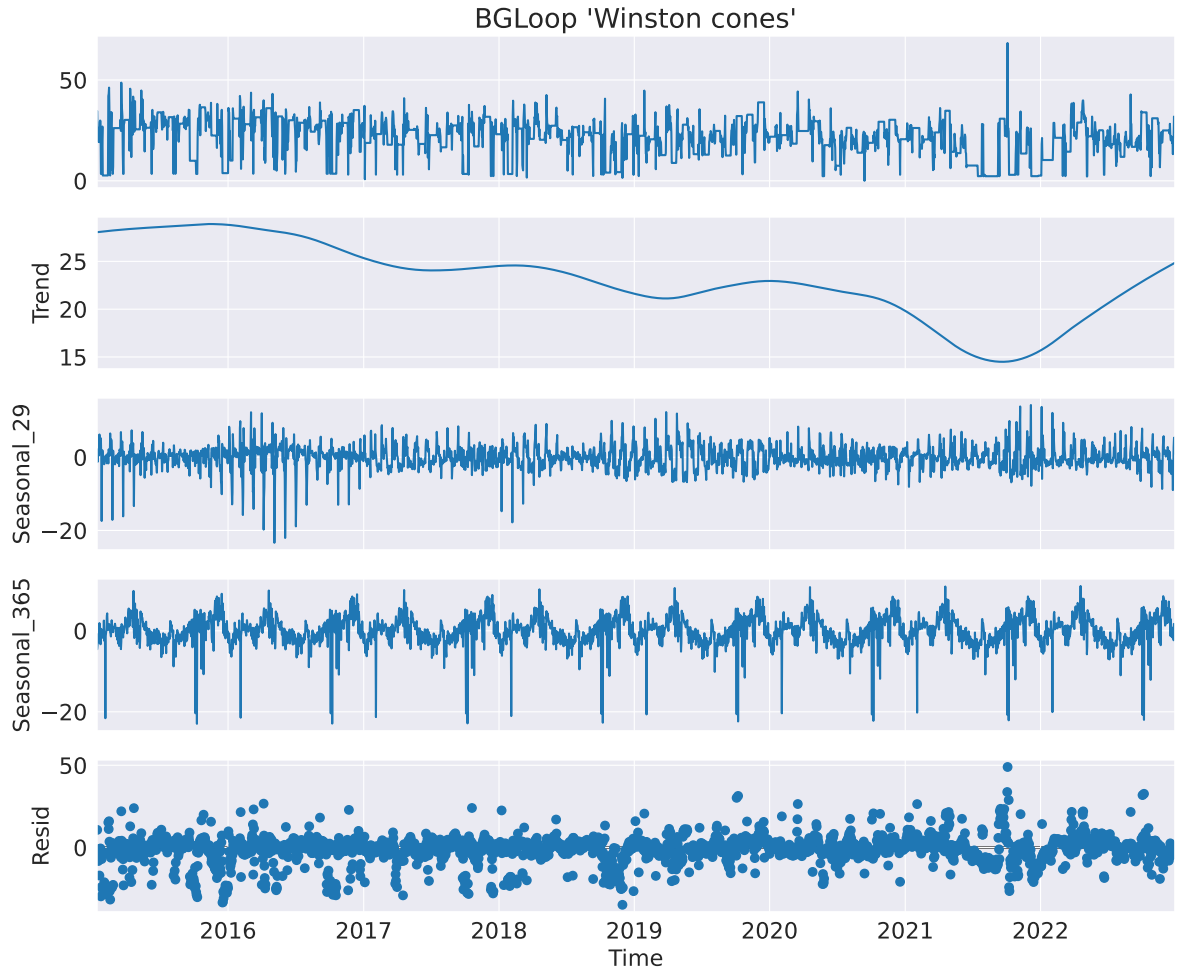

Figure 4.44: Daily mean background light measured with the 48 new PMTs plus attached Winston cones from 2015 to the end of 2022 (top). Decomposition into a trend, two seasonal components with periods of 29 and 365 days, and residuals.

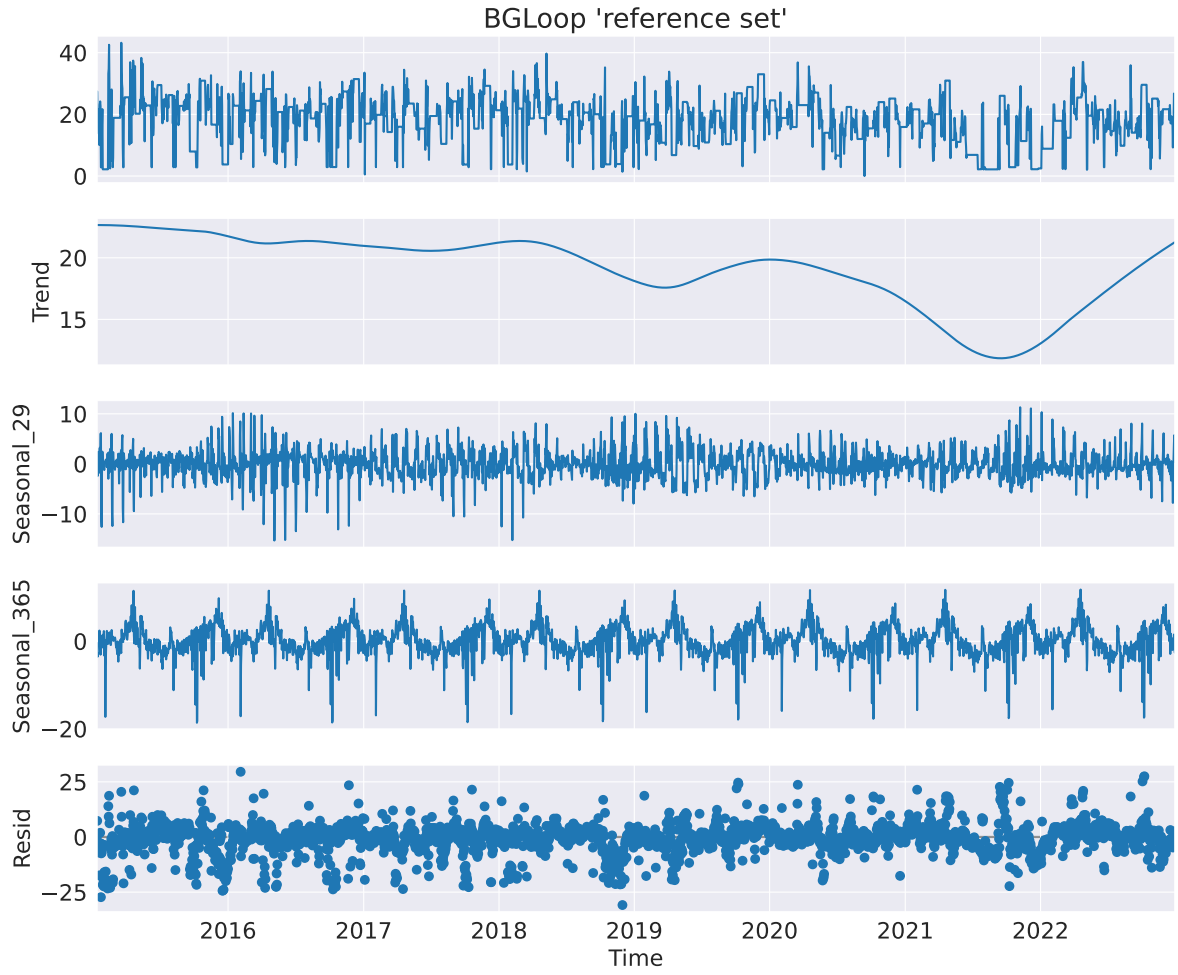

Figure 4.45: Daily mean background light measured with the 48 XP3062 reference PMTs from 2015 to the end of 2022 (top). Decomposition into a trend, two seasonal components with periods of 29 and 365 days, and residuals.

4.5 Conclusion & Future Prospects

The Hamamatsu R9420-100 PMT was well integrated into the FD camera and its read-out electronics and the very first PMTs are running flawlessly since 2012. The modified Winston cone performs well with the PMT, according to the tests of the relative calibration system.

As a further performance check, the newly introduced XY-scanner calibration [44, 92] could be used to compare the new light guides to the current system. Different than the calibration done in Section 4.4.2.3, this XY-scanner is installed in front of the aperture window, outside of the FD building, and scans the field of view with a small light spot. The light source is calibrated and it is intended to perform an absolute end-to-end calibration, replacing the Drum calibration mentioned in Section 3.2.1.1. Due to the long time period that the PMTs are in operation, stars could also be observed with the new PMTs. As was shown in [93] this can be used as an alternative way to perform an absolute calibration or at least be used as a cross-check on the sensors' efficiency.

The more efficient PMTs in combination with the adopted Winston cones provide an increased capability to detect light with the FD telescopes. As simulations showed, this should enhance the field of view and thus the exposure of the detectors. After the prototype test, the next step would be to equip one complete camera with the new system, preferably one of the HEAT cameras. Here, the enhanced FOV in combination with the Infill-array on the ground should result in a higher exposure.

As the laboratory tests showed, the R11920-100 PMT with its frosted window has an even higher photon detection probability. Due to its curved entrance window, the usage in combination with the Winston cone seems promising. In context of another work, a single PMT was installed in the prototype area in November 2017, but its supply voltage not adjusted to match the gain of the other surrounding PMTs, needed for a direct comparison. In the future, a few more of these types from the laboratory tests could be added to the detector and run with the same gain as the rest of the camera. Additional 105 PMTs were bought and after a quality measurements could be tested in the free spots of either bay 1 or 6 in Los Leones.

Chapter 5

Surface Detector Upgrade

To answer the unresolved question on the composition of cosmic rays at the highest energies, the Pierre Auger Observatory is upgrading the existing surface detector stations. To be more sensitive to the composition of the primary particles, the idea is to improve the separation of hadronic and electromagnetic shower components. Therefore, an additional scintillation detector is placed on top of each SD station. The few cm thick plastic scintillators will mainly measure the electromagnetic component while the signals in the Water Cherenkov Detectors (WCD) are dominated by the muon signals.

This chapter describes the design of the Scintillation Surface Detector (SSD) as part of the AugerPrime upgrade and focuses on the photosensitive part of the new detector component.

5.1 Design

With the current SD stations situated in the harsh environment of the Argentinian Pampas, the upgrade of the WCD with an additional detector has to be easy to realise, reliable and keeping maintenance as minimal as possible. This is achieved by equipping every SD station with a $4\,\mathrm{m}^2$ plastic scintillator on top [94]. The scintillator is packed in an aluminium box and can easily be mounted on top of the SD detector (see Fig. 5.1). The sensitive area is split into two parts of $\sim 2\,\mathrm{m}^2$ size each, with the read-out detector placed in between (Fig. 5.3). The detector consists of extruded polystyrene scintillator bars with a length of 1.6 m, produced at the Fermi National Accelerator Laboratory (FNAL) [95]. Each bar has a width of 5 cm, a thickness of 1 cm, and is coated with a highly reflective TiO_2 layer. A total of 24 bars is used per detector part. Each bar is perforated alongside twice, giving room for the routing of wavelength shifting (WLS) fibres, which will pick up the particle induced scintillation light and redshift its wavelength. As WLS fibres the Y11 by Kuraray is used. Its absorption spectrum (see Fig. 5.2, right, blue part) fits well to the UV emission spectrum expected from the scintillator (Fig. 5.2, left) and emits light in a spectrum peaking between 450 nm and 550 nm [96]. Within the fibres the light is guided via total reflection. The fibres are routed in an "U"-configuration and pass the sensitive area twice. All 96 fibre ends are routed to the centre of the detector and glued together, bundled as a 'cookie' with a diameter of 13 mm (Fig. 5.4). This fibre bundle is attached to a 22 mm silicon pad on a light detector. As default option a photomultiplier (PMT) will be used to measure the amount of light produced by the transient particles. In addition, novel detectors like silicon photomultiplier (SiPMs) will be tested in the SSD environment.

Complementary to the SSD installation, the AugerPrime upgrade will also enhance the dynamic range of the WCDs. This is achieved by installing an additional PMT with smaller active area next to the existing three large WCD PMTs, facing towards the water volume. By detecting only a fraction of the light compared to the large PMTs, the small PMT (SPMT) signal will not saturate as fast for stations detecting high energy events close to the shower core. Since the AERA array has proved that the radio detection is an important technique to measure cosmic rays, a radio antenna will be installed at each SSD station as well.

With the new detector components on top, additional read-out channels are needed. The currently used Unified Board (UB) (in operation since 15 years) lacks free channels for the SSD detector and the small PMT in the WCD, so an Upgraded Unified Board (UUB) is produced

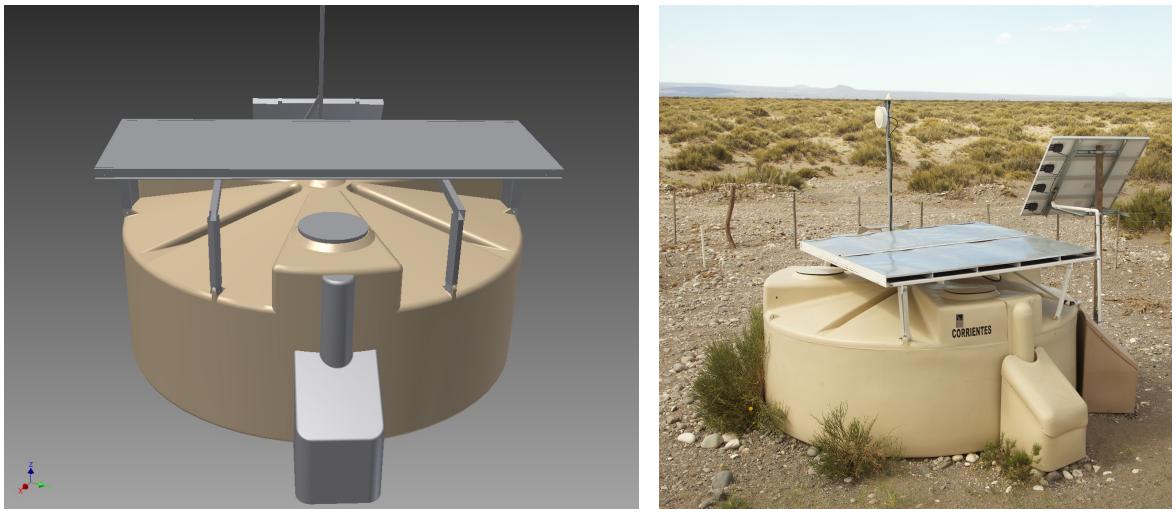

Figure 5.1: 3D model (left) and picture (right) of a WCD station with an assembled prototype scintillator detector on top.

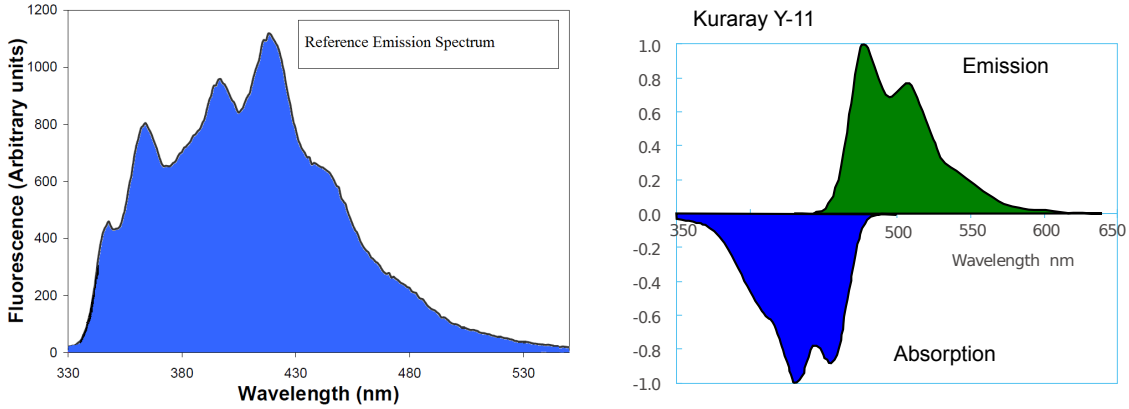

Figure 5.2: Emission spectrum of the FNAL plastic scintillator (left). Absorption and emission spectrum of the Kuraray Y11 wavelength shifting fibre (right) [94].

using up-to-date components. For signal digitisation a 12 bit 120 MHz FADC will be used, increasing the sampling rate from 40 MHz to 120 MHz. With the improved power consumption of the new components, the average power of 10 W, supplied by the existing solar panels, is sufficient to power the new detectors. Only in the Infill area an additional power system will be installed for the Underground Muon Detector.

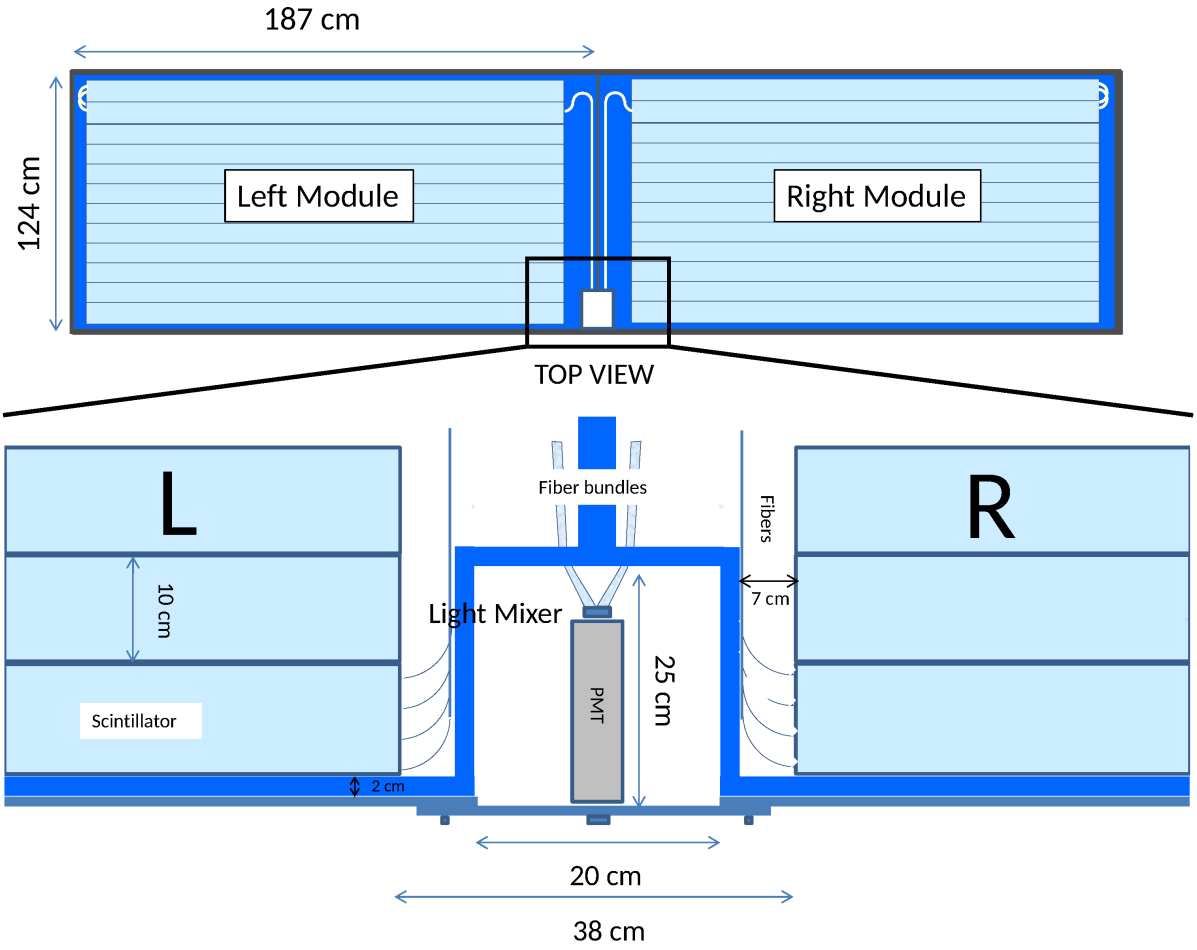

Figure 5.3: SSD setup of the scintillator stripes with a single fibre routing and the photodetector in the middle. Closeup view of the centre SSD part with two fibre bundles attached to the PMT [94].

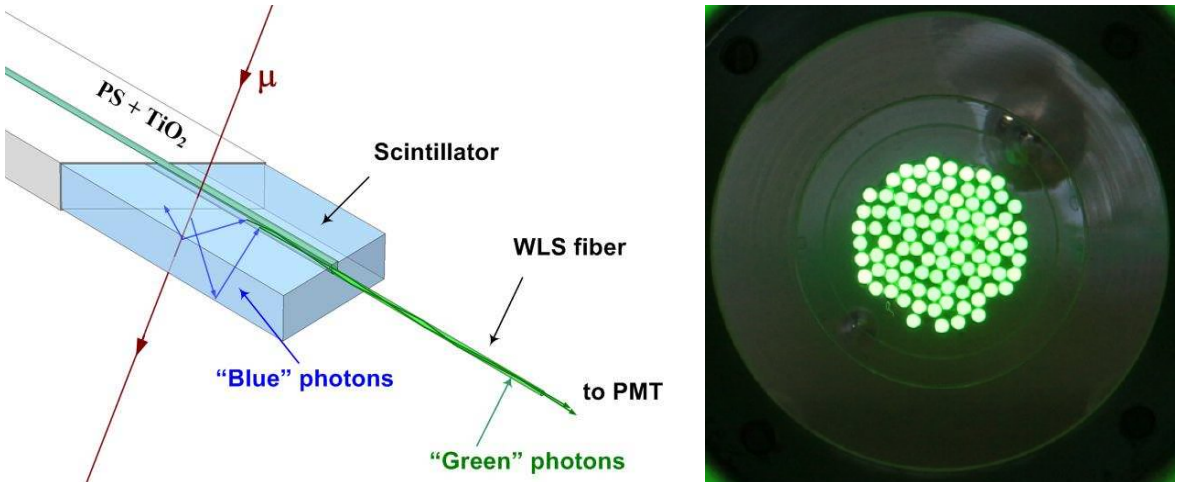

Figure 5.4: Schematics of the SSD detection principle (left) [97]. Glued WLS fibre ends merged as the 'cookie' (right) [98].

5.2 SSD PMT

The scintillation light of the mainly electromagnetic shower component will be transported to a light detector via wavelength-shifting fibres. While the signal for a minimum ionising particle (MIP) needs to be considerably well above the noise level, the main requirement is a high linearity of the SSD signal to be able to measure up to 20 000 MIPs. In the following section, several PMT candidates will be compared and evaluated for their suitability in the SSD detector.

5.2.1 PMT Candidates

The demanding properties to the PMT already limit the possible detector range to only a few matching models. To get the best performance of the detector, three different PMTs were tested for their applicability in the SSD. The considered PMT models are the Hamamatsu R9420 [99], which is the standard bialkali version of the R9420-100 (see Section 4.2), the Hamamatsu R8619 [100], which will also be used in the 'small PMT' upgrade, and the 9902KB by Electron Tubes [101].

While the R8619 is a circular 1 inch PMT with an active area of 22 mm in diameter, the R9420 and the 9902KB are both 1.5 inch PMTs with an active area diameter of 34 mm and 32 mm, respectively. Thus, all PMTs are significantly larger than the cookie size of 13 mm in diameter. All three candidates are head-on type PMTs with a flat entrance window and have a bialkali photocathode and a borosilicate glass tube. The R8619 and the 9902KB have 10 linear focused dynode stages while the R9420 has only 8 stages, which result in a lower gain for the R9420 at the same supply voltage. In respect to the lower nominal supply voltage, the 9902KB also has a typical lower dark current, compared to the Hamamatsu PMTs. The operating temperature range given as −30 °C to 50 °C for the Hamamatsu PMTs and −30 °C to 60 °C for the Electron Tubes PMT fit to the expected conditions found in the Argentinian Pampas (see Section 5.4.2).

Figure 5.5: Tested PMT candidates for the SSD upgrade. Top, the 1 inch Hamamatsu R8619. Two larger 1.5 inch PMTs, the R9420 by Hamamatsu and the 9902KB by Electron Tubes below.

		Ham. R8619	Ham. R9420	E.T. 9902
Tube size		1"	1.5"	1.5"
Min. effective area [mm]		⌀22	⌀34	⌀32
Dynode stages		10	8	10
Gain		2.6×10^6	5.0×10^5	2.0×10^5
Supply voltage [V]	typ.	1000	1300	750
	max.	1800	1500	900
Dark current [nA]	typ.	2	10	0.1
	max.	15	100	3
Operating temp. [°C]		-30 to $+50$	-30 to $+50$	-30 to $+60$

Table 5.1: Datasheet comparison of the two tested Hamamatsu PMTs R8619 [100], R9420 [99], and the Electron Tubes PMT 9902KB [101].

5.2.2 Quantum Efficiency

A key feature of the PMT is its ability to detect photons, specified by the quantum efficiency (QE) in percent. As described in Section 4.2.1, the QE is measured in reference to a calibrated photodiode, scanning the PMTs cathode response for different wavelengths. Figure 5.6 shows the measured QE of the considered PMTs in the spectral range from 200 nm to 800 nm. All PMTs show the typical bialkali response curve with a maximum efficiency around 400 nm. Both Hamamatsu PMTs with the standard bialkali photocathode (R8619, R9420) have nearly the same response with a maximum QE of 29%. Since all of the tested Hamamatsu PMTs use the same borosilicate glass, the efficiency cutoff at lower wavelength (< 290 nm) is a typical feature for these tubes. The Electron Tubes 9902KB differs slightly from the Hamamatsu PMTs response. With its maximum QE of about 26%, its efficiency is smaller compared to the Hamamatsu PMTs. In addition, the response is slightly shifted towards larger wavelength.

For the application in the SSD, the wavelength range of interest is determined by the WLS fibres emission spectrum (Fig. 5.2) and, combined with its absorption spectrum, has its maximum emission between 490 nm and 550 nm. In this area the difference between the three candidate PMT models is negligible and well within the margin of error. With the 9902KBs shifted spectrum all three PMTs are around 15% QE at 550 nm. In addition, the QE measurement of the Hamamatsu R9420-100, which will be implemented in the upgraded FD setup (see Section 4.2), with a more efficient super-bialkali photocathode is shown. While its QE at peak wavelength in the near UV region is about 30% higher, compared to the standard bialkali photocathode of the R9420, the advantage drops from 17.6% to 9.7% in the SSDs range of interest.

5.2.3 Uniformity

The scintillator of the SSD is pervaded with WLS fibres, which are collated to a bundle, and read out by the PMT. Thus, the PMT response needs to be uniform across the fibre bundle size to avoid a location sensitivity bias caused by the detector. The uniformity of the PMT response, and in particular the homogeneity of the cathode, is measured for the PMTs by a scan of the PMTs photosensitive area. As in Section 4.2, the scan was performed with a 405 nm laser diode with a spot size of about 1 mm. The Hamamatsu R9420 and the Electron Tubes 9902KB are both 1.5 inch PMTs, while the Hamamatsu R8619 is a 1 inch PMT, and the measured area is adjusted accordingly.

In Fig. 5.7 the QE uniformity scan of the Hamamatsu R9420 is shown. The response distribution shows an asymmetry towards the upper right corner, which is caused by the arrangement of the first dynode. In addition ring structures can be seen, probably caused by the glass tube

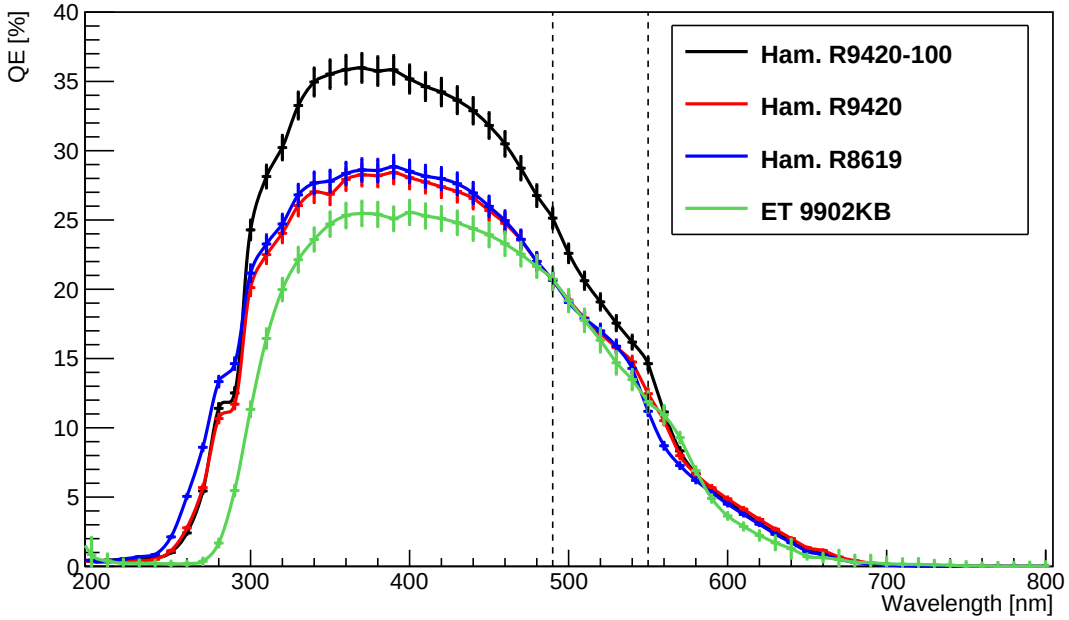

Figure 5.6: Quantum efficiency measurement of Hamamatsu R9420 (blue), R8619 (red), and Electron Tubes 9902KB (green) PMTs. In comparison the quantum efficiency of the R9420-100 (black) with a super-bialkali photocathode (see Section 4.2) and highlighted the region of interest from about 490 nm to 550 nm.

of the PMT. With a plain glass front but a spherical evaporated photocathode on the inside, there is a lens effect at the outer part of the PMT, creating a more sensitive rim at the edges for head-on incoming light. In the central region, which corresponds to the cookies size, the mean QE is about $(24.6 \pm 0.6)\%$. Shifting the cookie off centre would increase the QE for a relative increase of about 5%, while still remaining the same spread.

In Fig. 5.8 the smaller Hamamatsu R8619 can be seen. Measured in the same orientation as the R9420, the response is slightly asymmetrical in the upper right corner due to the dynode structure. Also the lensing effect at the outer rim is visible. The sensitive area of the smaller PMT still fits well to the size of the cookie. The mean QE is at $(23.85 \pm 0.60)\%$, comparable to the R9420 in height and spread. Shifting the cookie would only introduce a large inhomogeneity for only a small gain in total QE.

The spatially resolved QE response of the Electron Tubes 9902KB in Fig. 5.9 has a more prominent drop caused by the collection efficiency of the first dynode. In contrast to the Hamamatsu PMTs, the 9902KB has a plain photocathode on the inside, which results in a disappearing of the lensing effect on the outer rim. An isolating coating around the PMTs head, which is still visible from head-on view, reduces the active area of the PMT. While there is no lensing effect for the complete edge, there is a small gap in the housing, creating an increase in efficiency at the right side, while the grounding contact on the left side blocks an additional part of the photocathode. The efficiency distribution for the central part is due to the collection efficiency drop at 23.9% with a large spread of 2.3% absolute QE. This can be reduced drastically for a shifted cookie, while also increasing the total QE.

5.2.4 Linearity

One of the important properties of the SSD photodetector is its linearity. With the prospect of measuring air shower events at the highest energies with up to 20 000 particles, while still

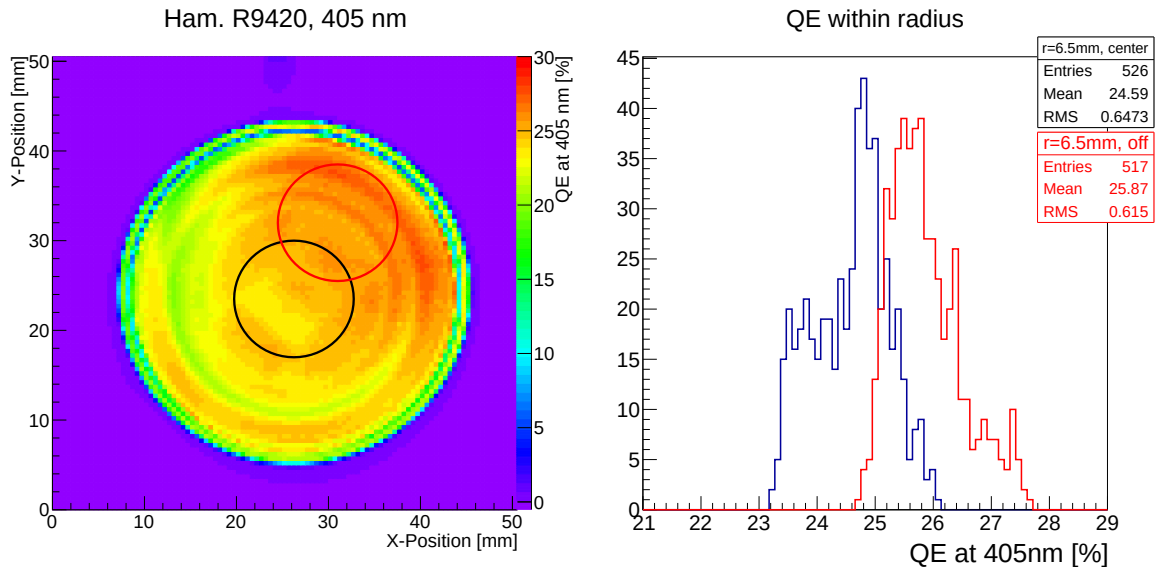

Figure 5.7: Uniformity measurement for the Hamamatsu R9420 at a wavelength of 405 nm with a step size of 0.5 mm. Circles give the size of the optical fibre bundle, placed in the centre (black) and shifted for higher QE (red) and the corresponding QE distribution (right).

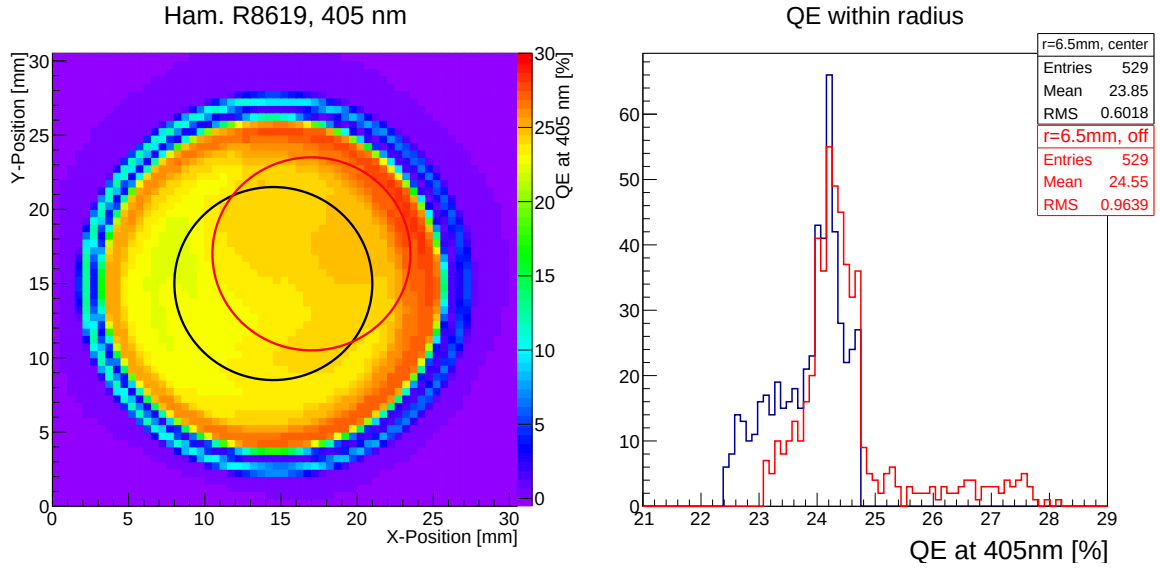

Figure 5.8: Uniformity measurement for the Hamamatsu R8619 at a wavelength of 405 nm with a step size of 0.5 mm. Circles give the size of the optical fibre bundle, placed in the centre (black) and shifted for higher QE (red) and the corresponding QE distribution (right).

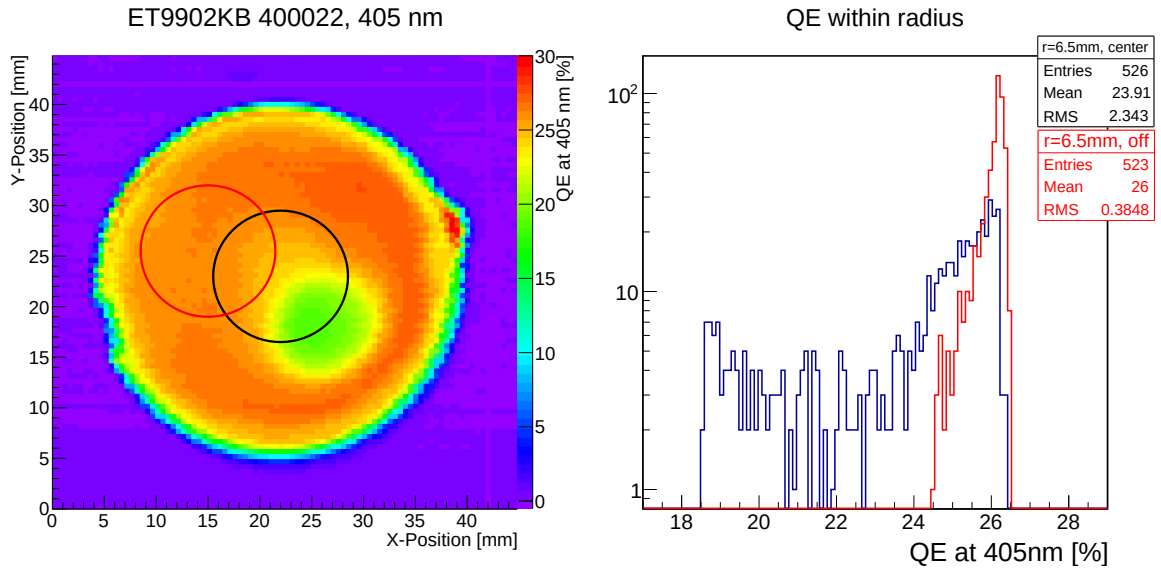

Figure 5.9: Uniformity measurement for the Electron Tubes 9902KB at a wavelength of 405 nm with a step size of 0.5 mm. Circles give the size of the optical fibre bundle, placed in the centre (black) and shifted for higher QE (red) and the corresponding QE distribution (right).

calibrating the detector with single, atmospheric muons, the PMT has to be able to cover this wide measurement range. The single muon signal will be needed to calibrate the entire system consisting of scintillator, WLS fibres, and PMT, including its gain. The interesting although rare high energy particle shower consist of several millions of particles, and especially at the shower core the particle density is very high.

The linearity of a PMT depends on the collection efficiency of the dynodes, the amplification factor of the single stages and the applied high voltage. With the electron multiplication through each dynode, the applied voltage needs to increase for the later dynode stages to keep the expanding electron cloud focused on the next dynode/anode. For the candidate PMTs different voltage dividers were tested to find the optimum voltage distribution for a high linearity.

For the final dividers the linearity was measured in a modified setup of the FD classification test [69]. In pulsed mode, the charge of an LED signal with different attenuation factors of calibrated neutral density filters was measured and the deviation from a linear fit calculated (see Appendix B.2). Figure 5.10 shows the linearity measurement for the R9420 (left) and the 9902KB (right). The R9420, measured at 900 V (gain of 8.4×10^4), deviates from linearity by more than 5% at a maximum peak current of about 114 mA. The 9902KB was measured at 800 V, which corresponds to a gain of 2.7×10^5. It reaches the 5% deviation already at a peak current of about 60 mA. This was independently measured and confirmed by the Lecce group [102]. While still having a higher gain than the R9420, the 9902KB has a worse linearity. The linearity of the R8619, which will also be used as the small PMT in the dynamic range upgrade of the WCD, has been measured by the Naples working group [103, 104]. While a peak current over 100 mA for a deviation from linearity smaller than 5% is achieved at high supply voltages, the peak current declines with decreasing PMT gain. In Fig. 5.11 (right) the distribution of maximum peak current at a gain of 7×10^5 is shown and it ranges from 50 mA (target minimum linearity for the small PMT) only up to 90 mA. Despite all PMTs were tested at a different gain, the maximum peak current of the R8619 and the 9902KB fall well below 100 mA at a gain still above 10^5, while the R9420 shows a peak current above 100 mA at a gain already below 10^5. Since the linearity does not decrease linearly with decreasing supply voltage, the R9420 has still a better linearity at a gain of 5×10^4 than the other contestants.

	HV	Gain	Peak Current
R9420	900 V	8.4×10^4	114 mA
9902KB	800 V	2.7×10^5	60 mA
R8619	$\sim$ 980 V	7×10^5	$<$ 90 mA

Table 5.2: Linearity measurement results of the tested PMTs.

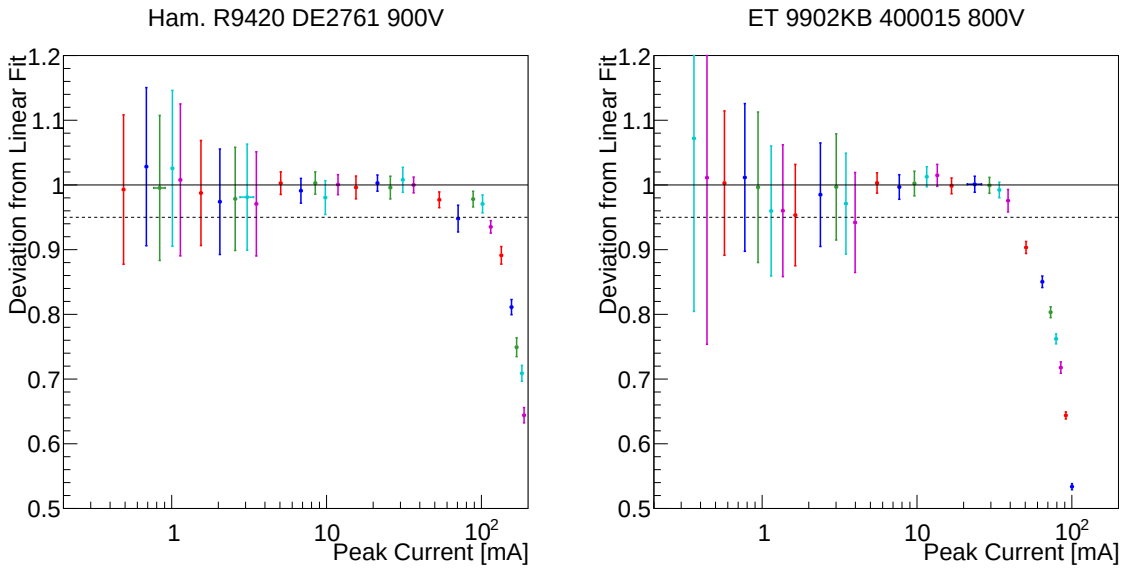

Figure 5.10: Linearity measurement for the Hamamatsu R9420 (left) and the Electron Tubes 9902KB (right). For further details of the measurement see Appendix B.2.

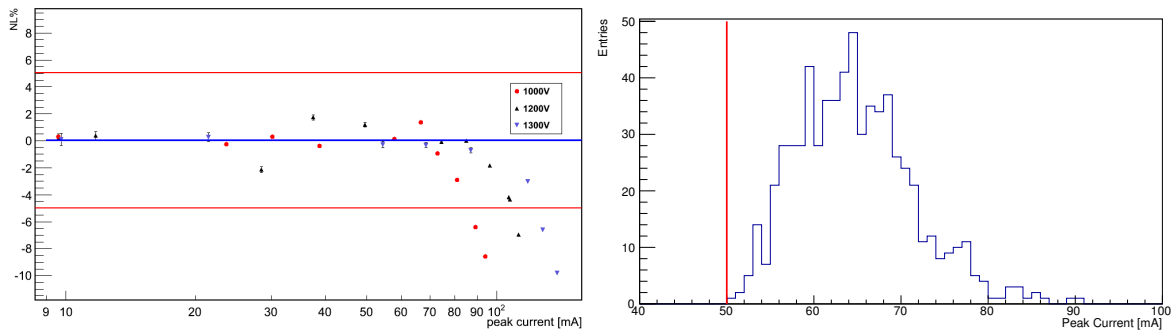

Figure 5.11: Linearity measurement for the Hamamatsu R8619 at a testing facility in Naples. The linearity was measured for different supply voltages (left) [104]. The distribution of peak current with a non-linearity deviation of 5% at a gain of 7×10^5 for the small PMT reaches up to 90 mA (right), with the red line indicating the specification value of the small PMT upgrade of 50 mA [103].

5.2.5 Conclusion

With quite specific demands as to the PMTs properties, three PMTs were tested for their performance in the SSD. All PMTs have a sufficient quantum efficiency in the wavelength range of interest. The uniformity of the tested Hamamatsu PMTs around the centre is more homogeneous than the Electron Tubes 9902KB PMT. With the fixed cookie position at the centre of the PMT, the 9902KB would introduce an inhomogeneity to the detector response. Since the main focus for the SSD is a high linearity, the Hamamatsu R9420 performed best of the three tested devices. As the dynamic range needs to be as large as possible, the eight-stage R9420 offers the best range and will be chosen as the photon detector for the SSDs.

5.3 PMT Application in the SSD

Parts of this section have appeared in:

S. Querchfeld, K.-H. Becker, K.-H. Kampert, and J. Rautenberg,
"Integrated HV-Supply for SSD PMTs", *GAP-Note 2017-014*, 2017

The Hamamatsu R9420 is found to be a suitable and reasonable choice as the photodetector in the SSD. The PMT will be operated with the existing power supply of the SD stations, which are charged by solar panels. This requires an efficient power supply and a high resistance voltage divider to keep the power usage low. With the need of additional read-out channels for the new detectors, the electronic board of the detector station will be upgraded to the newly designed UUB. The dedicated SSD channels are matched to the expected PMT signals.

5.3.1 UUB Integration

In order to achieve the demanding goal of detecting up to 20 000 MIPs with the SSD, the PMT as well as the electronics need to cover a large dynamic range. While the PMTs linearity needs to cover at least 5 orders of magnitude, the electronics need to cover even more for the SSD to perform an accurate calibration at the single MIP level. With the UB being redesigned for the upgraded stations, the read-out channels can be planned accordingly. To get the range of signals that need to be digitised, it is necessary to look at the total signal chain. Starting with the detection of a single MIP, as done for the self calibration of the station, the signal height depends on the light per MIP created inside the scintillator. This reaches the photocathode of the PMT via the wavelength-shifting light guides and creates single photoelectrons (SPEs) at the cathode stage of the PMT. Amplified by the PMTs gain (G_{PMT}), it is then possible to determine the total charge for a single MIP (see Eq. (5.1)). To determine the efficiency of the scintillator, the number of single photoelectrons (SPE) per vertical equivalent muon was measured for several SSDs in a quality test of the SSD fabrication and found to be about $28 \pm 2\,\mathrm{SPE/MIP}$ [105]. In order to keep the PMT at a lower supply voltage to extend its lifetime while still performing sufficiently, the supply voltage will be adjusted to get a gain of 5×10^4. This gives a charge (Q) per MIP of

$$\begin{aligned} Q_{\mathrm{MIP}} &= \#_{\mathrm{SPE}} \cdot e \cdot G_{\mathrm{PMT}} \\ &= 28 \cdot 1.602 \times 10^{-19}\,\mathrm{C} \cdot 5 \times 10^4 \\ &= 0.224\,\mathrm{pC}\,. \end{aligned} \tag{5.1}$$

Range	Intent	Dynamic range																		
bits		1	2	3	4	5	6	7	8	9	10	11	12	13	14	15	16	17	18	19
LowGain	MIP	AnodeX32																		
HighGain	Showers								Anode/4											
Ipeak (mA)		0.0006				0.01			0.1				1.25			10				160
Vpeak (mV)		0.03				0.5			4				62.5			500				8000
Npart (MIP)		0.07				1.2			10				156			1250				20000

Figure 5.12: Pattern of the SSD PMT signal implementation to the UUB readout electronics. The signal will be split up into two channels, with one channel being amplified by a factor of 32 (green) and the other channel attenuated by a factor of 4 (yellow). Taken from [94], exact numbers will differ for the final implementation.

With the UUBs sampling time of 8.33 ns and a 50 Ω termination this results in a signal height of about $\sim$ 1.35 mV and a corresponding peak current ($I_{\mathrm{MIP_{peak}}}$) of 26.92 μA. For a particle shower with up to 20 000 MIPs at the inner core, the charge will increase accordingly to

$$Q_{20\mathrm{k}} = 4.48\,\mathrm{nC}\,.$$

While a single MIP signal has a rather sharp time structure, the expected 20 000 MIPs of a high energy cosmic ray will be distributed over a time (T) of about 100 ns close to the shower core. The maximum peak current for a given signal shape is:

$$I_{20\mathrm{k}} = \frac{Q_{20\mathrm{k}}}{T} \tag{5.2}$$

$$\begin{aligned} I_{20\mathrm{k_{peak}}} &= 44.86\,\mathrm{mA} && \text{for a } 100\,\mathrm{ns}\sqcap \text{ signal} \\ &= 89.71\,\mathrm{mA} && \text{for a } 100\,\mathrm{ns}\wedge \text{ signal} \end{aligned}$$

The UUB is equipped with 12-bit ADCs with a 2 V input range. To match the PMTs large signal range to the readout electronics, the signal will be split into two channels inside the UUB. One will be amplified by a factor of 32 (LowGain) and the other attenuated by a factor of 4 (HighGain). This allows a measurement of the single MIP peak for the detector calibration in the LowGain channel and a detection of a large amount of particles, e.g. close to the shower core. This covers a range of 19 bits, with an overlapping region of 5 bits for cross-calibration between the two ADC channels. An illustration of the PMT signal read-out implementation in the new UUB is shown in Fig. 5.12[1].

5.3.2 Photomultiplier Base

Operating the SSD photomultipliers at an autonomous station in the field gives the challenge to have a stable HV supply connected to a solar panel/battery. Especially with integrating an

[1] Calculations for number of particles are from the pre-production phase with a PMT gain of 4×10^4 and only 12 photoelectrons per MIP and are obsolete for the prototype.

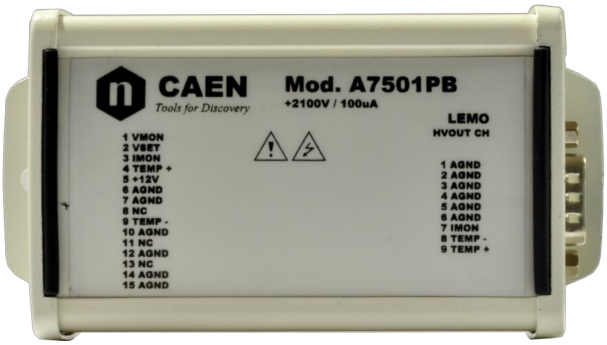

Figure 5.13: A7501PB HV power supply module by CAEN.

additional detector component into the existing infrastructure, a low power consumption for the SSD electronics is essential. In order to find the best suitable HV power supply for the SSD PMT, two different type of modules are tested, a commercially available external HV module developed by CAEN for the needs of the Auger Observatory, powering a passive PMT base, and an integrated active base with build in power generator developed in cooperation with ISEG.

5.3.2.1 CAEN Module

The conventional way of operating a PMT is by using a simple voltage divider chain and applying the full supply voltage in the order of 1 kV from anode to cathode. In order to generate a high voltage by using only the power provided by the WCDs solar panel, a very efficient HV power supply has to be used. The A7501PB by CAEN is a high efficient HV power supply designed for use in the Pierre Auger Surface Detector. It can generate up to +2100 V with a maximum output current of 100 μA. The high voltage output is delivered through a LEMO HV connector. A 4-pin Mini XLR connector is used as feed-through for the PMTs current monitor and external temperature sensor readout. The CAEN module is connected via a DB15 cable to the UUB. The HV set by the UUB has a set-voltage between 0 V and 2.5 V, while the read-out of the HV gives a response between 0 V and 5 V. The module has a metal case with the dimensions of 54 mm × 29 mm × 16 mm and will be placed inside the DOM with the electronics kit of the SD. When using the CAEN module, three cables (signal, HV and monitoring) will connect the PMT to the UUB and HV module. The PMTs passive voltage divider is a small circular PCB directly soldered to the PMT (see Fig. 5.15), where the full HV will be applied from anode to cathode. The divider ratio was optimised for high linearity. To keep the bleeder current[2] low and thus also the power consumption, the voltage divider needs to be high-resistive. The total resistance of the passive base is 28.4 MΩ.

This module will also be used to provide the HV for the small PMT, which is equipped with a passive voltage divider.

5.3.2.2 ISEG Base

The ISEG base PHQ9420 is an active voltage divider with very low power consumption, which is custom-designed for the operation of the 8-stage Hamamatsu R9420 PMT [106]. The HV is generated by a Cockcroft-Walton generator and distributed according to the voltage divider ratio, which was found to offer the best linearity. The base schematics is depicted in Fig. 5.14. Since the Cockcroft-Walton generates 250 V per pass, a classical voltage divider chain is employed for the first dynodes. Stabilisation of the last dynodes and anode is accomplished by capacitive buffering and additional stabilisation circuitries. The total resistance of the ISEG base is about

[2]Current flowing through the voltage divider in parallel to the PMTs dynodes to prevent a load down of the circuit.

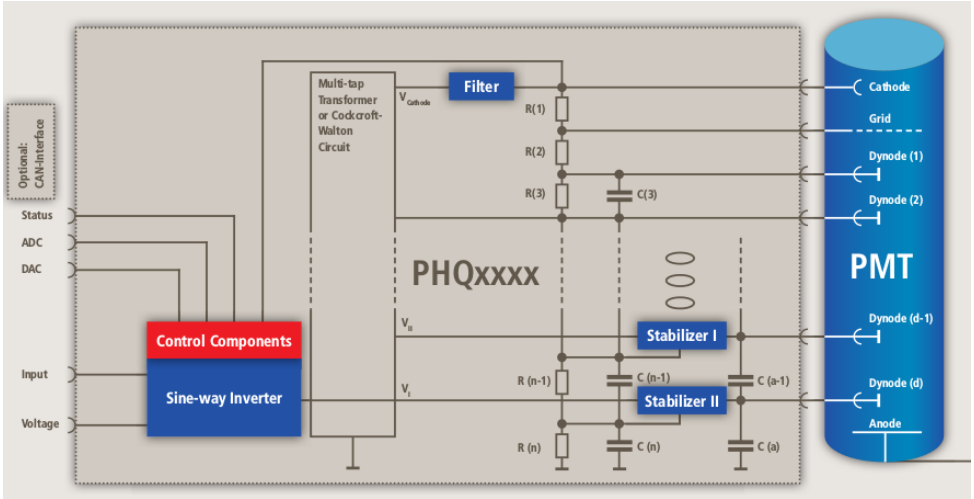

Figure 5.14: ISEG base schematics [106]. The first few stages employ a classical voltage divider and the last stages are actively buffered by capacitors in addition to stabilisation circuitries.

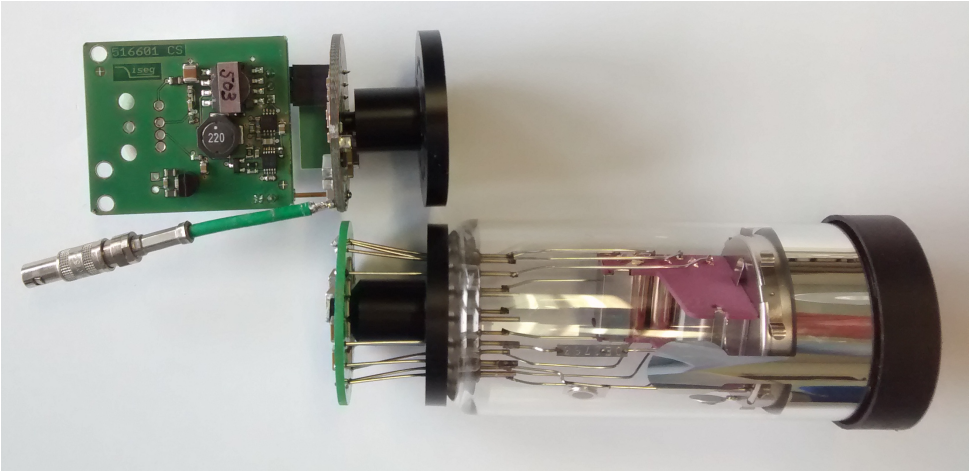

Figure 5.15: Hamamatsu R9420 PMT with attached passive voltage divider and ISEG base next to each other. The Cockcroft-Walton circuit only adds a few centimetre to the PMTs length and is attached with a similar plastic spacer. The cable with Lemo connector was used for signal readout in a test setup.

142 MΩ, resulting in a very small power consumption. Key specifications of the ISEG base are included in Table 5.3 and compared to the CAEN module. Like the CAEN module, the ISEG base is designed to be compatible to the UUB slow-control and thus is connected identically to the CAEN HV module. In contrast to the CAEN module, the monitor voltage is the same as the set-voltage (0 V to 2.5 V). Moreover, the maximum HV to be generated is limited to 1500 V, which is the PMTs maximum allowed HV as specified by Hamamatsu. A temperature sensor is on the PCB to monitor the PMT's environment.

Figure 5.15 shows the geometrical dimensions of the integrated base in comparison to the passive base used with the CAEN module. While the 'voltage divider' dimension stays the same (circular PCB), the HV generator (rectangular PCB) adds a few extra cm to the length of the PMT-unit. This has been accounted for in the PMT enclosure of the SSD. The ISEG base is placed inside the SSD and is soldered to the pins of the PMT like any classical passive base. Since the HV is generated inside the SSD at the PMT itself, only two cables from the UUB to the SSD are needed, with the signal cable being the same as for the CAEN module and PMT monitoring

Specification Item	CAEN	ISEG
Output Voltage HV_{out}	$0 - 2100\,\text{V}$	$0 - 1500\,\text{V}$
Stability ΔHV_{out}	$< 10^{-3}$	$< 10^{-4}$
Temperature Range	$-40°\text{C}$ to $+70°\text{C}$	$-20°\text{C}$ to $+70°\text{C}$
Temperature Coefficent	$< 6\text{ppm}/°\text{C}$	$< 5 \cdot 10^{-5}/°\text{C}$
Ripple and noise	typ. $5\,\text{mV}_{P-P}$; max. $10\,\text{mV}_{P-P}$	$< 20\,\text{mV}_{P-P}$
Voltage Supply	$+12\,\text{V}$	$+12\,\text{V}$
Power Requirement	$< 400\,\text{mW@2100}\,\text{V}$	$200\,\text{mW@1500}\,\text{V}$
V_{SET} Input	$0\,\text{V}$ to $+2.5\,\text{V}$	$0\,\text{V}$ to $+2.5\,\text{V}$
V_{MON} Output	$0\,\text{V}$ to $+5\,\text{V}$	$0\,\text{V}$ to $+2.5\,\text{V}$

Table 5.3: Datasheet comparison of the CAEN HV module [107] and the integrated ISEG PMT base [106].

plus HV setting being combined. With the ISEG base being custom made for the SSD purpose, some modifications have been done to improve the performance (see Appendix B.3). To test the two HV supply options in the SSD prototype, the UUB integration was set to match both systems. Hence the monitor HV resolution of the ISEG base is double that of the CAEN HV, with the CAEN module introducing a difference between set- and read-voltage.

5.3.2.3 PMT-Gain as a Function of HV

To test the range of high voltages over which the PMT can be operated stably, the anode signal response is measured for different HV settings. In this Gain-vs-HV (GHV) test we successively increased the HV applied to the PMT and measured the anode signal obtained from a pulsed LED that was operated at a pulse width of 200 ns and a light intensity corresponding to about 500 MIPs. Figure 5.16 shows the measurement for a passive (left) and an ISEG base (right). The passive base was powered by a standard external HV-supply operated in a NIM crate and the HV has been increased in steps of 50 V, starting from 600 V up to the maximum allowed value of 1500 V. For the ISEG base the set voltage V_{SET} was increased by 0.1 V per step, which corresponds to an increase of 60 V. The shown range starts at 600 V and also matches the maximum HV of 1500 V. Both bases show a linear behaviour with similar slope, which only depends on the voltage divider ratio. Despite the low bleeder current, the signal is stable up to the maximum rated HV. Thus the SSD PMT gain can be adjusted by lowering the applied HV within the shown range. Although it needs to be kept in mind that this also effects the PMTs maximum pulse linearity.

5.3.2.4 Linearity and Dynamic Range

While both HV supplies are able to handle the complete HV range for the R9420, the linearity of the PMT in general depends also on the used base. Especially the low bleeder current can cause a limit in detectable charge for a given gain. Since the linearity is also affected by the manufacturing process of the individual PMT which determines the exact focusing of every dynode stage, the same PMT is used to test the two different types of HV supply. Using the linearity test setup, described in Section 5.2.4, the resulting measurements are shown in Fig. 5.17. The CAEN module is shown on the left side and the ISEG base on the right side. With the expected large signals in the SSD being about a few 100 ns, the linearity is also tested for pulses with a pulse length of 50 ns (upper plots) and 200 ns (lower plots). While the exact determination of the linearity break to a single mA remains difficult with the given setup, a qualitative comparison can be drawn. For the two different sets the differences remain small,

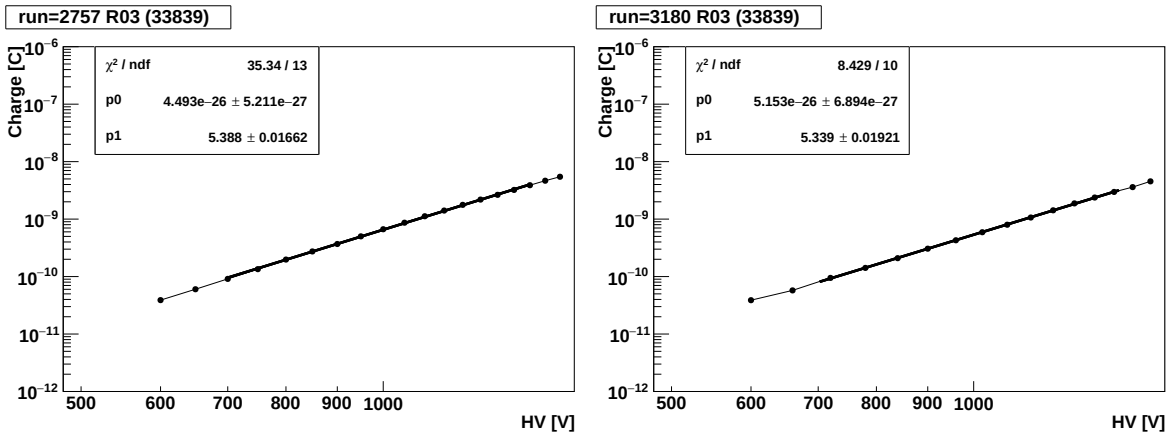

Figure 5.16: Gain-vs-HV for the passive base with external HV module (left) and an ISEG base (right) with the same divider ratio. Both bases show a linear behaviour and are well within the operating conditions of the PMT. The operating voltage in the field will be around 900 V.

with a deviation from linearity $> 5\%$ for the 50 ns pulses at a peak current slightly below 120 mA. For longer pulses the linearity decreases down to about 100 mA for both bases. With the pulse being orders of magnitude higher than the bleeder current to feed the dynodes, the difference in the total resistance of the bases is negligible and the pulse is fed by the buffer capacitors at the latest stages.

When discussing the overall dynamic range and the expected signal heights, it should be noted that the measurements reported here were done at a fixed pulse width of 200 ns, which is about the typical pulse width that is expected for a station close to the shower core. However, a single muon, to be used for absolute light calibration, distributes its light only over about $15 - 20$ ns. Thus, a maximum shower signal of $2 \cdot 10^4$ MIPs spread over 200 ns that is amplified by the PMT to a pulse height of 8 V (ADC limit), yields $8\,\mathrm{V}/2 \cdot 10^4 \times (200\,\mathrm{ns}/20\,\mathrm{ns}) = 4\,\mathrm{mV}$ signals for a single muon. This number is already well separated from the present noise level of 0.08 mV (see next subsection) and will be more separated by the reduced noise expected from the next generation of UUBs.

Moreover, at a gain set to $1 \cdot 10^5$ ($\mathrm{HV_{PMT}} \simeq 900\,\mathrm{V}$) and assuming 30 pe/MIP, a total of $2 \cdot 10^4$ MIPs yield a signal charge of $1 \cdot 10^5 \times 2 \cdot 10^4 \times 30\,\mathrm{pe} \simeq 10^{-8}\,\mathrm{C}$, which remains in the linear range observed in Fig. 5.17. The anode current drawn in this situation amounts to $10^{-8}\,\mathrm{C}/200\,\mathrm{ns} = 50\,\mathrm{mA}$, consistent with the quoted maximum linear current of 100 mA for the standard R9420 PMT[3].

5.3.2.5 Noise

To be able to use the complete dynamic range of the UUB, a low noise level of all detector components is important. With the SSD specification to resolve the detection of a single MIP at 1.35 mV or even lower, a low-noise baseline of the PMT signal is required.

In order to test if the PMT or the use of an active base introduces additional noise to the signal recording, both bases are tested and compared to the intrinsic UUB noise. The noise level was determined by analysing the baseline of ADC traces recorded at one of the PMT inputs of the UUB[4]. A PMT in a light-tight enclosure was connected to the signal input and the 'HIGH GAIN' (HG) channel with an amplification of ~ 32 was analysed. To get random noise traces without the threshold trigger, the ADC-readout is forced by a random software trigger.

[3] Hamamatsu is also offering selected PMTs with a maximum linearity up to 200 mA.
[4] A UUB V1 was used in this measurement.

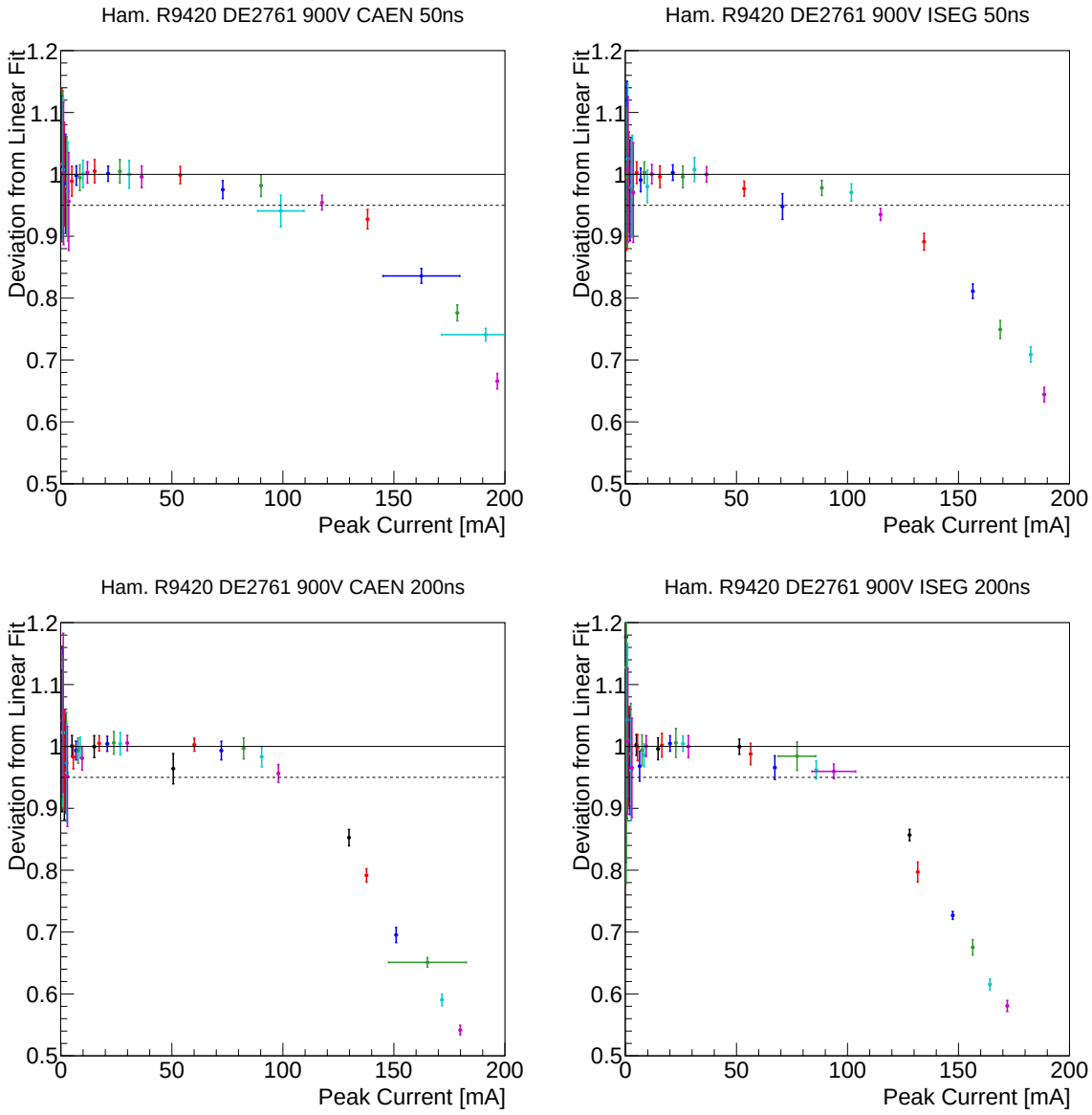

Figure 5.17: Linearity measurement of a passive base (left) and an ISEG base (right) for short (50 ns, top) and long (200 ns, bottom) pulses. To extend the electronics range, additional signal attenuators/amplifiers were used.

A total set of 1000 traces per measurement was taken and the width of the ADC distribution is calculated as an estimate of the noise level.

For the passive base, the CAEN module is connected to the UUB by a short ribbon cable while the HV and slow-control are connected by the same ~ 4 m long cables as are used in the detector in Argentina. The ISEG base is powered and controlled via a shielded ~ 2 m long light plastic-sheathed cable. In both cases, the PMT is connected via a short LEMO-to-SMA cable to the UUB front-end. To isolate the measurement from the noise level in the lab, the PMT was put into a metal tube, similar to its assembly in the SSD detector. The UUB plus CAEN module were operated inside of another metal box with only the UUB power supply and Ethernet cables going inside.

Figure 5.18 shows a noise measurement for the UUB with no PMT attached to the signal input. The upper left plot shows a random sample trace of 1000 measurements. The baseline has an offset of about 461 ADC counts. Besides several short time spikes of up to ± 30 ADC counts, a underlying modulation can be seen which broadens the noise distribution. The origin of

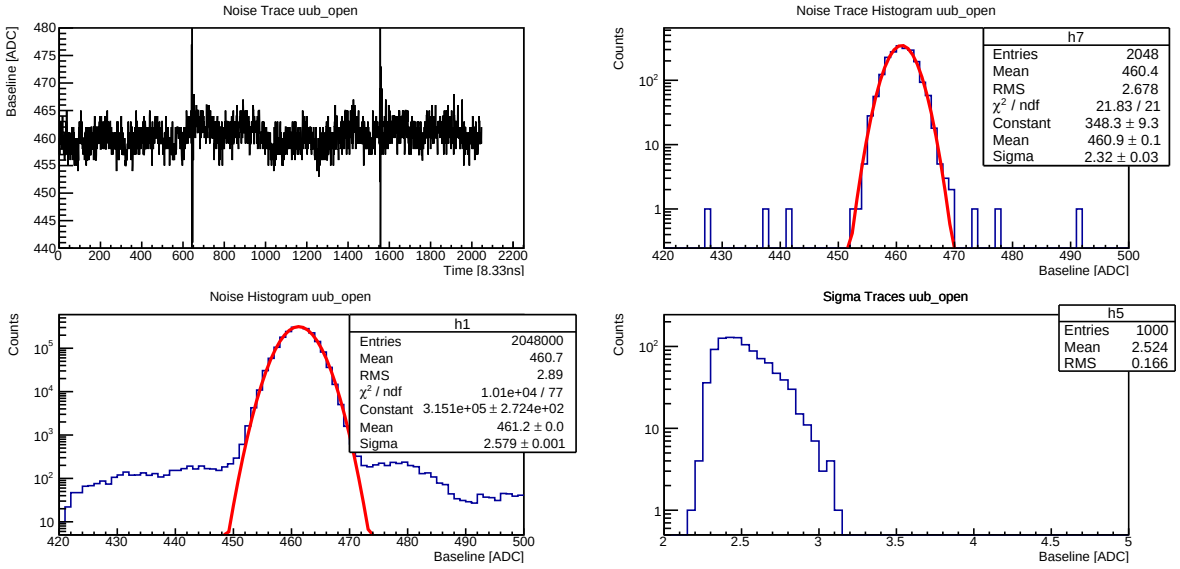

Figure 5.18: UUB noise measurement with no PMT connected. The upper left plot shows a single sample trace. A Gaussian distribution is fitted to the profile (upper right) to provide an estimate of the noise level. Bottom right shows the single trace sigma distribution for 1000 traces. Bottom left shows the combined profile of all these traces.

UUB baseline	2.52 ± 0.17		
	0V	900V	1500V
CAEN	2.45 ± 0.21	2.44 ± 0.21	2.45 ± 0.21
ISEG Rev.2	2.45 ± 0.21	2.50 ± 0.22	2.57 ± 0.22

Table 5.4: UUB noise measurement (all numbers are in units of ADC channels).

the spikes is unknown and appears to be an artefact observed in most, but not all of the UUB ADC channels (WCD and SSD). The modulation might be introduced by the power supply input, situated right next to the front end electronics, and is currently under revision for a UUB redesign. In the upper right plot, the profile of the trace shown in the left plot is shown. To determine the noise level and to reduce the influence of these short term spikes, the spread of a Gaussian distribution is calculated. The lower left plot shows the cumulated profile of all 1000 traces. The sigma distribution of the single traces is plotted in the lower right, resulting in an intrinsic noise of the UUB without a detector attached to the signal port of 2.52 ± 0.17 ADC counts. According to UUB specifications, this corresponds to a noise level of almost 0.08 mV which is sufficient to measure the expected MIP pulse of 1.35 mV.

The noise measurement of the PMT powered at 900 V by the CAEN HV-module is shown in Fig. 5.19. With respect to the open UUB measurement no additional noise can be seen for the passive base. The mean sigma is at 2.44 ± 0.21 ADC counts. As can be seen from Table 5.4 the noise level is also stable as a function of HV.

The measurement of the ISEG base at 900 V, shown in Fig. 5.20, results in a sigma of 2.50 ± 0.22 ADC counts and is comparable to the passive base. As listed in Table 5.4, increasing the voltage to the maximum of 1500 V shows a small increase in the noise level for the ISEG base, but is within the margin of error and close to the noise level without the PMT connected.

A separate laboratory test was performed and the PMT signal recorded with an oscilloscope. The measurement yielded no significant differences between the passive and integrated base. Noise levels in both cases were found to be below 0.05 mV and are at the level of the resolution of the scope (see Appendix B.7).

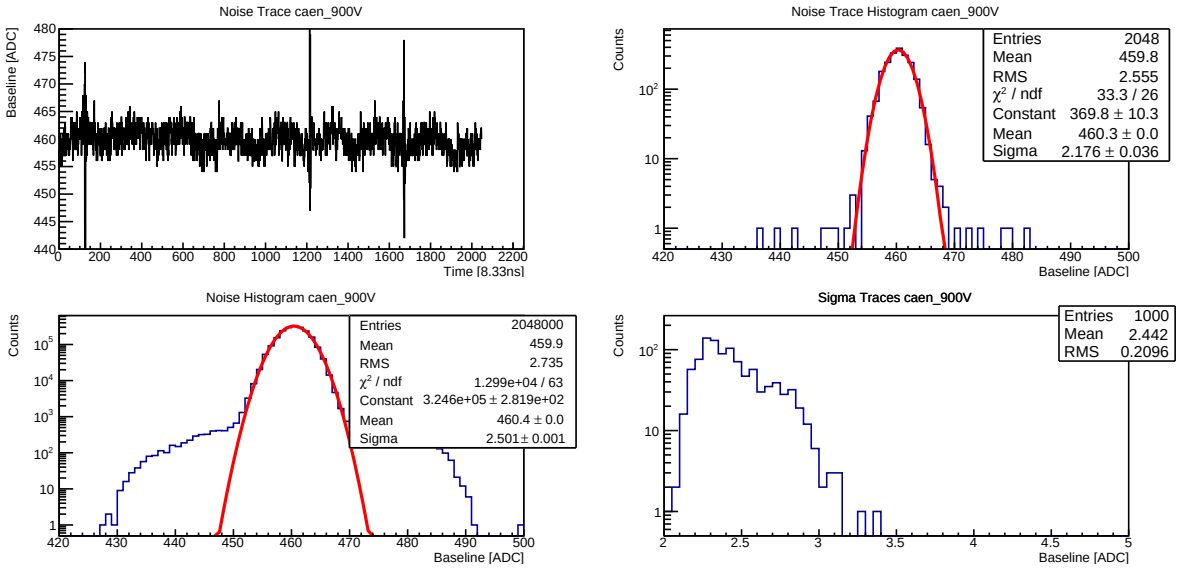

Figure 5.19: UUB noise measurement of the PMT with passive voltage divider and CAEN module. Upper left shows one sample trace. A Gaussian distribution is fitted to the profile (upper right) to determine an estimate of the traces noise level. Bottom right shows the single trace sigma distribution for 1000 traces. Bottom left shows the combined profile of all these traces.

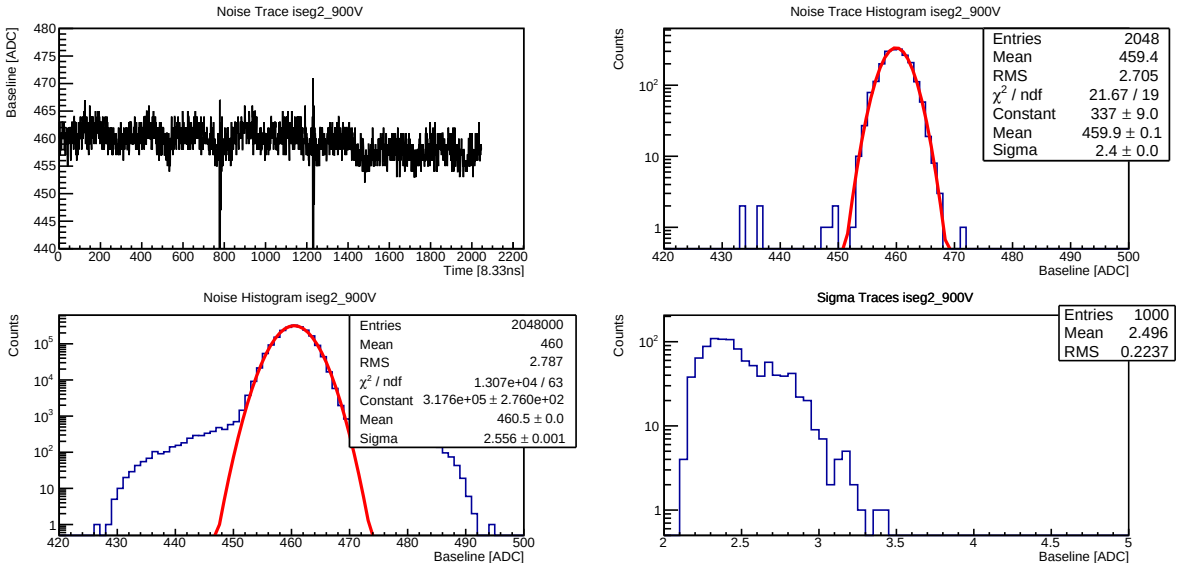

Figure 5.20: UUB noise measurement of the PMT with the ISEG base. Upper left shows one sample trace. A Gaussian distribution is fitted to the profile (upper right) to determine an estimate of the traces noise level. Bottom right shows the single trace sigma distribution for 1000 traces. Bottom left shows the combined profile of all these traces.

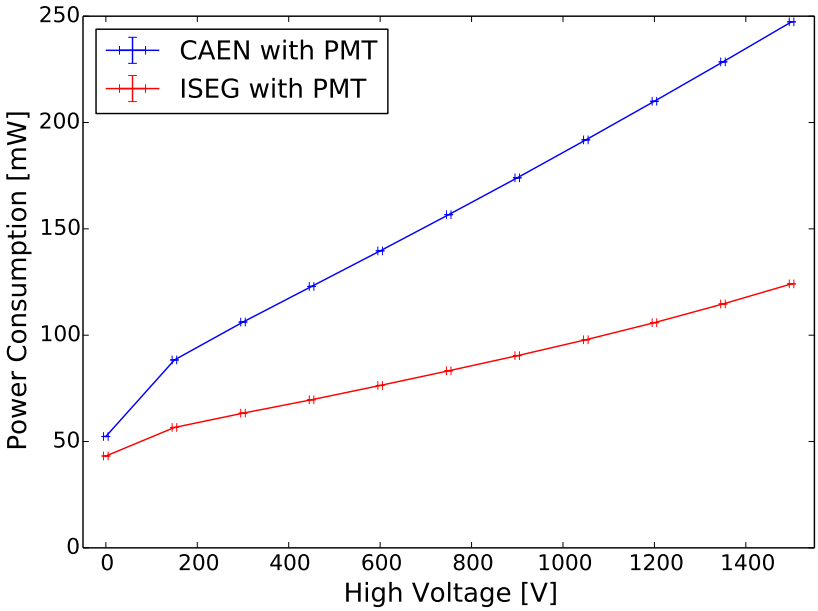

Figure 5.21: Measured power consumption of the ISEG and CAEN HV-modules as a function of HV when powered by the UUB. In both cases, a PMT is operated in a dark box. Additional power losses in the UUB are not accounted for.

5.3.2.6 Power Consumption

The total power consumption of the HV modules is of particular relevance for the solar powered AugerPrime detector stations. The CAEN HV-module itself has been optimised for low power consumption but still has to drive the bleeder current of the passive voltage divider chain. Integrated bases provide the operation potentials directly to the dynodes, so that a bleeder current is avoided and better power saving operation is achieved.

For operation in the field, both the CAEN HV-module and the integrated base obtain their power from the extension ports of the UUB. The associated drivers used on the tested version of the UUB consume about 1 W just for providing the power to the port, which is significantly more than the connected consumers themselves, as CAEN and ISEG specify a maximum consumption of 400 mW and 200 mW respectively (see Table 5.3).

To measure the power consumption of the SSD PMT system under realistic conditions, the two different types of bases were tested with the supply voltages taken from the UUB. Like in the SSD, the bases were connected to a PMT which was placed into in a dark environment to draw a negligible current. The power consumption was determined by measuring the current at the 12 V output-port of the UUB using a DVM, connected between PIN-5 (+12 V DC) of the PMT4 connector and the supply voltage entrance of the ISEG base and CAEN module, respectively. The HV was set by the slow-control of the UUB in steps of 150 V, taking into account the different ADC step size due to the different maximum HV of the modules. The measured current is multiplied by the 12 V of the supply voltage to calculate the power consumption of the consumers. This is shown in Fig. 5.21 for the two different setups as a function of HV. The error of the current measurement is estimated to be less than 0.005 mA.

While both bases have a similar power consumption at an output of 0 V, the increase of the CAEN module with HV is noticeably larger. At a HV of 900 V, which is close to value to be used in the field, the power consumption of the ISEG base is found to be about half of the value of the CAEN module (90.4 mW vs. 174 mW). The effective power consumption drawn from the solar system will be larger due to the inefficiency of the circuitry that provides the power to the port. The actual measurement turned out to be afflicted by large systematic uncertainties so

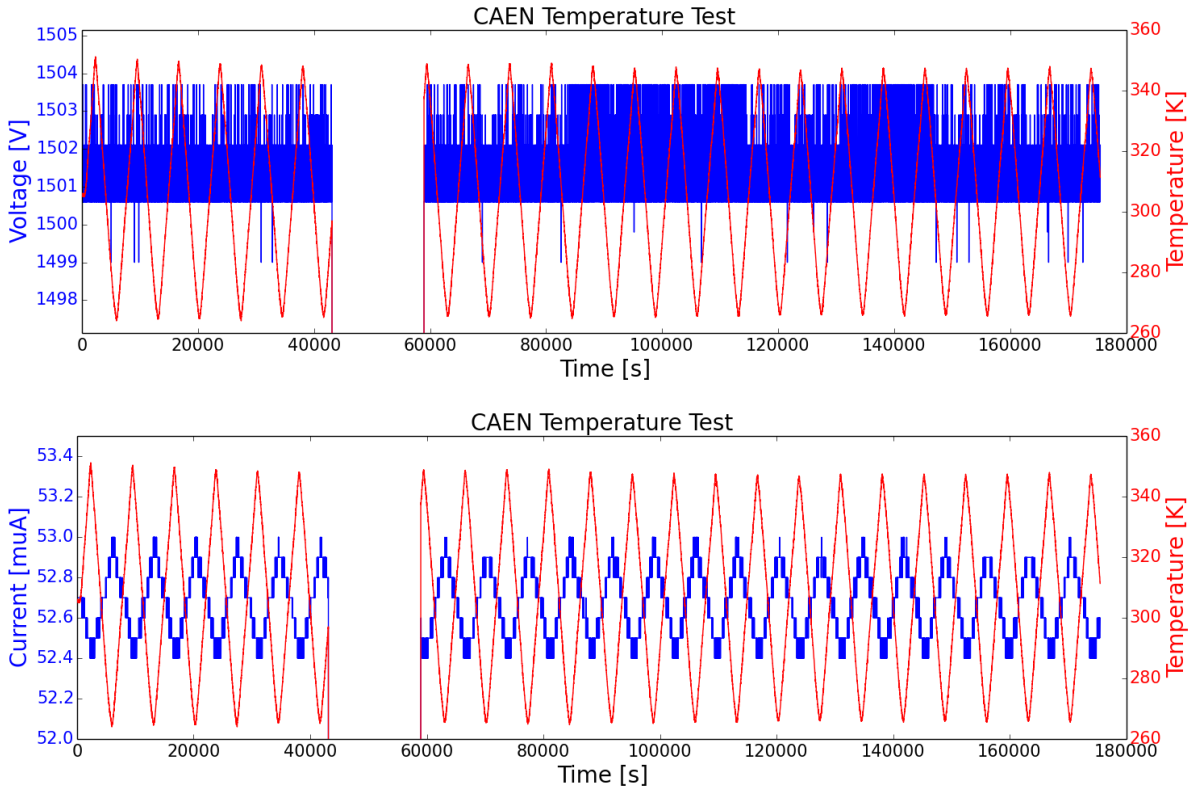

Figure 5.22: Temperature stability of a CAEN-HV module when powering a passive voltage divider at 1500 V. The upper panel shows V_{MON} and the lower one I_{MON}.

that the losses on the UUB can only be estimated to about $30\,\% - 60\,\%$ of the power provided to the external consumer. The daily power saving caused by the ISEG base thus will be at least 2.4 Wh up to about 3.5 Wh. This appears a marginal saving at present but becomes more relevant when optimisation is done to the UUB design for more power saving operations.

5.3.2.7 Temperature Dependence

With the SSD being operated in the harsh environment of the Pampas, the PMT and its base have to withstand large daily temperature cycles. To simulate these conditions in the lab, the single components were tested in a climate chamber. The temperature drift was programmed to cycle between $+70°\mathrm{C}$ and $-20°\mathrm{C}$, with a rise-/fall-time of 1 hour. As a first test, the bases were tested without a PMT, to verify whether the electronics is affected. During these tests, the bases were programmed and controlled via a UUB outside of the climate chamber. All parts were connected with the same cables as used in the engineering array. The temperature of the base was measured with the on-board sensor. For the CAEN module the monitor voltage V_{MON} and current I_{MON} were logged. As the prototype ISEG base available at the time of the measurement was missing a current monitor, only V_{MON} was logged. Both bases were operated at 1500 V which is the maximum HV rating for the R9420. Figure 5.22 (top) depicts the stability of the HV during the temperature cycling for the CAEN HV-supply. As can be seen the HV remains stable within ± 1 V for most of the time and does not exceed a drift of 3 V. Figure 5.22 (bottom) shows that the HV stability is achieved by changing the current contracyclical to the external temperature.

Figure 5.23 shows the measured V_{MON} along the tracked temperature for the ISEG base. Again, the HV remains stable within ± 2 V which is the single bin precision of the monitor (max. V_{MON} ISEG=2.5 V, see Table 5.3). Like for the CAEN module, a very few measurements show

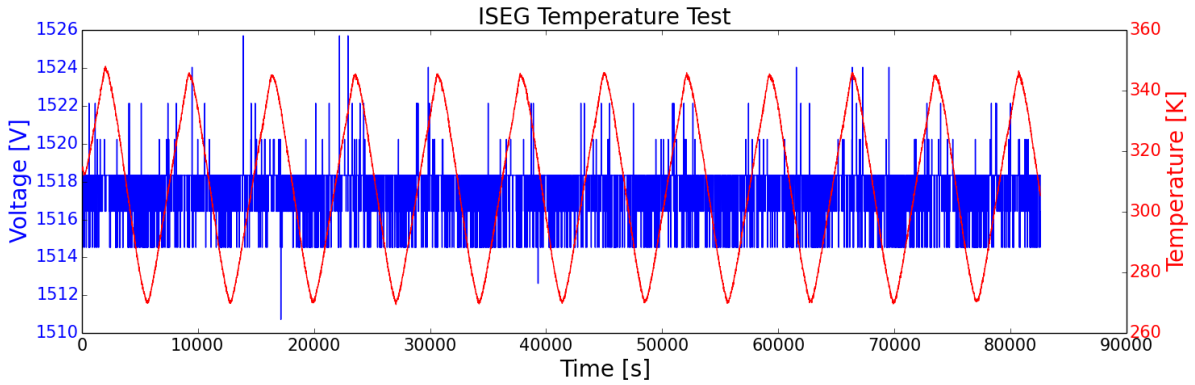

Figure 5.23: Temperature stability of the HV generated by an ISEG base. The temperature has been cycled between −20°C and +70°C.

departures of about twice that value.

5.3.3 PMT Temperature Sensitivity

The temperature fluctuations in the Argentinian Pampas can be quite large. Thus, the used sensors need to be robust in order to work for a long period of time. While the electronics can hold up to these fluctuations quite easily, the PMT is subject to higher variations in its response. This affects the noise level due to thermionic emission, as well as the signal response with the cathode sensitivity and the multiplication factor of the dynode stages being sensitive to the operation temperature, resulting in a change in gain. The cathode sensitivity change with temperature is wavelength dependent. For bialkali cathodes the change is about $-0.4\%/\,°\mathrm{C}$ at a wavelength of 500 nm [108].

To test the temperature effect on the signal response, two PMTs, with an ISEG base and a passive divider with CAEN module respectively, were operated inside a climate chamber (see Fig. 5.24). The signal of a LED with a pulse length of 200 ns and a wavelength of 480 nm was transmitted via optical fibre into the climate chamber. The temperature was cycled between −10 °C and 50 °C, which is the expected temperature range for the field operation (see Section 5.4.2), and the cycle time was set to 180 min. Each minute, 1000 LED shots were triggered and the average amplitude determined for the PMTs. The PMTs signal read-out was done with an UUB, which was kept at room temperature outside the climate chamber. Temperature and HV were monitored, like in the base-only test, with the UUB as well. Figure 5.25 shows a fraction of the measurement, with the monitored temperature of the ISEG base sensor and the amplitudes of the two different PMTs. The test ran for a total of 32 cycles. It can be seen, that the signal is anti-correlated with the temperature[5]. Figure 5.26 shows the correlation of the PMTs' signal to the temperature modulation. Both PMTs show a strong anti-correlation with a correlation factor of ~ 0.95. The slope for the PMT with ISEG base is at −1.83 ADC counts. In reference to the signal at a temperature[6] of 25 °C, the signal change with temperature is at $-0.416 \pm 0.008\%/\,\mathrm{K}$. This fits well with the expected $-0.4\%/\,\mathrm{K}$ for a PMT with bialkali photocathode and is in agreement with an independent measurement of the R9420 [109].

As seen already in the base-only test, the HV fluctuation for both types of bases is moderate and the correlation to the temperature cycle is small (see Fig. 5.27). Again, the effect is slightly more prominent in the ISEG base, but the overall deviation from the set HV is small. With the ISEG HV step size being double the passive base step size, the RMS is larger for the ISEG base.

[5]Due to the crowded space of the climate chamber and the limited bending power of the optical fibre, the simultaneous measurement of the two PMTs is not perfectly aligned, with the CAENs amplitude being about

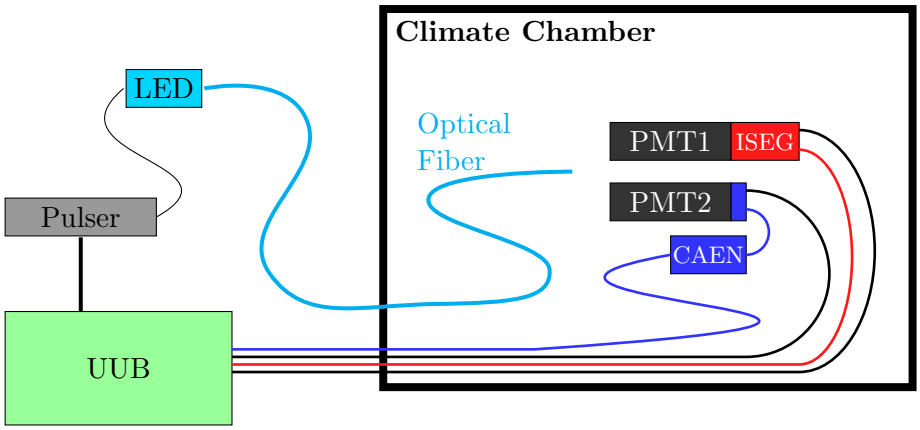

Figure 5.24: Schematic experimental setup of the temperature measurement. Two Hamamatsu R9420 PMTs with ISEG base and passive voltage divider plus CAEN module inside a climate chamber. Optical signal from a LED transmitted through an optical fibre, triggering and signal readout performed with an UUB.

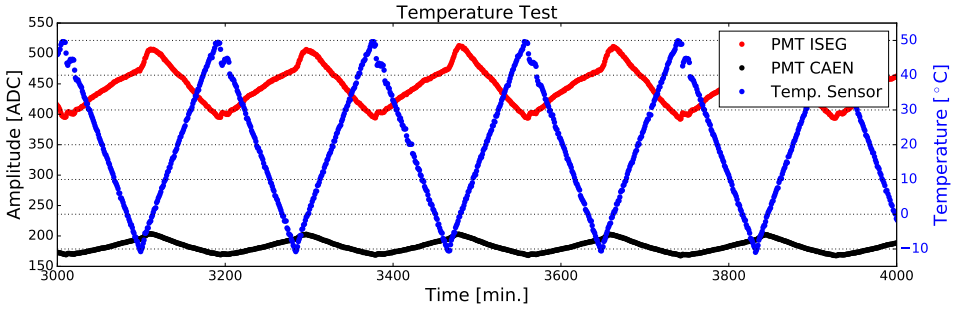

Figure 5.25: Temperature stability test of two R9420 PMTs with an ISEG base and a passive voltage divider with CAEN power supply respectively. Temperature cycles between −10 °C and 50 °C within 180 min.

5.3.4 Photomultiplier Quality Test

With the R9420, a base line photodetector was found. But since their usage in the SSD demands high requirements for some of the PMTs characteristics, which are defined in the manufacturing process, these need to be tested as to whether they hold up to the high standards. To confirm the manufacturers given properties of the individual PMTs, lab tests were performed on a first ordered batch of PMTs. The individual PMT's accompanying data sheet is the result of a standardised test by the manufacturer. Here the PMTs are illuminated by a tungsten lamp at a temperature of 2856 K [110]. The derived PMT properties include the cathode and anode luminous sensitivity, the PMT's dark current, and the cathode blue sensitivity index. The blue sensitivity index is obtained by measuring the same tungsten spectrum with an additional blue filter (Corning CS No. 5-58) with a peak transmittance at around 420 nm in front.

In the laboratory, the PMTs were tested for their QE and gain. A total of 25 PMTs were tested, with 9 PMTs being used imminently in the SSD prototype array and 14 spare PMTs, for further enlarging the testing site. Using the same setup as in Section 4.2, the measurement results can be seen in Fig. 5.28 (left). The QE curves for all PMTs are well aligned and feature the same shape, with a few exceptions at the filter changing positions at 340 nm and 540 nm of the QE test bench.

half of the ISEGs amplitude.
[6]Standard temperature from the Hamamatsu data sheet.

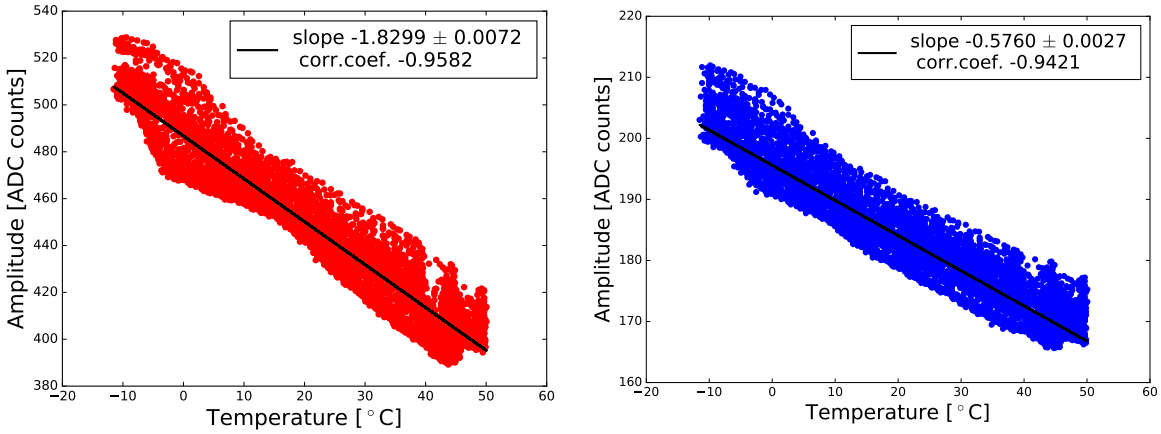

Figure 5.26: Correlation of the signal amplitude of the ISEG PMT (left) and CAEN PMT (right) with temperature.

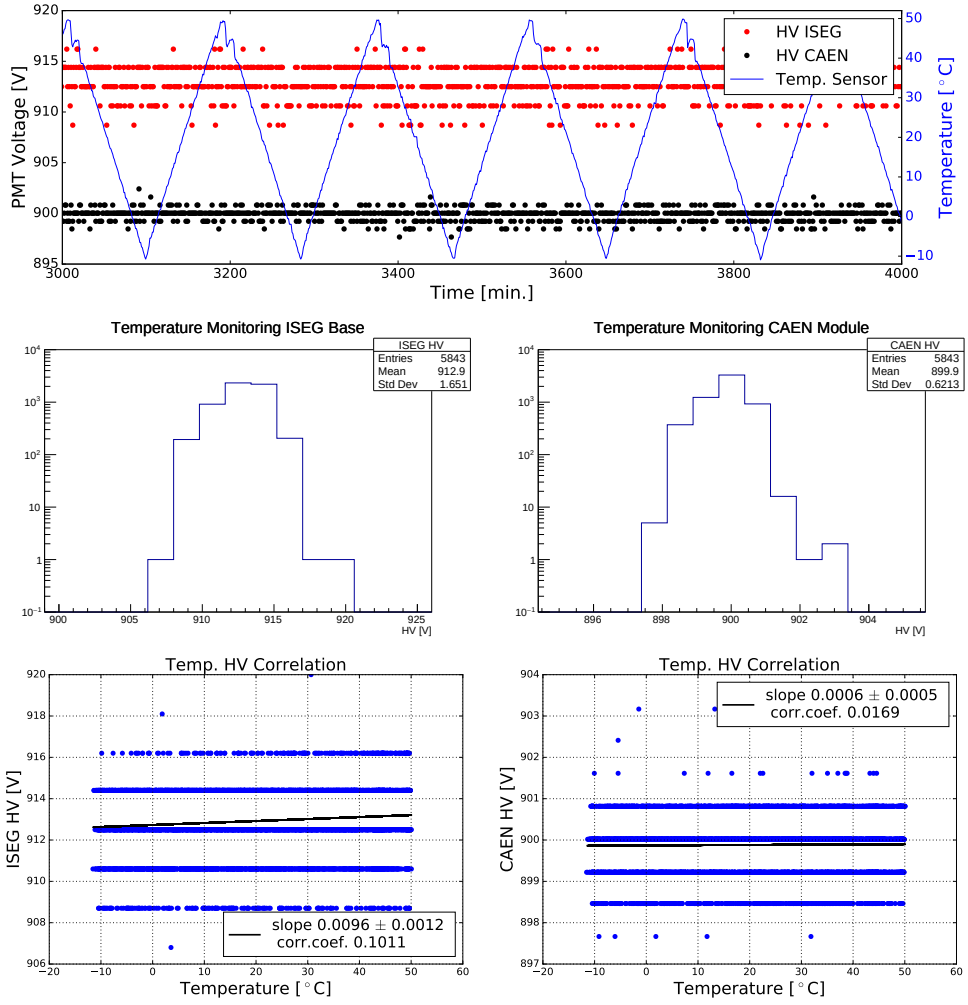

Figure 5.27: Monitoring of the high voltage supplies during the temperature test. Distribution and correlation to the temperature cycle of the HV monitoring with the UUB Rev.1. Due to the different specifications (Table 5.3), the step size for the ISEG base (left) is about double as for the CAEN module (right) (1.9 V versus ~ 0.8 V).

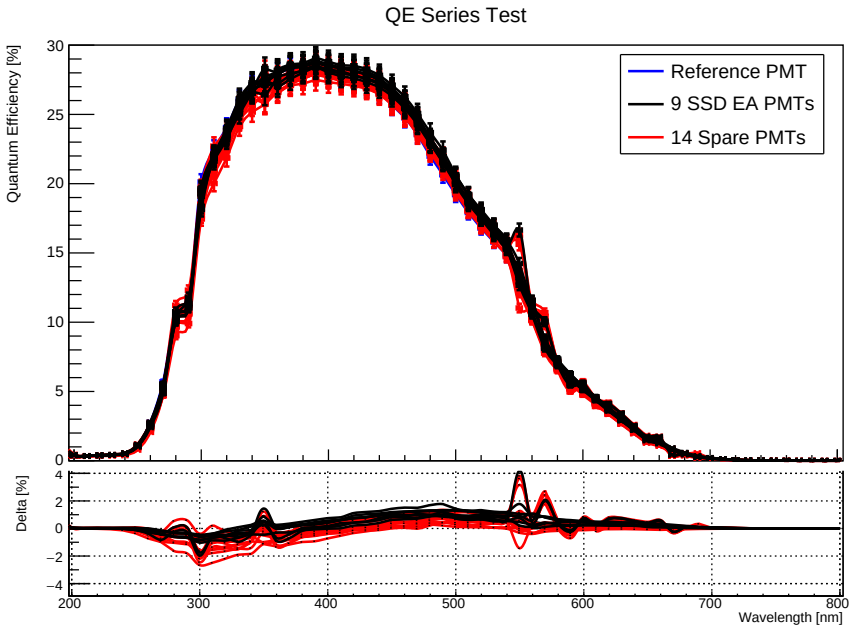

Figure 5.28: QE test of the prototype array PMTs. Deviation to a reference PMT shown at the bottom.

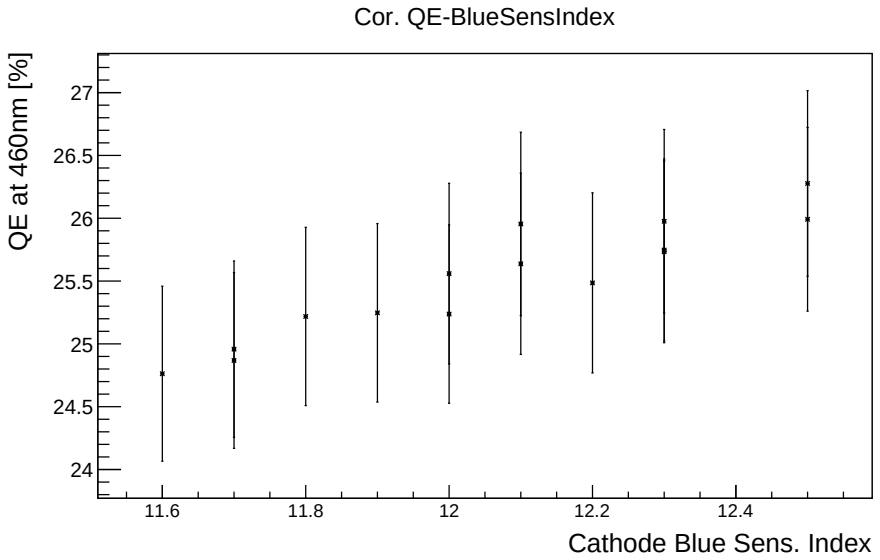

Figure 5.29: Correlation of the QE at 460 nm to the factory data for the blue cathode sensitivity index.

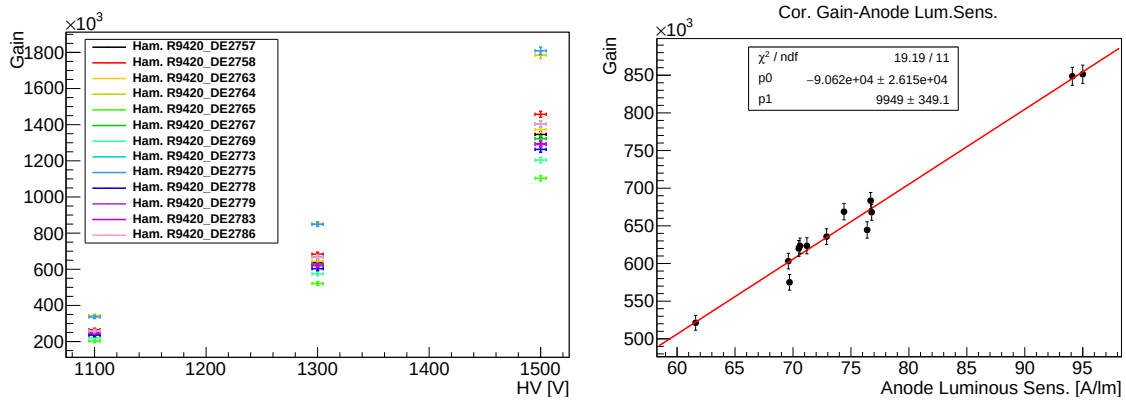

Figure 5.30: Absolute gain measurement at three different HV settings for the first batch of R9420 PMTs (left). Correlation of the measured gain at 1300 V to the factory data for anode luminous sensitivity (right).

While the measurement of the QE is quite extensive and time-consuming, it will be done for only a few randomly selected PMTs of the bulk order for the whole array. With the correlation between the cathode blue sensitivity and the QE at 460 nm (Fig. 5.29), the blue sensitivity can be used as an index for a sufficient QE.

The absolute gain of the PMTs was determined measuring the charge of single photons (details see Appendix B.1). For different HV settings the gain of a first batch of PMTs from the prototype is shown in Fig. 5.30 (left). As becoming more prominent for the highest HV, there are two outlier with a higher gain compared to the bulk of the measured PMTs. As the gain is already stressing the dynamic range of the SSD to its limits, operating the PMT at a too low HV to meet the electronic input can cause unwanted effects. As a comparison to the factory data shows, the gain is correlated with the given anode luminous sensitivity (Fig. 5.30, right). Thus, a preselection can be done to avoid using PMTs with a gain too high for operation in the field.

In order to operate all PMTs of the SSDs prototype at the same gain, the HV for a gain of 5×10^4 was determined using the absolute gain measurement and a separate gain versus HV measurement. Here, the gain dependence on the supply voltage is determined for the operating range from 600 V to 1500 V and the HV for the corresponding gain calculated. An overview of the PMTs test results can be found in Appendix B.5. While the supply voltage for the WCD PMTs is set to match a certain rate in incoming VEMs, it is not clear yet if this automated process will be applied to the SSD and the MIP measurement as well. With the correlation of the gain to the anode luminous sensitivity and the performed gain versus HV measurement of the qualification test, a preliminary alignment of the individual PMT's supply voltage can be performed to have all SSD PMTs at about the same gain in the array, without performing extensive tests.

5.4 SSD Engineering Array

Before equipping the entire SD array with about 1660 additional scintillators on top of the existing WCDs, the new detectors are tested on a smaller scale. Therefore, an engineering array (EA) with 12 SSD units was built to test the systems stability and function in its actual environment.

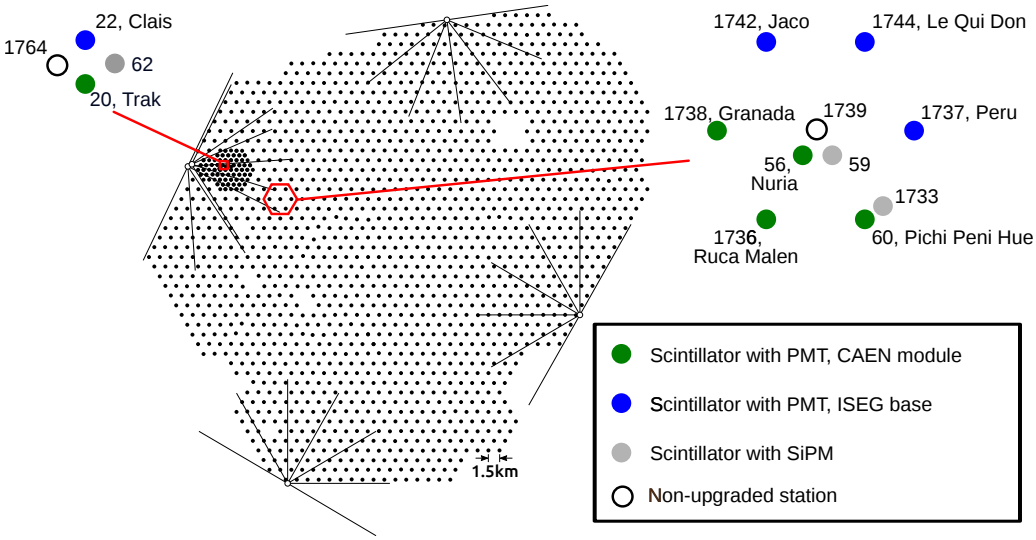

Figure 5.31: Layout of the SSD prototype stations in the Argentinian Pampas as of February 2017. A set of 7 SSD stations with PMTs is arranged in a regular hexagon. Two stations are installed next to a regular SD station inside the Infill area. PMTs with a passive base and a CAEN HV supply (green dots) and PMTs with an ISEG base (blue dots) are tested simultaneously.

5.4.1 Layout/setup

The scintillator boxes for the EA were built and tested at KIT[7]. Each SSD was tested in a muon tower to determine the homogeneity and the N_{pe}/VMIP before being shipped to Argentina [98]. The EA was build in September 2016 and the prototype configuration for the following analysis can be seen in Fig. 5.31. To study the SSD behaviour, one unitary cell, meaning a complete hexagon around a central station, of the regular SD array were equipped with a SSD on top. In addition, two SSD stations were installed next to a regular station in the Infill array, creating a 'twin' station with a high rate of coincident events to study. Three extra stations were used to study the use of a SiPM. Of the nine stations with a PMT, four stations were equipped with an ISEG base, while the other five stations have a passive voltage divider with a CAEN module for HV supply.

5.4.2 Station Monitoring

To keep track of the environmental conditions and to study weather influences on the detector performance, the SSD stations of the EA were equipped with extra sensors. A dedicated data logger records the temperature and humidity inside the SSD housing. Temperature sensors are placed in the middle of the two separated scintillator parts and a combined humidity/temperature sensor is put in the centre part of the SSD. A period of the recording can be seen in Fig. 5.32. Within the first two years the extreme ratings for temperature reached about 43 °C at maximum and a minimum of −13 °C. The humidity in the centre SSD part, where also the PMT is situated, ranges between 14% and 32%. In order to keep leakage current between the PMTs pins low, a humidity of less than 60% is advised [111]. Also, rusting of the PMT pins must be avoided to ensure long term operation of the SSD. This has been observed for a few of the large WCD PMTs but, isolated from the large water volume of the WCD, this is not as likely in the SSD.

In addition to the data logger, the temperature sensor on the SSD PMT base gives the temperature inside the sensor tube. In Fig. 5.33 (left) the PMTs temperature correlates very well

[7]Karlsruher Institut für Technologie

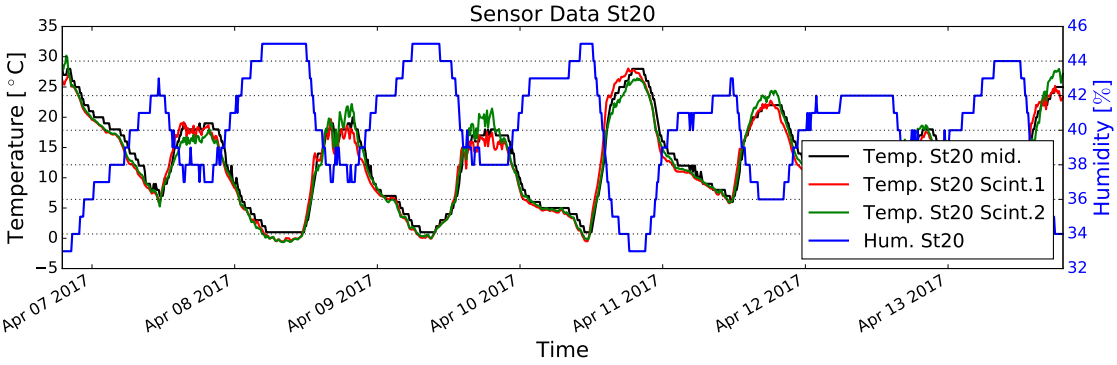

Figure 5.32: Period of the temperature and humidity recording of the data logger. Temperature and humidity are measured at the centre of the SSD aluminium box and separate temperature sensors in the two scintillator compartments.

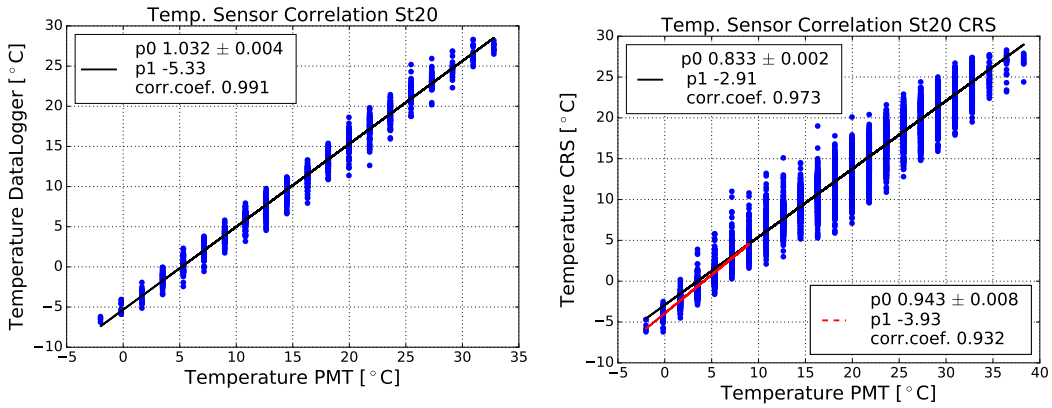

Figure 5.33: Correlation of temperature monitors inside the SSD station 20. Left plot shows the comparison of sensors at the PMT base inside the detector tube and an additional data logger sensor inside one of the scintillator modules. On the right side the correlation of the sensor at the PMT to the air temperature at the central radio station is shown.

to the data logger temperature, with an offset of about 5 °C. With the data logger being present only in the EA stations, the sensor at the PMT base measures the temperature development inside the SSD quite well, however an absolute value of the scintillator compartment is not logged due to the temperature offset. Across the array, the air temperature is measured at several spots. The closest spot for SSD station 20 is the central radio station (CRS). The correlation to the temperature measured at the CRS is shown in Fig. 5.33 (right). While the overall correlation is good, the spread is larger compared to the data logger measurement and the deviation of the two sensors increases at the higher temperatures, with the slope at just 0.83. With the enclosed aluminium box temperature changes are inert and once heated up, the thermal reservoir takes time to cool down again. For temperatures below 10 °C (red line) the behaviour is similar to the data logger correlation.

In Fig. 5.34 the temperature dependence of the monitoring HV for the SSD PMT can be seen. For both the CAEN module and the ISEG base, the variation of the HV is in the range of one bit, as measured in the lab[8] (see Section 5.3.2.7).

[8]Note the different bin size for CAEN and ISEG HV.

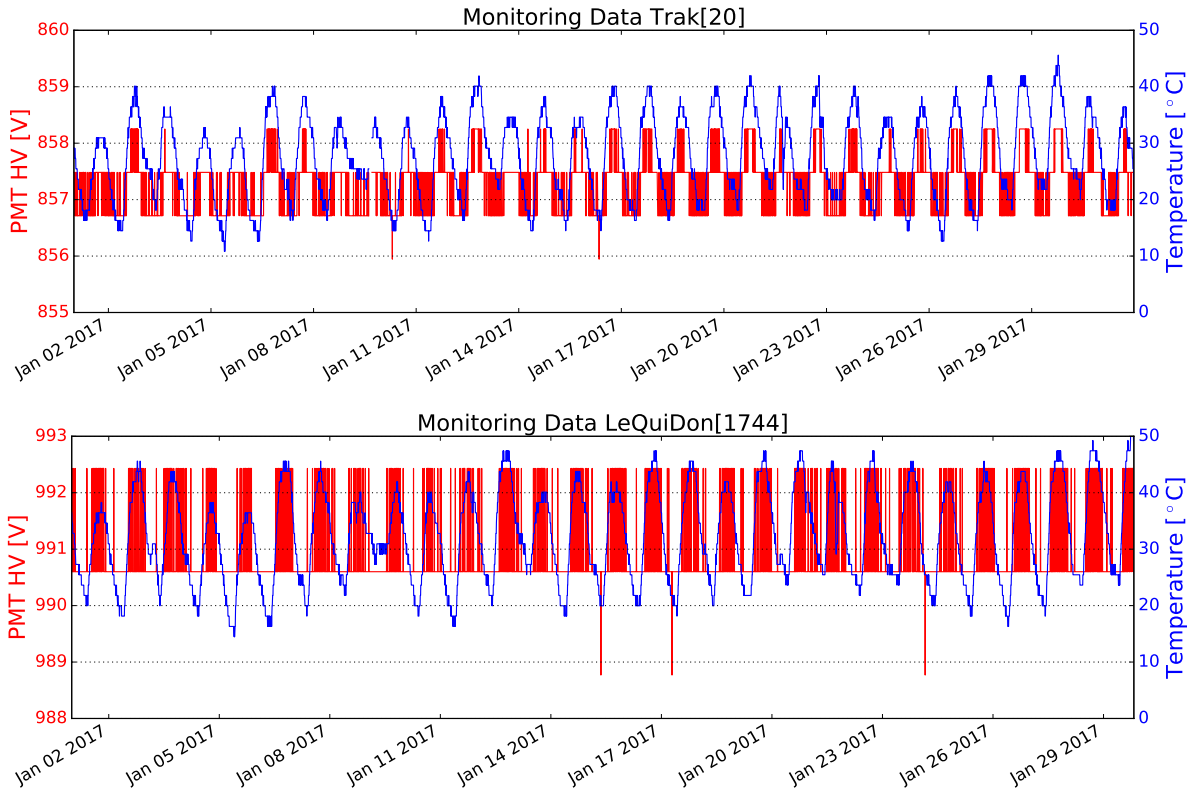

Figure 5.34: Monitoring data of the temperature sensor at the PMTs position inside the SSD stations 20 with CAEN HV module (top) and 1744 with an ISEG base (bottom).

5.4.3 Baseline

In field operation the traces are recorded with the UUB, which is located inside the electronic dome of the corresponding WCD. The baseline of the traces is set to an offset of about 5% of the 12 bit FADC range to cover a possible PMT signal undershoot after very large signals due to the capacitive coupling of the PMT. With a record length of about 17 μs, the events of the SSD arrive just before the WCD signals at around 6 μs. In this study, the first 500 time bins are defined as the baseline of the trace. For later analysis, the integrated signal is corrected for the average of the shifted baseline. The UUB measured baseline of the SSD traces is also correlated with temperature. Figure 5.35 shows the recorded baseline and variance in the measurement period. A positive correlation is found with the temperature measurement (Fig. 5.36). Independent from the PMT's base, the change is up to 0.10%/ °C. While the baseline is moving, the variance of the traces is not correlated with temperature. This indicates a mere shift of the baseline rather than an impact on amplification. It will be revised in detail for future UUB iterations.

5.4.4 Calibration Histograms

The SSD will be constantly calibrated by measuring the deposited signal of minimum ionising particles (MIPs). Like the VEM for the WCDs (see Section 3.1), these measurements are stored as separate histograms for every event and give the charge deposited by atmospheric muons for the last few minutes. A sample of the recorded histograms of one upgraded WCD for one event is shown in Fig. 5.37 (left). While the VEM histograms of the WCDs large PMTs have a broad peak, the SSD signal in grey has a narrow signal peak for the MIP. Due to the SSDs small height, the SSD signal is more time compressed in comparison to the multiple reflections inside the WCD. To get the maximum in dynamic range, the MIP peak needs to be put just above noise level, while still keeping the peak to valley ratio large enough for a clear separation. In

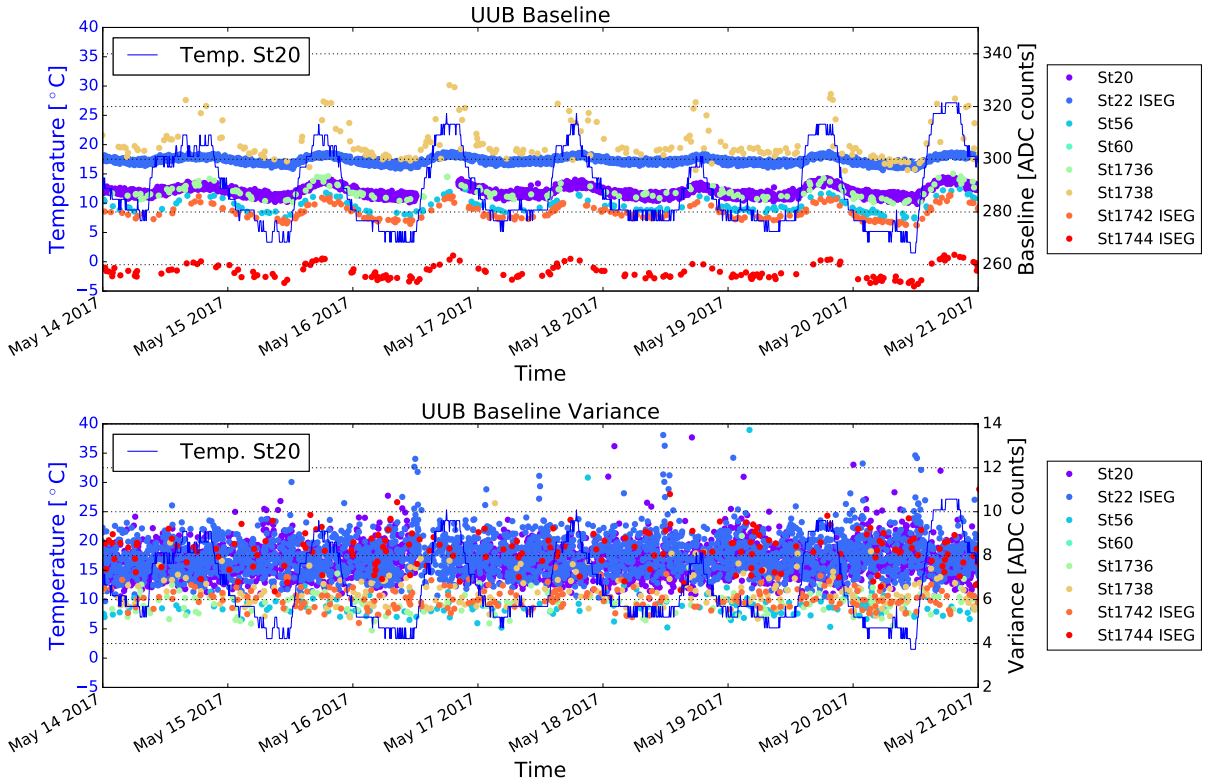

Figure 5.35: Baseline and variance evolution of the SSD channel for the eight prototype stations. In addition, the exemplary temperature of the PMTs sensor from station 20 is shown.

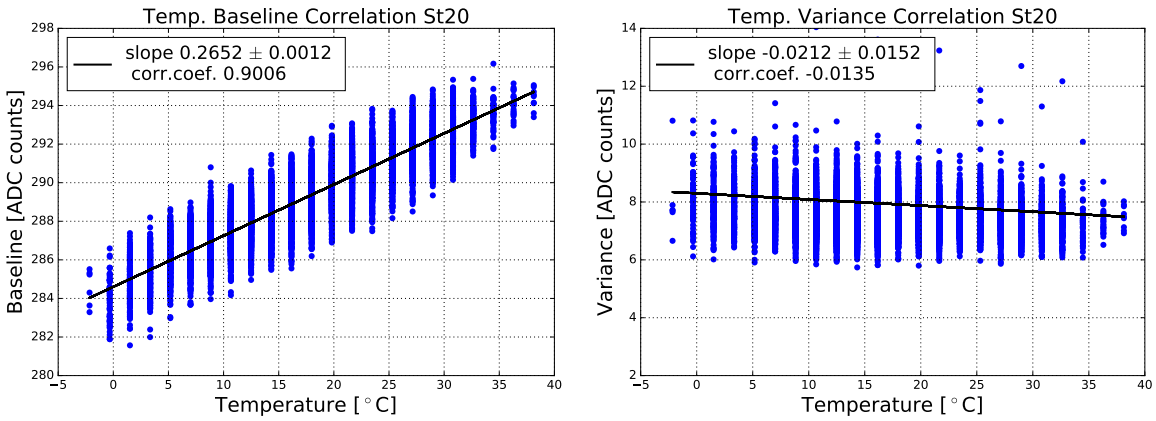

Figure 5.36: Correlation of the UUB baseline (left) and variance (right) from the SSD PMT trace and the temperature measured with the PMTs sensor of station 20.

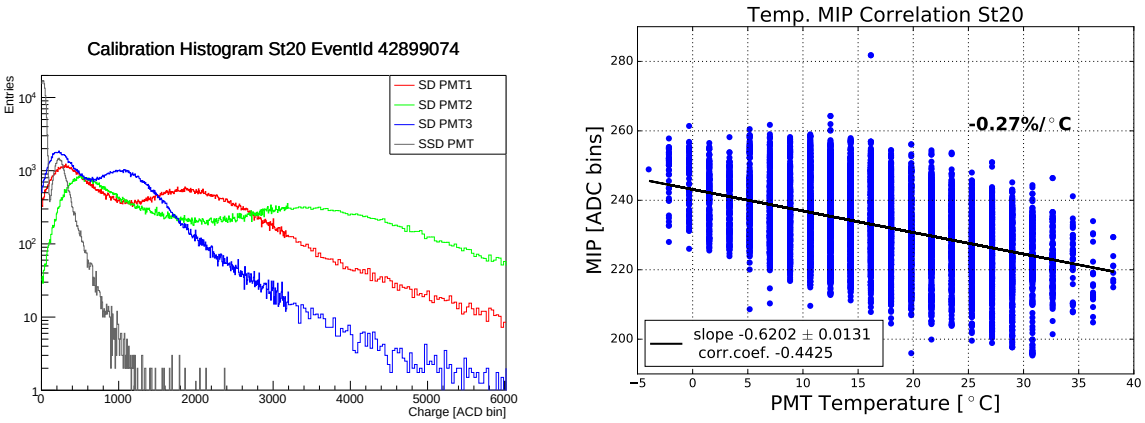

Figure 5.37: Left: Example of the charge calibration histograms of SSD station 20 for one event on 21st of May 2017. Right: Correlation of fitted MIP charge and temperature measured at the PMT base.

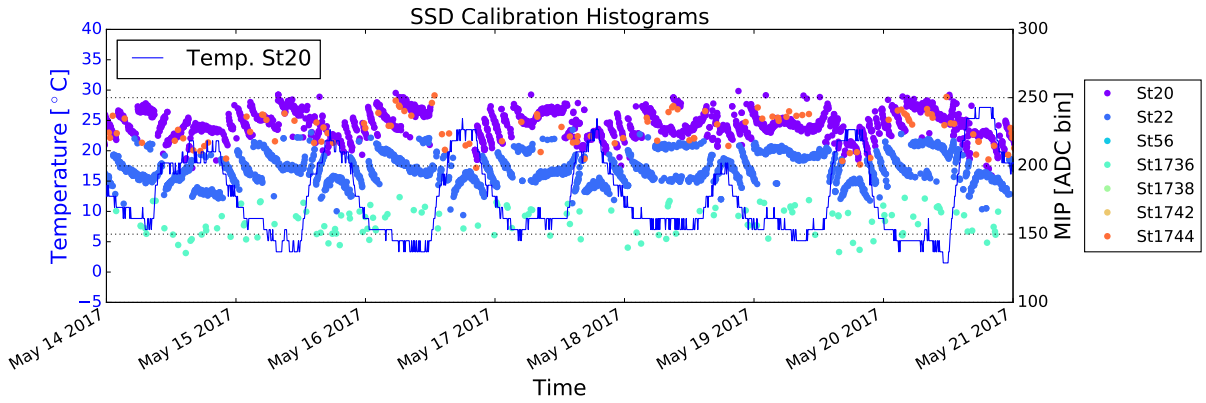

Figure 5.38: Calibration signal of single muons and SSD monitoring temperature over time.

this study, the MIP signal is extracted by fitting a Gaussian function to the second peak.

Figure 5.38 depicts the MIP signal of recorded events for different stations and the PMT temperature measured at SSD station 20. In contrast to the UUB baseline (see Fig. 5.35), the MIP signal is anti-correlated with temperature, although the correlation factor is only at 0.44. Figure 5.37 (right) shows the MIP peak versus temperature for the measurement period of March to mid June 2017. The slope is ~ -0.62 ADC counts, which corresponds to $-0.27\%/\,^{\circ}\mathrm{C}$. While this behaviour is expected due to the temperature dependence of the PMT signal with $-0.41\%/\,^{\circ}\mathrm{C}$ (see Section 5.3.3), the slope is not as steep as the PMTs response. In addition, the temperature drift of only the scintillator and WLS fibre are found to be about $-0.1\%/\,^{\circ}\mathrm{C}$ [112], the total detector drift was expected to be higher. Due to the continuously performed calibration, the temperature drift of the detector components does not effect the particle shower measurement.

5.4.5 First Events

In the engineering array the SSDs are triggered externally by the WCD. With this, first real cosmic ray events could already be recorded with SSDs. Figure 5.39 (left) shows the number of recorded events with an SSD trace for each station with a mounted scintillator on top. In black the amount of events with a signal above the threshold of 60 ADC counts is shown. The EA stations in the regular grid (Station ID $\geqq 56$) all show similar rates, with about 20% of the events containing traces with actual signal. This is due to the different area coverage of the

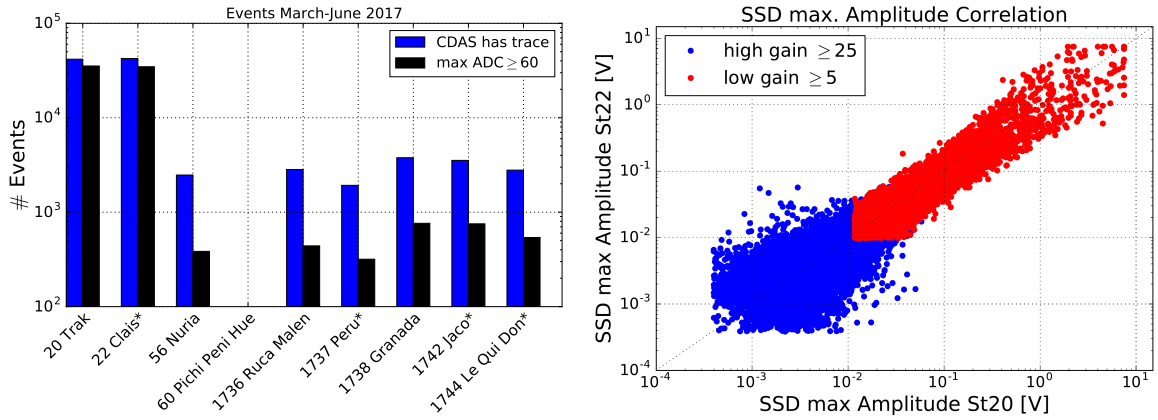

Figure 5.39: Left: Recorded events of the SSD engineering array from March to June 2017. Black bars show number of traces with a signal above 60 ADC counts. Asterisks indicate stations with an ISEG base. Station 60 was in maintenance during the selected time period. Right: Maximum signal amplitude correlation of the adjacent SSD stations 20 and 22.

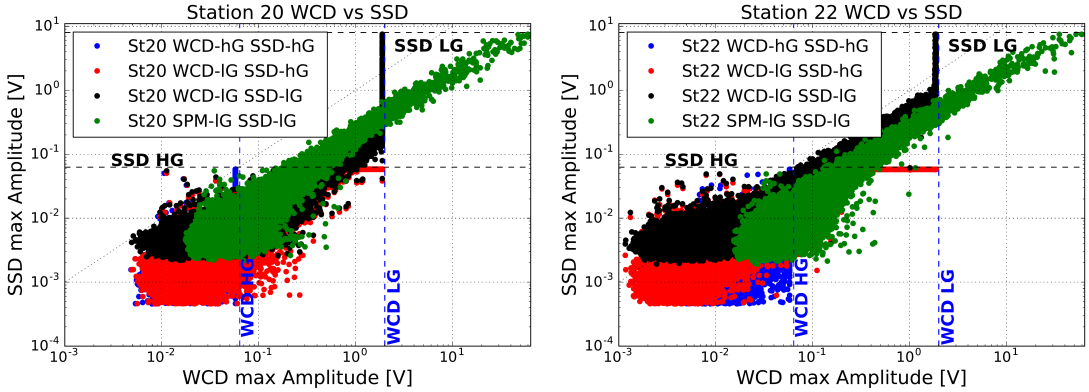

Figure 5.40: Maximum signal amplitudes of WCD and SSD for recorded events in stations 20 and 22 from March to mid June 2017.

SSD and the WCD. The twin SSD stations (ID 20 and 22) show an order of magnitude higher number of events, with about 80% also having an SSD trace. Due to the small distance between enough stations to create a T3, most of the traces belong to small energy events.

In Fig. 5.40 the combination of WCD and SSD can be seen. For station 20 (left, passive base) and 22 (right, ISEG base), the maximum signal amplitudes of events in the SSD and WCD are plotted, with good alignment of both detectors and no obvious differences for the two different SSD bases. Colour-coded are different combinations of the high gain and low gain of each detector, to demonstrate the boundaries of the channels. Both high gain channels saturate at 64 mV (WCD) and 62 mV (SSD) respectively. While the low gain channel of the WCD clips at 2 V, the SSD can reach up to 8 V. In green, the signal of the small PMT versus the SSD's low gain is shown. Only very few events saturate for the SSD. With an improved noise level of the UUB and optimising the baseline and MIP peak for each station, the SSD will be capable to cover the large dynamic range of the WCD.

Comparing the consistency of the SSD performance, the twin stations also show a good agreement among each other (see Fig. 5.39, right). While there is a spread for low energy events, it narrows for the low gain channel.

With stations 20 and 22 being right next to station 1764, the SSD twin stations are at the

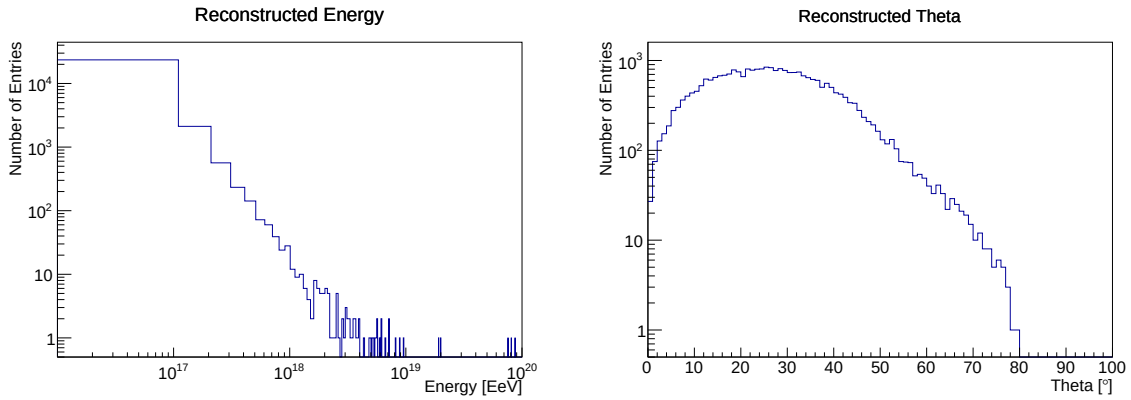

Figure 5.41: Reconstructed energy (left) and theta (right) of the AERALet events.

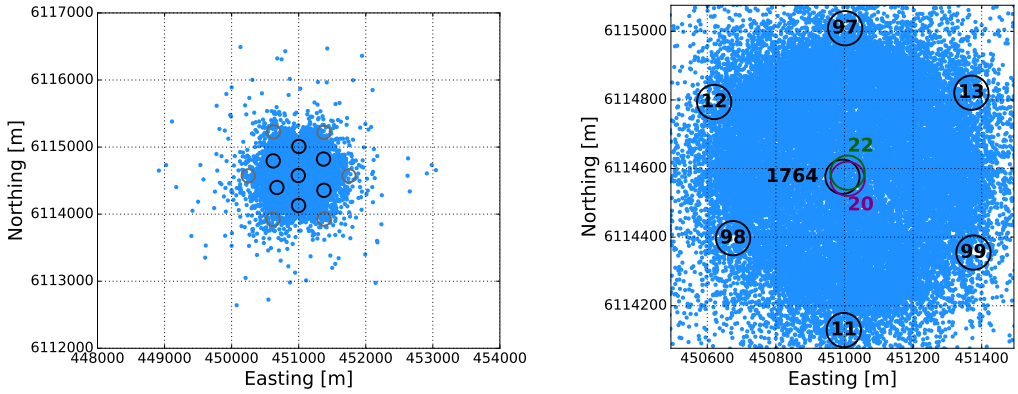

Figure 5.42: Reconstructed shower core of recorded events in the AERALet array from March to June 2017.

centre of the AERALet unitary cell. AERALet is a sub-array inside the InFill array, with an even further reduced station distance down to 433 m [113]. Thus, an event reconstruction for these low energy events using the Pierre Auger software Offline can be performed. Analysing the data from March to June 2017, a total of 27.186 events were reconstructed, with their energy and theta distribution shown in Fig. 5.41. Northing and easting of the reconstructed events, shown in Fig. 5.42, is distributed around the AERALet unitary cell. With the calibration of the SSD signals via the MIP measurement, a rough lateral distribution function can be derived for the SSD data. In Fig. 5.43, the calibrated SSD signal in units of MIPs over energy is plotted versus the shower core distance to the stations 20 and 22 respectively. Transparency of the entries is weighted with $\cos(\theta)^4$, as the efficiency of more inclined events is expected to fall due to the flat design of the SSD. Looking at all recorded events and calculating the fraction of events, which have an SSD signal (high gain $\geqq 50$ ADC counts), the amount is quite steady and even raises slightly with higher inclination just before it drops after 60°. This confirms the assumption of decreasing detection efficiency for inclined showers due to its flat construction.

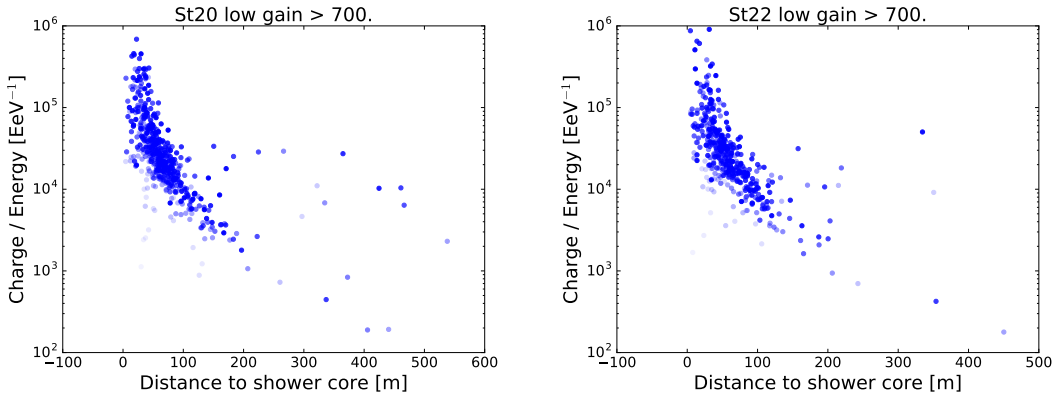

Figure 5.43: Lateral distribution of the estimated charge of SSD events over energy versus shower core distance.

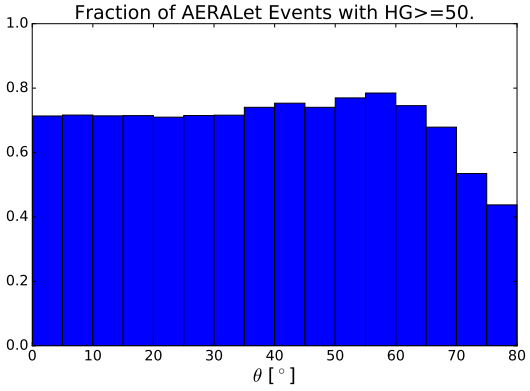

Figure 5.44: Fraction of reconstructed events with signal in the SSD (high gain $\geqq$ 50 ADC counts) versus inclination.

5.5 Conclusion & Future Prospects

In a selection process, the Hamamatsu R9420 was found as a suitable PMT candidate to be used in the SSD. It offers a sufficient quantum efficiency combined with a homogeneous response for the cookie size and a high linearity. A PMT base with integrated HV supply was introduced, capable of keeping up with the PMTs linearity at a low power consumption. This was tested in a first engineering array with a total of 12 stations. The temperature behaviour was as expected for a bialkali photocathode and the monitoring data of the EA shows no abnormalities. The recorded SSD signals of the EA correlate with the signals obtained from the WCD PMTs, including the dynamic range extension with the 'small PMT', and first level analysis with the raw data were performed.

After the successfully running detectors of the EA, about 1436 SD stations will be upgraded to an AugerPrime station with additional SSD and radio antennas on top of the WCD. As of May 2023, all station have the scintillator boxes installed on top, whereas 1260 stations are also equipped with the new electronics and the PMT (see Fig. 5.45). Data taken during the deployment of the first stations shows the detectors are operating as expected [114]. E.g. the RMS of the baseline was analysed for differences in daytime and night values to spot possible light leaks and advanced methods introduced to monitor the long term behaviour of the SSDs [115].

Analyses of the SSD signal are being developed, similar to the reconstruction of the WCDs (see Section 3.1.3). With the SSD being more sensitive to the electromagnetic component of

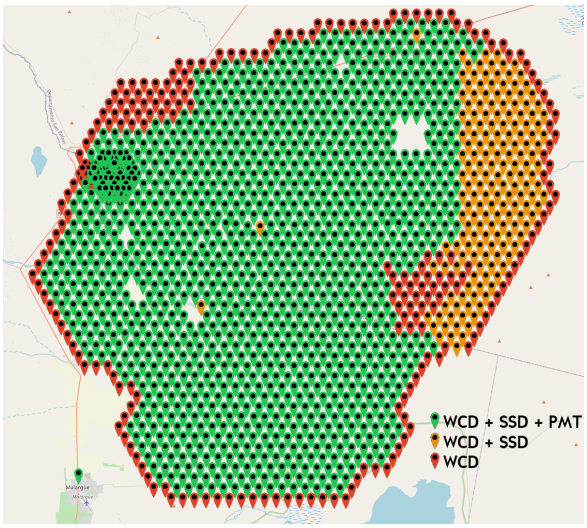

Figure 5.45: Map of the current deployment status of the SSDs as of May 2023. 1260 stations with a complete SSD including PMT are shown in green, whereas 176 stations have only the scintillator installed yet (indicated in orange) and red stations will only get new electronics installed.

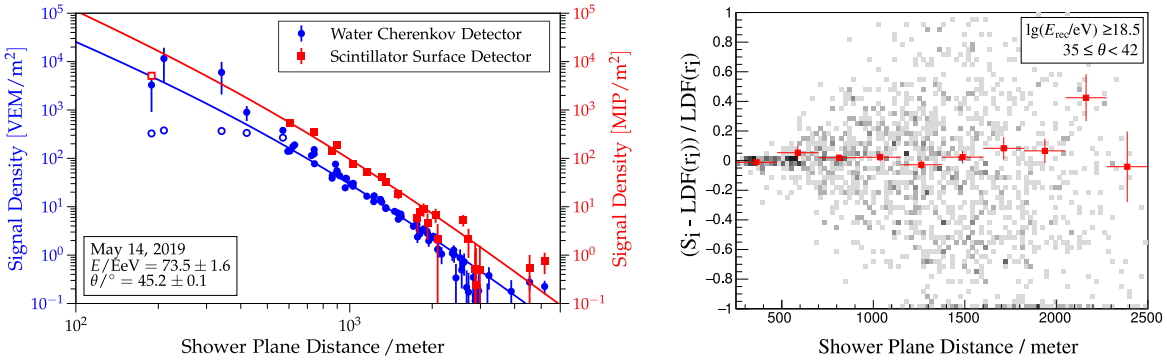

Figure 5.46: Sample event measured in the WCD and SSD of the pre-production array (left) and residuals to the fitted LDF (right) [116].

the shower, detector specific parameters as i.e. the VEM calibration or the integration window [116] need to be adapted. As the trigger to build the calibration histograms from the WCD is used, the factor to convert the MIP signal into VEM is obtained only from simulations yet. The time window to integrate the SSD's signal is determined by using the same algorithm as for the WCD and merging it with the WCD's integration window. The shower geometry is taken from the well-studied reconstruction of the WCD signals, and the contribution of the SSD to the improvement of the shower core position remains to be investigated. The same NKG-like lateral distribution function is used for the SSD. As the optimal distance r_{opt} is determined by the detectors spacing and the SSDs are co-located with the WCD, the shower size $S(1000)_{\mathrm{SSD}}$ is fitted while the shape of the LDF is parametrised yet. A sample event measured with the new AugerPrime stations is shown in Fig. 5.46.

As a first glimps on how the SSD contributes to the composition studies was done in [117]. Figure 5.47 shows the signal ratios $S_{\mathrm{SSD}}/S_{\mathrm{WCD}}$ of measurements with the AugerPrime stations for two zenith angle ranges. As the electromagnetic component is more condensed around the shower core, the ratio decreases with increasing distance. Due to its flat design, this effect is less prominent in more inclined showers. On the right side, only stations in a distance between 800 m and 1000 m are displayed versus the reconstructed energy. Since the EM component rising

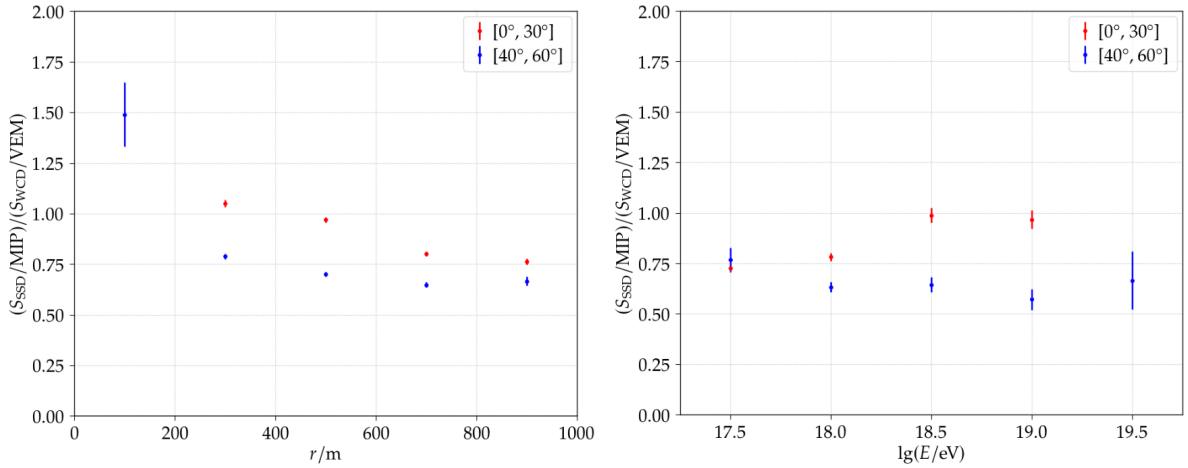

Figure 5.47: Signal ratio of the SSD and WCD from an AugerPrime station, divided into two zenith angle ranges. Left shows the ratio versus distance to the reconstructed shower core. Right shows the ratio for stations between 800 m and 1000 m to the shower core versus reconstructed energy. From [117].

faster with increasing energy compared to the muonic component, the ratio is expected to rise with increasing energy. This is implied by the raise for the more vertical showers. As for the more horizontal showers the increase is expected not as pronounced but the ratio stays rather constant. However, the number of detected events is still limited.

With more statistics and more elaborated analysis of the SSD signals, the next step towards resolving the composition at the highest energies is taken.

In the current SSD detector design, the detector's dynamic range is limited by the PMT's linearity. The PMT signal taken at the anode is split into two channels on the UUB and digitised by two 12 bit FADC with an overlap region of 5 bits. In order to extend the dynamic range of the detector, it is necessary to extend the linearity of the PMT. With the voltage divider already optimised for highest linearity at the anode output, this has to be achieved in a different way. A common technique to extend a PMT's dynamic range is to use the signal of large pulses already at one of the dynodes instead of the anode. With less stages participating in the amplification process, the signal in the early stages is smaller and the divergence of the electron cloud travelling through the PMT is smaller. This technique was already used in the bases of the three large SD PMTs, where the signal was taken from the last dynode and the anode to cover a large dynamic range [118, 119].

5.5.1 Dynode Decoupling

To measure the prospects of decoupling a dynode signal, the classical mono-signal voltage divider has to be modified. Figure 5.48 shows the circuit diagram of the modified base. The standard voltage divider based on the SSD design for high linearity output at the anode was modified by adding a decoupling capacitor (C_D) with 100 Ω (R_{12}) termination at the sixth dynode. With an additional resistor between the divider chain and the decoupling capacitor (R_{11}), the load onto the divider current is kept small.

Three different divider ratios were tested (see Table 5.5). With the first ratio being the same ratio as used for the SSD stations with an extra dynode read-out added. Another ratio was inspired by the LHAASO collaboration, using the same approach to extend the dynamic range [120]. Here the ratio for the latest stages is raised quite high. As third version an intermediate ratio is tested which is not as aggressive at the latest stages.

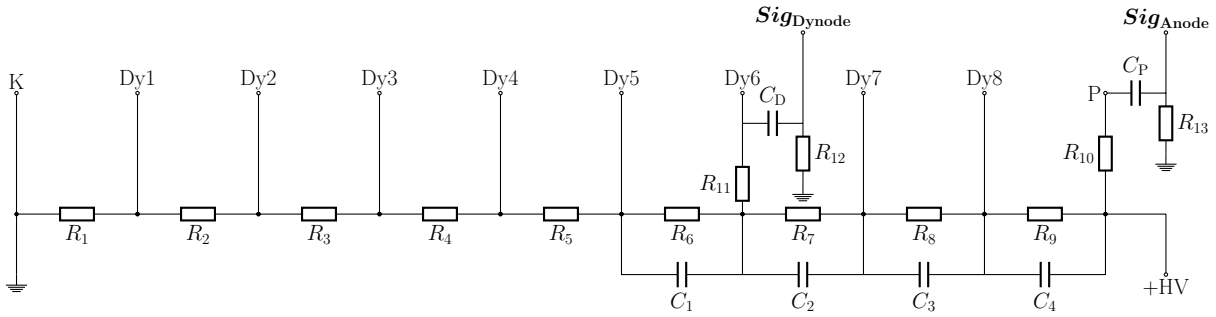

Figure 5.48: Modified PMT voltage divider for the Hamamatsu R9420 with additional signal read-out at the sixth dynode.

	K	Dy1	Dy2	Dy3	Dy4	Dy5	Dy6	Dy7	Dy8	A
SSD	2	1	1	1	1.2	1.5	2	3	1.5	
Intermediate	2	1	1	1.5	2.5	3	3.5	2.5	2.5	
LHAASO	2	1	1	1.5	2.5	4	6	5	5	

Table 5.5: Resistor ratios for different voltage divider tested for dynode decoupling read-out.

5.5.1.1 Measurement

To determine the linearity of the new base, the same setup as in Section 5.2.4 was used. A combination of neutral density filters and different LED driver settings are used to 'scan' different light intensities, and a deviation from the expected signal is calculated. In Fig. 5.49, the measurement for the LHAASO-like voltage divider is shown at a supply voltage of 1000 V, which corresponds to a gain of about 8×10^4. The two plots show the simultaneously recorded signal from the anode (left) and the sixth dynode (right). The dotted vertical line indicates the expected signal of 20 000 MIPs within 50 ns. For the anode output the deviation from a linear relation between detected light and PMT signal exceeds 5% at about 100 mA peak current, falling short of detecting 20 000 particles with the desired accuracy. But the dynode output (barely) keeps within the range of tolerance, even up to the highest light intensity. The measurements were done for the other ratios as well. For the 'SSD' base the linearity did not improve for the decoupled output and for the 'intermediate' base the dynode signal could extend the range just a bit, but still falling short of the maximum rating. Extended tests could further evaluate the usefulness of this method.

5.5.1.2 Modification of the UUB

To implement the dynode read-out in the UUB front-end, the two SSD channels need to be decoupled. This can be done by removing the resistor between the HG and LG (see channel schematics in [121]). In the EA this was already done for tests with SiPMs as light detector, which needed three individual channels. A possible signal integration into the UUB read-out is shown in Table 5.6. For a PMT gain of 8×10^4 and a dynode to anode ratio of 80, with the assumption of 25 photons per MIP and a total signal duration of 25 ns, the two channels can cover the measurement of 20 000 MIPs. Since the dynode/anode ratio is PMT dependent and must be determined for each sensor individually, a separate calibration is needed to be performed in the overlap region of the two channels. As the dynode signal is too small for single MIPs, this can not be achieved by measuring atmospheric muons and a different method needs to be introduced. It could be further investigated whether an absolute calibration of the ratio before the installation in the SSD would be stable over time.

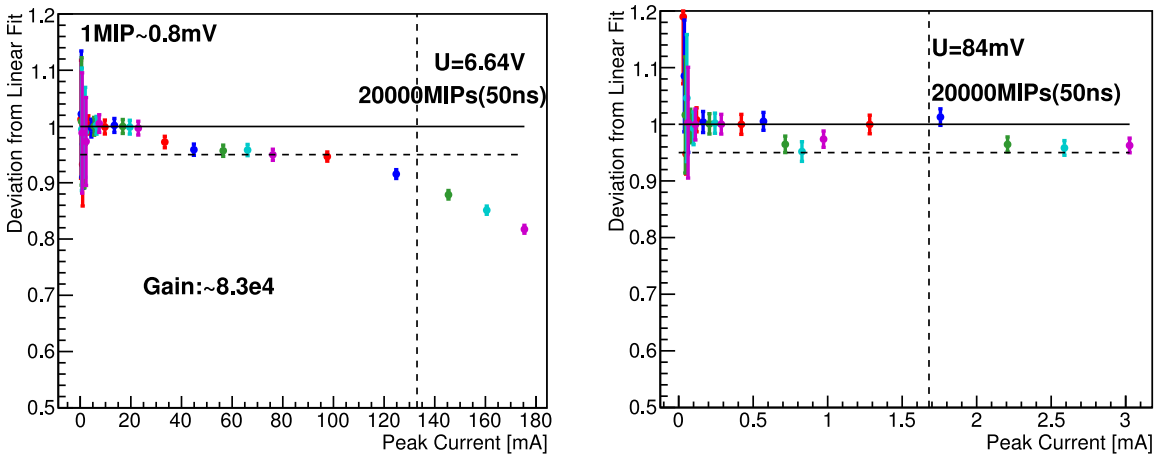

Figure 5.49: Linearity measurement of a R9420 PMT with decoupled dynode signal at 1000 V for 50 ns light pulses. Vertical dotted lines indicates the expected 20 000 MIPs signal.

Range	Intent	Dynamic Range																
bits		1	2	3	4	5	6	7	8	9	10	11	12	13	14	15	16	17
HighGain	MIP	Anode X8																
Ipeak [mA]		0.0012				0.195							5					
Vpeak [mV]		0.061				0.97							250					
Npart [MIP]		0.095				1.53							391					
LowGain	Showers						6th Dynode X12											
Ipeak$_D$ [mA]							0.0008											3.33
Vpeak$_D$ [mV]							0.04											166.7
Npart [MIP]							5.09											20833

Table 5.6: Possible UUB integration of a signal read-out for dynode decoupled signals. Assuming a gain of 8×10^4, a Dynode/Anode signal ratio of 80, 25γ/MIP, and a signal duration of 25 ns.

As a note to the candidate PMTs, this method was tested for the Electron Tubes 9902KB as well, but still fell way short of measuring a signal corresponding to 20 000 MIPs.

Chapter 6

Summary

With the development of new sensors, a detector upgrade can take well-established experiments like the Pierre Auger Observatory even further.

In this work, the usage of a more efficient PMT to be used as sensor in the camera of the Fluorescence Detector was presented. Two PMTs with an increased quantum efficiency compared to the currently installed PMTs were tested. With a gain of 24% and even more in photon detection efficiency, there is the prospect of increasing the exposure of the FD telescopes with these new sensors. Due to the discontinued hexagonal face-plate of the PMTs, a new light guide to cover the dead space between the round pixels was introduced. For the design, a Winston cone was modified to fit into the current camera optics. Simulations were performed on the loss in concentration power due to the modifications needed for the usage in the Schmidt telescope design. The cones were produced from a highly reflective anodised aluminium sheet. A prototype consisting of 48 PMTs plus Winston cones was installed at the end of 2014 and is running without incident since then. Comparisons of different calibration measurements show the improved photon detection capabilities of this combination in the telescope environment with about 17% more light being detected. Long term evolution of the calibration measurements show no efficiency loss due to ageing or dust for the new components. As a next step, one camera can be equipped with the new sensors, from which the HEAT telescopes would benefit most in terms of increased exposure.

For the AugerPrime upgrade of the Pierre Auger Observatory, three candidate PMTs were tested for their usage in the new Surface Scintillator Detector. Measuring quantum efficiency, uniformity, and linearity, a suitable PMT was found in the Hamamatsu R9420, which can meet the high requirements for use in the new detector. For this PMT, a base with an integrated high voltage generator has been introduced and compared to a conservative passive divider with separate HV supply. Stability and noise tests were performed, with special regards to the temperature behaviour of the components. Both bases were found to behave the same, with the integrated base reducing the additional power consumption to the existing supply of the WCD. A prototype of 12 stations, the SSD engineering array, was installed in 2016. For this, 25 PMTs have been tested and categorised for usage in the field. Station monitoring was evaluated and temperature influence on signal quality discussed. With the EA, first events were recorded with the SSD detectors. For the SSD twin stations inside the AERALet subarray, the recording of first events with the new detector were compared to the reconstructed events measured with the WCDs. With the successful operation of the EA, the complete upgrade of almost all 1600 WCDs is underway. As the large dynamic range of the SSD is vital for its detection of cosmic rays at the highest energies, a possible modification is presented to extend the range even further. By decoupling the PMTs signal from an earlier dynode stage, the PMTs linearity exceeds the measurement of 20 000 MIPs.

Appendices

Appendix A

FD Upgrade

A.1 PMT Datasheets

A.1.1 Photonis XP3062 [39]

High PHR, 8-stage, 40 mm (1.5") hexagonal tube

Applications :	For imaging cameras such as fly's eye arrays		
Description :	Window :	Material :	lime glass
		Photocathode :	bi-alkali
		Refr. index at 420 nm :	1.54
	Multiplier :	Structure :	linear focused
		Nb of stages :	8
	Mass :	55 g	

Photocathode characteristics

	Spectral range :				290-650	nm
		Maximum sensitivity at :			420	nm
	Sensitivity ① :					
		Luminous :			90	µA/lm
☑		Blue :	min.: 9	typ.:	11.5	µA/lmF
		Radiant, at 420 nm :		typ.:	90	mA/W

Characteristics with voltage divider A

	Gain slope (vs supp. volt., log/log) :				5.8	
	For an anode blue sensitivity of :				3	A/lmF
☑	Supply voltage :	max.:	1300	typ.:	1100	V
		min.:	880			
	Gain :			typ.:	$2.6x10^6$	
☑	Anode dark current ② :	max.:	20	typ.:	1	nA
☑	Pulse height resolution for ^{57}Co ③ :	max.:	12.5	typ.:	12	%
	Mean anode sensitivity deviation ④					
	long term (16 h) :				1	%
	after change of count rate :				1	%
	vs temperature from 0 to +40°C at 420 nm :				- 0.2	%/K
	anode sensitivity change for a magnetic field of 0.05 mT :				10	%

Characteristics with voltage divider ⑤ :		**A**		**C**	
For a supply voltage of :		1100		1000	V
	typical gain :	$2.6x10^6$		10^5	
	linearity (2%) of anode current up to :	60		80	mA
	anode pulse rise time ⑥ :	3		3.5	ns
	anode pulse duration at half height :	4.5		4.7	ns
	signal transit time :	30		31	ns
Capacitance	anode to all			5	pF

Recommended voltage divider

Type A for maximum gain

K	G	D1	D2	D3	D4	D5	D6	D7	D8	A	
0.05	3	1	1	1	1	1	1	1	1		(total : 11.05)

Type C for timing / linearity / gain compromise

K	G	D1	D2	D3	D4	D5	D6	D7	D8	A	
0.05	3	1	1	1	1	1	1.25	1.75	1.25		(total : 12.3)

K: photocathode G: focusing electrode Dn: dynode A: anode

Limiting values

Anode blue sensitivity ⑦ :			max.:	15	A/lmF
Supply voltage :			max.:	1600	V
Continuous anode current ⑧ :			max.:	0.2	mA
Voltage between	D1 and photocathode :	min.: 200	max.:	500	V
	consecutive dynodes :		max.:	300	V
	anode and D8 ⑨ :	min.: 30	max.:	300	V
Ambient temperature	short operation (< 30 mn) :	min.: -30	max.:	+80	°C
	continuous operation & storage :	min.: -30	max.:	+50	°C

Notes

☑ Characteristic measured and mentioned on the test ticket of each tube.

① Luminous sensitivity is measured with a tungsten filament lamp with a colour temperature of 2856 ± 5 K. The blue sensitivity, expressed in A/lmF ("F" as in Filtered) is measured with a tungsten filament lamp with a color temperature of 2856 ± 5 K. Light is transmitted through a blue filter Corning CS no. 5-58, polished to half stock thickness. The radiant sensitivity is measured with a tungsten filament lamp with a colour temperature of 2856 ± 5K. Light is transmitted throught an interference filter. Radiant sensitivity at 420 nm, expressed in mA/W, can be estimated by multiplying the blue sensitivity, expressed in µA/mF, by 7.5 for this type of tube.

② Dark current is measured at ambient temperature, after the tube has been in darkness for approximately 1 min. A lower value can be obtained after a longer stabilisation period in darkness (approx. 30 min.).

③ Pulse amplitude resolution for ^{57}Co is measured with a NaI(Tl) cylindrical scintillator with a diameter of 51 mm and a height of 51 mm. The count rate used is ~ 10^4 c/s.

④ The mean pulse amplitude deviation is measured by coupling a NaI(Tl) scintillator to the window of the tube. Long term (16h) deviation is measured by placing a ^{137}Cs source at a distance from the scintillator such that the count rate is ~ 10^4 c/s, corresponding to an anode current of ~ 300 nA. The mean pulse amplitude deviation after change of count rate is measured with a ^{137}Cs source at a distance from the scintillator such that the count rate can be changed from 10^4 to 10^5 c/s, corresponding to an anode current of ~ 1 µA and 0.1 µA respectively. Both tests are carried out according to ANSI-N42-9-1972 of IEEE recommendations.

⑤ To obtain a peak pulse current greater than that obtainable with divider A, it is necessary to increase the inter-dynode voltage progressively. Divider circuit C is an example of a progressive divider, giving a compromise between gain, speed and linearity. Other dividers can be conceived to achieve other compromises. It is generally recommended that the voltage ratio between two successive stages is less than 2.

⑥ Measured with a pulse light source, with a pulse duration (FWHM) of approximately 1 ns., the cathode being completely illuminated. The rise time is determined between 10 % and 90 % of the anode pulse amplitude. The signal transit time is measured between the instant at which the illuminating pulse of the cathode becomes maximum, and the instant at which the anode pulse reaches its maximum. Rise time, pulse duration and transit time vary with respect to high tension supply voltage Vht as (Vht)-½.

⑦ The voltage corresponding to this maximum anode blue sensitivity is equal to 1.5 times the voltage indicated on the test ticket of the tube.

⑧ A value less than 10 µA is recommanded for applications requiring good stability.

⑨ When calculating the anode voltage, the voltage drop across the load resistor should be taken into account.

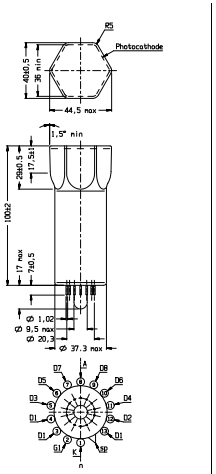

ref.: 22100023

sp: short pin
n: plane of symmetry of the multiplier

K: cathode G: focusing electrode
Dn: dynode A: anode

Typical gain curve

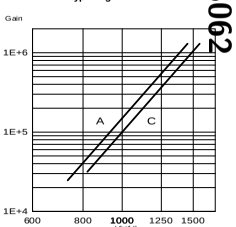

XP3062

Typical spectral characteristics

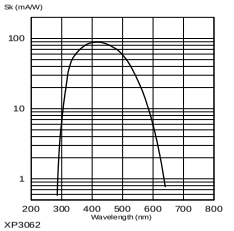

XP3062

Accessories

Socket :	for PCB	FE1113
	for wires	FE1113/W

Photomultiplier tubes

Tube diameter	Type No.	❶ Out-line No.	❷ Spectral response		Cathode characteristics				Anode characteristics						
			Spectral response range (nm)	Curve code	❸ Q.E. at peak Typ. (%)	❹ Lumi-nous Typ. (μA/lm)	❺ Blue sensitivity index (CS 5-58) Typ.	❻ Radiant Typ. (mA/W)	❼ Anode to cathode supply voltage (V)	❸ Lumi-nous Typ. (A/lm)	❻ Radiant Typ. (A/W)	❾ Gain Typ.	❿ Dark current Typ. (nA)	❿ Dark current Max. (nA)	⓫ Time response Rise time Typ. (ns)	⓫ Time response Transit time Typ. (ns)	⓫ Time response T.T.S. Typ. (FWHM) (ns)
10 mm (3/8")	R1635	❶	300 to 650	A-D	25	100	10.0	80	1250 ③	100	8.0×10^4	1.0×10^6	1	50	0.8	9	0.5
	R2496	❶	160 to 650	C-D	25	100	10.0	80	1250 ⑤	100	8.0×10^4	1.0×10^6	2	50	0.7	9	0.5
13 mm (1/2")	R647-01	❸	300 to 650	A-D	25	110	10.0	80	1000 ⑯	150	1.1×10^5	1.4×10^6	1	2	2.1	22	2.0
	R4124	❷	300 to 650	A-D	25	100	10.0	80	1000 ㉗	100	8.0×10^4	1.0×10^6	1	15	1.1	12	0.5
	R4177-06	❸	300 to 650	A-E	12	30	4.5	38	1500 ⑯	15	1.9×10^4	5.0×10^5	0.5	10	2.0	20	—
	R12421	❹	300 to 650	A-D	25	110	10	80	1000 ㉓	220	1.6×10^5	2.0×10^6	0.5	2	1.2	14	1.4
	R12421-300	❹	300 to 700	H	32	160	14	105	1000 ㉓	320	2.1×10^5	2.0×10^6	1	5	1.2	14	1.4
19 mm (3/4")	R1166	❺	300 to 650	A-D	26	110	10.5	85	1000 ⑳	110	8.5×10^4	1.0×10^6	1	5	2.5	27	2.8
	R1450	❻	300 to 650	A-D	27	115	11.0	88	1500 ㉕	200	1.5×10^5	1.7×10^6	3	50	1.8	19	0.76
	R3478	❼	300 to 650	A-D	27	115	11.0	88	1700 ⑩	200	1.5×10^5	1.7×10^6	10	300	1.3	14	0.36
	R3991A-04	❽	300 to 650	A-E	12	30	4.5	38	1500 ㉖	10	1.3×10^4	3.3×10^5	0.1	10	1.0	10	—
	R4125	❺	300 to 650	A-D	27	115	11.0	88	1500 ㉑	100	7.7×10^4	8.7×10^5	10	50	2.5	16	0.85
	R5611A-01	❾	300 to 650	A-D	26	90	10.5	85	1000 ㉖	50	4.7×10^4	5.5×10^5	3	20	1.3	12	0.8
25 mm (1")	R1288A-06	❽	300 to 650	A-E	12	30	4.5	38	1500 ㉖	10	1.2×10^4	3.3×10^5	0.1	10	1.3	13	—
	R1924A	❾	300 to 650	A-D	26	90	10.5	85	1000 ㉖	180	1.7×10^5	2.0×10^6	3	20	1.5	17	0.9
	R4998	❿	300 to 650	A-D	23	80	9.5	76	2250 ⑲	400	3.8×10^5	5.0×10^6	10	200	0.7	10	0.16
	R7899-01	⓫	300 to 650	A-D	27	95	11.0	88	1250 ㉗	190	1.8×10^5	2.0×10^6	2	15	1.6	17	0.6
									1500 ㉘	160	1.5×10^5	1.7×10^6	2	20	1.6	16	0.7
	R8619	⓬	300 to 650	A-D	27	95	11.0	88	1000 ㉗	250	2.3×10^5	2.6×10^6	2	15	2.5	28	1.2
	R9800	⓭	300 to 650	A-D	27	95	11.0	88	1300 ⑨	100	9.3×10^4	1.1×10^6	5	50	1.0	11	0.27
	R9800-100	⓭	300 to 650	F	35	130	13.5	110	1300 ⑨	140	1.2×10^5	1.1×10^6	10	100	1.0	11	0.27
	R13478	⓮	300 to 650	A-D	25	95	10.0	80	1500 ②	50	4.2×10^4	5.3×10^5	3	30	0.9	9.1	0.13
28 mm (1-1/8")	R3998-02	⓯	300 to 650	A-D	26	90	10.5	85	1000 ⑬	120	1.1×10^5	1.3×10^6	2	10	4.4	32	3.5
	R3998-100-02	⓯	300 to 650	F	35	130	13.5	110	1000 ⑬	130	1.1×10^5	1.0×10^6	5	25	4.4	32	3.5
	R6427	⓰	300 to 650	A-D	27	100	11.0	88	1500 ㉚	500	4.4×10^5	5.0×10^6	10	200	1.7	16	0.5
									1500 ㉛	190	1.7×10^5	2.0×10^6	4	80	1.8	17	0.5
	R7111	⓱	300 to 650	A-D	26	90	10.5	85	1000 ㉖	180	1.7×10^5	2.0×10^6	3	20	1.6	18	0.9
	R7525	⓲	300 to 650	A-D	27	95	11.0	88	1500 ⑥	45	4.7×10^4	5.3×10^5	5	100	1.3	14	0.55
									1500 ⑦	19	1.8×10^4	2.1×10^5	2	40	1.3	15	0.58
	R13449	⓳	300 to 650	A-D	25	95	10.0	80	1500 ②	50	4.2×10^4	5.3×10^5	3	30	0.9	10	0.17
38 mm (1-1/2")	R580	㉑	300 to 650	A-D	27	95	11.0	88	1250 ㉓	100	4.7×10^4	1.1×10^6	3	20	2.7	37	4.5
									1500 ㉔	75	7.0×10^4	7.9×10^5	2	15	2.7	40	4.5
	R11102	㉑	300 to 650	A-D	28	120	11.5	89	1000 ㉓	120	8.9×10^4	1.0×10^6	2	20	3.2	34	4.8
	R3886A	㉒	300 to 650	A-D	26	90	10.5	85	1000 ㉓	180	1.7×10^5	2.0×10^6	3	20	2.6	30	2.0
	R9420	㉓	300 to 650	A-D	27	95	11.0	88	1300 ⑨	47	4.4×10^4	5.0×10^5	10	100	1.6	17	0.55
	R9420-100	㉓	300 to 650	F	35	130	13.5	110	1300 ⑨	65	5.5×10^4	5.0×10^5	10	100	1.6	17	0.55
	R13408	㉔	300 to 650	A-D	25	95	10.0	80	1500 ②	50	4.2×10^4	5.3×10^5	3	30	1.2	13	0.19

Note: The data shown in ▭ is measured with tapered voltage distribution ratio.
Please refer to page 18 and 19 for each item in the above list.

(at 25 °C)

⓬ Max. ratings Anode to cathode voltage (V)	⓬ Max. ratings Average anode current (mA)	⓭ Typical pulse height resolution (%)	⓮ Stability Long term Typ. (%)	⓮ Stability Short term Typ. (%)	⓯ Pulse linearity 2 % deviation Typ. (mA)	⓯ Pulse linearity 5 % deviation Typ. (mA)	⓰ Remarks Dynode structure / stage	⓰ Remarks Socket & socket assembly ⓱	Note	Type No.
1500	0.03	23 / BGO *1	1.0	2.0	3	7	LINE / 8	E678-11* 1	UV type (R3878)	R1635
1500	0.03	23 / BGO *1	1.0	2.0	3	7	LINE / 8	E678-11* 1		R2496
1250	0.1	7.8	1.0	2.0	3	7	LINE / 10	E678-13F* 2	SILICA (R760) and UV (R960) types	R647-01
1250	0.03	8.1	1.0	2.0	2	5	LINE / 10	E849-68 3	UV type (R4141)	R4124
1800	0.02	12.0	2.0	2.0	8	13	LINE / 10	E678-13E*	Flying lead type (R4177-04)	R4177-06
1250	0.1	—	—	—	3	12	LINE / 10	E678-13F* 3	UV types (R12421-03)	R12421
1250	0.1	—	—	—	3	12	LINE / 10	E678-13F* 3	EGBA type	R12421-300
1250	0.1	7.8	1.0	2.0	4	7	LINE / 10	E678-12L* 4	SILICA (R762) and UV (R750) types	R1166
1800	0.1	7.8	1.0	2.0	4	8	LINE / 10	E678-12L* 5		R1450
1800	0.1	7.8	1.0	2.0	4	8	LINE / 8	E678-12L* 6	SILICA (R2076) and UV (R3479) types	R3478
1800	0.02	11.0	1.0	2.0	20	40	C+L / 10	E678-12R*		R3991A-04
1800	0.1	7.8	1.0	2.0	100	170	LINE / 10	E678-12L* 7		R4125
1250	0.1	8.0	1.0	2.0	10	20	LINE / 10	E678-12A*	Glass base type (R5611A)	R5611A-01
1800	0.02	9.0	1.0	2.0	30	50	C+L / 10	E678-14-03*	Flying lead type (R1288A-04)	R1288A-06
1250	0.1	7.8	1.0	2.0	30	50	C+L / 10	E678-14C* H	Flying lead type (R1924A-01)	R1924A
2500	0.1	8.0	1.0	2.0	40	70	LINE / 10	E678-12A*	SILICA type (R5320)	R4998
1800	0.1	7.8	1.0	2.0	30	50	LINE / 10	E678-12A*	Glass base type (R7899)	R7899-01
1800	0.1	7.8	1.0	2.0	100	150				
1500	0.1	8.0	1.0	2.0	5	8	LINE / 10	E678-12A*		R8619
1500	0.1	7.8	1.0	2.0	30	50	LINE / 8	E678-12A*		R9800
1500	0.1	—	—	—	30	50	LINE / 8	E678-12A*	SBA type	R9800-100
1750	0.1	8.0	—	—	10	25	LINE / 8	E678-20B*		R13478
1500	0.1	7.5	1.0	1.0	8	10	B+L / 9	E678-14C* H		R3998-02
1500	0.1	7.0	1.0	1.0	8	10	B+L / 9	E678-14C* H	SBA type	R3998-100-02
2000	0.1	7.8	1.0	2.0	10	30	LINE / 10	E678-14C* H I	UV type (R7056)	R6427
2000	0.1	7.8	1.0	2.0	100	150				
1250	0.1	7.8	1.0	2.0	30	50	C+L / 10	E678-14C* H		R7111
1750	0.2	7.8	1.0	2.0	10	30	LINE / 8	E678-14C*		R7525
1750	0.2	7.8	1.0	2.0	100	150				
1750	0.1	8.0	—	—	10	30	LINE / 8	E678-20B*		R13449
1750	0.1	7.7	1.0	1.0	40	60	LINE / 10	E678-12A* H		R580
1750	0.1	7.7	1.0	1.0	150	200				
1250	0.1	7.6	0.5	0.5	10	30	C+L / 10	E678-12A H		R11102
1250	0.1	7.5	1.0	2.0	20	30	C+L / 10	E678-12A* H		R3886A
1500	0.1	7.8	1.0	2.0	30	50	LINE / 8	E678-12A*		R9420
1500	0.1	7.0	1.0	2.0	30	50	LINE / 8	E678-12A*	SBA type	R9420-100
1750	0.1	8.0	—	—	20	50	LINE / 8	E678-20B*		R13408

Note 1: This data is measured with ^{22}Na source and BGO scintillator.

TECHNICAL INFORMATION

TENTATIVE
Jul. 2012

R11920-100-05

For Gamma-ray Telescope (CTA project), Fast time response, CC window
38 mm (1.5 inch) Diameter, Super Bialkali Photocathode, 8-stage, Head-On Type

GENERAL

Parameters		Ratings	Units
Spectral Response		300 to 650	nm
Peak Wavelength of Cathode Radiant Sensitivity		400	nm
Window	Material	Borosilicate glass	-
	Shape	Concave-Convex (R20)	-
Photocathode	Material	Super Bialkali	-
	Minimum Effective Area	30	mm dia.
Dynode Structure / Number of Stages		Linear Focused / 8	-
Base		JEDEC No.B12-43	-
Operating Ambient Temperature		-30 to +50	°C
Storage Temperature		-80 to +50	°C
Suitable Socket		E678-12A (option)	-

MAXIMUM RATINGS (Absolute Maximum Values)

Parameter		Maximum Ratings	Units
Supply Voltage	Between Anode and Cathode	1500	V
	Between Cathode and 1st Dynode	400	
	Between Anode and Last Dynode	250	
Average Anode Current		0.1	mA

CHARACTERISTICS (at 25 °C)

Parameters		Min.	Typ.	Max.	Unit
Cathode Sensitivity	Luminous (2856K)	-	100	-	μA/lm
Cathode Blue Sensitivity Index (Cs 5-58)		-	13.5	-	-
Radiant Sensitivity (at peak wavelength)		-	110	-	mA/W
Quantum Efficiency	at peak wavelength	32	35	-	%
	from 300nm to 450nm	25	-	-	
Collection Efficiency (at 400nm, simulation)**		-	95	-	%
1st Dynode Gain		6	10	-	-
Anode Sensitivity	Luminous (2856K)	-	4	-	A/lm
Gain		-	$4x10^4$	-	-
Single Photon counting Peak to Vally Ratio		1.8	2.5	-	-
Anode Dark Current (after 30min storage in the darkness)		-	5	20	nA
After Pulseing (threshold 4p.e. and Gain $4x10^4$ voltage)		-	0.02	-	%
Anode Pulse Rise Time**		-	2.6	-	ns
Anode Pulse Width (FWHM)**		-	-	3.5	ns
Electron Transit Time**		-	23	-	ns
Transit Time Spread (FWHM with single p.e.)**		-	-	2.0	ns
Pulse Linearity (+/-2% deviation)		15	20	-	mA
Life (50% drop in Gain)		200	-	-	C

NOTE : Anode characteristics are measured with a voltage distribution ratio and supply voltage shown below.

(** Collection Efficiency and Time response are defined with effective area of 30 mm in diameter.)

HAMAMATSU
HAMAMATSU PHOTONICS K.K. Electron Tube Division

TECHNICAL INFORMATION

TENTATIVE
Jul. 2012

VOLTAGE DIVIDER AND SUPPLY VOLTAGE

Electrodes	K	Dy1	Dy2	Dy3	Dy4	Dy5	Dy6	Dy7	Dy8	P
Ratio	350V(zener diode)	1	2	1	1	1	1	2	1	

Supply Voltage: 1000 V, K: Cathode, Dy: Dynode, P: Anode

DIMENSIONAL OUTLINE AND BASING DIAGRAM

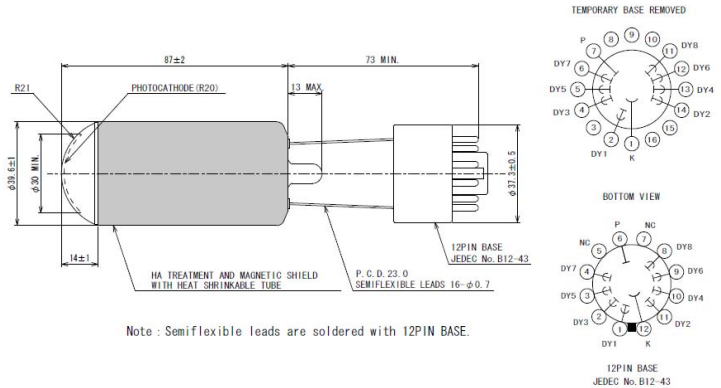

Figure 1: Dimensional Outline (Unit: mm)

This information is furnished for your Information only.
No warranty, expressed or implied, is created by furnishing this information.

NOTES

The material in the R11920-100-05 contains Copper-Beryllium (CuBe) Alloy. Please follow the applicable regulations regarding disposal of hazardous materials and industrial wastes in your country, state, region or province.

HAMAMATSU
HAMAMATSU PHOTONICS K.K. Electron Tube Division

A.2 Winston Cone Design

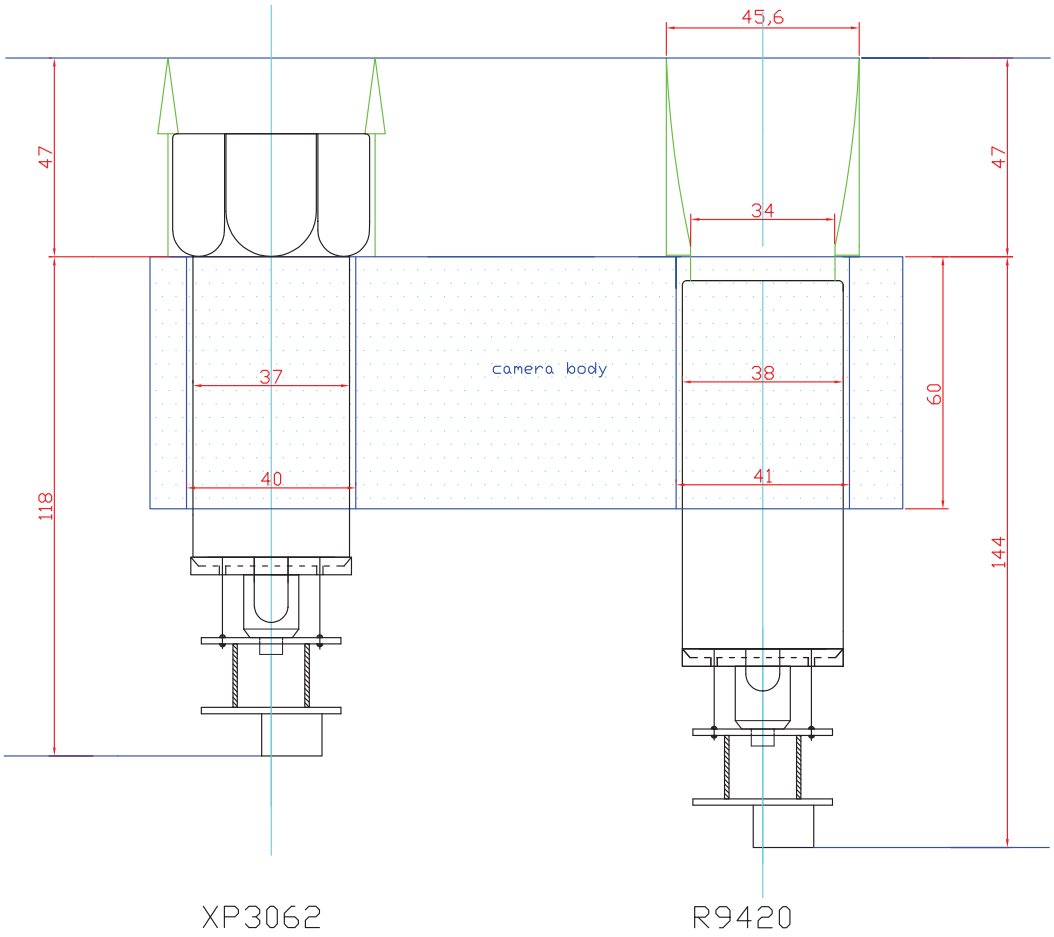

Figure A.1: Technical drawing of the PMT and reflector placement for the Photonis XP3062 with 'Mercedes stars' (left) and the Hamamatsu R9420-100 with Winston cone (right).

A.3 Gain Classes of the R9420-100

The photomultiplier of the Fluorescence Telescopes have only 10 HV supplies (20 in the HEAT telescopes) for 440 PMTs for each camera. Thus, PMTs are measured before instalment and classified into different gain classes to keep their response homogeneous. With the same setup used for the qualification tests for the Photonis XP3062 PMTs [69, 70], about 520 Hamamatsu R9420-100 PMTs were tested as well [62]. With a 'Gain vs High Voltage' (GHV) test, the correlation between the PMTs gain and the supply voltage, which is individual for each PMT, was determined and in combination with four reference PMTs with known gain the supply voltage for a gain of 2×10^5 is determined. With the narrow distribution and that few PMTs, the gain classes were specifically defined fitting 22 PMTs each, matching the total PMTs per power supply in the HEAT cameras.

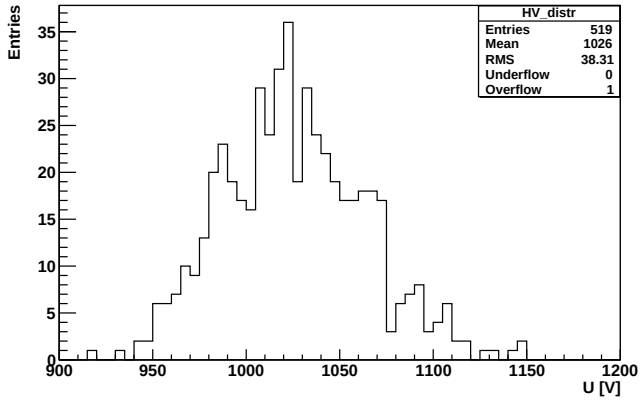

Figure A.2: High voltage distribution of the Hamamatsu R9420-100 for a gain of 2×10^5 from [62].

Gain Class	HV [V]	Gain Class	HV [V]	Gain Class	HV [V]	Gain Class	HV [V]
A	954	F	1000	K	1023	P	1049
B	971	G	1006	L	1027	Q	1056
C	981	H	1011	M	1032	R	1062
D	987	I	1015	N	1038	S	1070
E	993	J	1019	O	1043	T	1083

Table A.1: Gain classes and their respective mean high voltage values of the 520 Hamamatsu R9420-100 PMTs for a gain of 2×10^5.

For the installation in the FD camera the gain was calculated for a gain of 5×10^4 via

$$G = \frac{K \cdot (\mathrm{HV})^{\alpha}}{c}, \tag{A.1}$$

with K and α obtained from the GHV measurements and c combining constants for the specific experimental setup [70].

A.4 Correction Factor for Calibration A Comparison

The last calibration A with a fully equipped camera in bay 6 was taken on the 30.06.2009. Afterwards, about half of the sensors were used to instrument the new HEAT cameras. To test more efficient PMTs in the FD environment, these empty slots were used, running in parallel to the normal observation. Due to a time-dependent drift in the CalA response, a direct comparison of the new PMTs with the data from 2009 is not meaningful. In order to compare the different sensors and to determine the gain in efficiency, a reference group of the remaining PMTs was introduced. To account for similar sky coverage and for symmetry reasons a reference set of 48 PMTs, point-symmetrical to the centre of the camera, was chosen.

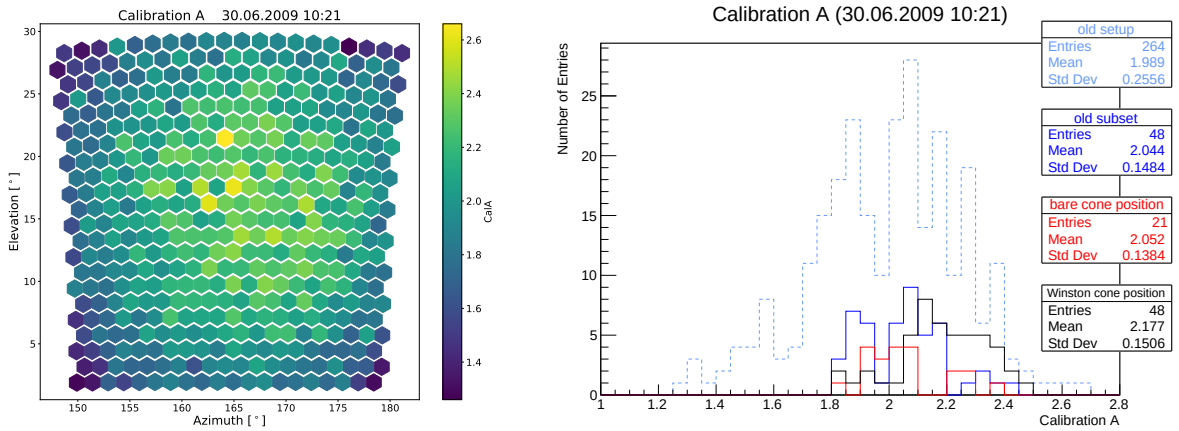

Figure A.3: Last calibration A from 30.06.2009 at 10:21 with the whole camera equipped with Photonis XP3062 PMTs. Left side shows the camera response in sky view of Los Leones bay6. Response of different subgroups on the right, with the positions the new cones replaced in black and the mirrored subgroup of the old setup in solid blue.

Figure A.3 shows the CalA data of the last full equipped camera. On the right side the data for each pixel is displayed in sky view and the left side shows the grouped data similar to Section 4.4.2.1. As can be deduced by the camera plot and inferred from the histograms that the alignment of the CalA light source is not exactly centred, with the mean CalA of the reference group is only 2.044 and the same sensor type at the Winston cone position measuring 2.177. This is consolidated by looking at the CalA data for a whole year. In Fig. A.4 the ratio of the mean CalA for the reference set and the Winston cone positions is shown for the period from 01.07.2008 to 30.06.2009. The correction to apply for the comparison of the new positions to the reference group is 0.94 with the assumption that the alignment of the CalA light source did not change since 2009.

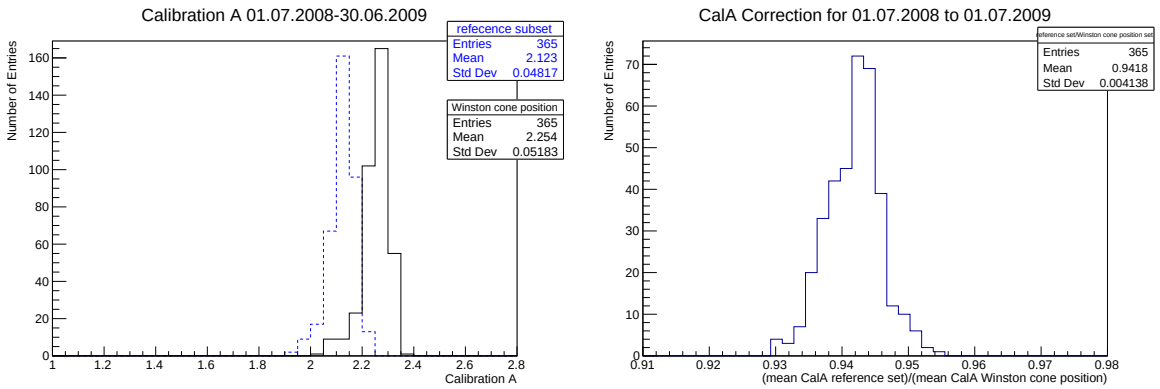

Figure A.4: Correction factor for the PMT comparison to account for the asymmetrical camera illumination of the CalA light source.

A.5 Calibration B & C

Up until 2018 the two relative calibrations B (CalB) and C (CalC) were performed on a regular basis, once at the end of each measurement night. Intended to identify the optical components responsible for possible variations in the telescopes response, the calibrations are installed in different placed than calibration A.

A.5.1 Calibration B

CalB is placed on the side of the camera frame, next to the PMTs, and is directed at the spherical mirror. Its light source is a xenon flash lamp, which is situated in a calibration room and the light is distributed via optical fibres to the telescope bays. In combination with a filter wheel plus five different neutral density filters, CalB is performing a linearity measurement. The used filters settings have a transmission of about 100%, 50%, 10%, 5%, and 1% for all wavelengths. The measured response to a single shot of CalB is shown in the EventDisplay in Fig. A.5.

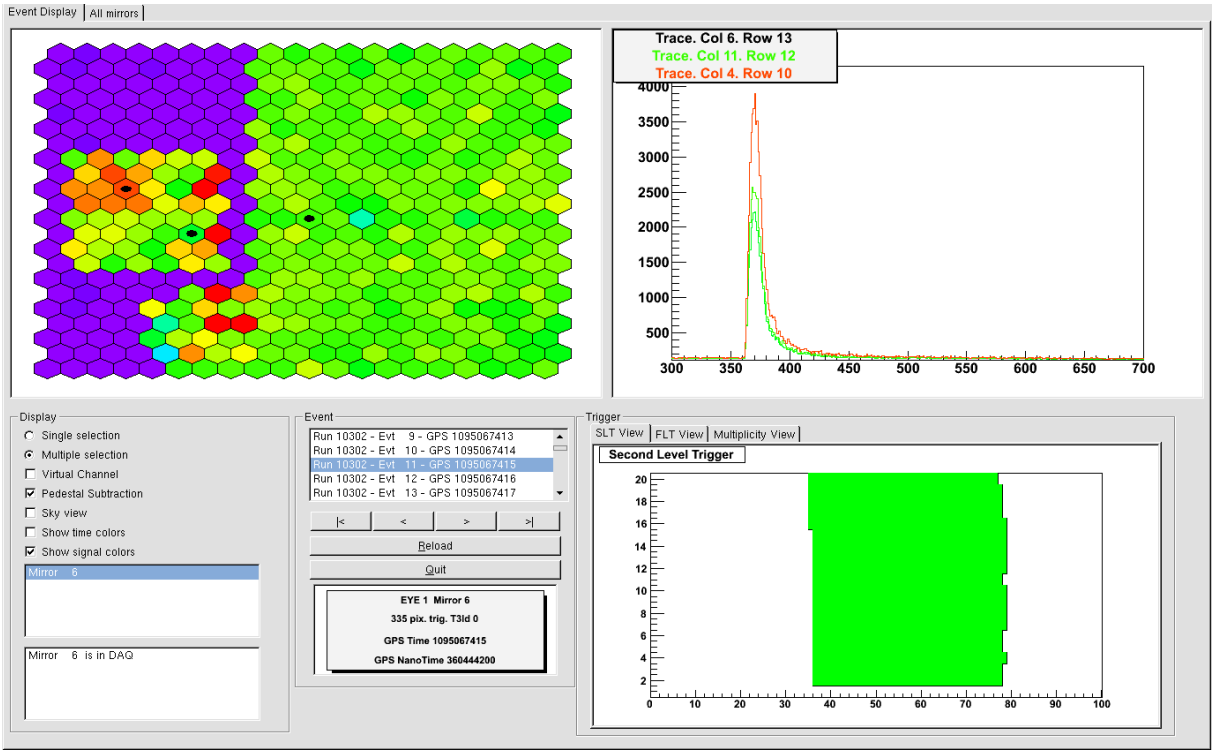

Figure A.5: Calibration B response of bay 6 in Los Leones. New PMTs (left side, camera view) show an increased response while running at the same gain as the other PMTs.

CalB values are stored on the monitoring server. The respective mean of the five CalB values for the Winston cone position is between 13.3% ± 0.5 and 14% ± 0.4 higher than the reference set in 2015 (see Fig. A.6, left). This corresponds to the result from CalA (Section 4.4.2.1), but although a diffuser is used at the fibres exit the camera is not homogeneously illuminated by the reflection of the mirror. As it was not clear from the documentation, how to obtain the linearity plot in [122] from the monitoring data, the CalB values were normalised to the first entry for a comparison of the two different PMTs (Fig. A.6, right). The differences are negligible.

A.5.2 Calibration C

Calibration C is positioned at the telescope's aperture, directed outwards. The light of a xenon flash lamp is reflected from the backside of the closed shutter door, which is covered with

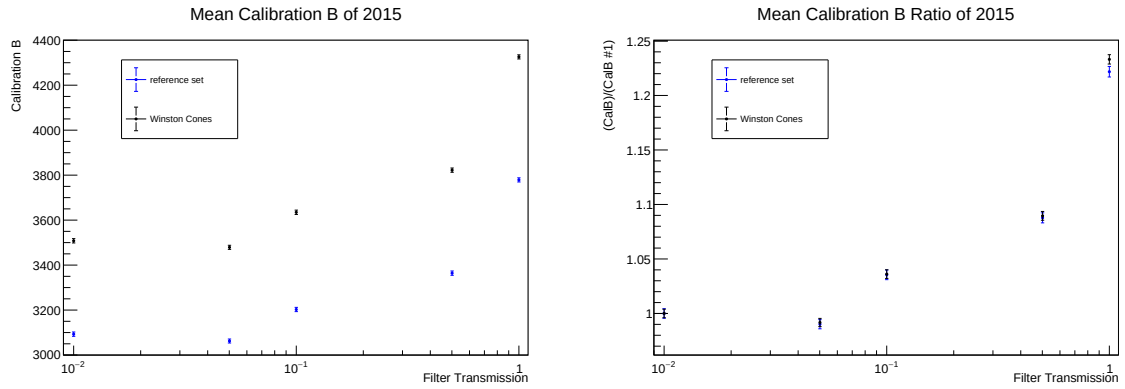

Figure A.6: Mean calibration B entries from the monitoring server for the Winston cone position (black) and the reference set (blue) from 2015 (left) and the ratio to filter setting #1 (right).

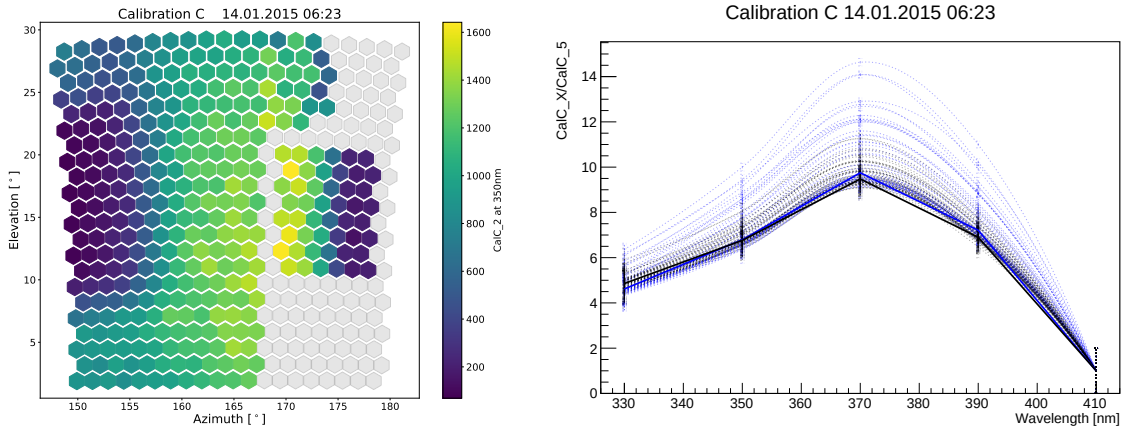

Figure A.7: Calibration C from 14.01.2015 at 06:23. Left side shows the camera response in sky view of Los Leones bay 6 with the new PMTs installed in the right half. On the right side, the relative response to the different wavelength filters is shown for the new PMTs plus Winston cones in black and a reference subgroup of the XP3062 in blue. Single pixels (dashed lines) and the mean (solid lines) are displayed, normalised to the signal at 410 nm.

reflective Tyvek foil. Five different interference filters, centred at wavelengths 330 nm, 350 nm, 370 nm, 390 nm and 410 nm, are covering the spectral acceptance of the telescope with the intend to spot wavelength dependent changes of the different telescope components. As calibration B, the calibration C was discontinued in 2018. A sample CalC measurement from 14.01.2015 is displayed in Fig. A.7. As can be seen on the left side, the illumination of the camera is not homogeneous at all which makes a direct comparison of the different PMTs in terms of efficiency gain rather difficult. But the spectral response can be investigated. On the right side, the obtained CalC values for the PMTs plus Winston cones (black) and the reference set (blue), normalised to the value at 410 nm, are shown. Both PMTs show an expected similar behaviour, as the measurement of the quantum efficiency in Section 4.2.1 already showed a similar but scaled response with respect to the wavelength in the range of interest. Indicated by the dashed lines for single pixels and the solid lines for the mean values, the spread for the new PMTs is smaller.

Appendix B

SSD

B.1 Single Photon Measurement

In order to determine the absolute gain of the first batch of PMTs to be used in the SSD engineering array, a calibration via the single photon peak was performed. For this purpose, a picosecond diode laser with a wavelength of 405 nm [123] was used with a pulse rate of 5 kHz. In combination with a neutral density filter, the light was attenuated to a signal to noise ratio of about 1 to 10, to ensure measuring the single photon peak within a sample time of 100 s. Due to the small signals of the R9420 with an expected gain of the order of 10^5 at a supply voltage of 1300 V, the single photon measurements were performed with a sensitive DAQ designed for the CBM experiment [124]. With a new readout chip, the n-XYTER, an ASIC was developed for high rate multi-channel neutron counting at GSI in Darmstadt [125].

Calibration of the n-XYTER

With the n-XYTER chip being too sensitive for the single photon signals, an additional attenuator board was used with different channels to be able to test the linearity of the PMTs from single photons up to about 10^6 photons. To extend the limited range of the n-XYTER with the needed precision, different attenuator channels were modified to be used with the R9420 PMT and fitting the expected signal. For the conversion from ADC counts to charge, the attenuator board was calibrated using a high-resistive current source. Well defined rectangular pulses with known width and amplitude were used with a 10 kΩ resistor to obtain a conversion for each channel (example shown in Fig. B.1).

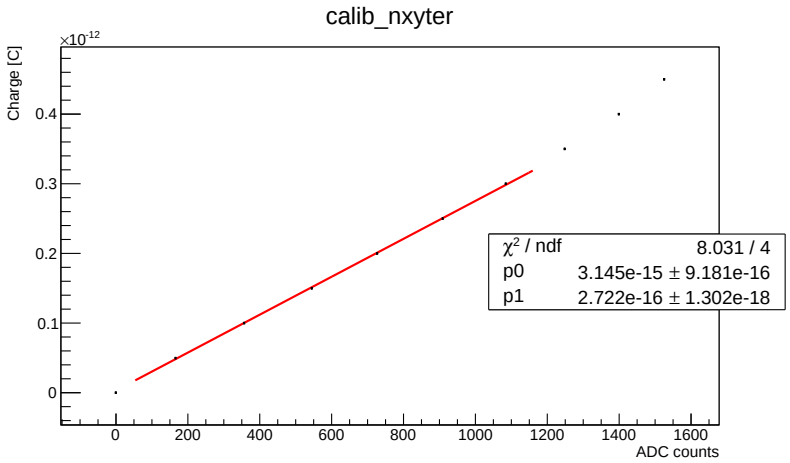

Figure B.1: Calibration measurement of one attenuator channel with the n-XYTER for the ADC counts to charge conversion.

R9420 Single Photon Measurements

The single photon peaks were measured for the first batch of PMTs to be used in the SSD EA at 1100 V, 1300 V, and 1500 V respectively. An example is presented in Fig. B.2. With the exact gain and an additional charge versus supply voltage measurement, the gain for a specific HV (or vice versa) can be calculated.

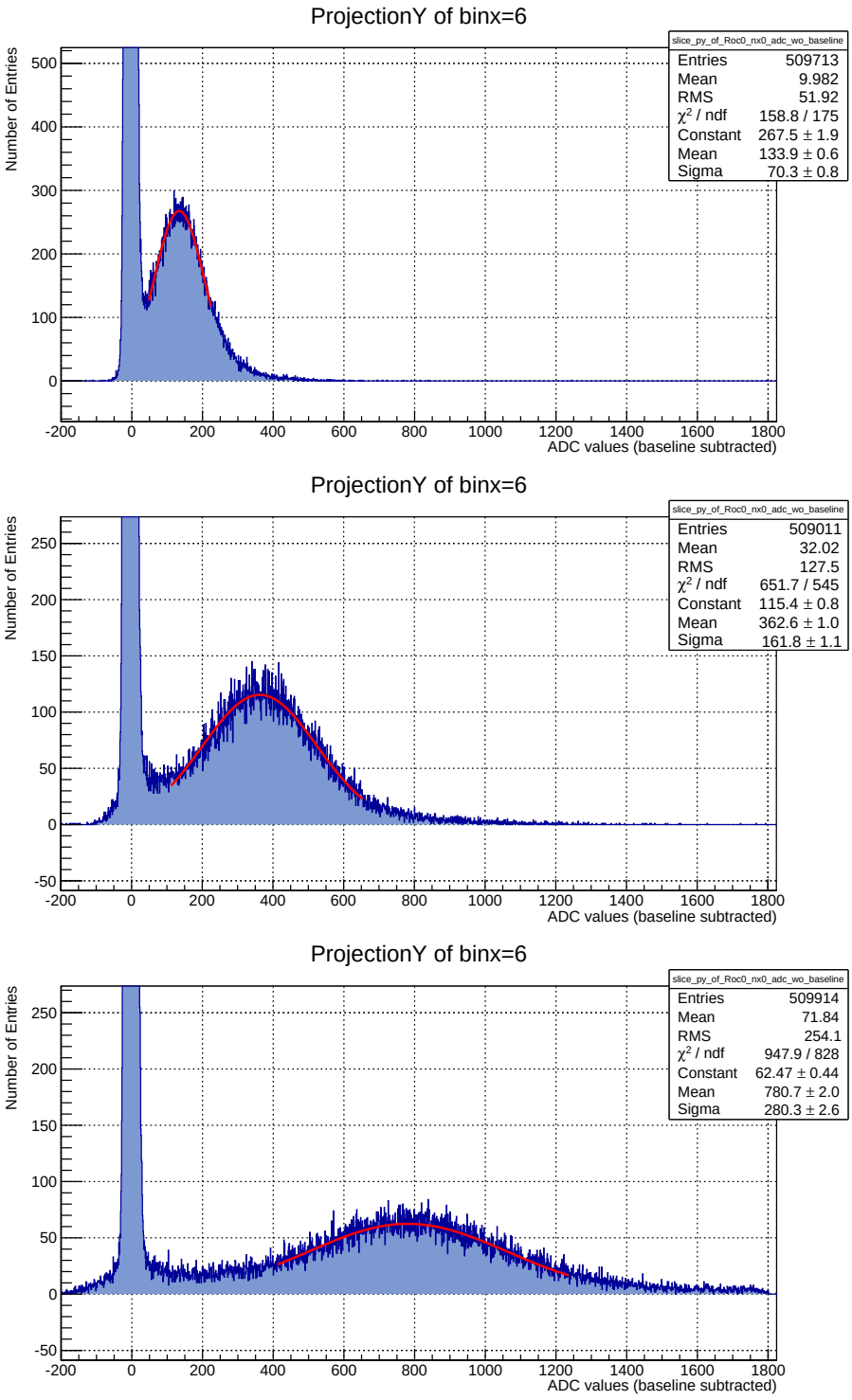

Figure B.2: Single photon peak measurements for a supply voltage of 1100 V, 1300 V, and 1500 V for a R9420 PMT.

B.2 SSD Linearity Measurement

The linearity for the SSD PMTs was measured using a modified setup of the FD classification test [70, 69]. Here, the linearity is measured in pulsed mode and a light source is attenuated by calibrated neutral density filters. The charge (Q) is measured for different transmission settings (T) and a linear fit is applied to the data,

$$Q = p1 \cdot T + p0. \tag{B.1}$$

Since the break from linear behaviour is expected for the large signals, the fit is limited up to 10% transmission. For the charge measurement the non-linearity (NL) for each transmission (T) is calculated:

$$\mathrm{NL}(T) = \frac{Q_{\mathrm{meas.}}(T)}{p1 \cdot T + p0}. \tag{B.2}$$

The neutral density filters have a transmission of 30%, 10%, 1%, 0.1%. To extend the measurement range, different combinations of those filters are used, covering a dynamic range in the order of 10^6. The light source is a blue high power LED with a wavelength of 470 nm. In order to fine scan the break from linearity, the light source intensity was adjusted as well. This is done by altering the driver voltage of the LED pulse between 8 V and 16 V in steps of 2 V. Since the LED light output is not linear to the applied pulsed voltage, the linearity fit is done for every LED power setting separately. The PMT signal was recorded using a VME crate with a Struck SIS3300 FADC card [126] with 100 MHz and 12 bit (1 mV) amplitude resolution. With a maximum of 2 V input signal, a 12db attenuator was used to match the largest PMT signals to the recording ADC range.

Figure B.3 shows the linearity measurement for the Hamamatsu R9420 and the Electron Tubes 9902KB, with the upper plots showing the measured charge for different filter settings and the applied fits. The lower plots show the deviation from the linear fit, colour-coded the different LED driver voltages. The R9420 was measured at 900 V, with a gain of 8.4×10^4 and the the 9902KB was measured at 800 V with a gain of 2.7×10^5. The gain was measured at the Lecce test facility [102]. The linearity of the 9902KB was measured in a different setup using the two LED technique [127]. Here the signal of two LEDs is measured separately and simultaneously. The measurement is in consistence with the filter measurement and shows a deviation from linearity at about 60 mA.

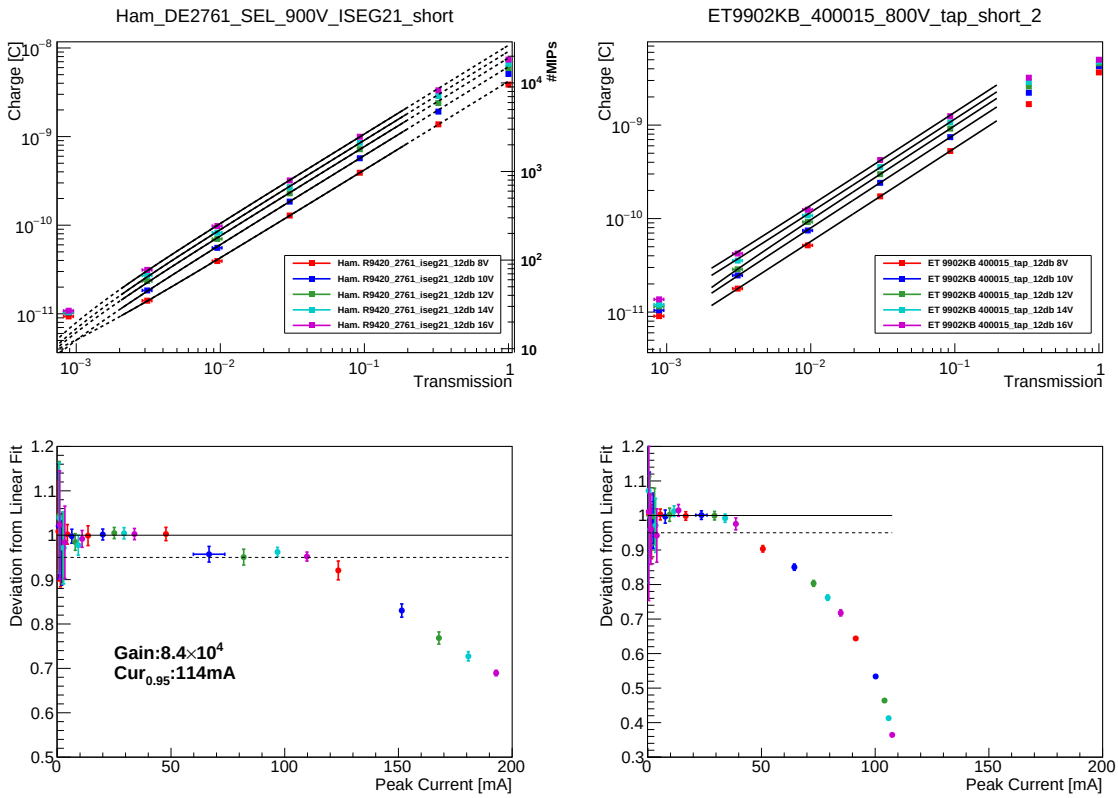

Figure B.3: Linearity measurement for the Hamamatsu R9420 and the Electron Tubes 9902KB. The upper plots show the measured charge for different calibrated neutral density filter settings with the applied fit from Eq. (B.1). The lower plots show the deviation from the linear fit

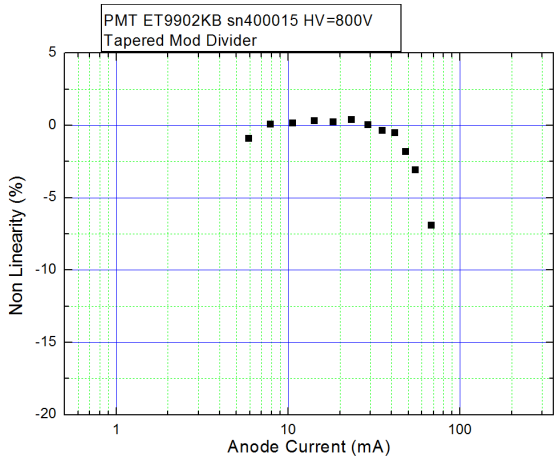

Figure B.4: Linearity measurement for the Electron Tubes 9902KB at 800 V with the double LED method [102].

B.3 ISEG Base Modifications

The ISEG base was customly made for the purpose of being used in the SSD. The dimensions were given by the possible space inside the plastic tube, where the PMT is sitting in. In alignment with the FD use of the same type of PMT, the fixation of the active base to the PMT was enhanced by a plastic spacer, to provide a stress relief towards the PMTs pins. The connection between spacer and base is done by having a small hole in the middle of the voltage divider PCB. As will be discussed in Appendix B.3, the limited space on the 'voltage divider' PCB for revision 1 and 2 induces some minor additional noise. The limited space was caused by the originally made requirement of leaving a hole in the centre of the PCB in order to ease the fixation of the PCB during soldering to the PMT. Moreover, revision 1 was designed for much larger average anode currents than expected for the operation in the SSD. Revision 2 relaxes the overpowered generator by removing a diode in the last stage of the multiplier chain. Moreover, it introduces two thin copper plates to the voltage divider PCB to serve as electromagnetic shielding of the signal decoupling capacitor (see Fig. B.5). Currently, revision 3 is produced by ISEG. It will eliminate the hole in the centre of the PCB to allow for an optimised routing and thereby better shielding of the signal lines by construction and it will also add a current monitor. This new version will be delivered by mid February 2017 for lab and field tests.

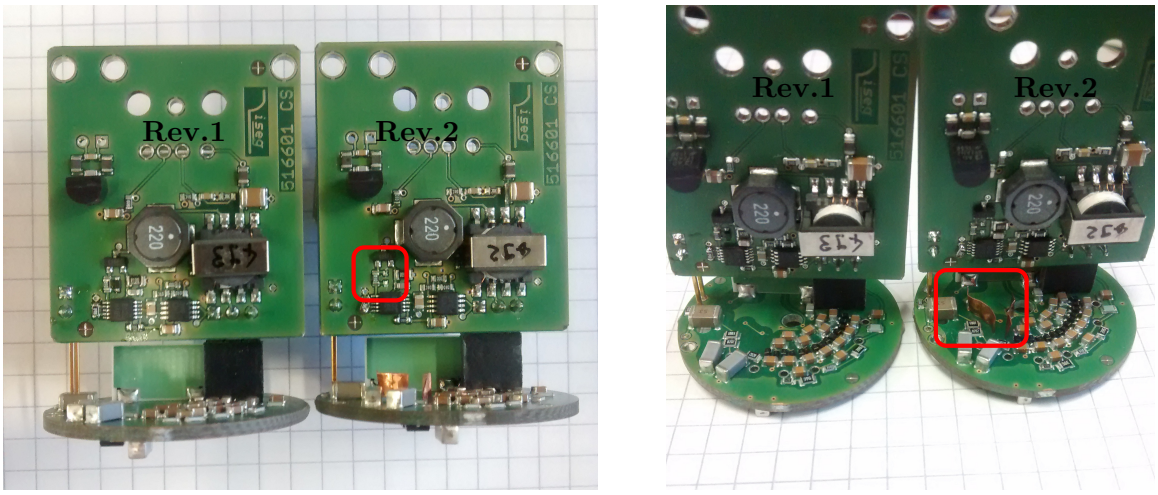

Figure B.5: ISEG revision2 modifications to reduce the noise level. Revision 2 has a diode removed to reduce power of the Cockroft-Walton generator (left) and has two additional copper plates introduced to shield the decoupling capacitor of the signal output (right).

Noise

The noise measurement with the UUB as in Section 5.3.2.5 shows the noise was reduced from revision 1 to 2. By reducing the power of the Cockroft-Walton generator and introducing two small copper shield to the decoupling capacitors, the noise level of the ISEG base rev. 2 could achieve the same noise level as the CAEN base.

UUB baseline	2.524 ± 0.166		
	0V	900V	1500V
ISEG Rev.1	2.475 ± 0.247	3.049 ± 0.187	3.424 ± 0.184
ISEG Rev.2	2.458 ± 0.209	2.496 ± 0.224	2.573 ± 0.220

Table B.1: UUB noise measurement (all numbers are in units of ADC channels).

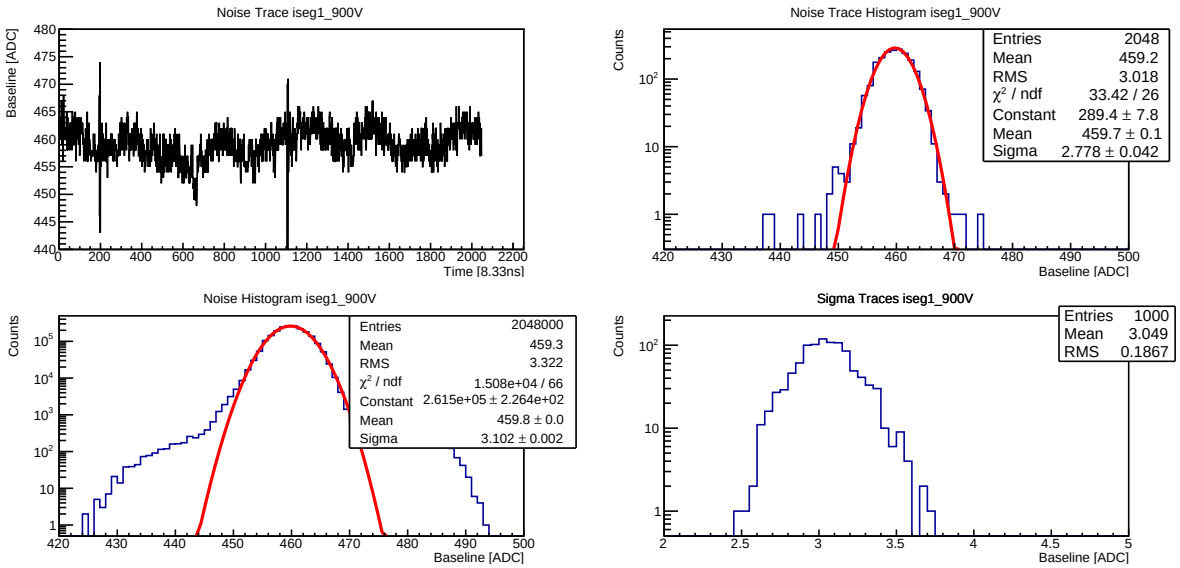

Figure B.6: UUB noise measurement of a PMT with ISEG Rev.1 base. Upper left shows one sample trace. A Gaussian distribution is fitted to the profile (upper right) to determine an estimate of the traces noise level. Bottom right shows the single trace sigma distribution for 1000 traces. Bottom left shows the combined profile of all these traces.

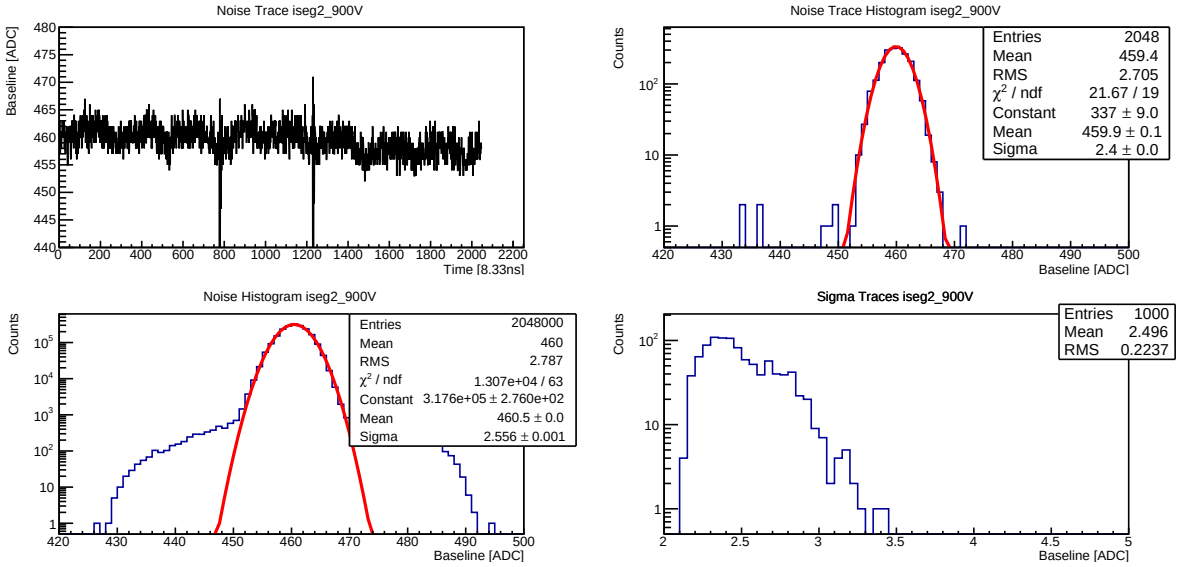

Figure B.7: UUB noise measurement of a PMT with ISEG Rev.2 base. Upper left shows one sample trace. A Gaussian distribution is fitted to the profile (upper right) to determine an estimate of the traces noise level. Bottom right shows the single trace sigma distribution for 1000 traces. Bottom left shows the combined profile of all these traces.

B.4 PMT Base Temperature Test

A temperature test of the ISEG base and the CAEN module with a passive voltage divider was also performed without an attached PMT in a climate chamber. The temperature is cycled between −20 °C and 70 °C, with a rise and fall time of 60 min. The high voltage is set to the maximum rating for the ISEG base (about 1500 V) and to 1500 V for the CAEN module, which is the maximum voltage for the R9420 PMT. The HV is set and monitored via an UUB, which is kept at room temperature outside the climate chamber. For the CAEN module the bleeder current is monitored as well, while for the used ISEG base (Rev. 2) the current monitor was missing. The temperature is measured with the dedicated sensors of the SSD engineering array's PMT module, which is installed on the ISEG base and is a separate sensor for the CAEN module.

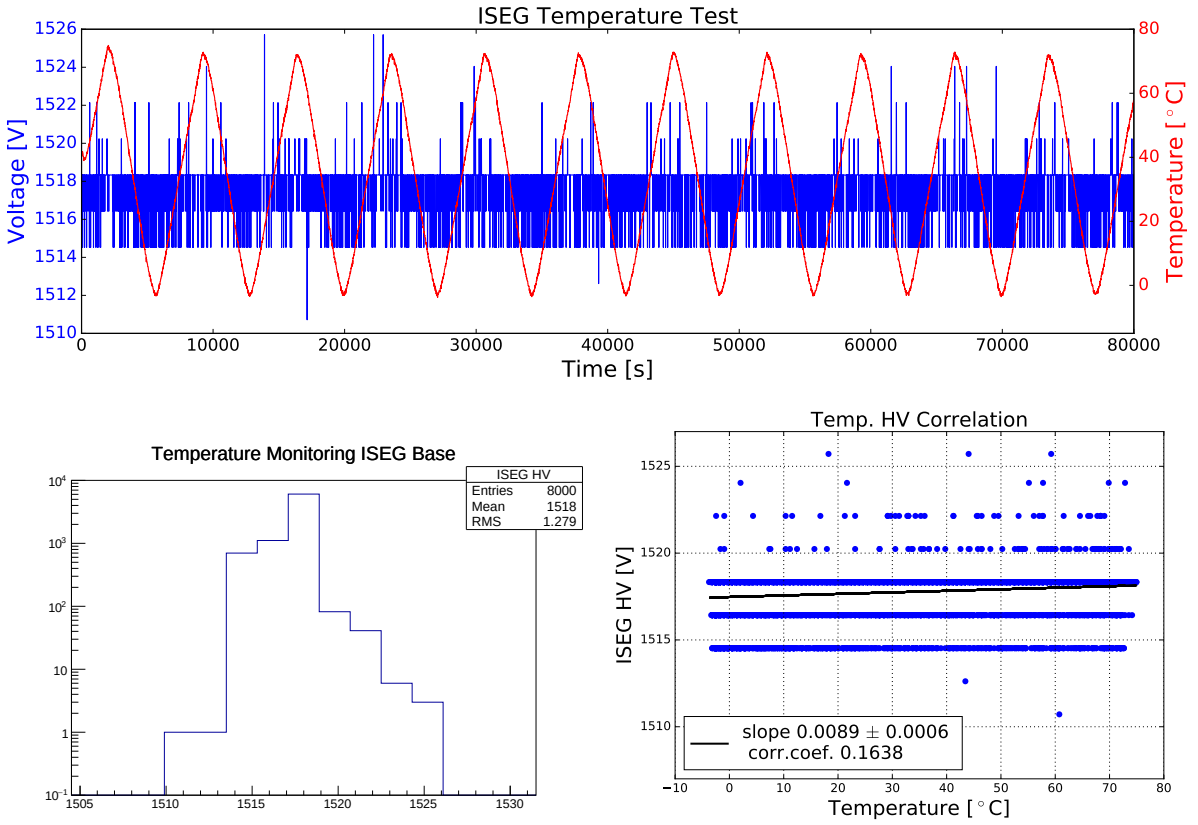

Figure B.8: Temperature test of the ISEG base without PMT. Temperature cycle from −10 °C to 70 °C. HV monitoring with an UUB at room temperature.

In Fig. B.8 the monitored HV is shown for the ISEG base, which is mainly distributed around 1518 V with an RMS of 1.28 V. Figure B.9 shows the same measurement for the CAEN module, with a mean of 1501 V and an RMS of 1.00 V. For the bulk of both measurements, the values are distribute within a 5 bit range of the corresponding ADC which is used to monitor the HV.

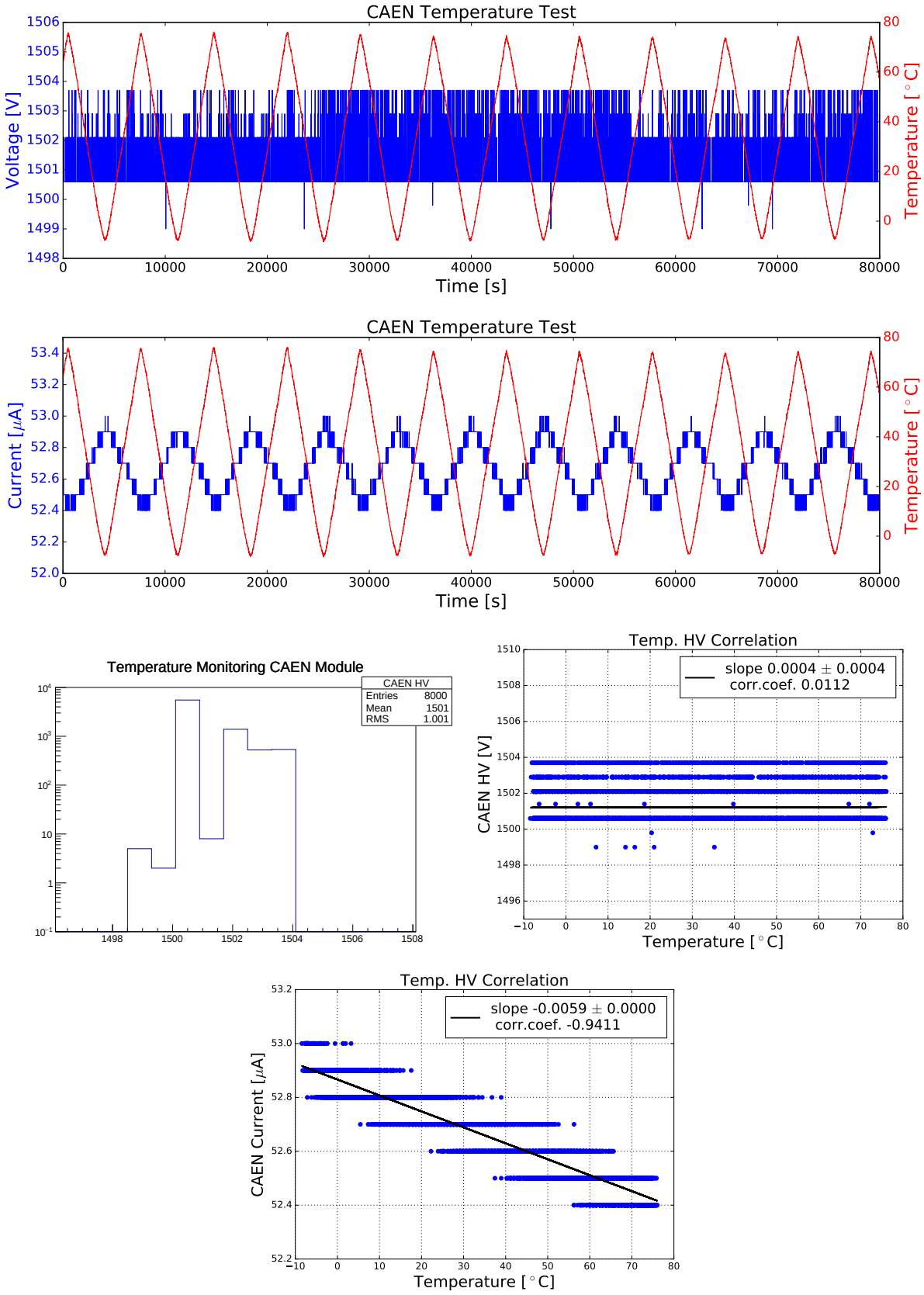

Figure B.9: Temperature test of the CAEN module and passive base without PMT. Temperature cycle from −10 °C to 70 °C. HV- and bleeder current monitoring with an UUB at room temperature.

B.5 SSD EA PMT Test Results

For the PMTs to be used in the SSD engineering array, the absolute gain was measured at a supply voltage of 1300 V. In addition, a gain versus high voltage measurement was performed for each PMT (see for example in Fig. 5.16) and the gain to expect at 900 V calculated. Later it can be used to determine the individual supply voltage of the PMTs to be used at a specific gain, depending on the performance of the self calibration with atmospheric muons.

Detector*	PMT type*	PMT SN*	Station name	Gain@1300 V	Gain@900 V	N_{pe}/MIP*
SSD EA 01	CAEN	DE2757	Pichi Peni Hue	$6.357E+5$	$8.814E+4$	31.1
SSD EA 02	CAEN	DE2786	Diddi	$6.671E+5$	$9.373E+4$	29.1
SSD EA 03	ISEG	DE3184	Le Qui Don	$864484^{\dagger}$	$1.227E+5$	30.0
SSD EA 04	ISEG	DE3179	Jaco	$868463^{\dagger}$	$1.232E+5$	32.2
SSD EA 05	CAEN	DE2778	Granada	$6.032E+5$	$8.413E+4$	31.8
SSD EA 06	CAEN	DE2769	Ruca Malen	$5.750E+5$	$7.999E+4$	29.5
SSD EA 07	CAEN	DE2775	Trak	$8.486E+5$	$1.136E+5$	30.5
SSD EA 08	CAEN	DE2765	Clais	$5.213E+5$	$7.231E+4$	30.8
SSD EA 09	SiPM	-	Svenja			24.3
SSD EA 10	SiPM	-	Cristian			25.4
SSD EA 11	CAEN	DE2767	Nuria	$6.234E+5$	$8.571E+4$	29.9
SSD EA 12	SiPM	-	Peteroa			24.8

Table B.2: SSD PMT voltages from the absolute gain measurement at 1300 V and the GHV measurements. *Information from [98],† estimated from PMT's data sheet of correlation between anode luminous sensitivity and gain.

B.6 SSD Afterpulse

As the afterpulse was more prominent in the Hamamatsu R9420-100 than in the currently used FD PMT (see Section 4.2.4), it is checked for the standard bialkali version used in the SSD as well. For the afterpulse check, the signal from the linearity measurement at 10% filter transmission is used, being a rather large signal but not saturating the electron multiplier of the PMT. The pulse width is 50 ns and the pulse height about 2 V. In Figs. B.10 and B.11 the signal is shown for the Hamamatsu R9420 and the Electron Tubes 9902KB, respectively. Both PMTs show similar pulse heights. The afterpulse is defined as the ratio of charge 2 μs after the initial signal region and the measured signal of the LED pulse. The R9420 afterpulse is at 1.0%, while for the 9902KB the charge after the signal is about 1.6%. While both PMTs are not as low as the Photonis XP3062, they are well below the super-bialkali version, the R9420-100.

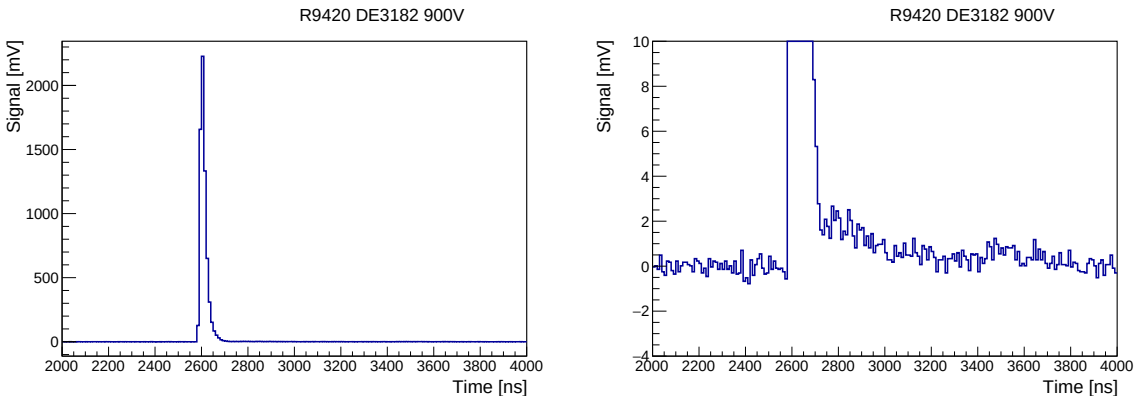

Figure B.10: PMT signal of the Hamamatsu R9420 from the linearity measurement at 10% transmission, averaged over 1000 pulses.

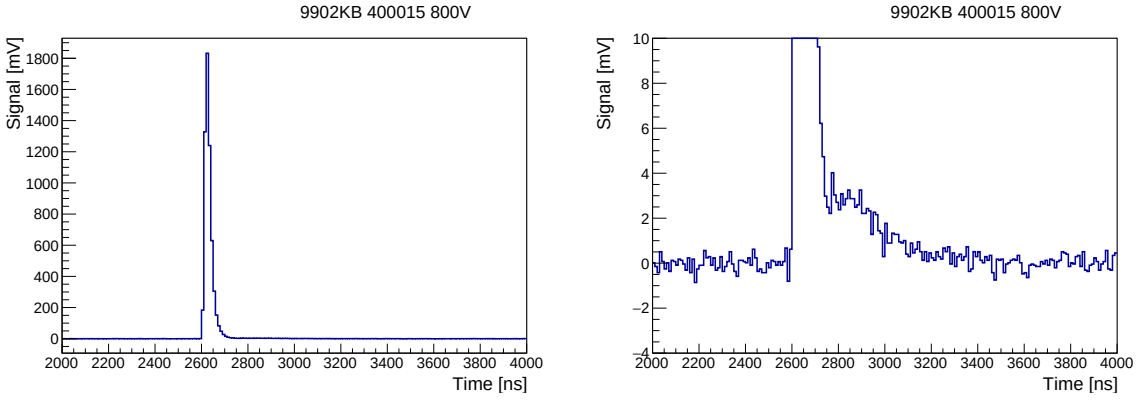

Figure B.11: PMT signal of the Electron Tubes 9902KB from the linearity measurement at 10% transmission, averaged over 1000 pulses.

B.7 SSD PMT Oscilloscope Noise Measurement

The noise measurement performed with the UUB and reported in Section 5.3.2.5 were independently verified also with an oscilloscope. In the same setup as described in Section 5.3.2.5, the signal cable was attached to the scope outside the metal box. A black cover was placed in front of the PMT window so that only cosmic muons hitting the photocathode or a dynode could cause a trigger, which was set for this measurement at a threshold of $-1\,\mathrm{mV}$. The bandwidth of the scope was limited to 200 MHz and an additional 100 MHz digital filter was used to provide comparable conditions as with the UUB which employs 120 MHz FADCs and 60 MHz anti-aliasing filtering.

Figure B.12 presents the noise measurement for the passive base with CAEN HV-module. In the top left one sample trace of 100 triggered signals is shown. The average pulse height is about 2 mV with a width $< 12\,\mathrm{ns}$. The total time per trace is 400 ns. The upper right plot shows the profile of the sample trace while the cumulative profile of 100 traces is shown in the bottom left. A Gaussian distribution is fitted in the range of $-1\,\mathrm{mV}$ to $+1\,\mathrm{mV}$ to get an estimate of the noise level. The sigma distribution for all 100 individual traces is plotted in the bottom right, with a mean spread of 0.047 mV. As can be seen from the trace, the noise fluctuations are in the single bin precision of the oscilloscope.

The same measurement is shown in Fig. B.13 for a PMT with an ISEG base. With a mean spread of 0.046 mV, there is no difference to the passive base within the oscilloscopes resolution.

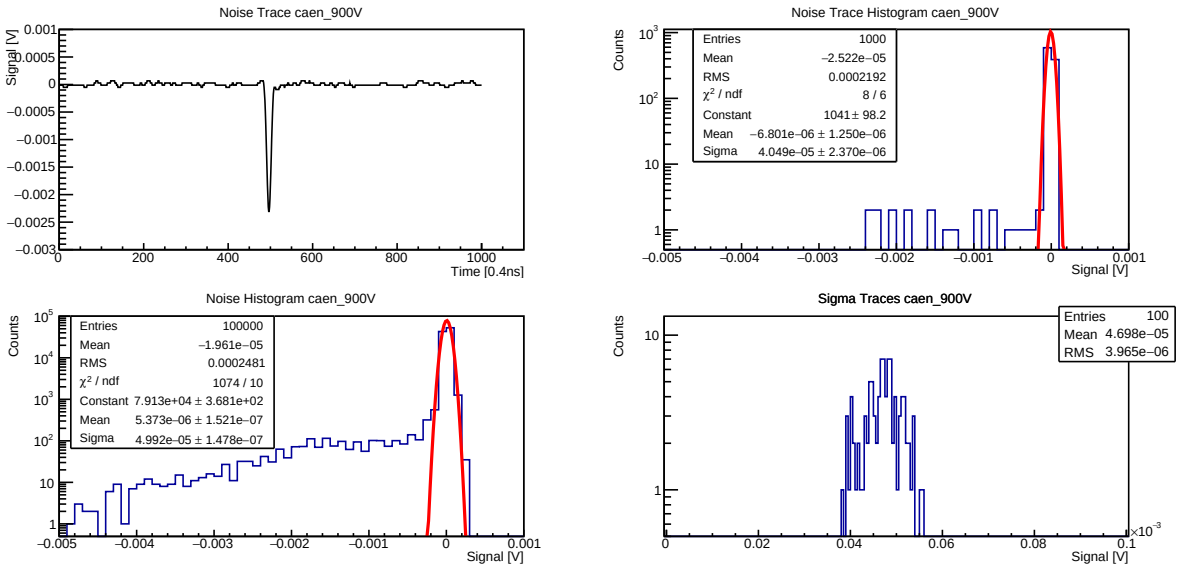

Figure B.12: Noise of the CAEN module and PMT with passive voltage divider measured with a scope. Upper left shows one sample trace. A Gaussian distribution is fitted to the profile (upper right) to determine an estimate of the traces noise level. Bottom right shows the single trace sigma distribution for 1000 traces. Bottom left shows the combined profile of all these traces.

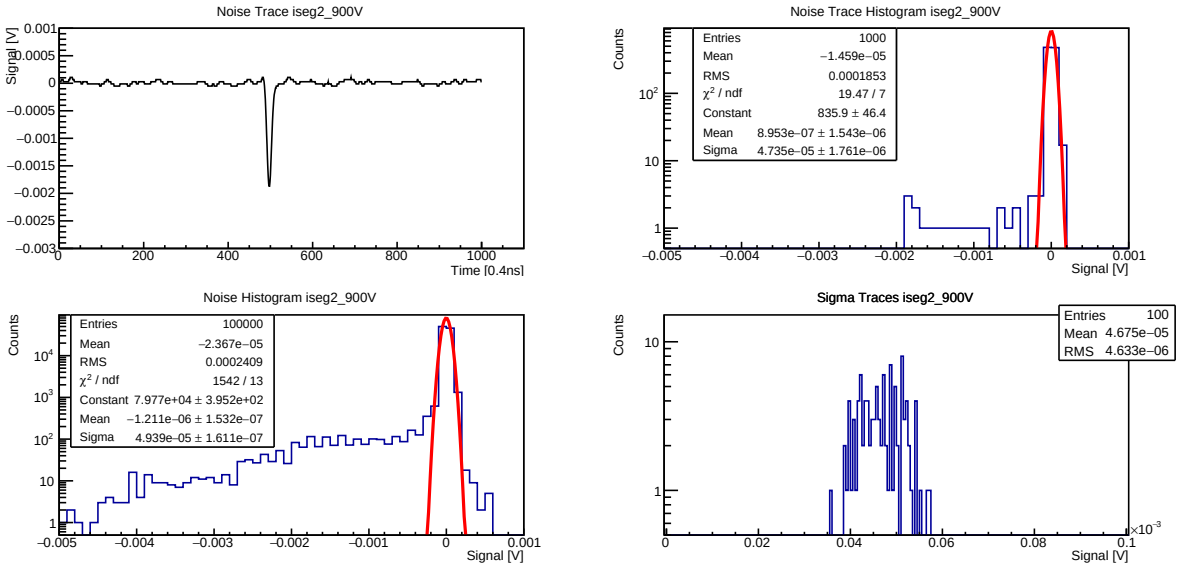

Figure B.13: Noise of a PMT with ISEG Rev.2 base measured with a scope. Upper left shows one sample trace. A Gaussian distribution is fitted to the profile (upper right) to determine an estimate of the traces noise level. Bottom right shows the single trace sigma distribution for 1000 traces. Bottom left shows the combined profile of all these traces.

Bibliography

[1] T. Wulf, "Beobachtungen über die Strahlung hoher Durchdringungsfähigkeit auf dem Eifelturm," *Phys. Z.* **11** (1910) 811–813.

[2] V. F. Hess, "Über Beobachtungen der durchdringenden Strahlung bei sieben Freiballonfahrten," *Phys. Z.* **13** (1912) 1084–1091.

[3] T. K. Gaisser, R. Engel, and E. Resconi, *Cosmic Rays and Particle Physics*. Cambridge University Press, 2 ed., 2016.

[4] P. Bhattacharjee and G. Sigl, "Origin and propagation of extremely high-energy cosmic rays," *Phys. Rept.* **327** (2000) 109–247, arXiv:astro-ph/9811011.

[5] **Particle Data Group** Collaboration, P. A. Zyla *et al.*, "Review of Particle Physics," *PTEP* **2020** no. 8, (2020) 083C01.

[6] G. V. Kulikov and G. B. Khristiansen, "On the Size Spectrum of Extensive Air Showers," *J. Exp. Theor. Phys.* **35** no. 3, (1958) 635–640.

[7] **Pierre Auger** Collaboration, P. Abreu *et al.*, "The energy spectrum of cosmic rays beyond the turn-down around 10^{17} eV as measured with the surface detector of the Pierre Auger Observatory," *Eur. Phys. J. C* **81** no. 11, (2021) 966, arXiv:2109.13400 [astro-ph.HE].

[8] K. Greisen, "End to the cosmic ray spectrum?," *Phys. Rev. Lett.* **16** (1966) 748–750.

[9] G. T. Zatsepin and V. A. Kuzmin, "Upper limit of the spectrum of cosmic rays," *JETP Lett.* **4** (1966) 78–80.

[10] F. W. Stecker and M. H. Salamon, "Photodisintegration of ultrahigh-energy cosmic rays: A New determination," *Astrophys. J.* **512** (1999) 521–526, arXiv:astro-ph/9808110.

[11] L. N. Epele and E. Roulet, "Comment on 'on the origin of the highest energy cosmic rays'," *Phys. Rev. Lett.* **81** (1998) 3295, arXiv:astro-ph/9806251.

[12] **AMS 02** Collaboration, R. Battiston, "The antimatter spectrometer (AMS-02): A particle physics detector in space," *Nucl. Instrum. Meth. A* **588** (2008) 227–234.

[13] J. Matthews, "A Heitler model of extensive air showers," *Astropart. Phys.* **22** (2005) 387–397.

[14] A. Haungs *et al.*, "The KASCADE Cosmic-ray Data Centre KCDC: Granting Open Access to Astroparticle Physics Research Data," *Eur. Phys. J. C* **78** no. 9, (2018) 741, arXiv:1806.05493 [astro-ph.IM].

[15] T. K. Gaisser and A. M. Hillas, "Reliability of the Method of Constant Intensity Cuts for Reconstructing the Average Development of Vertical Showers," in *International Cosmic Ray Conference*, vol. 8 of *International Cosmic Ray Conference*, p. 353. Jan., 1977.

[16] **Pierre Auger** Collaboration, A. Aab *et al.*, "The Pierre Auger Cosmic Ray Observatory," *Nucl. Instrum. Meth.* **A798** (2015) 172–213, arXiv:1502.01323 [astro-ph.IM].

[17] **Telescope Array** Collaboration, H. Kawai *et al.*, "Telescope array experiment," *Nucl. Phys. B Proc. Suppl.* **175-176** (2008) 221–226.

[18] **LHAASO** Collaboration, A. Addazi *et al.*, "The Large High Altitude Air Shower Observatory (LHAASO) Science Book (2021 Edition)," *Chin. Phys. C* **46** (2022) 035001–035007, arXiv:1905.02773 [astro-ph.HE].

[19] A. Haungs, "Ultra-High Energy Cosmic Rays: A Recap of the Discussions at the European Cosmic Ray Symposium 2014," *J. Phys. Conf. Ser.* **632** no. 1, (2015) 012093.

[20] T. Pierog, I. Karpenko, J. M. Katzy, E. Yatsenko, and K. Werner, "EPOS LHC: Test of collective hadronization with data measured at the CERN Large Hadron Collider," *Phys. Rev. C* **92** no. 3, (2015) 034906, arXiv:1306.0121 [hep-ph].

[21] F. Riehn, H. P. Dembinski, R. Engel, A. Fedynitch, T. K. Gaisser, and T. Stanev, "The hadronic interaction model SIBYLL 2.3c and Feynman scaling," *PoS* **ICRC2017** (2018) 301, arXiv:1709.07227 [hep-ph].

[22] S. Ostapchenko, "Monte Carlo treatment of hadronic interactions in enhanced Pomeron scheme: I. QGSJET-II model," *Phys. Rev. D* **83** (2011) 014018, arXiv:1010.1869 [hep-ph].

[23] **Pierre Auger** Collaboration, A. Castellina, "Highlights from the Pierre Auger Observatory," *PoS* **ICRC2019** (2021) 004, arXiv:1909.10791 [astro-ph.HE].

[24] **Pierre Auger** Collaboration, J. Abraham *et al.*, "The Fluorescence Detector of the Pierre Auger Observatory," *Nucl. Instrum. Meth.* **A620** (2010) 227–251, arXiv:0907.4282 [astro-ph.IM].

[25] M. C. Medina, M. Berisso, I. Allekotte, A. Etchegoyen, G. Tanco, and A. Supanitsky, "Enhancing the Pierre Auger Observatory to the 10^{17} to $10^{18.5}$ eV Range: Capabilities of an Infill Surface Array," *Nucl. Instrum. Meth. A* **566** (2006) 302–311, arXiv:astro-ph/0607115.

[26] **Pierre Auger** Collaboration, D. Nitz, "The front-end electronics for the Pierre Auger Observatory surface array," *IEEE Trans. Nucl. Sci.* **51** (2004) 413–419.

[27] P. D. J. Clark, D. Nitz, and Pierre Auger Observatory Collaboration, "Communications in the Auger Observatory," in *International Cosmic Ray Conference*, vol. 2 of *International Cosmic Ray Conference*, p. 765. Jan., 2001.

[28] **Pierre Auger** Collaboration, X. Bertou *et al.*, "Calibration of the surface array of the Pierre Auger Observatory," *Nucl. Instrum. Meth. A* **568** (2006) 839–846, arXiv:2102.01656 [astro-ph.HE].

[29] **Pierre Auger** Collaboration, M. Aglietta *et al.*, "Response of the Pierre Auger Observatory water Cherenkov detectors to muons," in *29th International Cosmic Ray Conference*. 7, 2005.

[30] **Pierre Auger** Collaboration, J. Abraham *et al.*, "Trigger and Aperture of the Surface Detector Array of the Pierre Auger Observatory," *Nucl. Instrum. Meth. A* **613** (2010) 29–39, arXiv:1111.6764 [astro-ph.IM].

[31] **Pierre Auger** Collaboration, A. Aab *et al.*, "Reconstruction of events recorded with the surface detector of the Pierre Auger Observatory," *JINST* **15** no. 10, (2020) P10021, arXiv:2007.09035 [astro-ph.IM].

[32] K. Kamata and J. Nishimura, "The Lateral and the Angular Structure Functions of Electron Showers," *Progress of Theoretical Physics Supplement* **6** (02, 1958) 93–155. https://doi.org/10.1143/PTPS.6.93.

[33] K. Greisen, "The extensive air showers," *Progress in Cosmic Ray Physics* **3** (1956) 1–141.

[34] **Pierre Auger** Collaboration, A. Aab *et al.*, "Measurement of the cosmic-ray energy spectrum above 2.5×10^{18} eV using the Pierre Auger Observatory," *Phys. Rev. D* **102** no. 6, (2020) 062005, arXiv:2008.06486 [astro-ph.HE].

[35] **Pierre Auger** Collaboration, C. Meurer and N. Scharf, "HEAT - a low energy enhancement of the Pierre Auger Observatory," *Astrophys. Space Sci. Trans.* **7** (2011) 183–186, arXiv:1106.1329 [astro-ph.IM].

[36] R. M. Baltrusaitis *et al.*, "THE UTAH FLY'S EYE DETECTOR," *Nucl. Instrum. Meth. A* **240** (1985) 410–428.

[37] J. H. Boyer, B. C. Knapp, E. J. Mannel, and M. Seman, "FADC-based DAQ for HiRes Fly's Eye," *Nucl. Instrum. Meth. A* **482** (2002) 457–474.

[38] Schott AG, "M-UG 6 Filter." https://www.schott.com/advanced_optics/english/products/optical-components/optical-filters/suntanning-filters/index.html. accessed October 2020.

[39] Photonis, *XP3062 Datasheet*. http://www.hzcphotonics.com/products/XP3062.pdf. accessed July 2021.

[40] S. Argiro *et al.*, "The analog signal processing system for the Auger fluorescence detector prototype," *IEEE Trans. Nucl. Sci.* **48** (2001) 444–449.

[41] "Tyvek." https://www.dupont.com/brands/tyvek.html. accessed November 2022.

[42] **Pierre Auger** Collaboration, P. Bauleo, J. Brack, L. Garrard, J. Harton, R. Knapik, R. Meyhandan, A. C. Rovero, A. Tamashiro, and D. Warner, "Absolute calibration of the Auger fluorescence detectors," in *29th International Cosmic Ray Conference*. 7, 2005. arXiv:astro-ph/0507347.

[43] J. T. Brack, R. Cope, A. Dorofeev, B. Gookin, J. L. Harton, Y. Petrov, and A. C. Rovero, "Absolute Calibration of a Large-diameter Light Source," *JINST* **8** (2013) P05014, arXiv:1305.1329 [astro-ph.IM].

[44] **Pierre Auger** Collaboration, P. Abreu *et al.*, "The XY Scanner - A Versatile Method of the Absolute End-to-End Calibration of Fluorescence Detectors," *PoS* **ICRC2021** (2021) 220.

[45] **Pierre Auger** Collaboration, R. Knapik *et al.*, "The Absolute, Relative and Multi-Wavelength Calibration of the Pierre Auger Observatory Fluorescence Detectors," in *30th International Cosmic Ray Conference*. 7, 2007. arXiv:0708.1924 [astro-ph].

[46] P. Bauleo *et al.*, " The generation of relative calibration constants for the FD," *GAP-Note* **2009-076** .

[47] **Pierre Auger** Collaboration, A. C. Rovero, P. Bauleo, J. T. Brack, J. L. Harton, and R. Knapik, "Multi-wavelength Calibration Procedure for the Pierre Auger Observatory Fluorescence Detectors," *Astropart. Phys.* **31** (2009) 305, arXiv:0811.1518 [astro-ph].

[48] S. Y. BenZvi *et al.*, "The Lidar System of the Pierre Auger Observatory," *Nucl. Instrum. Meth. A* **574** (2007) 171–184, arXiv:astro-ph/0609063.

[49] B. Fick, M. Malek, J. A. J. Matthews, J. Matthews, R. Meyhandan, M. Mostafá, M. Roberts, P. Sommers, and L. Wiencke, "The Central Laser Facility at the Pierre Auger Observatory," *JINST* **1** no. 11, (2006) P11003–P11003.

[50] D. Kuempel, K. H. Kampert, and M. Risse, "Geometry reconstruction of fluorescence detectors revisited," *Astropart. Phys.* **30** (2008) 167–174, arXiv:0806.4523 [astro-ph].

[51] The AERA Group, "AERA proposal for the construction of the 20 km^2 Auger Engineering Radio Array at the Southern Auger Observatory," *GAP-Note* **2009-172** .

[52] **Pierre Auger** Collaboration, A. Aab *et al.*, "Energy Estimation of Cosmic Rays with the Engineering Radio Array of the Pierre Auger Observatory," *Phys. Rev. D* **93** no. 12, (2016) 122005, arXiv:1508.04267 [astro-ph.HE].

[53] **Pierre Auger** Collaboration, A. Aab *et al.*, "Measurement of the Radiation Energy in the Radio Signal of Extensive Air Showers as a Universal Estimator of Cosmic-Ray Energy," *Phys. Rev. Lett.* **116** no. 24, (2016) 241101, arXiv:1605.02564 [astro-ph.HE].

[54] S. Argiro, S. Barroso, J. Gonzalez, L. Nellen, T. C. Paul, T. Porter, J. Prado, L., M. Roth, R. Ulrich, and D. Veberic, "The Offline Software Framework of the Pierre Auger Observatory," *Nucl. Instrum. Meth. A* **580** (2007) 1485–1496, arXiv:0707.1652 [astro-ph].

[55] P. Sommers, "Capabilities of a giant hybrid air shower detector," *Astropart. Phys.* **3** (1995) 349–360.

[56] **AIRFLY** Collaboration, M. Ave *et al.*, "Precise Measurement of the Absolute Fluorescence Yield of the 337 nm Band in Atmospheric Gases," *Astropart. Phys.* **42** (2013) 90–102, arXiv:1210.6734 [astro-ph.IM].

[57] **AIRFLY** Collaboration, M. Ave *et al.*, "Measurement of the pressure dependence of air fluorescence emission induced by electrons," *Astropart. Phys.* **28** (2007) 41–57, arXiv:astro-ph/0703132.

[58] D. Kruppke-Hansen and K.-H. Kampert, "High Quantum Efficiency Phototubes for Atmospheric Fluorescence Telescopes," in *31th International Cosmic Ray Conference*. 7, 2009. arXiv:0907.3670 [astro-ph.IM].

[59] D. Heck, J. Knapp, J. N. Capdevielle, G. Schatz, and T. Thouw, "CORSIKA: A Monte Carlo code to simulate extensive air showers,".

[60] D. Kruppke-Hansen. Private communication.

[61] D. Mandat, M. Pech, M. Palatka, L. Nozak, M. Hrabovsky, P. Schovanek, M. Prouza, and J. Ridky, "Optical properties of M-UG6 filter and the halo problem," *GAP-Note* **2009-164** .

[62] S. Querchfeld, "Test neuer Photomultiplier für die Entwicklung einer Auger-Nord Fluoreszenz Kamera," Diplomarbeit, Bergische Universität Wuppertal, Juli, 2010.

[63] D. Paneque, *The MAGIC Telescope: development of new technologies and first observations*. PhD thesis, Tech. U., Munich (main), 2004.

[64] **CTA Consortium** Collaboration, M. Actis *et al.*, "Design concepts for the Cherenkov Telescope Array CTA: An advanced facility for ground-based high-energy gamma-ray astronomy," *Exper. Astron.* **32** (2011) 193–316, arXiv:1008.3703 [astro-ph.IM].

[65] **CTA Consortium** Collaboration, T. Toyama *et al.*, "Novel Photo Multiplier Tubes for the Cherenkov Telescope Array Project," in *33rd International Cosmic Ray Conference*. 7, 2013. arXiv:1307.5463 [astro-ph.IM].

[66] Hamamatsu Photonics K.K., *R9420-100 Datasheet*. https://www.hamamatsu.com/resources/pdf/etd/High_energy_PMT_TPMZ0003E.pdf. accessed Mai 2017.

[67] Hamamatsu Photonics K.K., *Hamamatsu R11920-100 Datasheet*. private communication July 2014.

[68] J. M. Kopfer, *Development of a prototype camera and Monte Carlo studies for the optimisation of the CBM-RICH detector*. PhD thesis, Bergische Universität Wuppertal, 2014.

[69] K. H. Becker *et al.*, "Qualification tests of the 11000 photomultipliers for the Pierre Auger Observatory fluorescence detectors," *Nucl. Instrum. Meth.* **A576** (2007) 301–311.

[70] K.-H. Becker *et al.*, "Photomultiplier Testing for the Fluorescence Detector of the Pierre Auger Observatory in Wuppertal," *GAP-Note* **2004-053** .

[71] M. L. Knötig, "Light Sensor Candidates for the Cherenkov Telescope Array," Diplomarbeit, Technische Universität München, April, 2012.

[72] C. Aramo, F. Bracci, G. Gallo, *et al.*, "The Camera of the Auger Fluorescence Detector," *GAP-Note* **1999-027** .

[73] W. Welford and R. Winston, *The Optics of Nonimaging Concentrators: Light and Solar Energy*. Academic Press, Inc., 1978.

[74] V. K. Baranov, "Optiko-mekhanicheskaya promyshlennost," **6** (1965) 1–5.

[75] H. Hinterberger and R. Winston, "Efficient light coupler for threshold Cherenkov counters," *Rev. Sci. Instrum.* **37** (1966) 1094–1095.

[76] R. Winston, J. Minano, and P. Benitez, *Nonimaging Optics*. Academic Press, 2004.

[77] A. Okumura, K. Noda, and C. Rulten, "ROBAST: Development of a ROOT-Based Ray-Tracing Library for Cosmic-Ray Telescopes and its Applications in the Cherenkov Telescope Array," *Astropart. Phys.* **76** (2016) 38–47, arXiv:1512.04369 [astro-ph.IM].

[78] I. Antcheva *et al.*, "ROOT: A C++ framework for petabyte data storage, statistical analysis and visualization," *Comput. Phys. Commun.* **180** (2009) 2499–2512, arXiv:1508.07749 [physics.data-an].

[79] Alanod GmbH & Co. KG, *4300UP Datasheet*. https://alanod.com/_Resources/Static/Packages/Moon.AlanodAXAdapter/files-data/4300UP_de.pdf. accessed June 2015.

[80] Konica Minolta, *CM2500 Datasheet*. https://www5.konicaminolta.eu/en/measuring-instruments/products/colour-measurement/spectrophotometers-portable/cm-2600d-cm-2500d/specifications.html. accessed August 2018.

[81] Material House, *Miro 3UV*. https://www.materialhouse.co.jp/miro-top/miro-3uv/. accessed April 2023.

[82] Alux Luxar GmbH & Co. KG. `http://alux-luxar.de`. accessed June 2015.

[83] S. Querchfeld, K.-H. Kampert, and J. Rautenberg, "Development of a highly efficient PMT Winston-cone system for fluorescence measurement of extensive air showers," *PoS* **ICRC2015** (2016) 677.

[84] G. Matthiae, P. Petrinca, and V. Privitera, P. abd Verzi, "Results of the tests in Roma on the PMT/HE units of the Fluorescence Detector," *GAP-Note* **2004-064** .

[85] **Pierre Auger** Collaboration, J. Abraham *et al.*, "Calibration and Monitoring of the Pierre Auger Observatory," in *31st International Cosmic Ray Conference*. 6, 2009. `arXiv:0906.2358 [astro-ph.IM]`.

[86] A. Newman, S. Y. BenZvi, B. M. Connolly, M. Prouza, and S. Westerhoff, "Night sky brightness variations determined from FD background data," *GAP-Note* **2006-090** .

[87] M. Kleifges, A. Menshikov, D. Chernyakhovsky, and H. Gemmeke, "Statistical current monitor for the cosmic ray experiment Pierre Auger," *IEEE Trans. Nucl. Sci.* **50** (2003) 1204–1207.

[88] P. Nguyen, B. Dawson, and J. Bellido, "Cross Check of the Fluorescence Detector Calibration Using the Night Sky Background," *GAP-Note* **2016-005** .

[89] L. Niemietz, K.-H. Becker, K. Daumiller, D. Gonzalez, K.-H. Kampert, H.-O. Klages, J. Kleinfeller, A. Menshikov, and J. Rautenberg, "Pixel-by-Pixel calibration for the Pierre Auger fluorescence telescopes," *GAP-Note* **2010-124** .

[90] R. B. Cleveland, W. S. Cleveland, and I. Terpenning, "Stl: A seasonal-trend decomposition procedure based on loess," *Journal of Official Statistics* **6** no. 1, (03, 1990) 3–73.

[91] K. Bandara, R. J. Hyndman, and C. Bergmeir, "Mstl: A seasonal-trend decomposition algorithm for time series with multiple seasonal patterns," 2021.

[92] J. F. Debatin, *Preparation of the Operation and Calibration of the Fluorescence Detector of AugerPrime*. PhD thesis, Karlsruher Institut für Technologie (KIT), 2020. 51.03.03; LK 01.

[93] A. Segreto, "Using stars to verify the end-to-end absolute calibration and for the long term monitoring of the Fluorescence Detector telescopes at the Pierre Auger Observatory," *GAP-Note* **2016-042** .

[94] **Pierre Auger** Collaboration, A. Aab *et al.*, "The Pierre Auger Observatory Upgrade - Preliminary Design Report," `arXiv:1604.03637 [astro-ph.IM]`.

[95] D. Beznosko, A. Bross, A. Dyshkant, A. Pla-Dalmau, and V. Rykalin, "FNAL-NICADD extruded scintillator,".

[96] A. Dyshkant *et al.*, "About NICADD extruded scintillating strips,".

[97] Yashin, Igor and Ampilogov, Nikolay and Astapov, Ivan and Barbashina, N and Borog, Vladimir and Chernov, D and Dmitrieva, Anna and Kompaniets, K and A Petrukhin, A and V Shutenko, V and A Timashkov, D, "Scintillation hodoscope for muon diagnostics," *31st International Cosmic Ray Conference, ICRC 2009* (2009) .

[98] N. Barenthien, H. Bolz, K. Daumiller, R. Engel, H. Kern, M. Keßler, J. Maintok, H.-J. Mathes, M. Riegel, M. Roth, A. Schult, R. Smida, A. Streich, D. Veberic, and G. Woerner, "Scintillator Surface Detectors of the Engineering Array: Production and Validation," *GAP-Note* **2016-040** .

[99] Hamamatsu Photonics K.K., *Hamamatsu R9420 Datasheet*. `https://www.hamamatsu.com/resources/pdf/etd/R9420_TPMH1296E.pdf`. accessed Mai 2017.

[100] Hamamatsu Photonics K.K., *Hamamatsu R8619 Datasheet*. `http://www.hamamatsu.com/resources/pdf/etd/R8619_TPMH1331E.pdf`. accessed Mai 2017.

[101] Electron Tubes, *Electron Tubes 9902B Datasheet*, Mai, 2017. `https://my.et-enterprises.com/pdf/9902B.pdf`.

[102] G. Cataldi and M. R. Coluccia. Private communication.

[103] M. Buscemi *et al.*, "A facility to validate photomultipliers for the upgrade of the Pierre Auger Observatory.," *JINST* **15** no. 07, (2020) P07011.

[104] D. Bonanno, D. Bongiovanni, M. Buscemi, R. Caruso, D. Lo Pesti, F. Longhitano, C. Aramo, F. Barbato, R. Colalillo, F. Guarino, I. Rea, and L. Valore, "A facility to test the AugerPrime PMTs," *GAP-Note* **2017-004** .

[105] C. Berat, P. Brenas, A. Heusch, A. Jacquet, F. Montanet, J. Souchard, and P. Stassi, "Scintillator Surface Detector for the Upgrade of the Pierre Auger Observatory," *GAP-Note* **2019-064** .

[106] iseg, *ISEG High Voltage Power Supplies*. `http://www.iseg-hv.com/files/iseg-high-voltage-power-supplies.pdf`. accessed January 2017.

[107] CAEN, *CAEN User Manual 3262 Rev. 3*. `http://www.caen.it/servlet/checkCaenManualFile?Id=11612`. accessed January 2017.

[108] T. Hakamata *et al.*, *Photomultiplier Tubes - Basics and Applications*, ch. 13.1, pp. 234–239. Hamamatsu Photonics K.K., 3a ed., 2007.

[109] M. Aglietta *et al.*, " A measurement of the thermal sensitivity of the new AugerPrime photomultipliers," *GAP-Note* **2016-078** .

[110] T. Hakamata *et al.*, *Photomultiplier Tubes - Basics and Applications*, ch. 4.1.4, pp. 38–41. Hamamatsu Photonics K.K., 3a ed., 2007.

[111] T. Hakamata *et al.*, *Photomultiplier Tubes - Basics and Applications*, ch. 13.1, p. 239. Hamamatsu Photonics K.K., 3a ed., 2007.

[112] Z. Zong, G. Hull, M. Imre, M. Josselin, A. Maroni, T. Suomijärvi, K. Daumiller, R. Engel, H.-J. Mathes, M. Riegel, M. Roth, R. Šmída, A. Streich, and D. Veberič, "Study of light yield for different configurations of plastic scintillators and wavelength shifting fibers," *Nuclear Instruments and Methods in Physics Research Section A: Accelerators, Spectrometers, Detectors and Associated Equipment* **908** (2018) 82–90. `https://www.sciencedirect.com/science/article/pii/S0168900218309823`.

[113] S. Messina, *Extension to lower energies of the cosmic-ray energy window at the Pierre Auger Observatory*. PhD thesis, University of Groningen, 2016.

[114] **Pierre Auger** Collaboration, G. Cataldi, "The upgrade of the Pierre Auger Observatory with the Scintillator Surface Detector," *PoS* **ICRC2021** (2021) 251.

[115] G. Cataldi, M. Conte, F. Convenga, F. de Palma, and D. Martello, "Evaluation of control parameters for the operational stability of the SSD," *GAP-Note* **2022-038** .

[116] **Pierre Auger** Collaboration, P. Abreu *et al.*, "Reconstruction of Events Recorded with the Water-Cherenkov and Scintillator Surface Detectors of the Pierre Auger Observatory," *PoS* **ICRC2021** (2021) 218.

[117] A. Streich, *Performance of the Upgraded Surface Detector of the Pierre Auger Observatory*. PhD thesis, Karlsruher Institut für Technologie (KIT), 2023. 51.13.03; LK 01.

[118] **Pierre Auger** Collaboration, J. Abraham *et al.*, "Properties and performance of the prototype instrument for the Pierre Auger Observatory," *Nucl. Instrum. Meth. A* **523** (2004) 50–95.

[119] B. Genolini, M. Aglietta, A. Creusot, W. Fulgione, F. Gomez, I. Lhenry-Yvon, C. Morello, G. Navarra, T. Nguyen Trung, J. Pouthas, T. Suomijärvi, and C. Vigorito, "Low Power High Dynamic Range Photomultiplier Bases for the Surface Detectors of the Pierre Auger Observatory ," *GAP-Note* **2002-038** .

[120] **LHAASO** Collaboration, H. Lv, X. Sheng, H. He, J. Liu, Z. Zhang, C. Hou, and J. Zhao, "Extension of photomultiplier tube dynamic range for the LHAASO-KM2A electromagnetic particle detectors," *Nucl. Instrum. Meth.* **A781** (2015) 34–38.

[121] D. Nitz, "UUB V2 Analog Performance," *GAP-Note* **2018-019** .

[122] R. Ulrich, D. Pearson, and P. Sommers, "Relative FD-Calibration," *GAP-Note* **2010-116** .

[123] A. GmbH, *Picosecond Diode Lasers with Drivers*. `https://www.alphalas.com/images/stories/products/lasers/Picosecond_Pulse_Diode_Lasers_with_Driver_PICOPOWER-LD_ALPHALAS.pdf`. accessed June 2023.

[124] J. Adamczewski-Musch *et al.*, "The CBM RICH project," *Nucl. Instrum. Meth.* **A845** (2017) 434–438.

[125] U. Trunk *et al.*, "n-XYTER: A CMOS read-out ASIC for a new generation of high rate multichannel counting mode neutron detectors," in *Proceedings, 12th Workshop on Electronics for LHC and Future Experiments, Valencia, Spain, 25-29 September 2006*, pp. 534–538. 2006. `http://doc.cern.ch/yellowrep/2007/2007-001/p534.pdf`.

[126] Struck, *SIS3300 8 Channel 100 MHz 12-bit ADC*. `https://www.struck.de/sis3300.htm`. accessed April 2021.

[127] T. Hakamata *et al.*, *Photomultiplier Tubes - Basics and Applications*, ch. 4.3.2, pp. 54–58. Hamamatsu Photonics K.K., 3a ed., 2007.

Acknowledgements

This has been a very long but exciting journey that is finally coming to an end. From interesting conferences around the world to standing in the dark in the middle of nowhere and catching an octocopter in the Argentinian Pampas at night after a scorpion had just ran across the keyboard of the laptop - I will always cherish these memories. But it would not have been possible without the support of a number of people.

First of all, I am very grateful to Prof. Dr. Karl-Heinz Kampert for giving me the opportunity to work on various interesting topics in his research group. Since he was my mentor already in the first semester of the diploma, I am thankful for his guidance and expertise, which he also provided during late measurements in the lab.

I would like to thank Prof. Daniele Martello for agreeing to review my thesis and the collaboration on the PMT measurements for the AugerPrime update.

Many thanks are due to 'uncle Titus' Dr. Julian Rautenberg for his tireless support and sharing the most thrilling ride to (or to be more precise from) Argentina.

A special thanks to my fellow 'detectives' Lukas and Jens for being able to work with friends and here's to many more 'cases' to solve.

During my time in the astroparticle group many people have come and gone, and to mention them all would probably be even longer than this thesis. So a big thank you to all those with whom I shared these wonderful years and who made me feel so welcome that I didn't want to leave.

As one of the few people, who have been in this group longer than me, I would like to thank Karl-Heinz Becker for his technical support, teaching me how to solder, and how to come around an initial 'no' ;-).

A lot of gratitude to Maria and Joe for making this thesis more understandable.

I want to thank my family and friends for their loving support and standing by me all those years.

I am infinitely grateful to my two sons for always managing to cheer me up, especially in the last phase. And last but not least my biggest gratitude belongs to my wife Ruth, who supported me all this time and encouraged me to keep going even after missing deadline after deadline. I couldn't have done it without you.

Declaration of Authorship

English

I hereby declare that the thesis submitted is my own unaided work. All direct or indirect sources used are acknowledged as references.

This thesis was not previously presented to another examination board and has not been published.

Deutsch

Hiermit versichere ich, die vorliegende Arbeit selbstständig und unter ausschließlicher Verwendung der angegebenen Literatur und Hilfsmittel erstellt zu haben.

Die Arbeit wurde bisher in gleicher oder ähnlicher Form keiner anderen Prüfungsbehörde vorgelegt und auch nicht veröffentlicht.

Wuppertal, den _____ _____

(Sven Querchfeld)